

CANDU REACTOR INTERMITTENT BUOYANCY INDUCED FLOW ANALYSIS

ANALYSIS OF INTERMITTENT BUOYANCY INDUCED FLOW IN
ASYMMETRICALLY OBSTRUCTED CANDU NUCLEAR REACTOR FUEL
CHANNELS

By

J. Spencer

A Thesis

Submitted to the School of Graduate Studies

in Partial Fulfillment of the Requirements

for the Degree

Master of Applied Science

McMaster University

© Copyright by J. Spencer, April 2010.

MASTER OF APPLIED SCIENCE (2010)
(Engineering Physics)

McMaster University
Hamilton, Ontario, Canada

TITLE: Analysis of Intermittent Buoyancy Induced Flow in
Asymmetrically Obstructed CANDU Nuclear Reactor Fuel Channels.

AUTHOR: J. Spencer

SUPERVISOR: Dr. D.R. Novog

NUMBER OF PAGES: 221

ABSTRACT

CANDU reactors have a large number of active and passive systems which help to mitigate events such as a loss of forced cooling or a loss of electrical power. During these events, decay heat must be removed using either emergency power driven active systems or through natural circulation phenomena. Depending on the configuration of the core at the time of the event, single or two-phase natural circulation is available to transport energy from the core to the steam generators which act as a heat sink. However, in some configurations (such as during a maintenance outage) natural circulation to the boilers may be precluded due to either the boilers or heat transport system being partially drained. Under these conditions flow may stagnate in the horizontal fuel channels which will initiate a mode of circulation known as Intermittent Buoyancy Induced Flow (IBIF).

During IBIF, void generated in the center of the core will periodically reach a feeder and vent from the channel due to buoyancy induced forces, with liquid entering the channel from the opposite feeder, cooling the fuel. Analysis is typically performed to demonstrate that during the period of time from stagnation to venting fuel temperatures remain within their acceptance criteria. This mode of emergency heat removal can remove sufficient heat to preclude fuel failures until such time as forced flow can be re-established.

It is assumed in most analysis that completely symmetrical configurations represent the worst possible configuration since most asymmetries (i.e., in channel axial heat flux, channel creep etc.), would lead to earlier venting and hence lower fuel temperatures. However, asymmetry in the form of a partial obstruction in the fuel channel during IBIF may occur due to maintenance or inspection activities – a scenario that has not been included in previous experimental and computational work on IBIF. This paper presents the analysis of the impact of partial flow obstruction on IBIF scenarios. A model is constructed using the code GOTHIC, and is benchmarked against experimental data from the Cold Water Injection Test (CWIT) facility for both the symmetrical and asymmetrical configurations. The work demonstrates that for single-phase IBIF, the impact of partial obstructions is not prohibitive. Computational demands precluded the completion of two-phase simulations in a reasonable timeframe; however useful insights and observations are drawn from the early stages that are successfully simulated.

ACKNOWLEDGEMENTS

I am very grateful to the many people who have assisted me with this work. My thanks go first to Ontario Power Generation and AMEC NSS for supplying the funding, data, code access, and work space I made use of. I also greatly appreciate the time taken by Dr. Yuksel Parlatan and Guanjun Wang of OPG and Hisham Hasanein and William Bowman of AMEC NSS to review and approve the publication of my work.

While engaged in this venture, I have benefitted greatly from the knowledge, experience, and expert guidance of Dr. David Novog and Dr. Ab Tahir. The assistance provided by Shawn MacIntosh and Xi-Qing Chen with the practical application of GOTHIC illuminated many issues and saved me hours of frustration and confusion. Finally, the patches and detailed explanations of various aspects of the GOTHIC code provided by Tom George of Numerical Applications, Inc. were invaluable assets.

TABLE OF CONTENTS

1	INTRODUCTION.....	11
1.1	CANDU Reactor Design	13
1.2	Heat Sinks.....	16
1.3	Intermittent Buoyancy Induced Flow	19
1.4	Scope and Structure of Report.....	25
2	BACKGROUND & LITERATURE REVIEW	27
2.1	Best Estimate and Conservative Analysis	27
2.2	Approaches to Modelling IBIF.....	27
2.3	Literature in Areas Related to IBIF	34
2.3.1	Natural Circulation in CANDU Reactors	34
2.3.2	Natural Circulation in PWRs	42
2.3.3	Stability of Natural Circulation.....	47
2.3.4	Severe Accidents	49
2.4	Natural Circulation Modelling Using GOTHIC	50
3	METHODOLOGY.....	55
3.1	CWIT Facility Description	55
3.1.1	Fuel Element Simulators.....	56
3.1.2	Pressure Tube.....	57
3.1.3	End Fittings.....	58
3.1.4	Feeders and Headers	58
3.1.5	Thermocouples	61
3.1.6	CWIT Experimental Conditions	64
3.2	GOTHIC Code Description.....	64
3.3	Description of Reference Models	66
3.3.1	Modelling Assumptions.....	66
3.3.2	Modelling Methodology	68
3.4	Description of Sensitivity Models	89
3.4.1	Asymmetrical Obstruction Models	89
3.4.2	Grid Sensitivity Models.....	91
3.4.3	End Fitting – Feeder Flow Path Location Sensitivity Models	93
4	RESULTS	94
4.1	Simple Analytical Models of CWIT.....	96
4.1.1	Adiabatic Pin Heatup	96
4.1.2	Single-Phase Channel Heatup.....	99
4.1.3	Vapour Production Rate.....	105
4.1.4	End Fitting Heatup.....	107
4.2	Reference Case Results	112
4.2.1	Low Power.....	112
4.2.2	High Power	124
4.3	Sensitivity Simulation Results.....	139
4.3.1	End Fitting – Feeder Flow Path Location Sensitivity	139
4.3.2	Nodalisation Sensitivity.....	144
4.4	Benchmarking of Reference Simulations Against CWIT Facility Data	146
4.4.1	Low Power.....	146
4.4.2	High Power.....	157
4.5	Asymmetrical Obstruction Model Results.....	169

4.5.1	Low Power.....	169
4.5.2	High Power.....	180
5	CONCLUSIONS	182
5.1	Single-Phase IBIF.....	182
5.2	Two-Phase IBIF.....	182
5.3	Recommendations for Future Work.....	182
	REFERENCES	184
APPENDIX A	GOTHIC MODEL DEVELOPMENT	187
APPENDIX B	HIGH POWER OBSTRUCTION MODEL RESULTS	197
APPENDIX C	END FITTING HEAT TRANSFER COEFFICIENTS.....	217
APPENDIX D	REYNOLDS NUMBERS DURING TRANSIENTS	219
APPENDIX E	VERTICAL VAPOUR VELOCITY IN CENTRE OF CHANNEL	221

LIST OF FIGURES

Figure 1 - Decay Heat Produced in Fuel vs. Time After Shutdown From Full Power	12
Figure 2 - Fuel Channel Schematic A.....	13
Figure 3 - Fuel Channel Schematic B.....	14
Figure 4 - CANDU Primary Heat Transport System.....	15
Figure 5 - Secondary Side Heat Transport System Schematic	16
Figure 6 - IBIF Phase 1 – Onset of Boiling	20
Figure 7 - IBIF Phase 2 – Bubble Growth.....	21
Figure 8 - IBIF Phase 3 – Heat Transfer to End Fitting.....	21
Figure 9 - IBIF Phase 4 – Venting and Refill	22
Figure 10 - Percentage Difference Between Duration of Channel Flow Stagnation Predicted by Thermoss-II and Observed in Thermally Symmetric [6].....	29
Figure 11 - Comparison of the 450 °C Sheat Temperature Curve with the 400 °C Pressure Tube Temperature Curve [4]	31
Figure 12 - 450 °C Sheath Temperature Map Relating Initial Coolant Subcooling to Percent of 7.3 MW Channel Power and Channel Pressure for a Fuel Burnup of 50 MW h / kg U [4].....	32
Figure 13 - 450 °C Sheath Temperature Map Relating Initial Coolant Subcooling to Percent of 7.3 MW Channel Power and Channel Pressure for a Fuel Burnup of 230 MW h / kg U [4].....	33
Figure 14 - Effect of Pressure Tube Sag on Air Venting Time [9].....	34
Figure 15 - Heat Transport System Natural Circulation Model [10].....	36
Figure 16 - RD-14M Boiler Tube Friction Pressure Drop Multiplier vs. Gravity Head Difference [10]	38
Figure 17 - Predicted and Test Results for RD-14M Inlet-to-Outlet Header Pressure Differential vs. HTS Coolant Inventory (Secondary Side Pressure = 4.6 MPa) [10].....	39
Figure 18 - Predicted and Test Results for RD-14M Inlet-to-Outlet Header Pressure Differential vs. HTS Coolant Inventory (Secondary Side Pressure = 1.1 MPa) [10].....	40
Figure 19 - Predicted RD-14M Inlet-to-Outlet Header Pressure Differential vs. HTS Coolant Inventory (Secondary Side Pressure = 1.1 MPa) [10]	41
Figure 20 - Pickering RIH-to-ROH Pressure Differential vs. HTS Coolant Inventory with No	

Channel Flow Reversal [10]	42
Figure 21 - Characterisation of Natural Circulation Flow Regimes Based on Experimental Data and System Codes Calculations. [11]	45
Figure 22 - Evaluation of Natural Circulation Performance for Pactel and RD14M Simulators by Using the NCFM. [11].....	46
Figure 23 - Core Damage Progression in CANDU Reactor Beyond-Design-Basis Accidents [2].	50
Figure 24 - Comparison of Steam Generator Tube Temperature Profiles for Single-Phase Natural Circulation [19]	53
Figure 25 - Natural Circulation Characteristics Comparison [19].....	54
Figure 26 - Schematic of CWIT Facility [5].....	56
Figure 27 - CWIT End Fitting [5].....	58
Figure 28 - Feeder Geometry [5].....	60
Figure 29 - CWIT Thermocouple Locations – Planes	61
Figure 30 - CWIT Thermocouple Locations – Cross Section	62
Figure 31 - CWIT End Fitting Thermocouple Location Schematic – Planes	63
Figure 32 - CWIT End Fitting Thermocouple Location Schematic – Cross Section.....	63
Figure 33 - GOTHIC Momentum Balance [26]	66
Figure 34 - GOTHIC Model Schematic	69
Figure 35 - GOTHIC Model Channel Nodalisation Cross-Section	70
Figure 36 - GOTHIC Model Fuel Element Simulator Heated Section Thermal Subdivision	79
Figure 37 - Schematic of End Fitting Model	82
Figure 38 - Schematic of End Fitting Opening.....	87
Figure 39 - Flow Path Sensitivity Locations	93
Figure 40 - Near-Adiabatic Pin Heatup During CWIT Test #1613	99
Figure 41 - Single Phase Channel Heatup Rates	101
Figure 42 - Single Phase Channel Heatup Rate, Comparison of Simple Model Prediction to CWIT Test #1613 Data – Plane B	102
Figure 43 - Single Phase Channel Heatup Rate, Comparison of Simple Model Prediction to CWIT Test #1613 Data – Plane F1.....	103
Figure 44 - Single Phase Channel Heatup Rate, Comparison of Simple Model Prediction to CWIT Test #1617 Data – Plane B	104
Figure 45 - Single Phase Channel Heatup Rate, Comparison of Simple Model Prediction to CWIT Test #1617 Data – Plane F1.....	105
Figure 46 - Upstream End Fitting Temperature Transients – CWIT Test #1613	110
Figure 47 - Downstream End Fitting Temperature Transients – CWIT Test #1613	111
Figure 48 - Pin 10 Temperature vs. Time, Planes F1 and G1.....	113
Figure 49 - Flow Into End Fittings From Feeders	114
Figure 50 - Flow Velocity Profile Cells – Channel	115
Figure 51 - Flow Velocity Profile Cells – End Fitting.....	116
Figure 52 - 20 kW Reference Case Axial Flow Velocity Profile – Planes B and F1.....	117
Figure 53 - 20 kW Reference Case Axial Flow Velocity Profile – Planes G1 and K.....	118
Figure 54 - 20 kW Reference Case Axial Flow Velocity Profile – Planes U1 and U4.....	119
Figure 55 - 20 kW Reference Case Axial Flow Velocity Profile – Planes D1 and D4.....	120
Figure 56 - Temperature Transients At Plane F1.....	121
Figure 57 - Pin 10 Temperature Transients Along Channel	122
Figure 58 - Upstream End Fitting Temperature Transients	123
Figure 59 - Downstream End Fitting Temperature Transients	124
Figure 60 – High Power Reference Case Feeder Flow Rate Transients	125
Figure 61 – Temperature Transients, Plane F1	127
Figure 62 – Vapour Fraction and Liquid and Vapour Velocity Profiles, Plane B	129
Figure 63 – Vapour Fraction and Liquid and Vapour Velocity Profiles, Plane F1.....	130
Figure 64 – Vapour Fraction and Liquid and Vapour Velocity Profiles, Plane G1	131
Figure 65 – Vapour Fraction and Liquid and Vapour Velocity Profiles, Plane K.....	132

Figure 66 – Element Temperature Transients, Plane F1.....	134
Figure 67 – Pin 10 Temperature Transient Along Channel.....	135
Figure 68 – Upstream End Fitting Temperature Transients.....	136
Figure 69 – Downstream End Fitting Temperature Transients.....	137
Figure 70 – Extrapolated End Fitting Heatup.....	138
Figure 71 - Temperature Transient, Pin 10, Plane F1, Feeder Position Sensitivity.....	140
Figure 72 - Feeder Flow Rate, Feeder Position Sensitivity.....	141
Figure 73 - Axial Flow Velocity Profile In Upstream End Fitting, Feeder Position Sensitivity – Plane U1.....	142
Figure 74 - Axial Flow Velocity Profile In Upstream End Fitting, Feeder Position Sensitivity – Plane U1.....	143
Figure 75 - Pin 10, Plane F1 Temperature Transient – Fine Mesh vs. Reference Model.....	145
Figure 76 - Flow Rate Into End Fittings From Feeders – Fine Mesh vs. Reference Model.....	146
Figure 77 - Maximum Temperature Reached At Different Planes During IBIF – Pin 10.....	147
Figure 78 - Predicted and Observed Temperature Transients, Pin 10 – Test #1617.....	149
Figure 79 - Predicted and Observed Temperature Transients, Pin 10 – Test #1617.....	150
Figure 80 - Predicted and Observed Temperature Transients, Pin 37 – Test #1617.....	151
Figure 81 - Predicted and Observed Temperature Transients, Pin 37 – Test #1617.....	152
Figure 82 - Predicted and Observed Temperature Transients, Pressure Tube – Test #1617.....	153
Figure 83 - Predicted and Observed Temperature Transients, Pressure Tube – Test #1617.....	154
Figure 84 - Predicted and Observed Temperature Transients, Plane U1 – Test #1617.....	155
Figure 85 - Predicted and Observed Temperature Transients, Plane D1 – Test #1617.....	156
Figure 86 – Predicted and Observed Temperature Transients, Pin 10 – Test #1613.....	158
Figure 87 – Predicted and Observed Temperature Transients, Pin 10 – Test #1613.....	159
Figure 88 – Predicted and Observed Temperature Transients, Pin 24 – Test #1613.....	160
Figure 89 – Predicted and Observed Temperature Transients, Pin 24 – Test #1613.....	161
Figure 90 – Predicted and Observed Temperature Transients, Pin 37 – Test #1613.....	162
Figure 91 – Predicted and Observed Temperature Transients, Pin 37 – Test #1613.....	163
Figure 92 – Predicted and Observed Temperature Transients, Pressure Tube – Test #1613.....	164
Figure 93 – Predicted and Observed Temperature Transients, Pressure Tube – Test #1613.....	165
Figure 94 – Predicted and Observed Temperature Transients, Plane U1 – Test #1613.....	167
Figure 95 – Predicted and Observed Temperature Transients, Plane D1 – Test #1613.....	168
Figure 96 - Maximum Pin Temperatures Reached During IBIF Cycle.....	170
Figure 97 - Temperature Transients For 0% - 91% Obstruction Cases - Pin 10, Plane F1.....	171
Figure 98 - Fluid Flow Through Downstream Feeder For 0% - 91% Obstruction Cases.....	172
Figure 99 - Logarithmic Plots of Fluid Flow Through Feeders For 0% - 91% Obstruction Cases.....	173
Figure 100 - Temperature Transients For 92% - 95% Obstruction Cases - Pin 10, Plane F1.....	174
Figure 101 - Fluid Flow Through Downstream Feeder For 92% - 95% Obstruction Cases.....	175
Figure 102 - Logarithmic Plots of Fluid Flow Through Feeders For 92% - 95% Obstruction Cases	176
Figure 103 - Temperature Transients For 96% - 100% Obstruction Cases - Pin 10, Plane F1.....	177
Figure 104 - Fluid Flow Through Downstream Feeder For 96% - 100% Obstruction Cases.....	178
Figure 105 - Logarithmic Plots of Fluid Flow Through Feeders For 96% - 100% Obstruction Cases	179
Figure 106 – CWIT and Modelled Power Level As a Function of Axial Channel Position.....	196
Figure 107 – Pin 10 Temperature Transient Variation With Blockage, Plane F1.....	198
Figure 108 – Feeder Flow Difference (Upstream Flow – Downstream Flow).....	200
Figure 109 – Vapour Fraction Profile as a Function of Blockage: Plane B, 245 s.....	202
Figure 110 – Vapour Fraction Profile as a Function of Blockage: Plane F1, 245 s.....	203
Figure 111 – Vapour Fraction Profile as a Function of Blockage: Plane G1, 245 s.....	204
Figure 112 – Vapour Fraction Profile as a Function of Blockage: Plane K, 245 s.....	205
Figure 113 – Vapour Temperature Profile as a Function of Blockage: Plane B, 245 s.....	207
Figure 114 – Vapour Temperature Profile as a Function of Blockage: Plane F1, 245 s.....	208

Figure 115 – Vapour Temperature Profile as a Function of Blockage: Plane G1, 245 s	209
Figure 116 – Vapour Temperature Profile as a Function of Blockage: Plane K, 245 s	210
Figure 117 – End Fitting Temperature Profile, Reference Case	212
Figure 118 – End Fitting Temperature Profile, 99% Blockage Case	213
Figure 119 – Downstream End Fitting Temperature Profiles, Middle Elevation	215
Figure 120 – Heat Transfer Coefficient Between Liquid and Top of End Fitting, Low Power Reference Case	217
Figure 121 – Heat Transfer Coefficient Between Liquid and Top of End Fitting, High Power Reference Case	218
Figure 122 – Liquid Reynolds Number Transient, Low Power Reference Case	219
Figure 123 – Liquid Reynolds Number Transient, High Power Reference Case	220
Figure 124 – Vapour Reynolds Number Transient, High Power Reference Case	220
Figure 125 – Vertical Component of Vapour Velocity, Plane F1, High Power Reference Case, Linear Scale	221
Figure 126 – Vertical Component of Vapour Velocity, Plane F1, High Power Reference Case, Log Scale	221

LIST OF TABLES

Table 1 – Typical CANDU Heat Sinks	17
Table 2 - Processes and Phenomena Involved in IBIF	23
Table 3 - Number of RD-14M Boiler Tubes Experiencing Vapour-Lock [10]	37
Table 4 - RD-14M Test Parameters	38
Table 5 - Comparison of GOTHIC Results and Test Data in Primary Cooling Modes [19]	52
Table 6 - CWIT Experimental Conditions	64
Table 7 - Power Profile Factors	75
Table 8 - Dead Space Equivalent Conductor Composition	85
Table 9 - Feeder Volume Details (in order from end fitting to header)	88
Table 10 - Characterisation of Obstruction Cases	90
Table 11 - Characterisation of Obstruction Cases with a Refined Mesh	92
Table 12 - Case Matrix	94
Table 13 - Axial Location Correspondence Between CWIT Rig and Model	95
Table 14 - CWIT Thermocouple Data Used for Comparison to Simulation Results	96
Table 15 - Adiabatic Pin Heatup Rates – 20 kW / Channel	97
Table 16 - Adiabatic Pin Heatup Rates – 131 kW / Channel	97
Table 17 - Single-Phase Channel Heatup Rates	100
Table 18 - Vapour Production Rates At Saturated Conditions	106
Table 19 - End Fitting Component Thermal Characteristics	107
Table 20 - End Fitting Heatup Rate	108
Table 21 - End Fitting Heatup Time From 30C to Saturation	108
Table 22 - End Fitting Heatup From 30C to Saturation Axial Progression Rate	109
Table 23 - Nodalisation Details Used For Reference and Sensitivity Models	144
Table 24 - Deviation of GOTHIC Results from CWIT Data	147
Table 25 - Maximum Pin Temperatures Reached During IBIF Cycle	170
Table 26 - Material Data – Inconel-600 [28]	187
Table 27 - Material Data – Zircalloy-2.5% Niobium	187
Table 28 - Material Data – Type-403 Stainless Steel	188
Table 29 - Material Data – Water Substitute	188
Table 30 – Pin Location in Channel Control Volumes	188
Table 31 – High Power Case FES Volumetric Power (kW/m ³)	189
Table 32 – Low Power Case FES Volumetric Power (kW/m ³)	190

Table 33 – Initial Pressure in Each Volume – Low Power Case (feeder volumes in order from closest to end fitting to path to boundary condition)	190
Table 34 – Initial Pressure in Each Volume – High Power Case (feeder volumes in order from closest to end fitting to path to boundary condition)	190
Table 35 – Minor Loss Coefficients for Feeder Components.....	193
Table 36 – Feeder Flow Path Geometry (in order from closest to end fitting to path to boundary condition).....	193
Table 37 – Feeder Flow Path Information A (in order from closest to end fitting to path to boundary condition).....	194
Table 38 – Feeder Flow Path Information B (in order from closest to end fitting to path to boundary condition).....	194

1 INTRODUCTION

At present there are over 30 CANada Deuterium Uranium (CANDU) reactors in operation around the world. Assuring the safety of these reactors, both during operation and while shut down, is of the utmost importance. While safety is of cardinal importance, both society and the environment also benefit from any increase in efficiency and economy that can be realised in the production of electrical power using Nuclear Power Plants (NPP).

Safety analysis of NPPs involves the use of computer codes, supplemented with experimental data, to assess plant responses to postulated accidents under all possible initial conditions. Where uncertainties exist, traditional nuclear safety analysis employs conservative assumptions. This approach can be seen in the restrictions placed on maintenance procedures performed while CANDU reactors are shutdown. After a reactor is shut down, the fuel continues to produce decay heat at a rate that falls over time (Figure 1). Throughout the shutdown period, careful planning and analysis is performed to ensure sufficient heat removal from the fuel. A heat sink is defined as the physical systems (pumps, piping, heat exchangers, etc.), which can be used as a pathway for heat removal from the fuel.

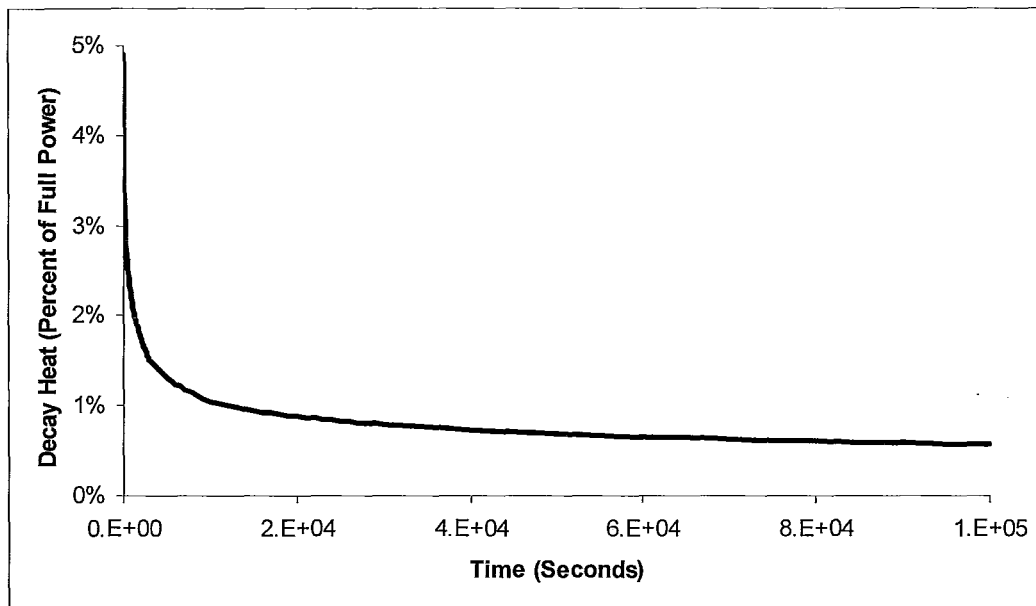


Figure 1 - Decay Heat Produced in Fuel vs. Time After Shutdown From Full Power [1]¹

Despite the fact that power at decay heat levels is much lower than during normal operation, safety can still be compromised if cooling fails for periods as short as several minutes. Some maintenance procedures carried out during a shutdown must be delayed until decay heat has reached a level such that it can be demonstrated that both primary and backup heat sinks are capable of cooling the fuel. However, uncertainties regarding the effectiveness of some heat sinks necessitate the inclusion of conservatism in the power levels at which the fuel can be dependably cooled, and hence the time after shutdown at which the procedures can be safely undertaken. If the uncertainties associated with the limiting heat sink can be reduced, some maintenance procedures can be commenced more quickly, potentially reducing shutdown times.

¹ The data for this decay heat curve is taken from the ANS standard for decay heat in light water reactors [1]. The variation between this curve and that for CANDU fuel would be expected to be minimal.

1.1 CANDU Reactor Design

CANDU reactors are power reactors typically fuelled by natural uranium contained in horizontal fuel channels. The fuel channels are enclosed by a pressure tube composed of zirconium alloy, and contain the fuel and high pressure, high temperature heavy water coolant (Figure 2 and Figure 3). Standard CANDU fuel contains natural Uranium and is arranged in 37 fuel pins which are 50cm long. Twelve of these fuel bundles are contained in each fuel channel. Each pressure tube is in turn encased by a calandria tube (also composed of zirconium alloy), with a gap between the pressure tube and the calandria tube containing a circulating annulus gas (typically carbon dioxide). Depending on the version of the CANDU reactor, either 380 or 480 fuel channels are contained in the calandria vessel. The volume between the calandria tubes and inside the calandria vessel is filled with a circulating, low temperature, low pressure heavy water moderator.

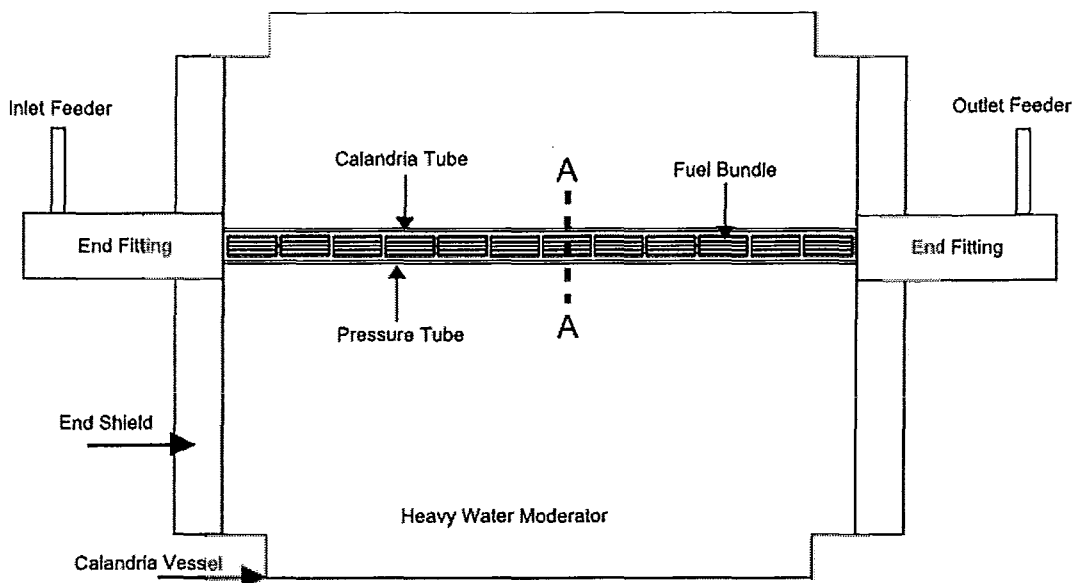


Figure 2 - Fuel Channel Schematic A

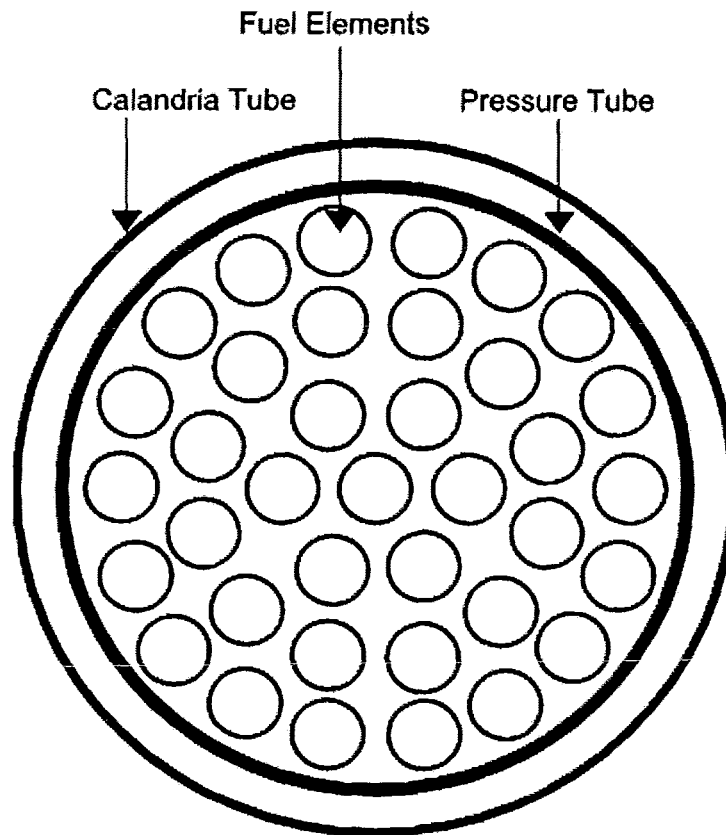


Figure 3 - Fuel Channel Schematic B

The primary heat transport system is typically configured in figure-of-eight pathway (Figure 4). Circulation is driven by large primary heat transport system pumps, and removes heat from the fuel in the fuel channels and expels it in the boilers. The boilers are located at a higher elevation than the reactor core, allowing for thermosyphoning if forced circulation is unavailable.

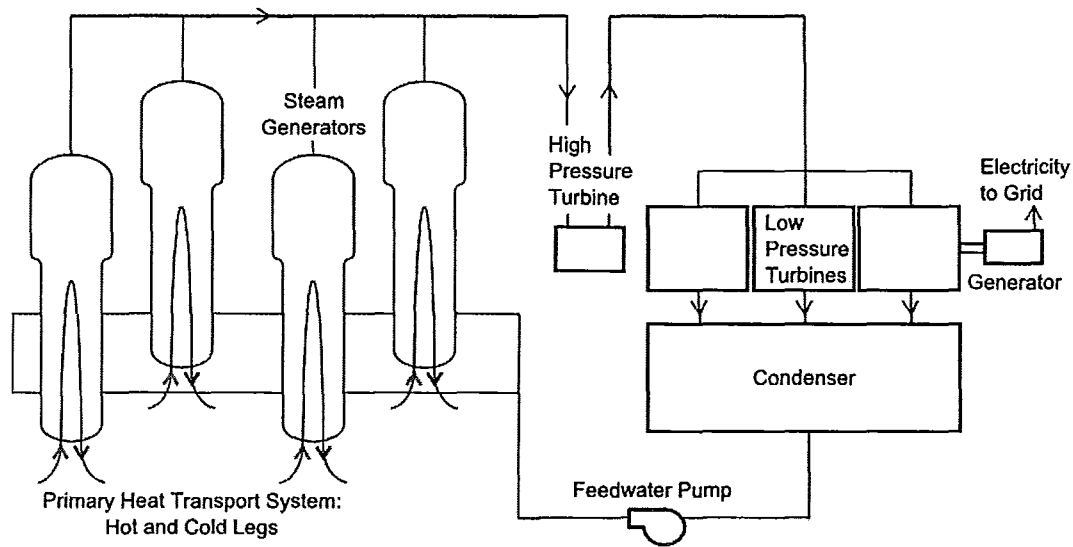


Figure 5 - Secondary Side Heat Transport System Schematic

1.2 Heat Sinks

In what is sometimes referred to as the ‘golden rule of reactor safety’, it is asserted that reactor fuel poses no threat to the public or environment so long as, at all times, the reactor power is controlled, the fuel is cooled, and the radioactivity is contained. During normal operation, the fuel in CANDU reactors is cooled by forced circulation of the heavy water coolant, which expels heat to the steam generators. Under accident conditions a number of other heat sinks may be employed, including the Emergency Core Cooling System (ECCS), feed and bleed, and the large mass of subcooled liquid in the moderator system.

A list of generally cited CANDU heat sinks, as well as their dependence on electrical power, service water, and steam generator steam discharge, is provided in Table 1.

Table 1 – Typical CANDU Heat Sinks [2]

System	Description	Dependencies		
		Electrical Power	Service Water	Steam Generator Steam Discharge
Feedwater	Water supply to SGs from deaerator, condenser hot well, condensate storage tank, and demineralized water tank via the boiler feed pumps.	Y	-	Y
Auxiliary feedwater	Water supply to SGs from deaerator, condenser hot well, condensate storage tank, and demineralized water tank via auxiliary boiler feed pumps.	Y	-	Y
Shutdown cooling	Closed recirculating system capable of being brought into service at ~170 C or at full system pressure and temperature under emergencies.	Y	Y	-
SG emergency cooling	Interim heat sink that provides water to SGs for a minimum of 15 min of heat removal at shutdown.	Y	-	Y
ECCS	Maintains the HTS full and removes decay heat with the HTS partially or fully depressurized. The function is a combination of coolant injection and recirculating recovery modes of operation.	Y	Y	-
Emergency water system	Provides water to SGs and makeup to moderator and HTS as well as cooling water to special safety system (ECCS and	Y	-	Y

	containment) heat exchangers.			
Feed and bleed	Approximately 1.3% full power heat can be removed through the bleed cooler using combined bleed-and-feed recirculation through the HTS.	Y	Y	-
Moderator	Passive heat removal following channel heatup and pressure tube deformation into contact with the calandria tube. Limited-duration heat sink unless water makeup provided.	-	-	-
Shield water	Passive heat removal from calandria vessel following core disassembly. Limited duration heat sink unless water makeup provided.	-	-	-

In most cases, the shutdown cooling system is capable of cooling the fuel up to 5% of full power, and is typically used to remove decay heat when the reactor is not in operation. This capability allows for maintenance procedures on steam generators and heat transport system pumps after the reactor is shut down. The shutdown cooling system is powered either from the station power buses or from the emergency diesel generators. In the event of a loss of Class IV power coupled with a failure of diesel generators, heat may still be removed from the fuel through natural circulation phenomena, aided by the placement of the steam generators at a higher elevation than the reactor core (see Figure 4). Thus, in the event of multiple system failures (such as failure of the grid, station power, and diesel generators), a heat sink will still be available.

Several modes of natural circulation are possible in CANDU reactors. Single and two phase thermosyphoning are powered by the pressure differential resulting from the low temperature coolant flowing from the steam generators to the core and the hotter, less dense coolant flowing from the core to the steam generators (that is, buoyancy induced flow). Some conditions such as a reduction in coolant inventory – either intended (during an outage), or not – may result in flow stagnation, leading to the phenomenon of Intermittent Buoyancy Induced Flow (IBIF).

1.3 Intermittent Buoyancy Induced Flow

Intermittent buoyancy induced flow can be described as a series of stages from stagnation to ‘venting’.

- a) Channel stagnation: Flow in a fuel channel may stagnate in some situations. The initial stagnation conditions of IBIF give rise to the term ‘standing start cycle’ sometimes used in reference to IBIF.
- b) Channel heatup: The decay heat supplied by the fuel elements heats the liquid in the channel. Stratification in the channel results, with a slug of hot liquid forming at the top, or potentially the formation of a vapour bubble (Figure 6).
- c) Bubble or hot slug growth: As heating of the channel continues, the vapour bubble or slug of hot liquid expands and comes into contact with one or both of the end fittings (Figure 7).
- d) End fitting penetration: The hot liquid slug or vapour bubble enters one or both end fittings and continues toward the feeder. The end fittings have a large mass and are typically at temperatures well below saturation during shutdown. This temperature difference results in heat transfer from the

coolant to the end fitting body, through conduction and convection and possibly through condensation as well, if vapour is present (Figure 8).

- e) **Venting:** Eventually the hot liquid or vapour bubble reaches a feeder at one end or the other, setting up a pressure differential across the fuel channel. A venting process ensues, with the hot fluid or vapour bubble rising through one feeder, and cold water entering the end fitting and channel from the opposite feeder (Figure 9). While some heat is transferred to the moderator and shield water during stages a – d of the IBIF cycle, venting allows for the removal of heat from the primary heat transport system through the steam generators, convective heat transfer from the feeders and headers to containment (and ultimately to containment cooling, etc.), depending on the system configuration.

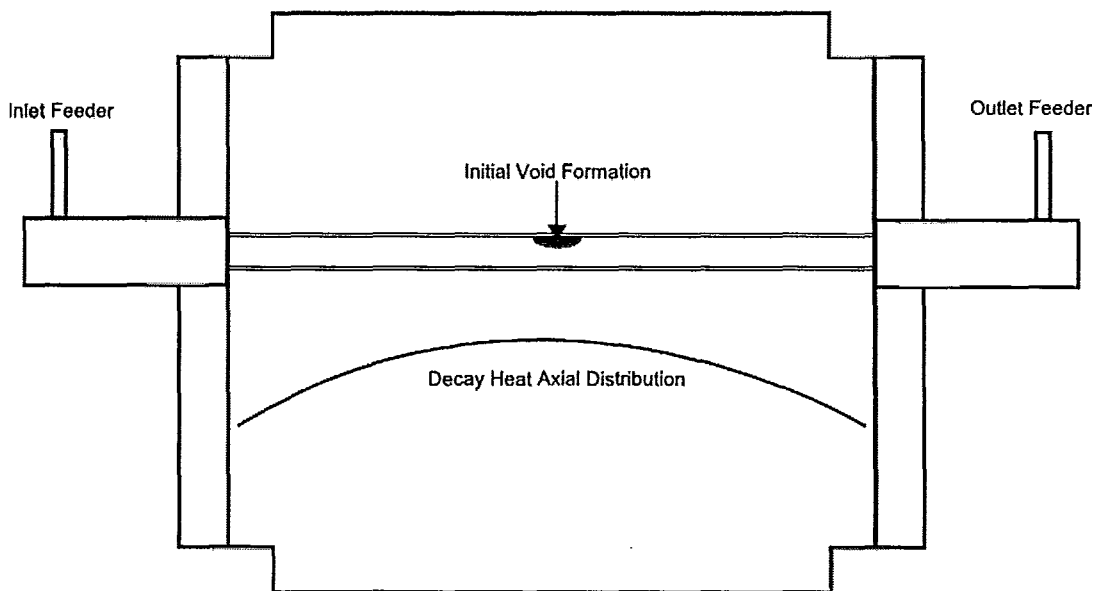


Figure 6 - IBIF Phase 1 – Onset of Boiling

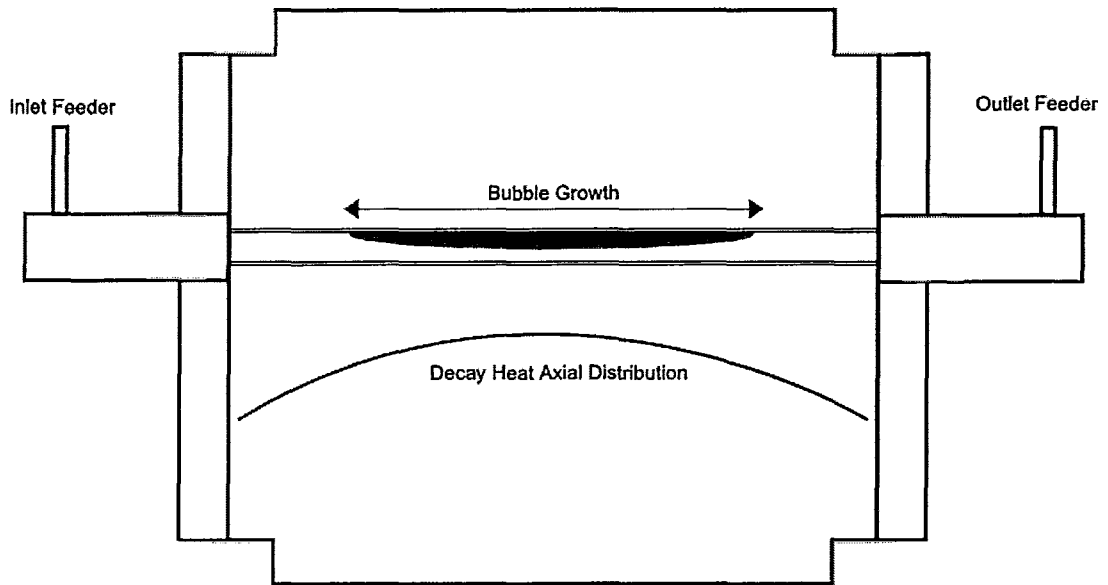


Figure 7 - IBIF Phase 2 – Bubble Growth

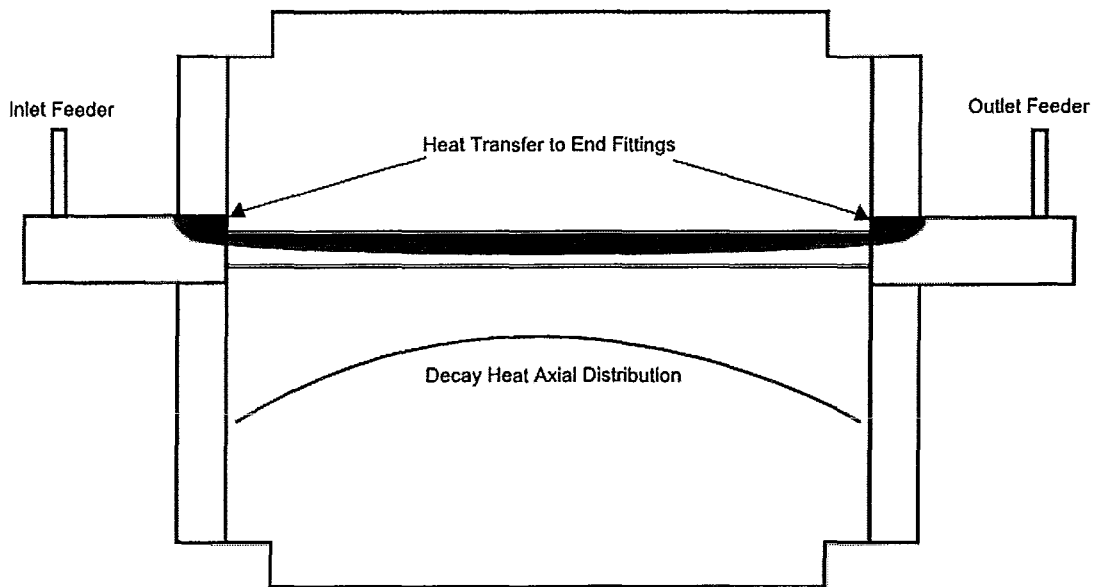


Figure 8 - IBIF Phase 3 – Heat Transfer to End Fitting

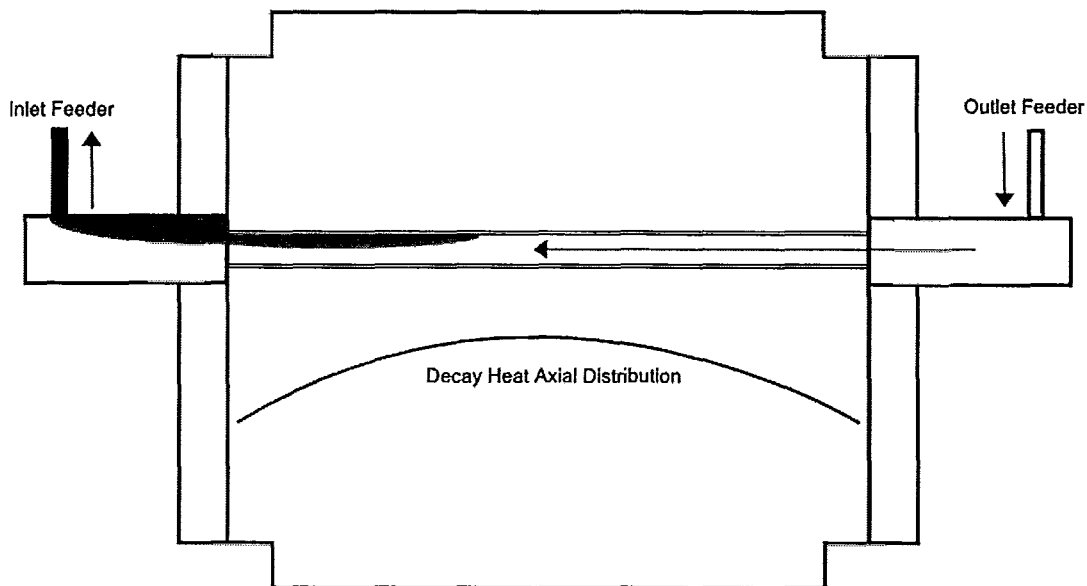


Figure 9 - IBIF Phase 4 – Venting and Refill

IBIF cycles may be repeated as long as the conditions (such as coolant inventory, stagnated flow, heat generation rate, etc.), remain favourable. Key outcomes to be considered during an IBIF cycle include fuel and pressure tube temperature. These values may impact fuel and channel integrity if they reach excessive levels.

In order for IBIF to take place, flow in a channel must stagnate. A channel may stagnate as a result of the introduction of an obstruction to flow, or else through a lack of forced flow coupled with a failure of natural circulation. Natural circulation may fail as a result of very low power levels (reduced driving force), reduced primary heat transport system inventory (removing the flow path from header to header, the loss of:

- Very low power levels: The driving force needed to maintain natural circulation may not exceed flow resistance around the loop if very little heat is added in the core.

- Reduced primary heat transport system inventory: Thermosyphoning requires the coolant level in the system to be high enough to allow a flow path around the loop.
- Loss of steam generators as a heat sink: If feedwater to the steam generators is lost, the descending leg of the natural circulation will no longer be cooled, eliminating the driving force.
- U-tube vapour lock²: If the tops of some of the u-tubes in the steam generator are filled with vapour, flow resistance through the steam generator is increased significantly. If all u-tubes are vapour locked, a flow path through the steam generator does not exist. U-tube vapour lock may follow from loss of steam generator feedwater or the presence of non-condensing gasses³ in the primary heat transport system.

The relevant physical processes that take place during IBIF, along with the more fundamental phenomena that are associated with each process, are listed in Table 2.

Table 2 - Processes and Phenomena Involved in IBIF

Process	Phenomena
Heat production in fuel pins	Nuclear decay heat production
Heat storage in fuel pins	Spatially dependent pin temperature variation as a function of time
Heat transfer from fuel pins to liquid or vapour	Heat transfer through conduction, convection, and radiation
Boiling of liquid in channel	Nucleate and film boiling
Heat transfer from liquid or vapour to pressure tube and end fitting	Heat transfer through conduction, convection, and condensation
Heat storage in pressure tube and end	Spatially dependent pressure tube and

² U-tube vapour lock is explained more fully in Section 2.3.1.

³ The most likely source of non-condesible gases in the primary heat transport system would be nitrogen introduced to the system in solution during and emergency coolant injection.

fittings	end fitting temperature increase
Heat transfer from pressure tube and end fitting to the moderator and end shield	Heat transfer through conduction and convection
Density driven flow in the fuel channel and end fittings in the vertical and horizontal directions	One and two phase fluid flow
Density and pressure driven venting through feeders	One and two phase fluid flow

While IBIF is relied upon as a backup heat sink in some situations, the potential presence of a vapour bubble raises some concern. If the bubble exposes fuel to steam and does not move or vent in a timely manner, it is possible that the temperature of the exposed fuel pins may rise sufficiently to cause damage to either the fuel or the pressure tube. The danger to the pins follows from the drastic reduction in heat transfer to steam relative to liquid, while the pressure tube is endangered through potential heating from superheated steam inside the channel (along with radiative heating from the fuel).

Demonstrating the effectiveness of IBIF as a heat sink thus depends on establishing that fuel and pressure tube temperatures remain within acceptable limits (450 °C and 400 °C, respectively, for return to service without inspection [3]). This can be accomplished either through demonstrating that for a given set of conditions, no voiding takes place (i.e. that it vents in single phase), or else by demonstrating that fuel pin temperatures (which are closely associated with venting times), stay below established limits. Increased understanding of IBIF thus has significant potential impact on the optimisation of safety and economics in CANDU operation.

Past work has shown that fuel temperatures are the limiting parameter in most cases, namely that any rise of pressure tube temperatures above acceptable limits will be preceded by fuel temperatures exceeding their limits [4], so attention can be focussed on peak fuel temperatures. Repeated IBIF cycles

involving temperature swings within acceptable limits are also a potential danger, however previous work has established that this is not a credible threat [4]. Hence the focus of this work is the peak fuel temperatures reach during a single IBIF cycle.

While IBIF relies on stagnant flow in the fuel channel, further conservatism has historically been applied including complete symmetry (particularly fuel bundle location and axial flux profile), and lack of channel sag and creep. As lengthening of venting times relies on a delicate balance of pressures maintaining stagnation, most asymmetry can be easily seen to result in faster venting times. However, the favourable impact of asymmetry on the effectiveness of IBIF has not been established in the case of partial, asymmetrical obstruction of the flow channel - such as may result from the insertion of inspection tools into fuel channels during outage maintenance procedures. Therefore, a main objective of this thesis is to examine the impact of partial flow blockages on maximum pin temperatures. To this end, the computer code GOTHIC will first be benchmarked against experimental data, and then applied to asymmetrical flow blockage cases to determine the impact of this scenario.

1.4 Scope and Structure of Report

The work presented explores the effects of asymmetrical, partial obstructions of fuel channels on the effectiveness of IBIF as a heat sink. As presented in the Background section, there is very little material available in publicly available literature on the topic of IBIF, and none dealing with partial obstructions or asymmetrical situations. A review of possible approaches to modelling the processes and phenomena involved in IBIF is presented in the Theory section of this report.

While it is not currently described in public literature, the Cold Water Injection Test (CWIT) facility [5] was designed to mimic the structure and

behaviour of single CANDU fuel channels. This facility and the tests in question are described in the Methodology section of this report. A series of ‘standing start’ tests involving stagnant channels and IBIF at decay power levels were carried out in the CWIT facility. Models of two of these tests, constructed in the computer code GOTHIC 7.2b, are presented in the Methodology section as well.

Simulations of the CWIT experiments are performed using the GOTHIC 7.2b models, with the results interpreted and compared to data from the CWIT experiments in the Results section. This section also details the results of simulations in which asymmetrical obstructions have been introduced in the channel. The impact of obstructions of varied size on venting time and peak pin and pressure tube temperature are presented and interpreted. Finally, the Conclusions section summarizes the findings of the study and presents recommendations for future work.

2 BACKGROUND & LITERATURE REVIEW

2.1 *Best Estimate and Conservative Analysis*

The discussion of what constitutes best estimate in the case of IBIF is somewhat nuanced. While it has been established that natural circulation in a variety of reactor types may be unstable under some conditions, and can result in stagnation or reversal, it is reasonable to say that complete flow stagnation is unlikely, and if it does occur, is not likely to persist for periods long enough for the channel to approach saturation. This is significant, as the IBIF cycles resulting in the highest peak pin temperatures take place in totally stagnated and pressure balanced conditions. In this sense, applying fully stagnated initial conditions and pressure balanced boundary conditions is a highly conservative treatment of the problem. Many core parameters such as channel sag and power profile would in fact preclude or mitigate flow stagnation. While this view would be appropriate for analyses of the probability of IBIF occurring, this work is intended to establish trends and sensitivities in the event of a worst case stagnation – in other words, this work can be characterised as consequence analysis rather than probabilistic or frequency based. As a result, the term best estimate in the case of IBIF analysis does not refer to probabilities of core geometry required for the channel to stagnate, but to other parameters such as heat transfer correlations and symmetry of axial power profile.

2.2 *Approaches to Modelling IBIF*

Historically the assumption regarding asymmetrical partially blocked geometries has been that the effect would be conservative, speeding venting times due to increased asymmetry. Although the conjecture that symmetrical geometries are bounding has been questioned recently, no experimental or analytical work has been published on the topic. Both experimental and analytical work has, however, been performed on IBIF in symmetrical geometries. While

the results of the most significant experimental work are not publicly available, there are a small number of publications describing analytical models and results from approximately 10 – 20 years ago, along with the results of one simplified experimental study.

The code THERMOSS-II [6] was developed to predict the duration of stagnated conditions, stratification, and fuel heatup in a CANDU fuel channel in subcooled, stagnant initial conditions. THERMOSS-II makes a number of simplifying assumptions, some of which are conservative, and others which may be considered best estimate simplifications. The model assumes that a pressure gradient is necessary for steam flow, with the result that a bubble forms with an axial profile along the channel defined by equating the frictional pressure drop in the steam and the hydrostatic head based on the water depth in the channel. The condensation heat transfer coefficient between the steam and the end fitting is treated as infinite, which, given the very high heat transfer coefficient for condensation, is a reasonable approximation. Non-uniform end fitting temperatures are accounted for in a simplified way as well. A fraction of the end fitting mass is determined to come in contact with steam, which is then treated in a lumped fashion with its temperature rising to saturation. The remaining submerged portions of the end fitting mass are taken to remain at the initial subcooled temperature.

THERMOSS-II was validated against experimental results from the Modified Cold Water Test (MCWIT) facility [6]. Venting times were typically overpredicted, with the venting times for the most symmetrical cases (that is, cases where the heatup of the end fittings was measured to be nearly equal) being overpredicted by at most 10% (Figure 10) – although the less symmetrical cases were overpredicted by greater margins. It is worth noting that the venting times recorded using the Cold Water Test (CWIT) facility were markedly longer than those of the MCWIT facility. While reasonable agreement between

THERMOSS-II predictions and experimental results is achieved, avoiding some of the simplifying assumptions – particularly the treatment of the end fitting and the profile of the vapour bubble – is desirable and should result in a sounder best estimate code.

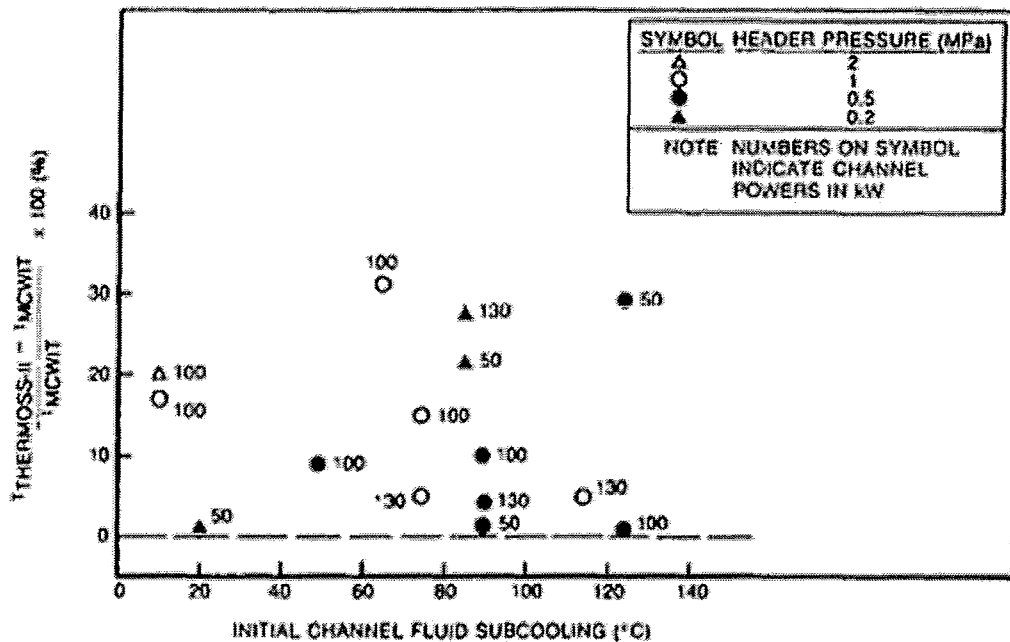


Figure 10 - Percentage Difference Between Duration of Channel Flow Stagnation Predicted by Thermoss-II and Observed in Thermally Symmetric [6]

Lei et al. [4] present the results of analyses defining a set of conditions for return to full power operation without inspection or analysis after repeated IBIF cycles in a planned annual outage of the GENTILLY-2 reactor. This analysis represents a more powerful approach than THERMOSS-II [6], and employed the codes: THERMOSS-III, HOTSPOT, ELESTRES, and ELOCA.Mk6 Mod 2.1, to model various aspects of the transients. ELOCA.Mk6 is a code used to model thermo-mechanical response and associated fission gas release behaviour of CANDU fuel elements during high-temperature transients [7]. The behaviour is calculated as a function of radius with subdivision the fuel element into axial segments. ELESTRES is a finite-element code which models fuel element

behaviour resulting from irradiation under normal operating conditions. It is typically used to provide fuel conditions such as temperature distribution, sheath strain, and internal gas temperature, at the beginning of a postulated accident [8]. In the context of this study, HOTSPOT is a code used to calculate effective sheath-to-coolant heat transfer coefficients in a stagnant, saturated steam environment, along with pressure tube temperature transients [6].

THERMOSS-III was used to model an IBIF cycle, producing data such as the length of time required for coolant to reach saturation, the length of time pins are dry, and the coolant temperature at the end of the cycle. These results were used by HOTSPOT to calculate the transient pressure tube temperature and heat transfer coefficient between the pins and the steam. ELESTRES was used to produce a set of initial conditions for each IBIF cycle. Finally, all of these results were employed by ELOCA.Mk6 Mod 2.1 to determine the thermal-mechanical behaviour of the fuel elements, an important issue due to the cumulative effect of the repeated thermal cycles on plastic sheath strain.

Fuel degradation mechanisms were considered, including: Oxygen embrittlement, beryllium-assisted crack penetration, longitudinal ridges, collapse of sheath into axial gap, plastic sheath strain, thermal stress and plastic strain fatigue, and sheath hydriding and hydride precipitation. Assessment of these mechanisms determined that fuel and fuel channels could be considered fit for service provided that maximum sheath and pressure tube temperatures were below 450 °C and 400 °C, respectively. It was determined that for standing start cycles, if fuel sheath temperature limits are not exceeded, the pressure tube temperature limits will not be exceeded (Figure 11).

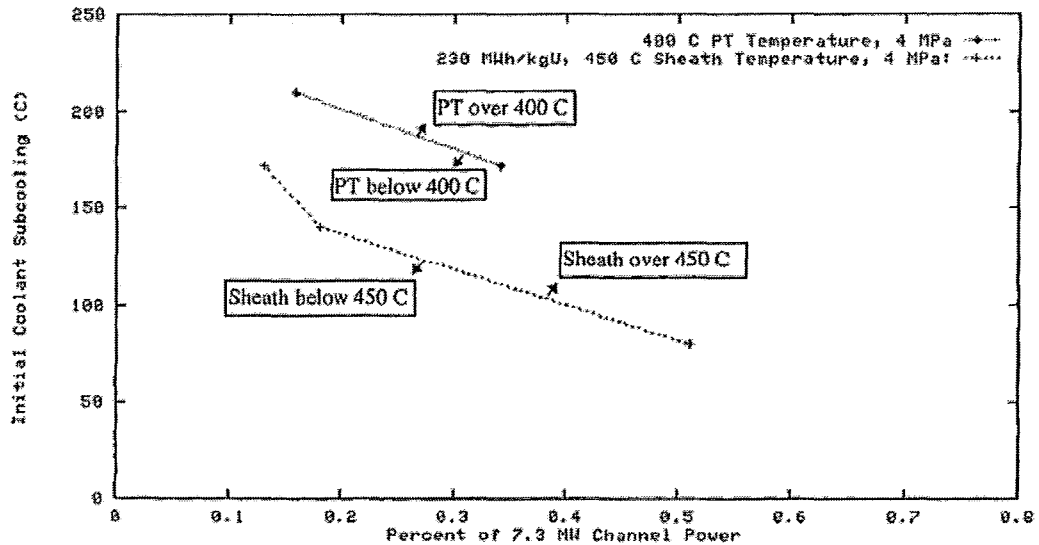


Figure 11 - Comparison of the 450 °C Sheath Temperature Curve with the 400 °C Pressure Tube Temperature Curve [4]

Operation envelopes considering power level and initial channel subcooling were defined for different fuel burnup levels, to define conditions under which fuel and channels can be returned to service in the event of a loss of forced cooling while in a shutdown state (Figure 12 and Figure 13). A comparison between these results indicates that the operating envelope for higher burnup fuel is more restrictive.

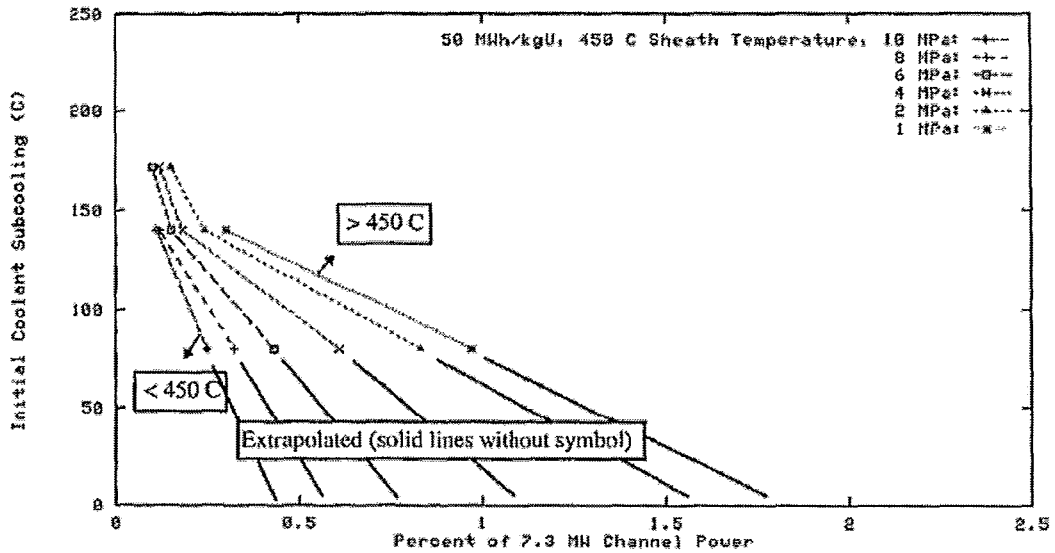


Figure 12 - 450 °C Sheath Temperature Map Relating Initial Coolant Subcooling to Percent of 7.3 MW Channel Power and Channel Pressure for a Fuel Burnup of 50 MW h / kg U [4]

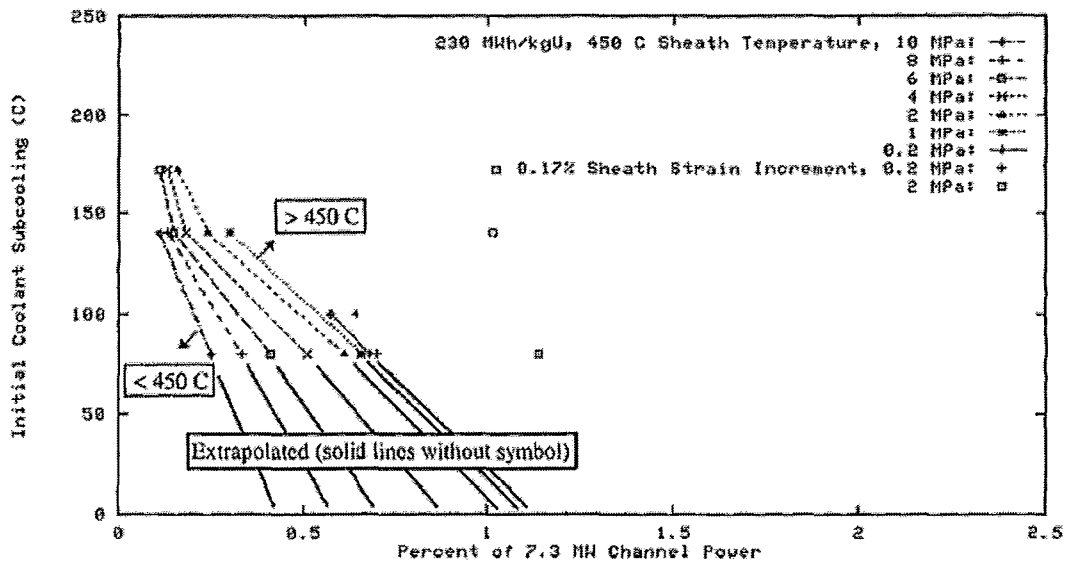


Figure 13 - 450 °C Sheath Temperature Map Relating Initial Coolant Subcooling to Percent of 7.3 MW Channel Power and Channel Pressure for a Fuel Burnup of 230 MW h / kg U [4]⁴

Pressure tube sag can reasonably be expected to speed the transport of hot liquid or vapour from the centre of the fuel channel toward the end fittings and feeders. This should have the effect of shortening venting times and reducing peak pin temperatures. Karchev et al. [9] present the results of a series of experiments involving air injection into a full scale acrylic pressure tube containing thirteen fuel bundles with zircalloy end plates and acrylic fuel pins.

As expected, the experiments indicate that bubbles reach the end fitting more quickly as pressure tube sag is increased (Figure 14). It was also determined that the greatest reductions in ‘venting’ time were realised as a result of the initial departures from a horizontal pressure tube, that is, that most of the benefit occurs as a result of a relatively small degree of sag. While confirmation of the expected general trend is worth noting, the location of the feeders immediately adjacent to

⁴ Symbols without connecting lines represent the plastic sheath strain increment of 0.17% at the end of IBIF cycles

the pressure tube and the absence of mechanisms such as condensation on the pressure tube and end fitting, along with the very short (2-6 second), venting times limit the applicability of the data to reactor calculations. The study also does not address the impact of sag on single-phase venting, or conditions which may affect the threshold between single-phase and two-phase venting. With that said, the study indicates that void produced near the centre of the channel will migrate, and hence pin exposure to steam will tend to be greater at the channel ends where the element power is lowest. While this is not applicable in a quantitative sense, confirmation of this tendency is valuable.

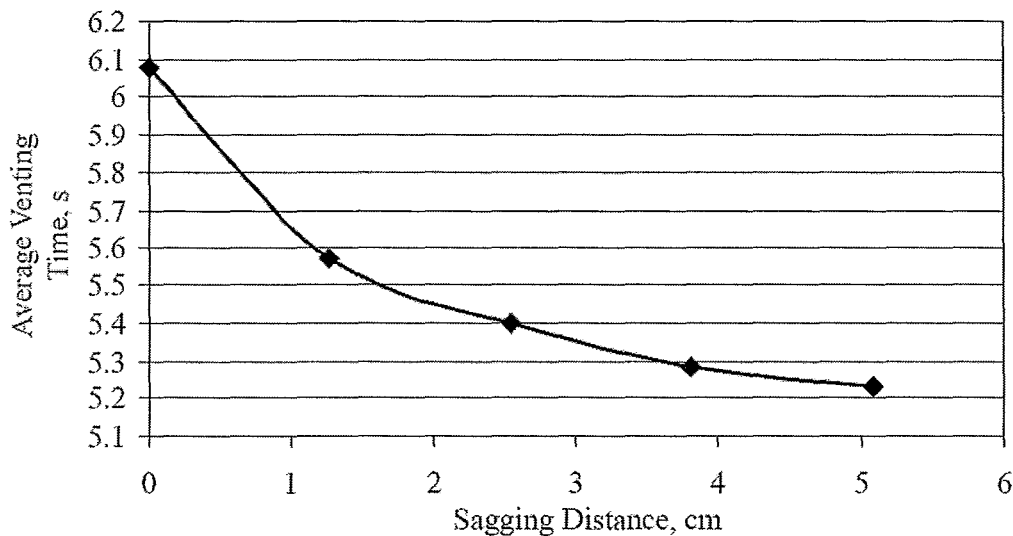


Figure 14 - Effect of Pressure Tube Sag on Air Venting Time [9]

2.3 Literature in Areas Related to IBIF

2.3.1 Natural Circulation in CANDU Reactors

Seodijono et al. [10] present a steady state, analytical approach to the prediction of header to header pressure difference and thermosyphoning under two phase natural circulation with steam generators as a heat sink in a CANDU

reactor. The model was validated against RD-14M experimental results, with trends and magnitude of behaviour reflected well in the model predictions for both high (4.6 MPa), and low (1.1 MPa), secondary side pressures.

The RD-14M test loop is a scaled representation of a CANDU reactor, with figure-of-eight primary loop. The model represents the primary loop as a figure-of-zero⁵ (Figure 15). A figure-of-eight loop can be viewed as two figure-of-zero loops in series, two total core passes are made rather than one. The fuel channels are represented as two parallel channels, one above and one below the core centreline. Conservation equations are solved for momentum, mass, and energy, and boundary conditions of channel power, secondary side temperature (pressure), and inlet header pressure are applied.

⁵ A figure-of-zero loop is one that involves a single core pass and a single pass through a steam generator.

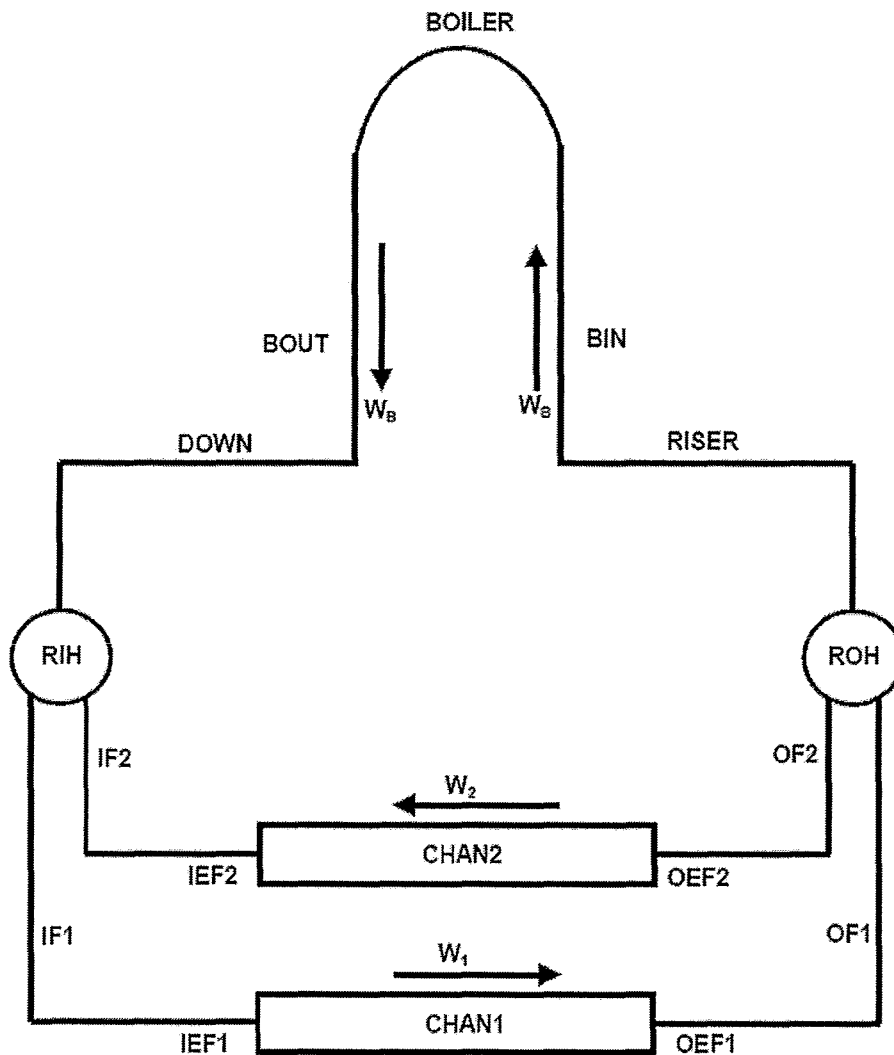


Figure 15 - Heat Transport System Natural Circulation Model [10]

Under natural circulation conditions, the lowest pressures in the primary loop are at the tops of the boiler tubes. In some circumstances, two-phase conditions may develop at the tops of some tubes, which can break the thermosyphoning flows in these tubes – a situation referred to as vapour lock. The vapour locking of some tubes increases the overall flow resistance through the steam generator, and the flow will decrease. This process ultimately results in a flow reversal in some fuel channels. As this is typically a slow process, the approach of approximating it as a series of steady state conditions at different

coolant inventory levels is warranted. Flow reversals were seen in both the RD-14M tests and the model predictions, demonstrating the instability of natural circulation under these conditions in CANDU reactors, raising the possibility of stagnated channels and IBIF processes.

Consequently, a model of flow resistance across the steam generators as a result of vapour locking was used in the Seodijono model. A friction factor K_{fb} is defined, which is dependent on the fraction of U-Tubes that are vapour locked. Data for K_{fb} is given for both RD-14M (Table 3 and Figure 16) and Pickering B. Finally, the model applies a flow reversal criterion comparing header to header pressure differences and the gravitational driving forces originating from the inlet and outlet feeders.

Table 3 - Number of RD-14M Boiler Tubes Experiencing Vapour-Lock [10]⁶

Head Difference (kPa)	Number of Vapour-Locked Tubes
0.0	0
0.3	8
0.6	19
0.9	32
1.17	44

⁶ The total number of boiler tubes is 44.

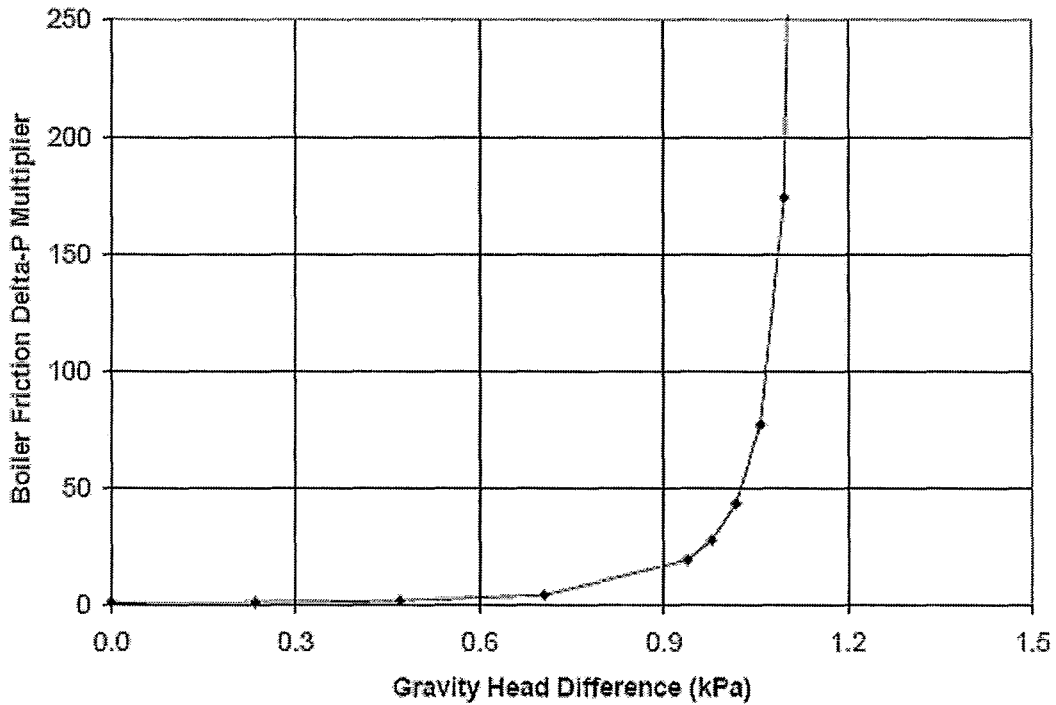


Figure 16 - RD-14M Boiler Tube Friction Pressure Drop Multiplier vs. Gravity Head Difference [10]

Simulations were performed for two sets of RD-14M tests. The first set of tests was performed at a secondary side pressure of 4.6 MPa, and primary loop inventory at tests were simulated with primary loop inventory at 95%, 85%, and 80%; at 95% and 85%, flow was unidirectional in all channels, while flow reversal was evident at 80%. At 1.1 MPa secondary side pressure, tests were conducted at 90%, 80%, and 70% primary loop inventory levels, each exhibiting unidirectional flow. Further relevant parameters of the tests are detailed in Table 4.

Table 4 - RD-14M Test Parameters

	1.1 MPa Tests	4.6 MPa Tests
Secondary Side Steam Generator Temperature (°C)	184	258

Inlet Header Pressure Range (kPa)	3000 – 1100	7000 - 4600
Channel Power (kW)	~160	~160
Inlet Feeder Trace Heating (kW)	10	10
Outlet Feeder Trace Heating (kW)	11	11
HTS Pumps	Stopped	Stopped

A comparison between simulation results and 4.6 MPa test data from RD-14M of predicted header to header pressure differential as a function of coolant inventory is shown in Figure 17. The trends and magnitudes of pressure differentials are predicted reasonably well.

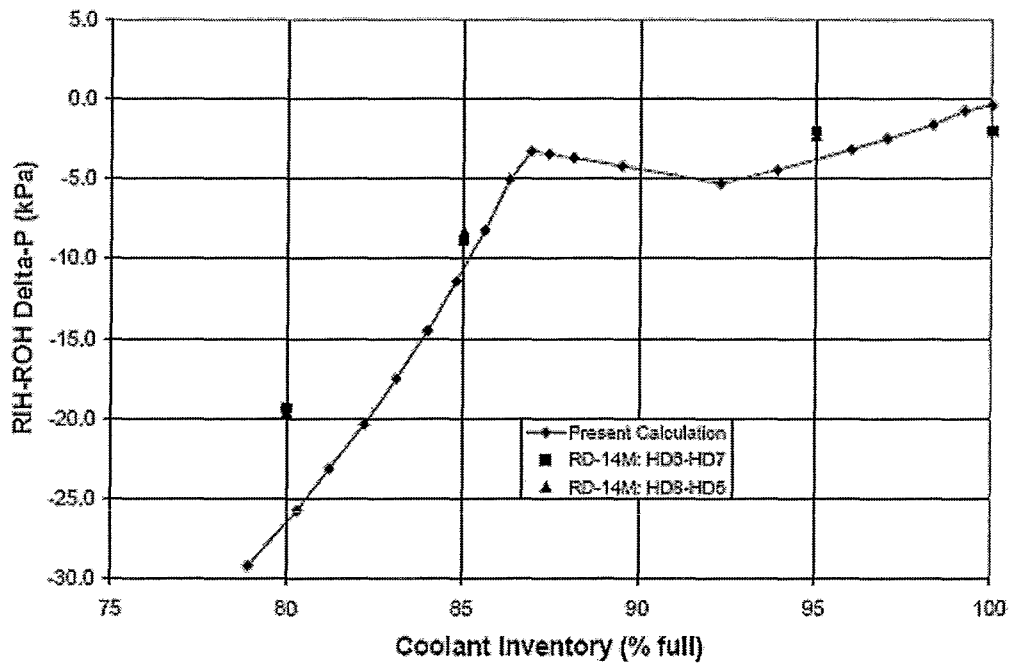


Figure 17 - Predicted and Test Results for RD-14M Inlet-to-Outlet Header Pressure Differential vs. HTS Coolant Inventory (Secondary Side Pressure = 4.6 MPa) [10]

Similar behaviour can be observed in the 1.1 MPa test data and simulation results. A comparison between predicted and observed data (Figure 18), again shows a reasonably accurate prediction of the trends and magnitudes of the impact of reduced coolant inventory.

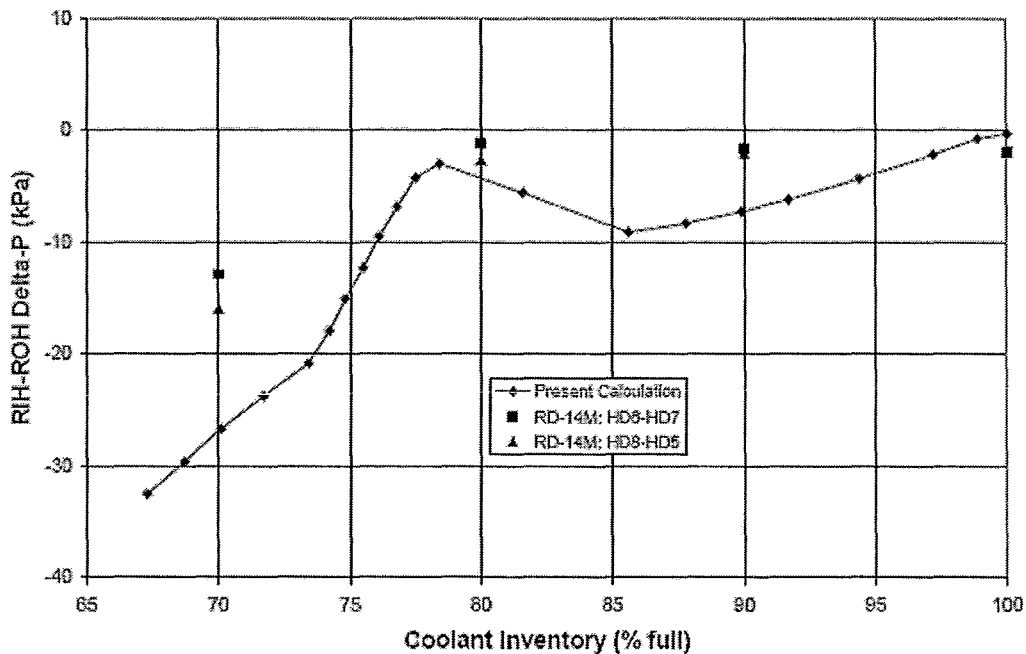


Figure 18 - Predicted and Test Results for RD-14M Inlet-to-Outlet Header Pressure Differential vs. HTS Coolant Inventory (Secondary Side Pressure = 1.1 MPa) [10]

Having established the success of the model at predicting header pressure differentials, a comparison to the gravity head differential in the feeders can determine whether the flow reversal criterion is fulfilled. In the 1.1 MPa experiments, no flow reversal was observed, which is reflected in the simulations (Figure 19); however, a flow reversal was predicted slightly below the range of coolant inventories tested in the RD-14M facility. Although this is not directly validated against experimental results, the prediction of a reversal near this inventory level is supported by the successful simulation of header to header pressure differential at higher coolant inventory and the downward trend of results.

Simulations of the 4.6 MPa experiments were successful in predicting the observed flow reversal between 80% and 85% coolant inventory. As noted above, the potential for flow reversal opens the possibility of transient channel stagnation and IBIF processes (though this is not a typical path to IBIF).

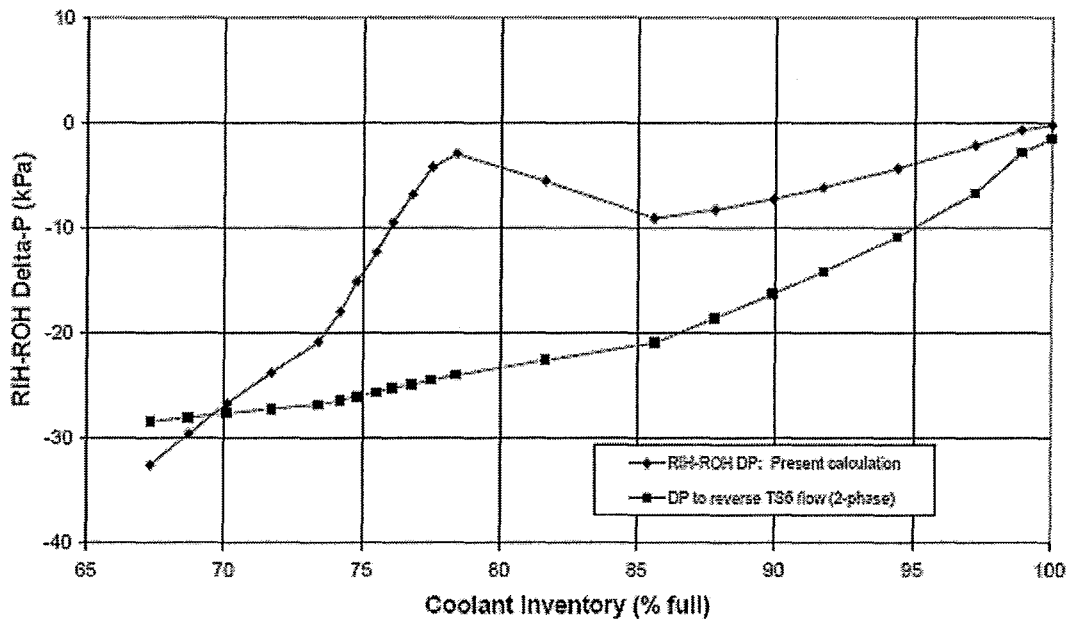


Figure 19 - Predicted RD-14M Inlet-to-Outlet Header Pressure Differential vs. HTS Coolant Inventory (Secondary Side Pressure = 1.1 MPa) [10]

The model was also adapted for application to Pickering B. Similarly to the RD-14M model, Pickering B fuel channels were represented by four equivalent parallel channels. Simulations were conducted at 3% full power, with a secondary side boiler temperature of 250 °C and inlet header pressures ranging from 8800 kPa to 4000 kPa. Vapour lock of boiler tubes was seen beginning at 86% primary loop inventory (Figure 20). Flow reversal in row A channels and row B channels can be seen at approximately 84% and 82% coolant inventory, respectively. Further channel flow reversals are predicted for row C below 77% inventory, and row D below 66% inventory.

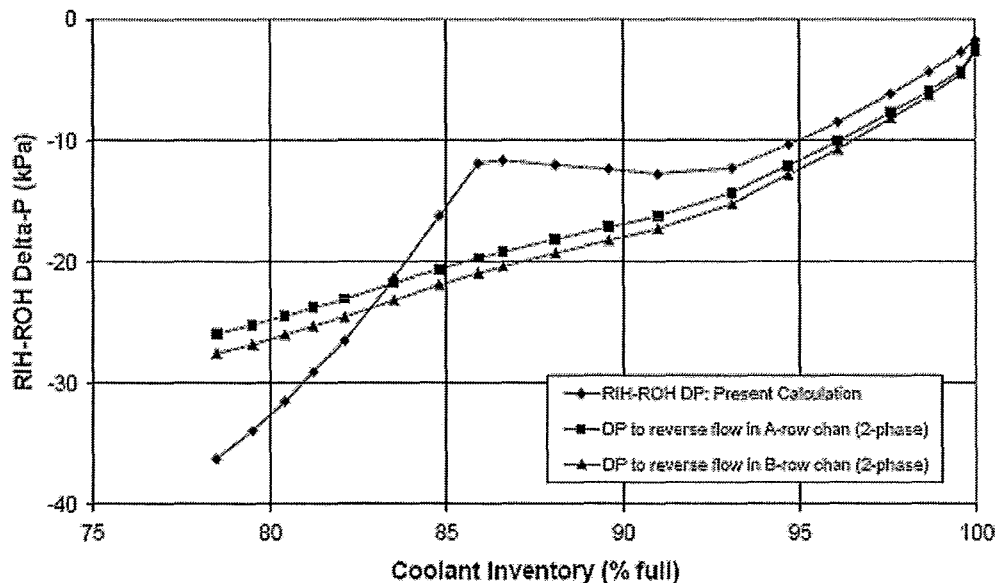


Figure 20 - Pickering RIH-to-ROH Pressure Differential vs. HTS Coolant Inventory with No Channel Flow Reversal [10]

The Pickering B model also predicts complete vapour lock of boiler tubes below 59% inventory. With total vapour lock, inlet and outlet header voids are equalised at 50%, with top channel flows reversed and bottom channels flowing forward.

2.3.2 Natural Circulation in PWRs

D'Auria et al. [11] present work dealing with natural circulation with PWRs. The results of experimental work are synthesised in a flow map evaluating natural circulation performance in PWRs. This is followed by an analytical assessment of the capabilities of natural circulation for removing heat in PWRs at power levels higher than decay heat.

D'Auria et al. analysed both single-phase and two-phase natural circulation data from the PWR simulators: Semiscale, Spes, Lobi, Bethsy, Pkl, and Lstf. The data of interest were produced in experiments conducted with a primary loop in single-phase and two-phase, with:

- constant primary system pressure close to the hot leg saturation pressure in nominal conditions,
- core power at decay heat levels ranging from 1 - 5% nominal,
- steam generators at nominal level and pressure conditions,
- available feedwater flowrate and temperature sufficient to remove core power,
- stepwise draining of primary coolant achieving a quasi steady-state at each inventory level.

This synthesised data is presented in the form of a flow map (Figure 21). Flow is characterised as one of four flow patterns (each of which are capable of successful core cooling in the range of the flow map), or as dryout, depending on the mass inventory of the primary loop. The flow patterns and dryout are detailed below:

1. Single phase natural circulation with no void in the primary system excluding the pressurizer and the upper head - The core flowrate derives from a balance between frictional forces and driving head – which results from the density difference between the descending half of the U-Tubes and the vessel downcomer on one side and the core and ascending half of the U-Tubes on the other side. No film boiling is present in this flow pattern, heat is transferred through subcooled nucleate boiling or forced convection. Consistent with PWR design, the experimental database indicates that single phase natural circulation is capable of removing nuclear decay heat, provided the availability of steam generator cooling.
2. Stable co-current two phase natural circulation resulting from decreased primary system fluid inventory - Heat transfer in the core is via forced convection and subcooled and saturated, while condensation takes place in the U-Tubes of the steam generators. Flow rate again results from a

balance between driving and resistant forces, and both of these increase with decreasing inventory. For typical PWR geometries, the balance of these forces results in an increase in core mass flow rate with small decreases in inventory and an eventual reduction in core mass flow rate as inventory is further reduced (see Figure 21).

3. Unstable two-phase natural circulation and occurrence of siphon condensation – Oscillations of the core inlet flow rate arise from: the decrease in natural circulation driving forces, the small temperature difference across the U-Tubes in the steam generators, and the occurrence of the Counter Current Flow Limiting Phenomenon (CCFL) at the entrance of the U-Tubes. CCFL begins at primary system mass inventories of approximately 70% as a result of the efficiency of condensation heat transfer leading to almost all the core thermal power being expelled on the ascending side of the U-Tubes. The liquid level builds up (over a period on the order of 10s), during this interval the flowrate at the core inlet is close to zero and boiling progresses in the core. When the liquid reaches the top of the U-Tubes, a siphon effect empties the ascending side of the U-Tubes, and core inlet flow rate is re-established. Complexity in this flow pattern follows from the interactions between thousands of U-Tubes at different stages of oscillation, and may result in flow reversal in tube bundles.
4. Stable reflux condensation with liquid flowing countercurrent to steam in the hot legs – This flow pattern is capable of core power for primary loop mass inventories above 30 – 40% of the nominal values. At inventory levels between these minimums and those resulting in unstable two-phase natural circulation, liquid that is condensed or entrained on the ascending side of the U-Tubes may flow back to the core through the hot legs, resulting in stratified counter-current steam and liquid flow and mass

flowrates at the core inlet of close to zero. Core thermal power is removed by saturated nucleate boiling.

5. Dryout – At primary loop inventories below 30 – 40%, dryout results from a combination of low flow and high void fraction. Film boiling heat transfer is experienced in the core, with the associated poor heat transfer resulting in unstable heat removal and rod surface temperature increases in some parts of the core. D’Auria et al. note that the extent of the post-dryout temperature excursion is very sensitive to primary system pressure and thermal power levels. At pressures of 15 MPa (nominal operating pressure for PWRs), rod surface temperature increases may be as low as a few tens of Kelvin, and remain within an acceptable mechanical range for the rod-clad material.

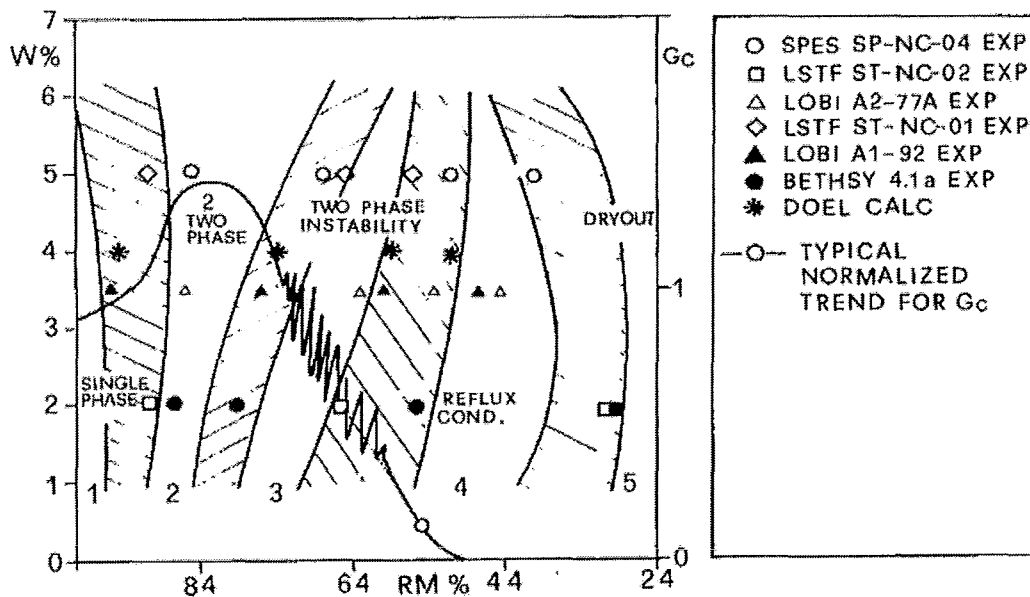


Figure 21 - Characterisation of Natural Circulation Flow Regimes Based on Experimental Data and System Codes Calculations. [11]⁷

⁷ RM% represents primary system mass inventory as a percentage of the nominal value, W% represents the core power level as a percentage of nominal operating power, GC represents

D'Auria et al. used the flow map (Figure 21) to evaluate the natural circulation performance in other facilities, most saliently RD-14M, a CANDU simulator. It is observed that reflux condensation is not evident in the RD-14M database. Two different behaviours are evident, depending on which experiment is considered (Figure 22), which is cited as evidence that further investigation is needed.

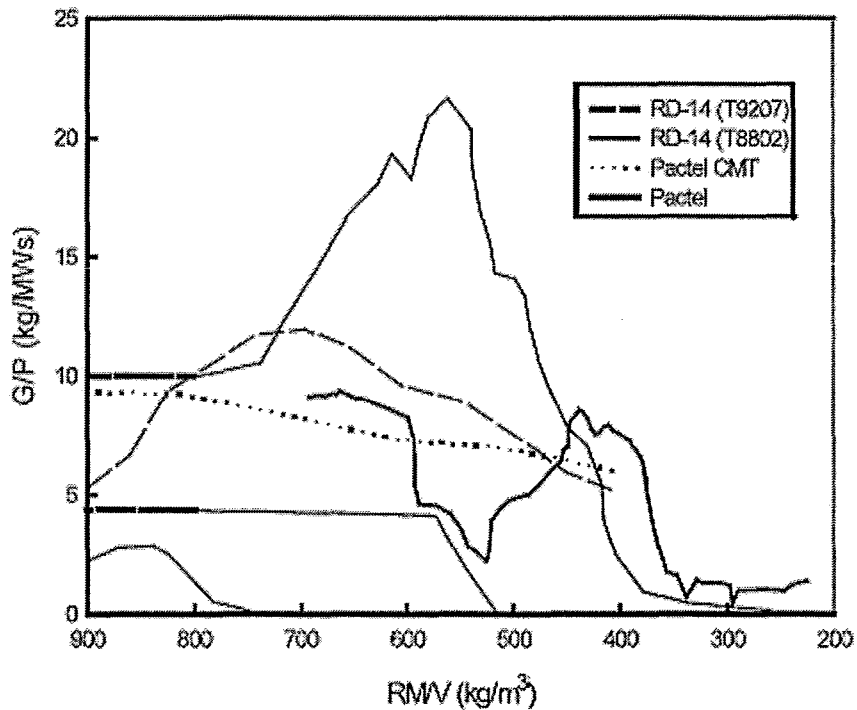


Figure 22 - Evaluation of Natural Circulation Performance for Pactel and RD14M Simulators by Using the NCFM. [11]⁸

D'Auria et al. [11] also present analytical work establishing an estimate of the maximum thermal power removal capabilities of natural circulation in PWRs. Relap 5 models were used to simulate natural circulation in integral test facilities

normalised flow rate. The hatched areas of the figure represent transition zones between flow regimes.

⁸ G/P represents flow rate divided by power level. RM/V represents average density of coolant in the primary loop, that is, primary loop inventory.

and PWRs. This work did not consider the impact of neutron kinetics that would be associated with changes in coolant density in a real reactor, instead treating power as a control variable. For most integral test facilities, removal of up to 70% core power was shown to be possible before dryout is reached. Using nominal operating conditions in PWRs, the analysis indicates that single-phase natural circulation is present up to 20% of full power, and two-phase natural circulation is capable of removing up to 70%. Further analysis indicated that an increase in primary system pressure and a reduction in steam generator pressure to 2.5 MPa allow for the removal of more than 90% of full power through natural circulation.

2.3.3 Stability of Natural Circulation

While IBIF is possible only in reactors with horizontal fuel channels, it is worth noting that the stability of natural circulation in other reactor types has been studied extensively. An analytical treatment of the reliability of natural circulation was conducted by Jafari et al. [12] using probabilistic techniques. The experimental and analytical work available in literature concerns reactor types including: VVER-440 [13], VVER-1000 [14], PWR [15], and a 5 MW heating reactor [16].

Jafari et al. [12] present a probabilistic study of the reliability of natural circulation using the Reliability Evaluation of Passive Safety Systems (REPAS) methodology. This methodology is applied to TTL-1, separate effects thermal-hydraulic experimental loop. Natural circulation in TTL-1 was simulated using 137 different sets of parameters (37 with deterministically selected parameters, and 100 with stochastically selected parameters). A typical Probabilistic Safety Assessment (PSA) assigns a reliability value of 1 to natural circulation, indicating that it is fully reliable; whereas Jafari et al. found this to not be the case when the subject is considered using the REPAS methodology. The reliability of natural circulation was assigned a value between 0.7 and 0.85, a reliability comparable to that of the pumps in the TTL-1 loop. This divergence from the commonly held

opinion of natural circulation as a fully reliable passive safety system is significant.

Puustinen [13] presents the results of an experimental study of two-phase natural circulation flow stability in the PArallel Channel TESt Loop (PACTEL) facility, a volumetrically scaled model of a VVER-440. The experiments simulate the effect of a cold leg Small Break Loss Of Coolant Accident (SBLOCA) and a partial failure of the high-pressure injection system. A trend of increasing mass flow rates with decreasing inventory was noted and attributed to the combined effect of break size, pressure range, and the secondary side feed and bleed procedure. Flow reversal in the lowest steam generator tubes was also observed.

Mousavian et al. [14] present work on natural circulation during SBLOCA in the cold leg of a VVER-1000, using RELAP5. The models are benchmarked against data from the Kozloduy nuclear power plant unit 6 tests and the PSB-VVER integral test facility. Single-phase and two-phase circulation, as well as both stable and unstable regimes are evident, and the impact on these behaviours of varied relative elevations between the core and steam generators was studied. It was found that increasing the difference in elevation between the core and the steam generators increased the flow rate and resulted in greater stability of natural circulation.

In response to concerns over the potential for primary loop stagnation during natural circulation cooldown in PWRs, Chang [15] analysed this process using the RETRAN computer code. It was determined that the stability of natural circulation is jeopardised if the cooldown rate is too high. Normal procedures calling for cooldown at a maximum rate of 50 °F / hr are acceptable under normal circumstances, but it was found that if one or more steam generator dries out, the cooldown rate must be reduced below 25 °F / hr.

Jiang et al. [16] present experimental work on flow excursions in natural circulation in a 5 MW heating reactor. Slow, long term flow excursions were observed and included dynamic effects involving two-phase flow. The flow excursions were interpreted using the characteristic curves of the loop flow resistance and driving head and the operating curve of natural circulation in the loop.

2.3.4 Severe Accidents

While the scenarios considered in this study of IBIF neither imply nor follow from severe accident scenarios, there are some severe accident processes in CANDU reactors in which IBIF may play a precursory role. These can be identified using the categorisation presented by Luxat [2]. There are three classes of events that can lead to severe accidents in CANDU reactors: loss of coolant accidents, transient events with loss of shutdown, and loss of multiple heat sinks (Figure 22). Severe accidents following loss of multiple heat sinks progresses through the following phases:

- i. Steam generator inventory depletion
- ii. Heat transport system heatup and liquid swell
- iii. Heat transport system inventory depletion
- iv. Fuel channel heatup and heat transport system component failure potential
- v. Moderator system response
- vi. Reactor heatup and disassembly

IBIF may be manifest in any of the first three phases, depending on post-shutdown heat loads and reactor conditions post-accident, and may play a role in operator timing immediately after a loss of heat sink event.

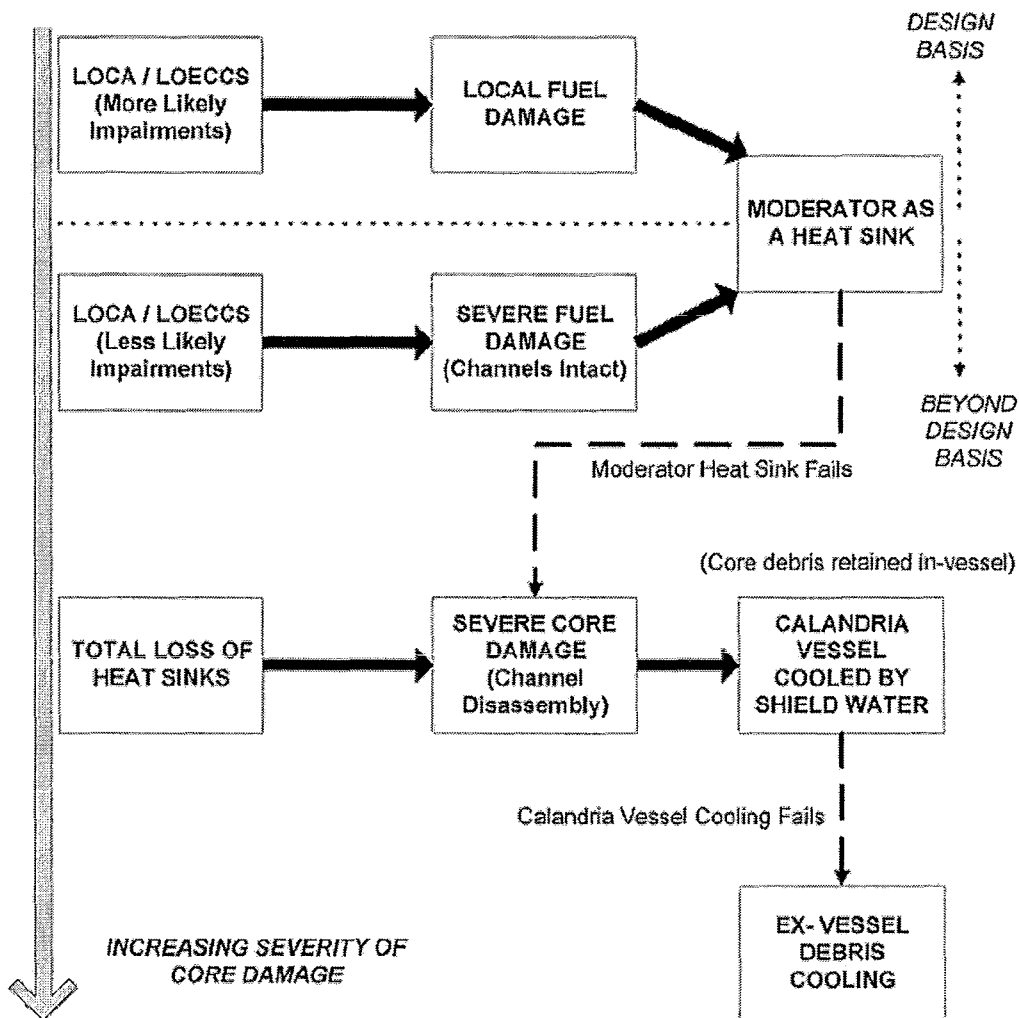


Figure 23 - Core Damage Progression in CANDU Reactor Beyond-Design-Basis Accidents [2]

2.4 Natural Circulation Modelling Using GOTHIC

GOTHIC (Generation of Thermal Hydraulic Information in Containments) is a general-purpose thermal-hydraulics software package. GOTHIC solves mass, momentum, and energy conservation equations for multi-component, multi-phase flow. The treatment of interfaces between phases covers all flow regimes and

allows for thermal non-equilibrium and unequal phase velocities. GOTHIC also provides an optional two equation, k - ϵ turbulence model [17, 18].

While GOTHIC has been used primarily for containment response analysis, it has recently been employed in industry for fuel channel analysis, including IBIF. There is only one document in publicly available literature involving a similar use of GOTHIC which can be used to establish a precedent for the effectiveness of the code in this area. Ofstun et al. [19] present the results of simulations of the Full Length Emergency Cooling Heat Transfer Separate Effects and Systems Effects Test (FLECHT SEASET) natural circulation tests using GOTHIC. This work demonstrates GOTHIC's ability to model single-phase forced and natural circulation, two-phase natural circulation, reflux condensation, subcooled pool boiling, nucleate boiling, counter-current flow, and flooding.

The FLECHT SEASET test facility is a full height, 1/307 volumetrically scaled model of a 4-loop PWR. Heating in the system is provided by electrical heater rods, representing a section of a 17x17 fuel assembly. While there are a number of differences between the layout of the facility and a PWR reactor, the tests (jointly conducted by Westinghouse, NRC, and EPRI), were found to contain all the essential phenomena present in the shutdown cooling mode. The effective modelling of these phenomena (rather than the fidelity of the overall system behaviour to that of PWRs), is the primary interest in establishing the appropriateness of GOTHIC for analysing natural circulation.

The wide range of wall and interphase heat transfer modes encountered in the FLECHT SEASET experiments necessitated the use of a number of models available in GOTHIC including:

- For single-phase liquid, Dittus-Boelter correlations for turbulent forced convection [20] and turbulent natural convection on vertical planes or cylinders [21].

- For single-phase vapour, a coefficient that is the maximum of values based on: conduction through a stagnant vapour, the Dittus-Boelter correlation for turbulent forced convection [20], and a correlation for turbulent natural convection on vertical planes or cylinders [21].
- For nucleate boiling, the Chen correlation [22] was used.
- For subcooled boiling, an extension of the Chen correlation [17] was used.
- For condensation heat transfer, the heat and mass transfer were obtained from the maximum of the Uchida [23] and Gido/Koestel [24] correlations.

The results of the GOTHIC simulations agreed well with the experimental data under both single-phase and two-phase conditions⁹. Table 5 compares the GOTHIC predictions to the test results in single-phase natural circulation, peak two-phase flow, and reflux condensation. The spatial distribution of these values in the model and test facility can be seen in Figure 24.

Table 5 - Comparison of GOTHIC Results and Test Data in Primary Cooling Modes [19]¹⁰

Nominal Condition (Mass Inventory)		Vessel Pressure (psia)	Loop Flow (lbm/s)		SG Inlet Temp. (F)		SG Outlet Temp. (F)	
			IL	BL	IL	BL	IL	BL
Single-phase natural circulation (100%)	GOTHIC	724	1.1	0.4	164	164	133	132
	Test Data	745	1.1	0.3	166	164	136	137
Two-phase natural circulation (84%)	GOTHIC	414	3.6	0	141	139	133	135

⁹ As shown in Table 5, predictions of flow through loop IL match the experimental results to approximately 9% relative error for single-phase and two-phase natural circulation.

¹⁰ IL and BL are the two steam generator loops present in the test facility and the model.

	Test Data	379	3.9	0	141	139	133	135
Reflux Condensation (38%)	GOTHIC	345	0.1	0	136	137	132	132
	Test Data	317	0	0	137	134	136	135

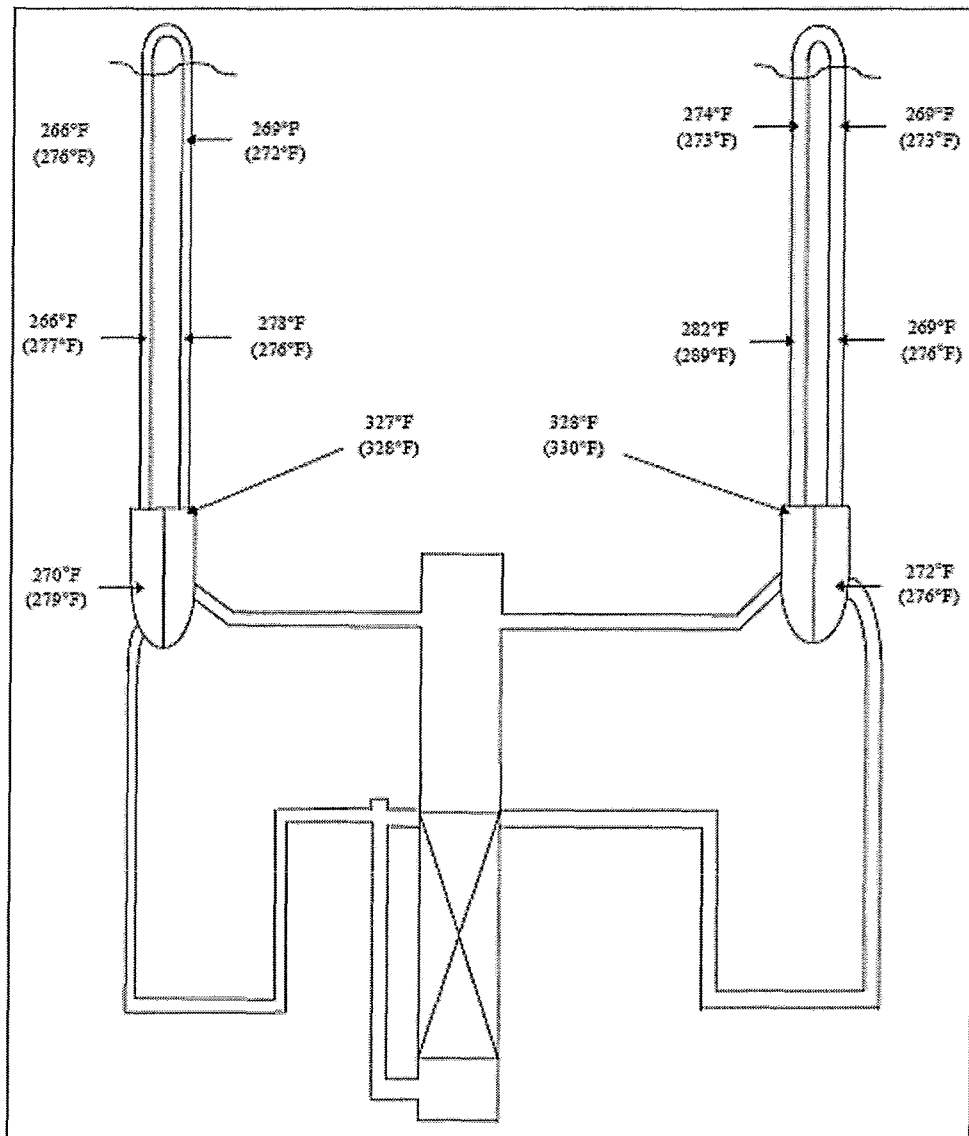


Figure 24 - Comparison of Steam Generator Tube Temperature Profiles for Single-Phase Natural Circulation [19]

The overall system behaviour is displayed in a plot of total primary flow versus mass inventory (Figure 25). While the match between experimental data and GOTHIC predictions is not exact, the overall behaviour is very similar, and the main phenomena were captured by GOTHIC.

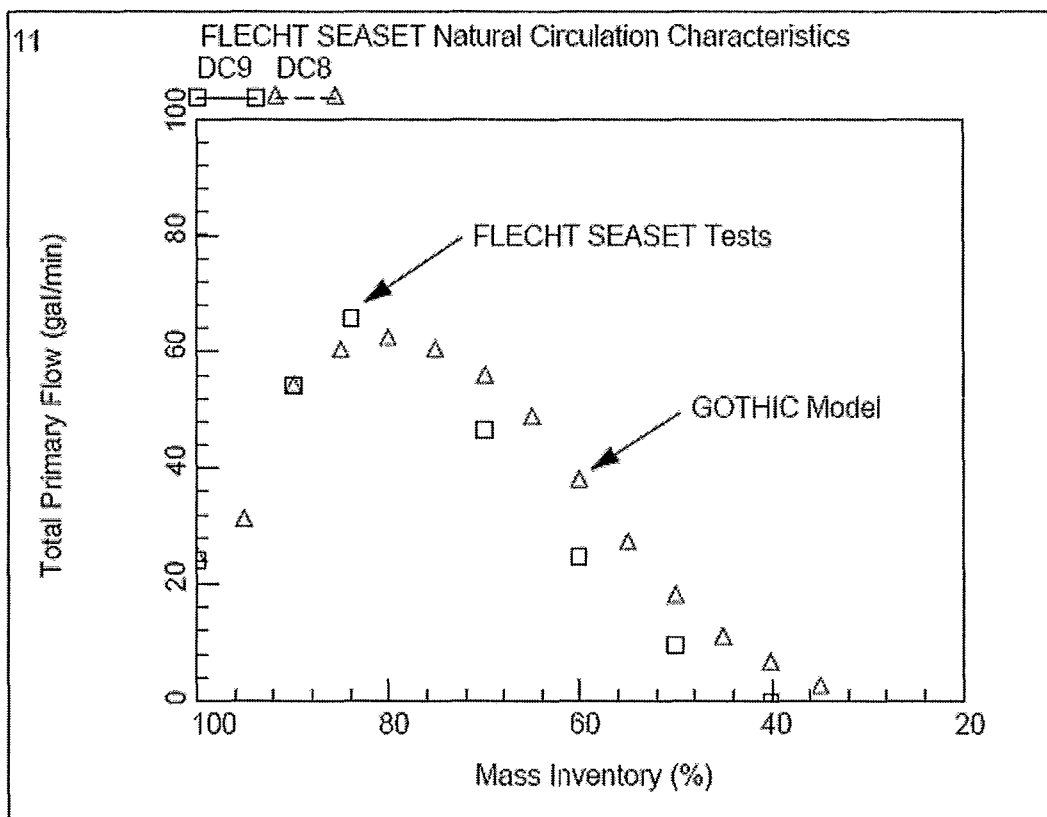


Figure 25 - Natural Circulation Characteristics Comparison [19]

3 METHODOLOGY

The Cold Water Injection Test (CWIT) facility is a test loop simulating a CANDU reactor. The facility and the experiments performed there were funded by Ontario Hydro / Ontario Power Generation. In this work, two experiments (exhibiting symmetrical geometries), performed at the CWIT facility are simulated using the computer code GOTHIC, for the purpose of validating the code. The GOTHIC model is then extended to include asymmetrical obstructions, with the impacts of obstruction being the primary focus of this study. The details of the CWIT facility, the simulated experiments, and the GOTHIC code and CWIT experiment models are presented in this section.

3.1 CWIT Facility Description

The Cold Water Injection Test (CWIT) facility is a test loop simulating a CANDU reactor. It includes two horizontal test channels with end fittings, inlet and outlet feeders, inlet and outlet headers, water injection lines, a blow-down tank, pumps, pressure and temperature control systems, and inter-connecting pipes [5]. The components most relevant to the standing start tests in question are depicted in Figure 26.

The centrelines of the fuel channels are 5 m and 10 m lower in elevation than the centrelines of the headers. This corresponds to the elevation of the highest and lowest fuel channels in a CANDU reactor. Only the lower of the two channels was used in the standing start tests [5].

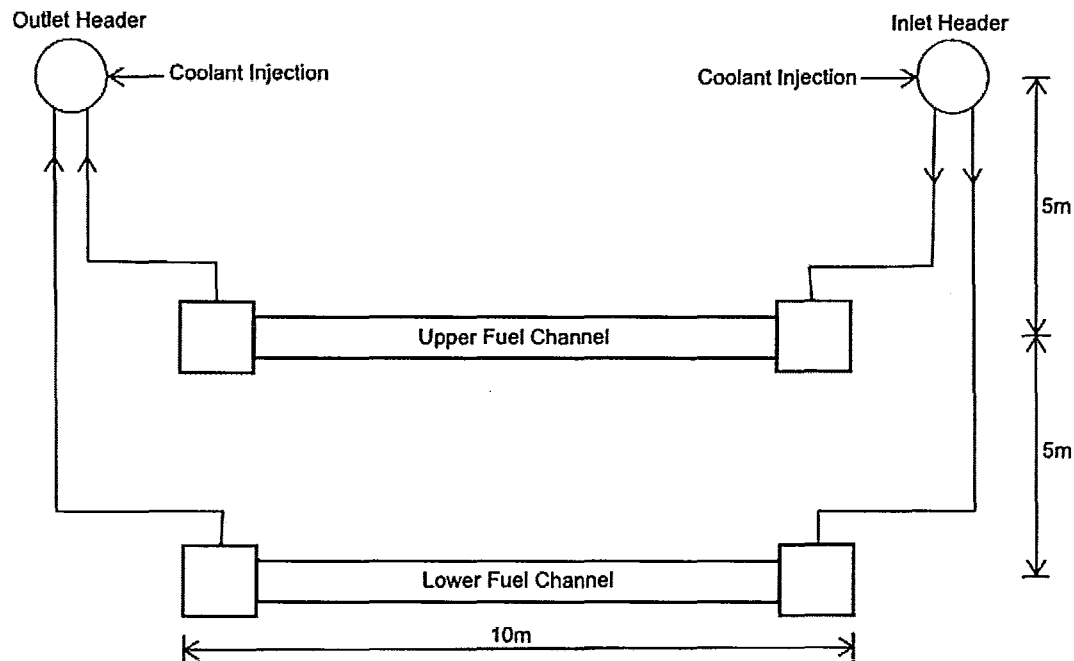


Figure 26 - Schematic of CWIT Facility [5]

3.1.1 Fuel Element Simulators

The electrically heated fuel element simulators (FES) are 11.6 m in length (including an extension beyond the end fittings to allow connections with the electrical supply), with a heated portion of approximately 6 m [5]. They are located concentrically in the pressure tube, in the same arrangement as the fuel elements in a 37 element bundle. In the heated section, each FES is composed primarily of an Inconel-600 heater filament surrounded by an Inconel tube with an outer diameter of 13.08 mm – the same as a fuel element [5]. The heated section of each FES has twelve segments, representing fuel bundles. Each segment is 482.6 mm in length with the end plates represented by an intervening unheated segment of 12.7 mm. The heat capacity of each FES is calculated to be 5.6 J/°C-cm of element length, at 800 °C [25]. The composition of the fuel element simulators changes outside the heated section, but the internal composition remains comparable in terms of heat capacity and mass, and the Inconel sheath extends into the end fitting dead-space (see Figure 27).

The power profile in the heated section varies radially and axially. The radial depression ratio¹¹ from outer FES pins to central FES is 1 – 0.81 – 0.72 – 0.68 [5]. The axial power distribution is described by the equation:

$$\frac{q(x)}{q_{ave}} = 1.485 * \cos(0.49 * x) \quad (1)$$

where x is the axial distance from the centre of the channel and $q(x)$ is the power output per unit length [5]. This results in normalised power levels ranging from 1.485 at the centre of the channel to 0.149 at the extremities of the heated sections¹².

The end plates present in a real CANDU fuel bundles are not included in the CWIT facility. This results in a small reduction in the amount of metal present in the channel, reducing the heat capacity of the channel and possibly resulting in a slightly faster heat up. However, due to the small mass of the end plates this effect is expected to be insignificant. This may however have some impact on the pressure drop along the channel.

3.1.2 Pressure Tube

The pressure tube is composed of Zircalloy 2.5% Niobium with inner and outer diameters of 103.8 mm and 112.4 mm, respectively [5]. A square enclosure 0.356 m wide and 5.49 m long surrounds the channel and is filled with water during the standing start tests, simulating the thermal effects of the moderator.

¹¹ The radial depression ratio refers to the ratio of the heat generation rate per pin in each ring of pins. The values presented are normalised such that the power of the outer ring is 1.

¹² The axial power variation is superimposed on the radial variation. The mid-channel to channel extremity ratio of 1.485 : 0.149 applies to any given ring of pins.

3.1.3 End Fittings

The end fittings were typical CANDU end fittings that had been modified to allow the passage of the FES unheated extensions. The FES extensions pass through the end fittings and exit through an O-ring equipped bundle flange (Figure 27). Three baffle plates are present in each end fitting, with the intended functions of maintaining fuel geometry and simulating the effects of the shield plug. To this end, the baffle plate closest to the centre of the channel isolates the 'dead space' containing the fuel extensions in the centre of the end fitting. The dead space has a volume of approximately $.0085 \text{ m}^3$ [5].

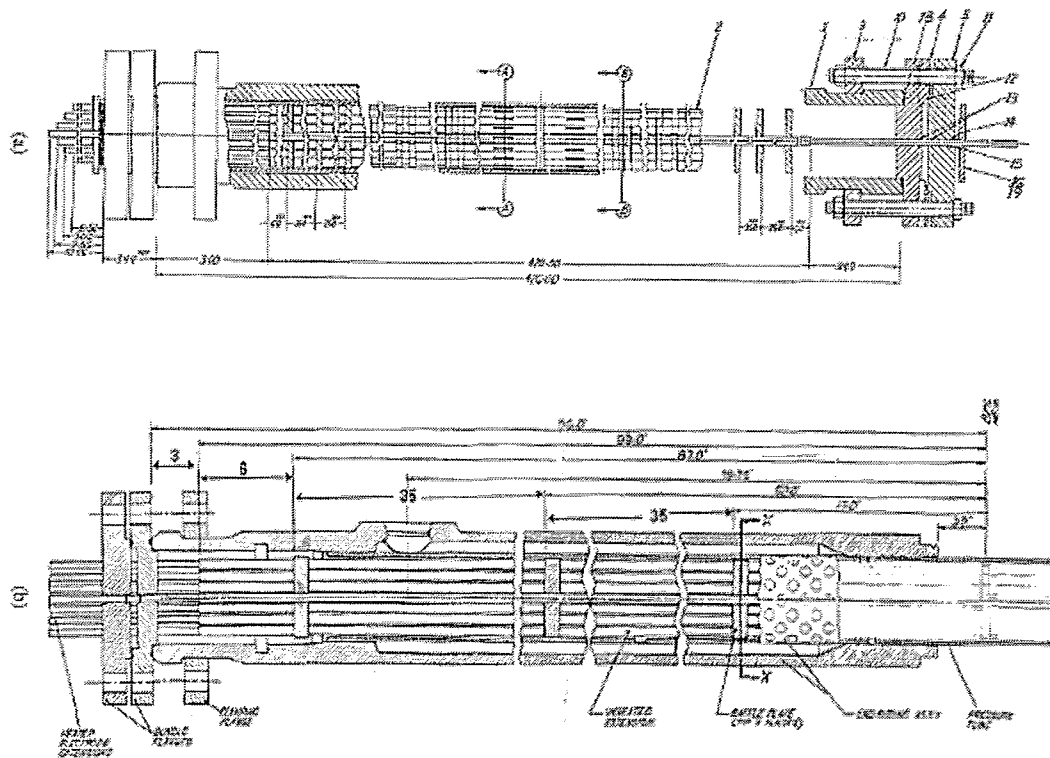


Figure 27 - CWIT End Fitting [5]

3.1.4 Feeders and Headers

The feeders have a complex geometry (see Figure 28), and are wrapped in 50 mm thick high temperature fibreglass insulation [5]. They are composed of

pipings with diameters of 73.7 mm, 59 mm, and 49.2 mm. Trace heating¹³ of the feeders was not used.

For practical reasons, the headers do not represent typical CANDU headers, but are each composed of 1.2 m of 254 mm Schedule 120 stainless steel pipe [5].

¹³ Trace heating is electrical heating which, in this case could be used to maintain the temperature of the feeders.

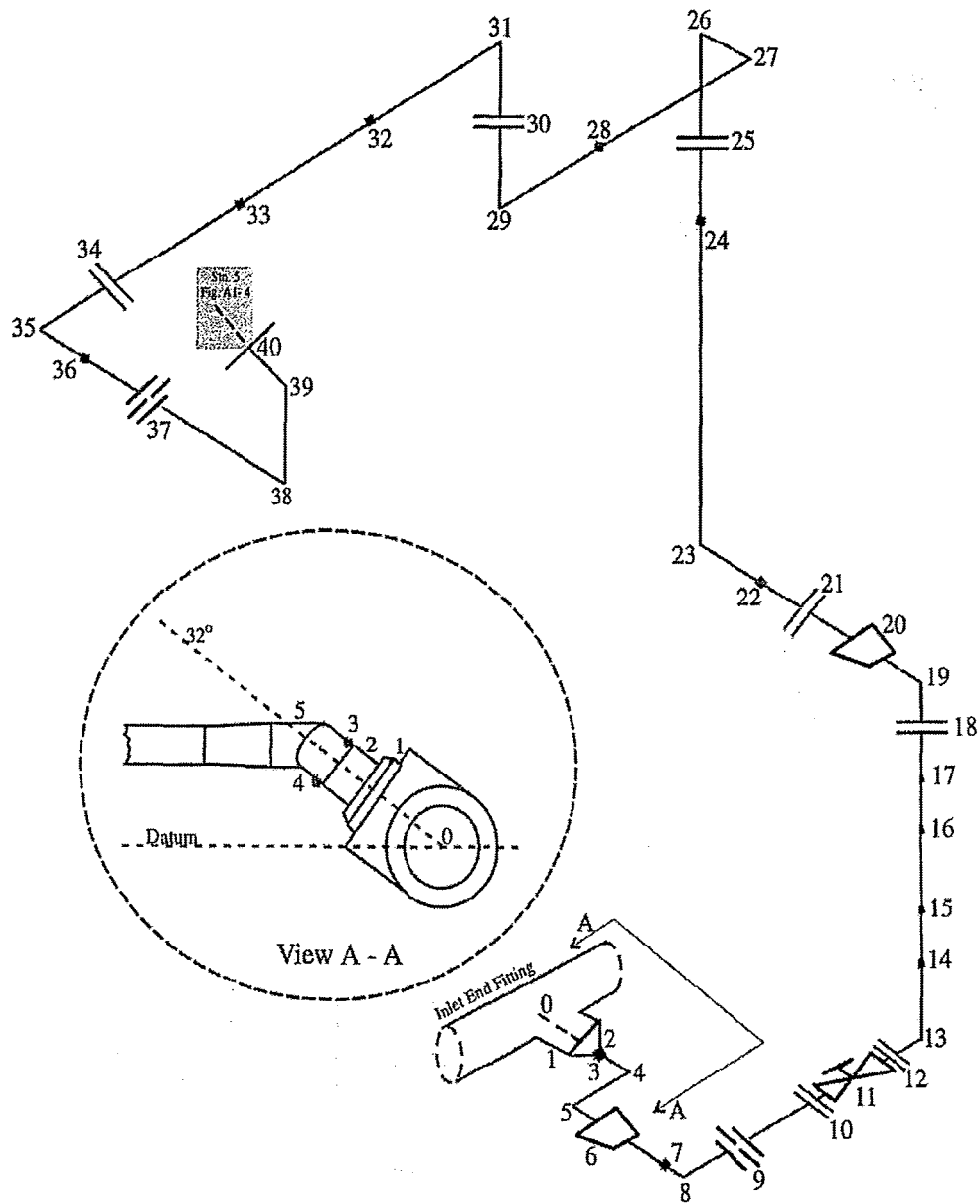


Figure 28 - Feeder Geometry [5]

3.1.5 Thermocouples

Over 100 thermocouples are located on the pressure tube and various fuel element simulators, at a number of locations along the heated portion of the channel. The location of each fuel channel instrumentation plane along the fuel channel is shown in Figure 29. The locations of the thermocouples measuring the surface temperature of the FES and the pressure tube in each of the instrumentation planes are shown in Figure 30.

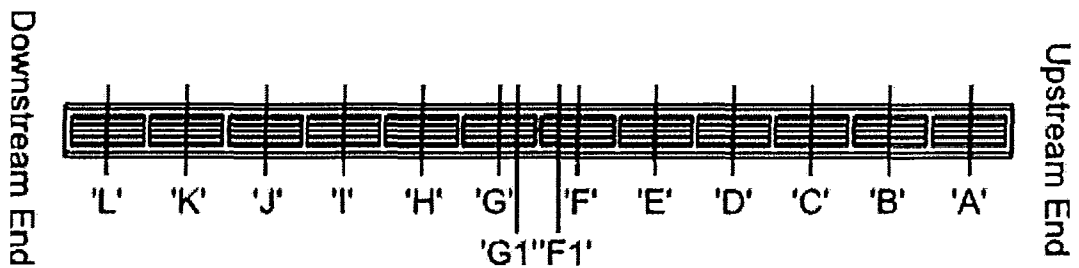


Figure 29 - CWIT Thermocouple Locations – Planes¹⁴

¹⁴ Representation of bundles is for illustrative purposes, the pins in the CWIT test rig were continuous throughout the channel.

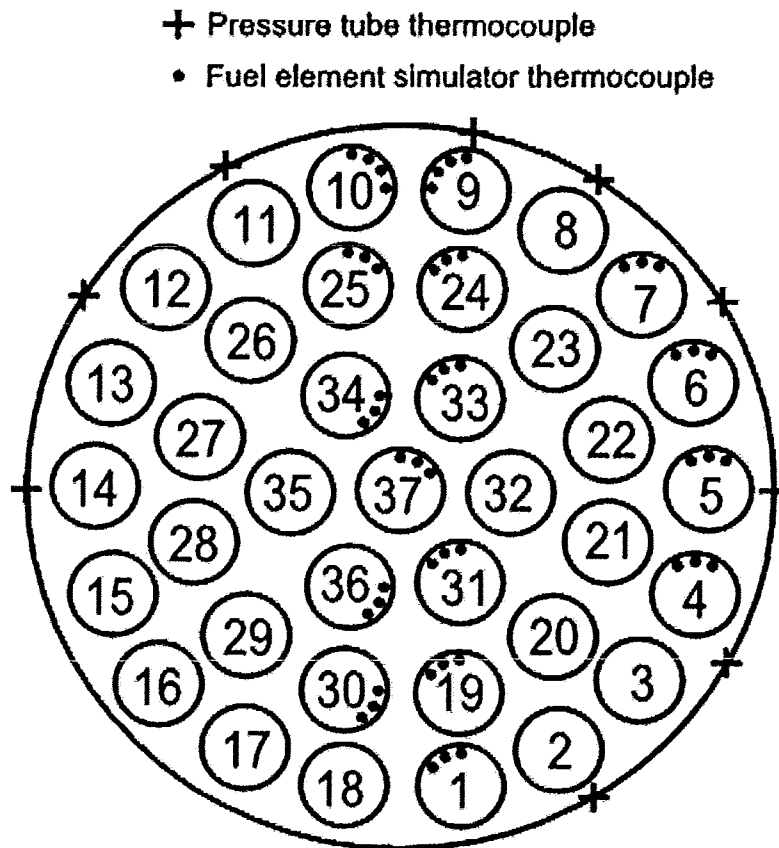


Figure 30 - CWIT Thermocouple Locations – Cross Section¹⁵

There are also fuel element simulators located in four planes in each of the end fittings. A large number of thermocouples are located on the pressure tube and various fuel element simulators, at a number of locations along the heated portion of the channel. The location of each end fitting instrumentation plane is shown in Figure 31. The locations of the thermocouples measuring the surface temperature of the end fitting body in instrumentation planes 1 and 4 are shown in Figure 32.

¹⁵ Pin thermocouple locations are at planes A, B, C, D, E, F, G, H, I, J, K, and L, as viewed from the upstream end of the channel. Pressure tube thermocouple locations are at planes B, D, F1, G1, I, and K, as viewed from the upstream end of the channel.

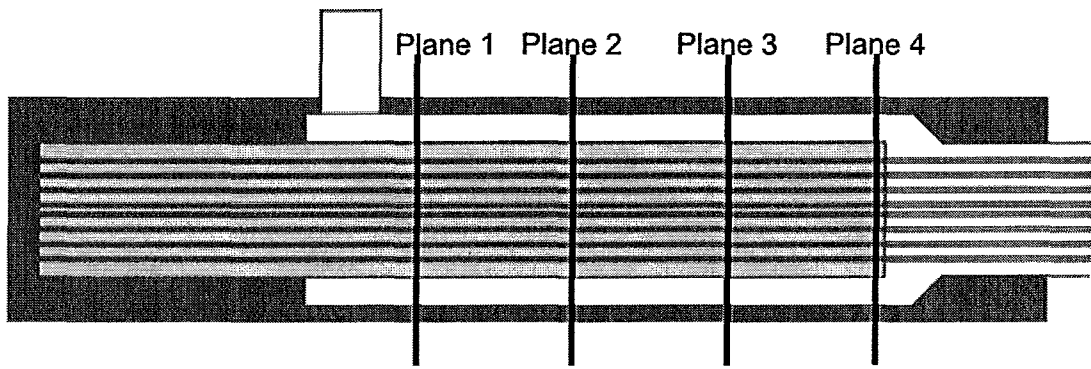


Figure 31 - CWIT End Fitting Thermocouple Location Schematic – Planes

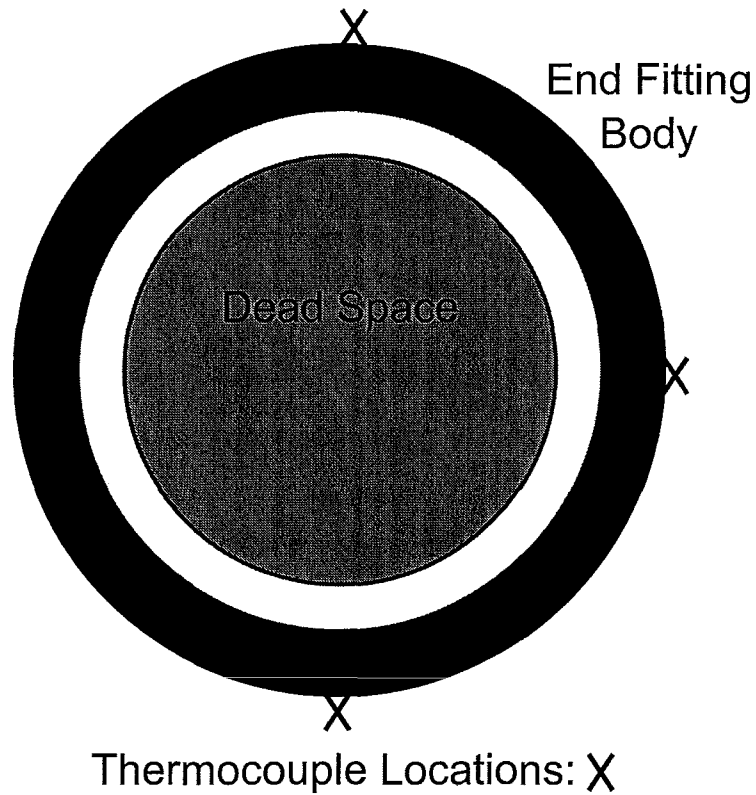


Figure 32 - CWIT End Fitting Thermocouple Location Schematic – Cross Section

3.1.6 CWIT Experimental Conditions

In the present study, two of the tests performed at CWIT are modelled: #1617 and #1613. These tests were chosen because one resulted in single phase venting (#1617), and one led to two phase venting (#1613). The experimental conditions are outlined in Table 1.

Table 6 - CWIT Experimental Conditions

	Header Pressure (kPa)	Initial Temperature (°C)	Channel Power (kW)	Saturation Temperature (°C) ¹⁶
#1617	7000	30	30	286.8
#1613	2000	30	131	214.9

3.2 GOTHIC Code Description

GOTHIC (Generation of Thermal Hydraulic Information in Containments) is a thermal-hydraulics software program, utilising a control volume approach, and solving mass, energy, and momentum conservation equations for multi-phase flow [17, 18]. Historically, GOTHIC has been applied primarily to nuclear containment analysis, but some analysis of natural circulation in primary heat transport systems has been successfully performed more recently (see Section 2.4).

GOTHIC solves mass, momentum and energy balances for three separate phases: vapor, continuous liquid (pools, films, etc.) and dispersed liquid (drops). Mechanistic models and correlations are used to couple the phase balance equations for interface mass, energy and momentum transfer for single phase

¹⁶ Measured in the channel, which is at a pressure approximately 100 kPa above the header pressure.

flows and a variety of two-phase flow regimes. Thermal non-equilibrium between phases and unequal phase velocities are also accounted for in GOTHIC's interface models [17, 18].

The control volume approach employed by GOTHIC allows for subdivision of control volumes in rectangular grids in up to 3-dimensions. Geometrical layouts can be further refined through the introduction of blockages to volumes, which impact the volume and area porosities of affected cells in subdivided volumes. Control volumes can be connected by flow paths that conserve momentum in up to 3-dimensions.

An optional two equation, k - ϵ turbulence model accounts for turbulent shear and mass and energy diffusion in applicable situations. In this study, the k - ϵ turbulence model is activated for situations such as venting or condensation in the end fittings, where Reynolds numbers may be sufficiently high to induce turbulence. Where flow is laminar or negligible, the k - ϵ turbulence model is not used.

Heat structures in GOTHIC allow for modelling of the thermal properties of materials as well as heat production. In this study, heat structures are used extensively in modelling the end fittings and fuel channel – including the heat-producing fuel element simulators.

Blockages and bends modelled in subdivided control volumes in GOTHIC result in intrinsically calculated flow losses [26]. These irreversible losses follow from fluid momentum lost from cell to cell, and typically result in reasonable k -values for a variety of structures [26]. Figure 33 shows the momentum balance as treated by GOTHIC. In the event that there is a blockage immediately downstream of a given cell, the downwind ($jx+$), momentum term will be discarded, inducing an irreversible pressure loss. The k -values calculated by

GOTHIC for the obstructions modelled in this study are discussed in Section 3.4.1.

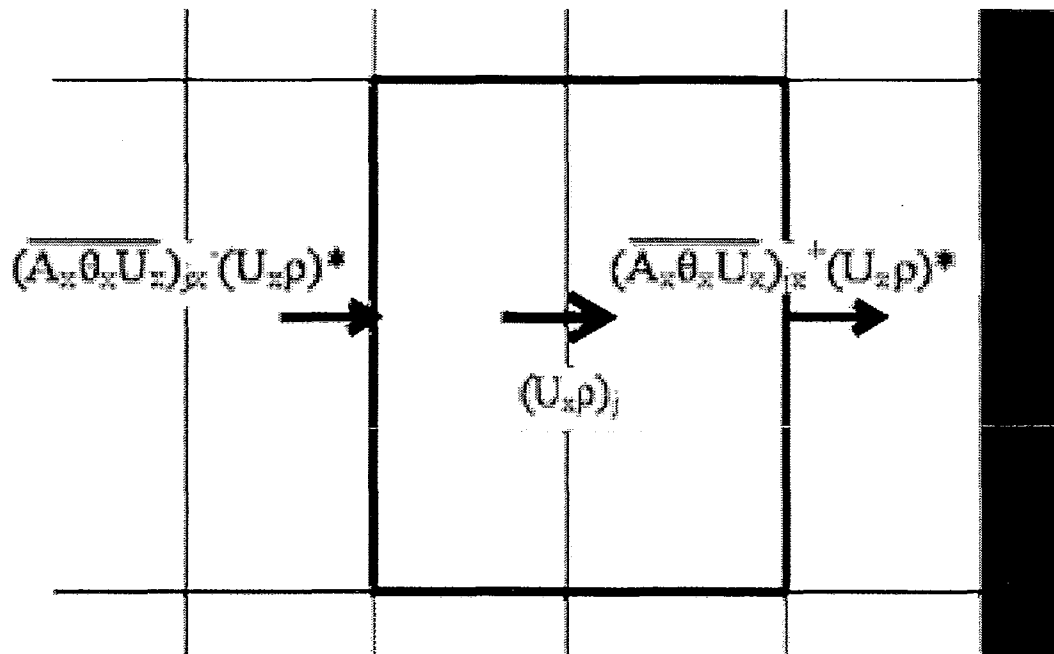


Figure 33 - GOTHIC Momentum Balance [26]¹⁷

3.3 Description of Reference Models

3.3.1 Modelling Assumptions

The following assumptions and simplifications were applied in developing the GOTHIC model of the CWIT facility:

¹⁷ θ_x represents the area porosity of the cell's x-face. A_x represents the area of the cell's x-face. U_x represents the fluid velocity through the cell's x-face. ρ represents the fluid density.

1) Bundle end plates are not modelled, and no additional flow losses to account for their absence are included. This could result in slightly faster venting, however losses due to the end plates are considered insignificant relative to those resulting from the FES, and this effect is expected to be minimal. Bundle end plates were also not used in the CWIT facility.

2) The bundles are assumed to be concentrically located in the channel. In the test rig, the fuel element simulators are held in a concentric location by supports at each end of the channel. Some sagging may occur over the length of the channel, but the impact of this is expected to be small and conservative¹⁸ [9].

3) Heat loss from the feeders is neglected. The CWIT feeders are insulated [5], and further, high temperatures are only present in the feeders when venting has already initiated.

4) Heat loss from the end fitting body is not modelled. Heat transfer from the end fitting body to the atmosphere is not expected to be significant.

5) Axial power distribution in the model is non-uniform from half-bundle to half-bundle in the heated section of the channel, but is uniform within each half bundle (that is, the channel power is segmented). As the total power is conserved, this level of resolution is expected to be sufficient to capture channel behaviour¹⁹.

6) The calandria tube and moderator are not modelled. Instead, total heat loss from the fuel channel to the moderator is accounted for using a correlation derived from measurements taken at the facility [25].

¹⁸ The impact of pressure tube sag on IBIF effectiveness is may not be conservative in cases where asymmetrical channel blockages are present.

¹⁹ A figure comparing the CWIT axial power profile to the modelled axial power profile is provided in Appendix A.

3.3.2 Modelling Methodology

3.3.2.1 Main Model Components

Both subdivided and lumped-parameter volumes have been applied to simulate the CWIT facility. Subdivided volumes are used to model the fuel channel, including both the Fuel Element Simulators and End-Fittings, and the inlet and outlet feeders are modelled using lumped-parameter volumes. The GOTHIC model layout is shown in Figure 34. The model consists of the following components:

- a) Fuel channel including the heated 6m of the fuel element simulators (Vols. 1s-24s)
- b) Inlet and outlet end fittings (Vols. 25s-28s)
- c) Inlet and outlet feeder piping (Vols. 29-46)
- d) Boundary conditions representing inlet and outlet headers (1P and 2P)
- e) 3D flow connectors (1-27)
- f) 1D flow paths (1-36)

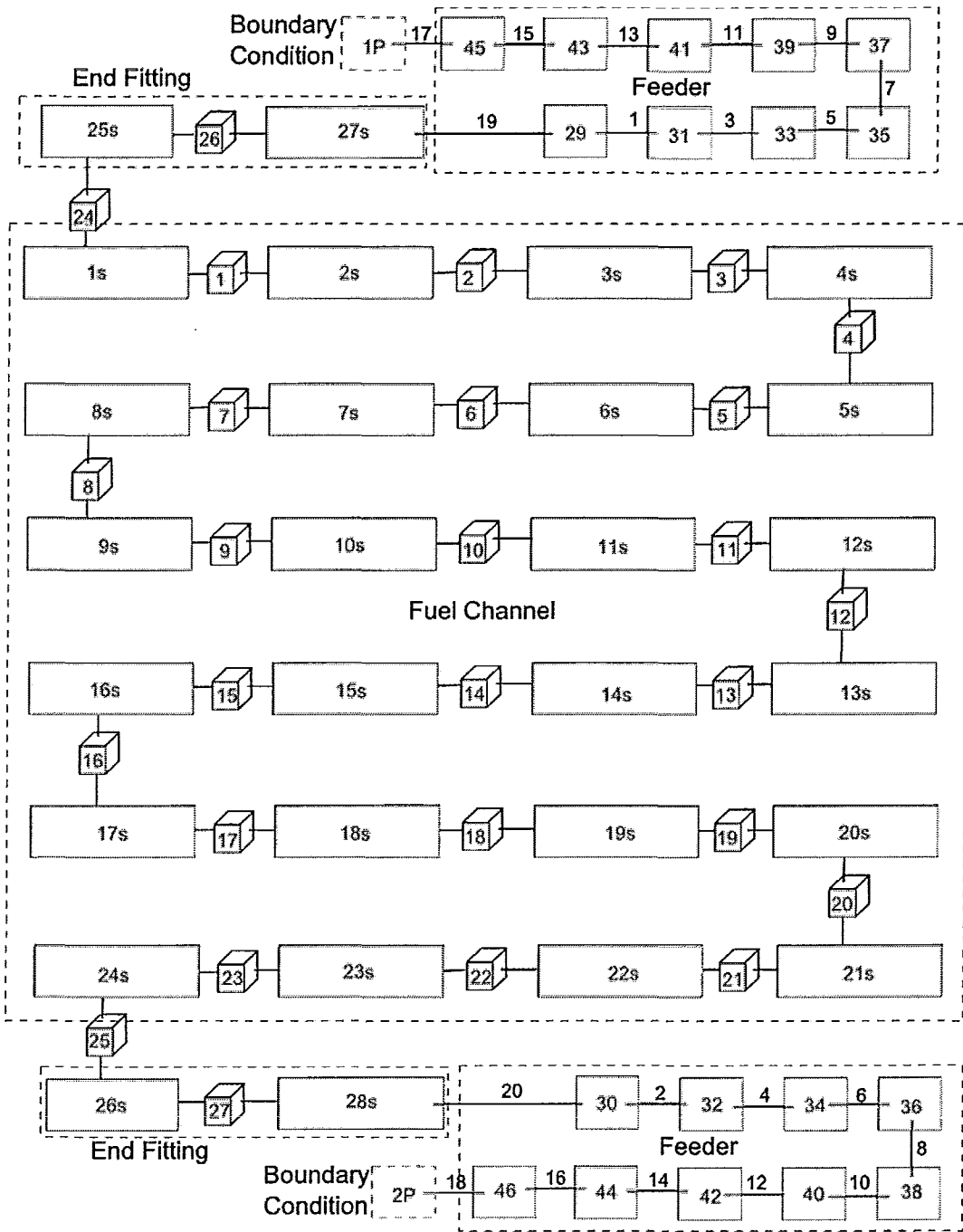


Figure 34 - GOTHIC Model Schematic

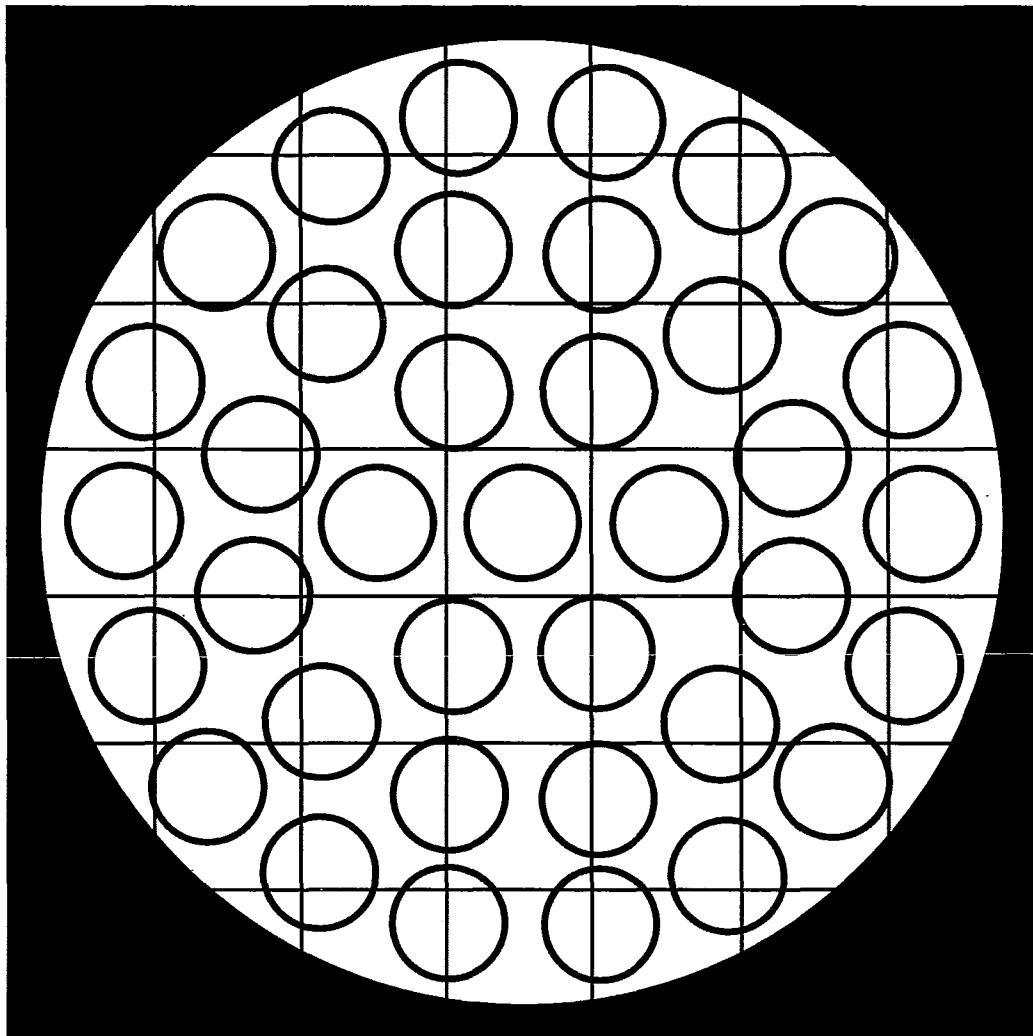


Figure 35 - GOTHIC Model Channel Nodalisation Cross-Section

i. Heated Portion of the Channel

The geometry and thermal characteristics of the CWIT facility are modelled, with 37 FES concentrically located inside the pressure tube as described. Each of the 24 volumes in the heated portion of the channel is subdivided into a 3x7x7 grid. Each of the cells in the grid is treated as a porous region (see Figure 35).

ii. Inlet and Outlet End-Fittings

Each end fitting is modelled as two control volumes. The first represents the approximately 25 cm adjacent to the fuel channel, and is the location of the obstruction in cases where one is introduced, while the second represents the rest of the end fitting. The dead space in the end fitting is represented as a thermal conductor, with a heat capacity calculated to be equal to that of the CWIT dead space. The obstruction volume is subdivided using the same 3x7x7 grid as the volumes in the channel, and the larger end fitting volume is subdivided using a 5x10x10 grid.

iii. Inlet and Outlet Feeders

Nine lumped parameter volumes are used to represent each of the inlet and outlet feeders. The geometry of the feeders as well as the flow losses associated with elements [5] found in them are incorporated in the volumes and the 1D flow paths between them.

iv. Boundary Conditions

The boundary conditions represent the headers, and are defined using the header pressures and initial temperatures listed in Table 1.

v. Fluid Flow Junctions

Fluid flow is modelled using both 1D flow paths and 3D flow connectors. The 1D flow paths are applied between the lumped parameter volumes representing the feeders. The 3D flow paths, which allow for transfer of momentum in three dimensions, are used in the fuel channel and end fittings where non-axial momentum is important.

3.3.2.2 Heat Transfer Correlations

Two approaches to heat transfer are used in the model. The first is the empirically based coefficient for heat loss from the pressure tube to the moderator. This heat transfer coefficient is derived from measurements taken at the CWIT facility, and has a value of 5.9 W/m-K [25].

The second approach is a ‘built-in’ heat transfer option in GOTHIC referred to as ‘film’. This is a compilation of heat transfer correlations capable [17, 18] of modelling heat transfer to single phase liquid or vapour (Dittus-Boelter [20]), as well as saturated or subcooled nucleate boiling (Chen [22]), and condensation (a ‘wet wall model’ estimating heat and mass transfer [17]). The ‘film’ heat transfer option is applied to all other thermal conductor surfaces: fuel element simulators, the inside of the pressure tube, and the end fitting body and dead space.

3.3.2.3 Materials Modelling

Four materials are defined in this model: Inconel-600 (representing the fuel element simulators and extensions), Zircalloy 2.5% Niobium (used in the pressure tube), Type-403 Stainless Steel (used in the end fitting), and a representative material used to replace the heat capacity of water in the dead space. The relevant quantities for these materials are density, thermal conductivity, and specific heat as a function of temperature. The values used in defining these materials can be found in Appendix A.

3.3.2.4 Fuel Element Simulator Modelling

3.3.2.4.1 Fuel Element Simulator Geometry

The heated section of the fuel element simulators (~6m) is composed of a number of elements, most significantly an outer sheath of Inconel-600, with an outer diameter of 13.08 mm [5]. The pins are modelled as a tube-type conductor composed of Inconel-600 with an inner diameter calculated to yield the appropriate heat capacity in view of the outer diameter of 13.08 mm. Each of these 37 conductors is oriented on an appropriately located blockage (see Appendix A), representing the fuel element simulator in each fuel channel control volume. The heat capacity for the heated section of the pins is measured to be 452 J/C-m [25].

Inconel-600 heat capacity = 444 J/C-m

Inconel-600 density = 8430 kg/m³

Heater element heat capacity = 452 J/C-kg

Pin outer radius = .00654m

Pin mass per unit length:

$$\frac{452[J/C - kg]}{444[J/C - m]} = 1.018[kg/m] \quad (2)$$

Pin cross sectional area:

$$\frac{1.018[kg/m]}{8430[kg/m^3]} = .00012[m^2] \quad (3)$$

Pin inner radius:

$$(.00654[m])^2 - \frac{.00012[m^2]}{\pi} = .00208[m] \quad (4)$$

The coordinates locating each of the fuel element simulators were calculated for a concentrically located geometry, and are listed in Appendix A.

3.3.2.4.2 Fuel Element Simulator Power

Volumetric power levels for each ring in each half bundle are varied to reflect the radial and axial flux profile across the channel. The radial depression ratios²⁰ for each ring are [5]:

Outer – 1

Mid – 0.81

Inner – 0.72

Centre – 0.68

While the listed depression ratios are normalized to the outer ring, renormalizing them to have a weighted (based on the number of pins in each ring), average value of 1 is more appropriate for calculating specific power levels:

Outer – 1.131

Mid – 0.916

Inner – 0.814

Centre – 0.769

The axial profile is described by the equation: $P=1.485*\cos*(0.49*x)$, where x is the distance from the centre of the channel. The product of the axial profile at each half bundle and the weighted depression ratio for each ring yields a factor which can be multiplied by the average volumetric power to produce the volumetric power for a given ring and volume (Table 2).

²⁰ The radial depression ratio refers to the ratio of the heat generation rate per pin in each ring of pins. The values presented are normalised such that the power of the outer ring is 1.

Table 7 - Power Profile Factors²¹

	O-ring	M-ring	I-ring	Centre
Volume 1	0.270419	0.219039	0.194701	0.183885
Volume 2	0.470518	0.38112	0.338773	0.319952
Volume 3	0.663566	0.537488	0.477767	0.451225
Volume 4	0.846668	0.685801	0.609601	0.575734
Volume 5	1.017081	0.823835	0.732298	0.691615
Volume 6	1.17225	0.949523	0.84402	0.79713
Volume 7	1.309851	1.060979	0.943092	0.890698
Volume 8	1.42782	1.156534	1.02803	0.970917
Volume 9	1.524389	1.234755	1.09756	1.036585
Volume 10	1.598112	1.294471	1.15064	1.086716
Volume 11	1.647883	1.334785	1.186476	1.12056
Volume 12	1.672956	1.355095	1.204528	1.13761
Volume 13	1.672956	1.355095	1.204528	1.13761
Volume 14	1.647883	1.334785	1.186476	1.12056
Volume 15	1.598112	1.294471	1.15064	1.086716
Volume 16	1.524389	1.234755	1.09756	1.036585
Volume 17	1.42782	1.156534	1.02803	0.970917
Volume 18	1.309851	1.060979	0.943092	0.890698
Volume 19	1.17225	0.949523	0.84402	0.79713
Volume 20	1.017081	0.823835	0.732298	0.691615
Volume 21	0.846668	0.685801	0.609601	0.575734
Volume 22	0.663566	0.537488	0.477767	0.451225
Volume 23	0.470518	0.38112	0.338773	0.319952
Volume 24	0.270419	0.219039	0.194701	0.183885

Finally, the specific volumetric power for each pin can be determined after calculating the average volumetric power for the fuel across the channel.

Pin outer radius = .00654m

²¹ The ring abbreviations O, M, and I represent the outer, middle, and inner rings of elements in a 37-element CANDU fuel bundle.

Pin inner radius = .002084m

Bundle length = .4953m

Fuel volume:

$$\pi * (.00654[m]^2 - .002084[m]^2) * 37 * .4953[m] * 12 = .026549[m^3] \quad (5)$$

High power:

$$\frac{131[kW]}{.026549[m^3]} = 4934[kW / m^3] \quad (6)$$

Low power:

$$\frac{20[kW]}{.026549[m^3]} = 753[kW / m^3] \quad (7)$$

The specific volumetric power rating for each ring and control volume can be found in Appendix A.

3.3.2.4.3 Fuel Element Simulator Unheated Extensions

Like the heated section of the pins, the unheated pin extensions are thermally modelled using an equivalent conductor composed of a tube of Inconel-600. Measurements of the heat capacity of the pin extensions are not available, consequently it has been calculated based on the components. Some degree of approximation is used, with only the two main constituent parts (Nickel and Inconel-600), being considered, and with the composition of the pin extensions treated as constant over their length.

Nickel Density: 8912 kg/m³

Nickel Heat Capacity: 444 J/C-kg

Nickel Mass:

$$\pi * .003175[m]^2 * 2.4384[m] * 37 * 8912[kg / m^3] = 25.46[kg] \quad (8)$$

Nickel Heat Capacity:

$$25.46[kg] * .444[kJ / C - kg] = 11.3[kJ / C] \quad (9)$$

Inconel-600 Volume:

$$\pi * (.00654[m]^2 - .00595[m]^2) * 37 * 2.3622[m] = .00202[m^3] \quad (10)$$

Inconel-600 Heat Capacity:

$$.00202[m^3] * 3598[kJ / C - m^3] = 7.28[kJ / C] \quad (11)$$

$$\text{Equivalent Inconel-600 Mass: } \frac{18.58[kJ / C]}{.444[kJ / C - kg]} = 41.86[kg]$$

(12)

Equivalent Inconel-600 Volume:

$$\frac{41.86[\text{kg}]}{8430[\text{kg} / \text{m}^3]} = .00497\text{m}^3 \quad (13)$$

Pin Inner Radius:

$$\left(.00654[\text{m}]^2 - \frac{.00497[\text{m}^3]}{2.4384[\text{m}] * \pi * 37} \right)^{\frac{1}{2}} = .005025[\text{m}] \quad (14)$$

3.3.2.4.4 Fuel Element Simulator Subdivision

The fuel element simulators are subdivided to allow for more accurate treatment of temperature profiles across the conductors. The GOTHIC auto-divide option is used, which spaces the divisions automatically based on composition and the magnitude of the heat transfer coefficient at the surface(s) of the conductor. In recognition of the possibility of nucleate boiling on the heated sections of the fuel element simulators and condensation on the unheated sections, a heat transfer magnitude of ‘very high’²² was chosen for both, resulting in the heated and unheated sections of the fuel element simulators being subdivided into 8 and 6 thermal regions, respectively (see Figure 36).

²² The ‘very high’ designation reflects a heat transfer coefficient on the order of 60000 W/m²-C [user manual].

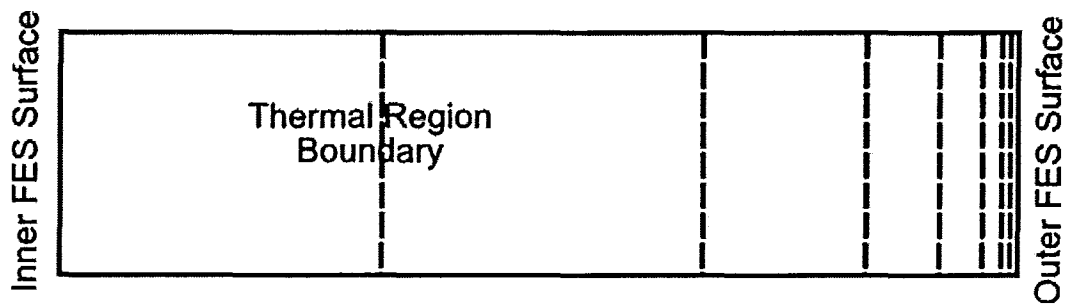


Figure 36 - GOTHIC Model Fuel Element Simulator Heated Section Thermal Subdivision

3.3.2.5 Pressure Tube Modelling

The pressure tube has inner and outer radii of 103.8 mm and 112.4 mm, respectively; and is composed of Zircalloy-2.5% Niobium. Subdivision of the pressure tube conductor is performed using the GOTHIC auto-divide option. The magnitude of the heat transfer coefficients specified during the auto-divide process are ‘very high’²³ for the inside and ‘medium’²⁴ for the outside of the pressure tube, in recognition of the potential for condensation heat transfer on the inside of the tube and the empirically based heat transfer correlation applied to the outside. The auto-divide process resulted in a thermal division of the pressure tube 9 regions.

3.3.2.6 Obstruction Modelling

Asymmetrical obstructions were not included in the CWIT facility, and the range of scenarios to which these results may be applied has not been ascertained. As a result, it is desirable in cases where an obstruction is included, to model the obstruction in a generic fashion. To this end, a cylindrical blockage with a length of 10 cm, is placed in the centre of volume 25s (see Figure 34). This location corresponds to approximately the halfway point between the end of the heated

²³ (see above)

²⁴ The ‘medium’ designation reflects a heat transfer coefficient on the order of 600 W/m²-C [user manual].

section of the fuel element simulators, and the point in the end fitting where they pass through the inner baffle plate and into the dead space. In defining the obstruction geometry, the cylindrical blockage is superimposed over the existing unheated fuel element simulator extensions. Finally, the obstruction is not modelled thermally.

While this geometry does not necessarily reflect any real asymmetrical obstruction scenarios (such as an inspection tool), parametric variation of the radius of the obstruction is representative of a range of possible situations. Information for each obstruction case, including the obstruction radius, the volume porosities of the cells in a cross section intersecting the obstruction, and the k-values that result from simulated single-phase flow through volume 25s (see Figure 34) can be found in Section 4.4.1. It is hoped that this characterisation of obstructions in multiple ways will lead to more direct applicability of the results of these simulations to specific asymmetrical blockage scenarios.

3.3.2.7 End Fitting Modelling

Four main components of the end fitting are included in this model: the outer end fitting assembly, the unheated pin extensions, the dead space located in the centre of the end fitting, and the feeder opening through the outer end fitting assembly representing the Grayloc fitting.

3.3.2.7.1 End Fitting Assembly

Some of the measurements required to model the end fitting assembly are, necessitating some approximation. The masses of the modelled end fitting components are calculated below.

Liner tube mass:

An approximate value is employed, as details on the end fitting components are somewhat obscure. An average of the inlet and outlet values [27] is used.

$$(44 \text{ lbs} + 59.5 \text{ lbs}) / (2 * 2.2 \text{ lb/kg}) = 23.5 \text{ kg} \quad (15)$$

End fitting assembly mass:

Since the liner tube is the only component of the end fitting mass modelled separately from the assembly, the assembly mass is taken to be the difference between the total end fitting mass [28] and the mass of the liner tube.

$$171.7 \text{ kg} - 23.5 \text{ kg} = 148.2 \text{ kg} \quad (16)$$

Roughly, the end fitting assembly (not including the liner tube), is composed of a hollow tube that has thicker walls at each end and thinner walls in the centre. For simplicity, these regions are labelled 1, 2, and 3 in the Figure 37. The inner radii in regions 1 and 2 are known, and the inner radius of region 3 is estimated to be the same as that of region 1. The outer radius is taken to be constant across the end fitting, and must be calculated such that it is consistent with a mass of 148.2 kg of type-403 stainless steel.

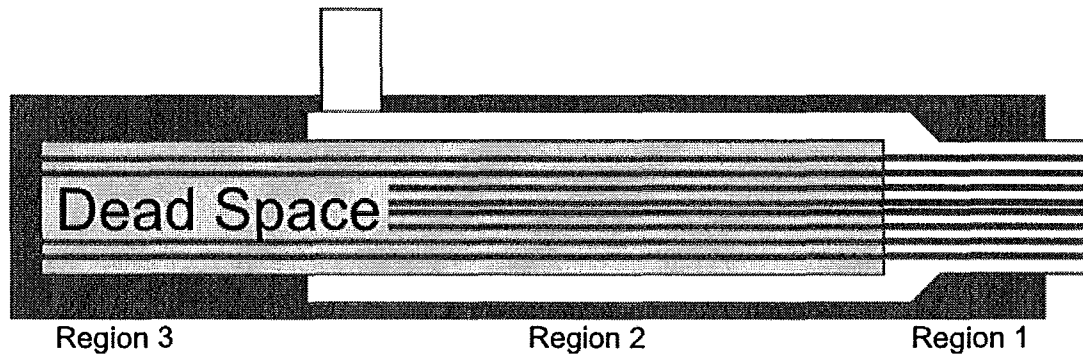


Figure 37 - Schematic of End Fitting Model

Region 1

-inner radius: .0562 m

-length: 7.75" = .19685 m

Region 2

-inner radius: .0709 m

-length: 70.5" = 1.7907 m

Region 3

-inner radius: .0562 m

-length: 14.75" = .37465 m

Assembly body volume:

$$\frac{148.2[\text{kg}]}{7750[\text{kg}/\text{m}^3]} = .019123[\text{m}^3] \quad (17)$$

Assembly outer radius:

$$\left(\frac{.019123[m^3]}{\pi * 2.3622[m]} + \frac{.0562[m]^2 * .19685[m]}{2.3622[m]} + \frac{.0709[m]^2 * 1.7907[m]}{2.3622[m]} + \frac{.0562[m]^2 * .37465[m]}{2.3622[m]} \right)^{1/2} \quad (18)$$

$$= .08457[m]$$

The end fitting assembly is thus modelled as a tube of type-403 stainless steel with an outer radius of .08457 m and an inner radius of .0562 m in regions 1 and 3, and .0709 m in region 2.

Thermal subdivision of the end fitting conductor is performed using the GOTHIC auto-divide option. The magnitude of the heat transfer coefficient specified during the auto-divide process is ‘very high’²⁵, in recognition of the potential for condensation heat transfer on the end fitting body. The auto-divide process resulted in a thermal division of the end fitting conductor in 10 regions for sections 1 and 3, and 9 regions for section 2.

3.3.2.7.2 Unheated Pin Extensions

The unheated pin extensions extend with the same concentric geometry and thermal characteristics from the heated section of the pressure tube to the dead space in each end fitting. Inside the dead space, the thermal characteristics of the pin extensions are modelled as outlined in Section 4.3.2.7.3.

3.3.2.7.3 End Fitting Dead Space

The dead space in the CWIT experimental rig is separated from the free volume of the end fitting by the stainless steel liner tube and baffle plate. Though the seal is not water-tight, it is assumed that flow between the two volumes is low

²⁵ The ‘very high’ designation reflects a heat transfer coefficient on the order of 60000 W/m²-C [user manual].

enough to be ignored entirely. Geometrically, the dead space is simply modelled as a blockage, but modelling it thermally with GOTHIC is somewhat more complicated.

The dead space can be described most accurately as an external conductor, however GOTHIC does not allow an external conductor to be oriented on a cylindrical blockage such as the dead space. Consequently, the approach most reflective of the experimental situation is to ignore the movement of the water inside the dead space and treat the dead space as an equivalent thermal conductor composed of solid materials. The contents of the dead space include: the type 403 stainless steel liner tube and baffle plates, unheated fuel element simulator extensions, and water. Additionally, the portion of the end fitting assembly that is not in contact with the end fitting free volume is included in the dead space volume.

As the layers of the conductor are nested, the modelled order is significant. From the outside in, the order of the layers is: liner tube, water substitute, fuel element simulators, end fitting assembly. The end fitting assembly is located innermost because in the experimental setup, heat must be conducted over a greater distance from the liner tube through the water to reach most of the end fitting assembly than is the case for the fuel element simulators. A substitute for the water must be used, as flow cannot be modelled in conductors; also, the volume of material in the dead space is such that it cannot be fit in the modelled conductor without increasing the density of at least one of its components. As a result, while its heat capacity is conserved, the density of the water substitute is increased.

The composition of the dead space is shown in Table 3, and the calculation of these details is presented in Appendix A.

Table 8 - Dead Space Equivalent Conductor Composition

Material	Inner Radius (cm)	Outer Radius (cm)
End Fitting: Type 403 Stainless Steel	1.034	3.200
Heater Extensions: Inconel-600	3.200	4.231
Water Substitute	4.231	5.118
Liner Tube: Type 403 Stainless Steel	5.118	5.667

Thermal subdivision of the dead space conductor is performed using the GOTHIC auto-divide option. The magnitude of the heat transfer coefficient specified during the auto-divide process is ‘very high’²⁶, in recognition of the potential for condensation heat transfer on the liner tube. The auto-divide process resulted in 32 thermal regions in the dead space, with the number of divisions increased as a result of the composite nature of the dead space.

3.3.2.7.4 End Fitting – Feeder Opening

In order for fluid to flow from the end fitting to the feeder, an opening must be modelled in the end fitting assembly, representing the Grayloc fitting. To do this, an opening-type blockage is defined in the appropriate location in the end fitting volume. The coordinates of the inner end of the opening blockage must be chosen carefully to avoid interfering with the dead space blockage, but once this has been done the outer coordinates can be calculated with a recognition of the 32 degree angle the feeder makes with the end fitting (see Figure 28 and Figure 38), and some trigonometry.

²⁶ The ‘very high’ designation reflects a heat transfer coefficient on the order of 60000 W/m²-C [user manual].

Opening radius: .0295 m

Inner Y coordinate²⁷:

$$.057[m] * \cos(32) + .071[m] = .1193[m] \quad (19)$$

Inner Z coordinate:

$$.057[m] * \sin(32) + .071[m] = .1012[m] \quad (20)$$

Outer Y coordinate²⁸:

$$.15[m] * \cos(32) + .071[m] = .1982[m] \quad (21)$$

Outer Z coordinate:

$$.15[m] * \sin(32) + .071[m] = .1505[m] \quad (22)$$

²⁷ Where where .071 m is half the width and height of the volume, and .057 m is a distance from the centre of the volume chosen such that the dead space blockage is not interfered with.

²⁸ Where .15 m is a distance from the centre of the volume chosen such that the opening extends sufficiently to exit the volume at all points.

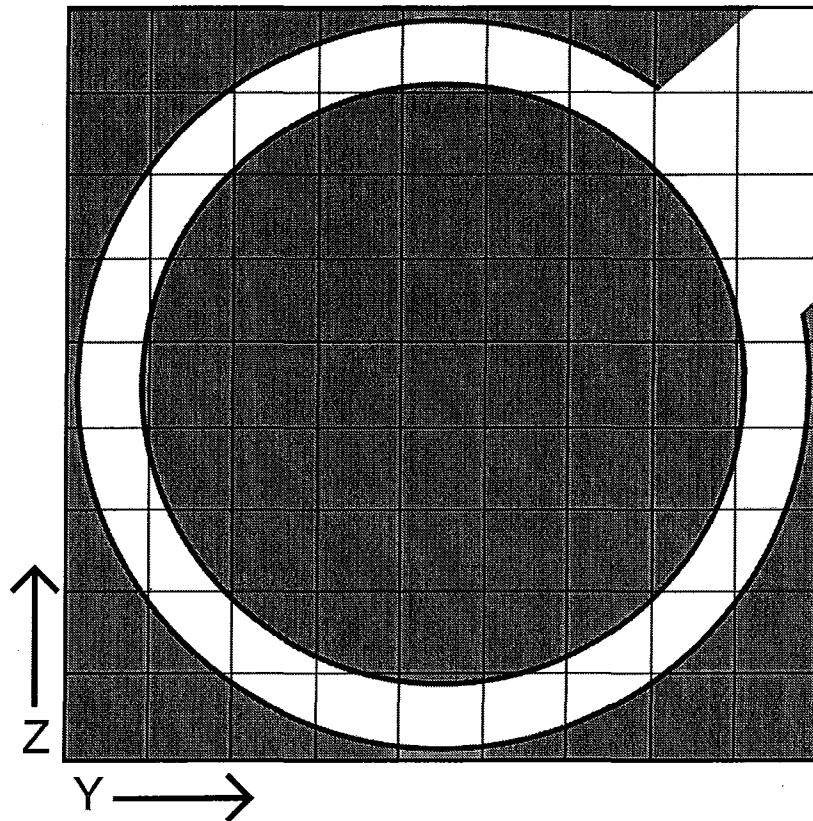


Figure 38 - Schematic of End Fitting Opening

3.3.2.8 End Fitting – Feeder Flow Paths

Due to the nature of the venting process in IBIF, modelling of the flow paths connecting the end fittings and the feeders must be approached with some care. It is expected that hot liquid or vapour will reach the feeders first via the ‘top’ (highest elevation) of the angled Grayloc connection (see Figure 38). Including a flow path connecting the first feeder volume to the end fitting cell affected by the opening whose elevation is highest is thus imperative.

Ideally, flow paths would also be included connecting the first feeder volume to all of the other end fitting cells impacted by the opening; however, due to the separate consideration of 1D flow paths in GOTHIC, inclusion of multiple

parallel paths results in massive, non-physical, counter-current flow²⁹. A single flow path located at the highest cell impacted by the opening has thus been used to represent the connection between the end fitting and the first feeder volume. Due to the importance of this aspect of the model, sensitivity simulations have been performed (see Section 3.4.3), examining the effect of varying the location of the flow path from the end fitting to the feeder.

3.3.2.9 Inlet and Outlet Feeder Modelling

The CWIT feeders are composed of approximately 40 sections [5], however, they have been grouped by elevation, angle, and pipe diameter to 9 representative volumes for this model. Components that incur a form loss are incorporated in the flow paths by adding flow losses. The volume, elevation, height, and hydraulic diameter of each of the feeder volumes is presented in Table 4.

The relative roughness of the feeders is not expected to have a large impact on the progress of the model, but a value is included for each path, based on a typical absolute roughness value for a fresh feeder: 7.62 μm . The relative roughness is obtained by dividing the absolute value by the pipe diameter in the volume in question.

Table 9 - Feeder Volume Details (in order from end fitting to header)

	Volume (m ³)	Elevation (m)	Height (m)	Hydraulic Diameter (m)
1	0.000364	0.105946	0.140147	0.059

²⁹ No shear stress is modelled between the multiple parallel flow paths representing a single pipe in the GOTHIC model. This is contrary to the situation in the experiment, where shear stress limits counter-current flow in the feeder. As a result of the total absence of shear stress in the model, the flow paths at higher elevation experience flow from the end fitting into the feeder, and the lower flow paths experience flow in the opposite direction. In addition to being non-physical, the flow rates in each direction reach levels that severely limit timestep sizes.

2	0.003783	0.187093	0.059	0.050628
3	0.010865	0.246093	5.715	0.0492
4	0.012112	5.899643	0.0737	0.072404
5	0.012999	5.973343	3.047	0.0737
6	0.005584	8.946643	0.0737	0.0737
7	0.003251	9.020343	0.762	0.0737
8	0.015268	9.708643	0.0737	0.0737
9	0.001109	9.782343	0.221045	0.0737

Minor loss coefficients for a number of components in the feeders are accounted for. These losses generally take place at the junction between two volumes, and are applied to the corresponding flow path. The minor loss coefficients are detailed in Appendix A, Table 35. The various parameters input in GOTHIC to model the 1D flow paths connecting the feeder volumes are detailed in Appendix A, Table 36 - Table 38.

3.4 Description of Sensitivity Models

3.4.1 Asymmetrical Obstruction Models

As outlined in Section 3.3.2.6, asymmetrical obstructions are modelled as 10 cm long cylinders in the centre of volume 25s (see Figure 34). A range of obstruction sizes have been modelled, from 0% to 100% channel blockage (Table 10). Each of these is characterised in several ways: radius, percentage of the area of an empty pressure tube blocked, cell porosity of a cross section of the cells containing the blockage, and the k-factor calculated intrinsically by GOTHIC for volume 25s.

Table 10 - Characterisation of Obstruction Cases

Area (% Of Channel)	Radius (cm)	(1-Porosity)			Intrinsically Calculated K-Factor of Vol. 25s
		Percentage of Volume Area ³⁰	Percentage of Pressure Tube Area ³¹	Percentage of Flow Area ³²	
0	0	67.73	58.83	0.43	2.7
50	3.670	83.24	78.62	48.29	15.4
90	4.924	92.53	90.46	76.94	445.4
91	4.951	93.09	91.18	78.66	746.1
92	4.978	93.75	92.02	80.71	1415.2
93	5.005	94.52	93.01	83.10	1339.0
94	5.032	95.31	94.01	85.52	3242.4
95	5.059	96.09	95.01	87.93	9179.7
96	5.085	96.87	96.01	90.34	17724.7
97	5.112	97.65	97.01	92.76	92696.6
98	5.138	98.43	98.00	95.17	1007839.6
99	5.164	99.22	99.00	97.59	63241589.7
100	5.190	100.00	100.00	100.00	~∞

³⁰ The volume is defined in rectangular coordinates, with the pressure tube defined as a cylinder inside it. The area of the volume is thus greater than that of the pressure tube.

³¹ This is the percentage blockage relative to an empty pressure tube. The effect of the fuel element simulator extensions can be seen in the 0% blockage case, where porosity is non-unity.

³² The flow area here is defined as the free area inside the pressure tube which is not occupied by fuel element simulator extensions.

The results of simulations using these asymmetrically obstructed models are the primary findings of this study, and are presented in Section 4.5.

3.4.2 Grid Sensitivity Models

The sensitivity of the model to nodalisation is examined by increasing the number of cells in the fuel channel and end fittings by a factor of approximately three. The grid in volumes 1s-26s (see Figure 34) is increased from $3 \times 7 \times 7$ to $3 \times 10 \times 10$. The grid in volumes 27s and 28s is increased from $5 \times 10 \times 10$ to $7 \times 14 \times 14$. The results of this mesh refinement are noticeable, but not significant, and are examined in Section 4.3.2.

It is worth noting that the computational demands of decreases in mesh size are very large, with refined-mesh single-phase simulations taking several weeks to complete and two-phase simulations requiring many months.

3.4.2.1 Grid Sensitivity of Obstructions

The porosity and intrinsic k-factor are affected by a change in nodalisation, warranting a separate examination of this effect. Comparing the porosity and k-factor data for the finer mesh presented in Table 10, to those for the reference case (Table 11), it is apparent that the porosity variation is practically nil, however there is some sensitivity of the intrinsically calculated k-factor to mesh size.

Table 11 - Characterisation of Obstruction Cases with a Refined Mesh

Area (%) Of Channel)	Radius (cm)	(1-Porosity)			Intrinsically Calculated K-Factor of Vol. 25s ³⁶
		Percentage of Volume Area ³³	Percentage of Pressure Tube Area ³⁴	Percentage of Flow Area ³⁵	
0	0	67.73	58.82	0.42	2.9
50	3.670	83.24	78.62	48.29	17.3
90	4.924	92.53	90.46	76.94	332.6
91	4.951	93.09	91.18	78.66	517.1
92	4.978	93.75	92.02	80.70	608.1
93	5.005	94.52	93.01	83.10	1250.2
94	5.032	95.31	94.01	85.51	2919.4
95	5.059	96.09	95.01	87.93	4661.6
96	5.085	96.87	96.00	90.34	16299.5
97	5.112	97.65	97.01	92.76	61531.8
98	5.138	98.43	98.00	95.17	675913.7
99	5.164	99.22	99.00	97.59	44069070.7
100	5.190	100.00	100.00	100.00	~∞

³³ The volume is defined in rectangular coordinates, with the pressure tube defined as a cylinder inside it. The area of the volume is thus greater than that of the pressure tube.

³⁴ This is the percentage blockage relative to an empty pressure tube. The effect of the fuel element simulator extensions can be seen in the 0% blockage case, where porosity is non-unity.

³⁵ The flow area here is defined as the free area inside the pressure tube which is not occupied by fuel element simulator extensions.

³⁶ Details of the calculation of the k-factors are presented in Appendix A.

3.4.3 End Fitting – Feeder Flow Path Location Sensitivity Models

As described in Section 3.3.2.8, there are several end fitting cells affected by the feeder opening that have non-zero surface porosities. Four models are created in order to examine the sensitivity of the simulations to flow path location in the end fitting opening (see Figure 39). Both the reference flow path and the flow path for the first sensitivity model (in Figure 39, labelled ‘Ref.’ and ‘s1’, respectively), are connected to the same cell, however the elevations of the flow path connections and the direction of momentum transfer to and from the 1D flow path are different.

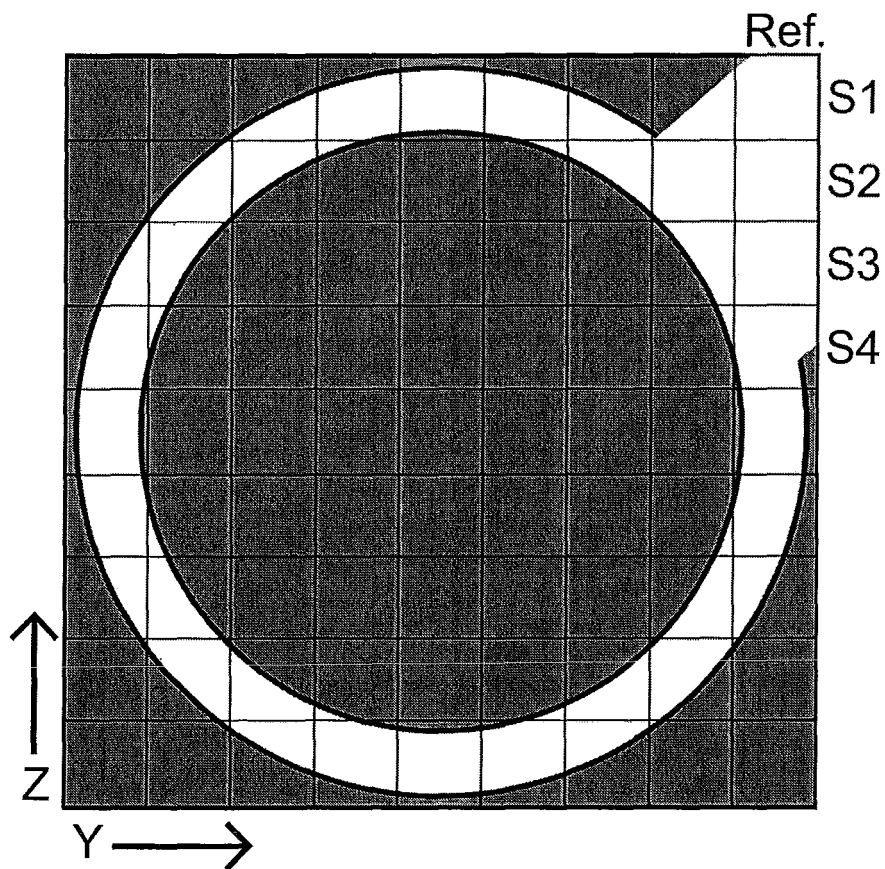


Figure 39 - Flow Path Sensitivity Locations

4 RESULTS

This section presents the results of the cases simulated using GOTHIC. 31 simulations are presented, 13 low power obstruction cases, 5 sensitivity simulations at low power, and 13 high power obstruction cases (See Table 12). The GOTHIC cases are also compared to results from the CWIT facility tests #1617 and #1613.

Table 12 - Case Matrix

Category	Description	Number of Cases	Obstruction (Expressed as % of Pressure Tube Area)
Low Power (Test #1617)	Reference case	1	0%
	Asymmetrical Blockage Sensitivity	12	50%, 90%, 91%, 92%, 93%, 94%, 95%, 96%, 97%, 98%, 99%, 100%,
High Power (Test #1613)	Reference case	1	0%
	Asymmetrical Blockage Sensitivity	12	50%, 90%, 91%, 92%, 93%, 94%, 95%, 96%, 97%, 98%, 99%, 100%,
Nodalisation Sensitivity	Low power reference case, refined grid	1	0%
End Fitting – Feeder Flow Path Location Sensitivity	Low power reference case, varied flow path location	4	0%

Limitations on timestep size have resulted in prohibitive simulation run times for the high power cases³⁷. Each of the simulations has progressed to between 245 s and 295 s, with two-phase conditions and end fitting heatup having

³⁷ Approximately 1 day of CPU time is required to simulate 1 second of the high power cases once condensation on the end fittings begins.

begun. The factors limiting the timestep size will be discussed in Section 4.2.2, along with potential solutions to the issue.

The correspondence between instrumentation planes of the CWIT test rig (see Figure 29 and Figure 31), and model locations (see Figure 34), used in examining the results in this section are shown in Table 13.

Table 13 - Axial Location Correspondence Between CWIT Rig and Model

Plane	Model Location
B	Right third of volume 3
D	Right third of volume 7
F	Right third of volume 11
F1	Right third of volume 12
G1	Left third of volume 13
G	Left third of volume 14
I	Left third of volume 18
K	Left third of volume 22
U1	Left fifth of volume 27
U2	Right fifth of volume 27
D1	Left fifth of volume 28
D2	Right fifth of volume 28

The data gathered by a number of thermocouples in different planes are examined in this section. Not every plane was equipped with thermocouples at every location shown in Figure 30, and further, not every thermocouple functioned properly. The properly functioning thermocouples considered in each instrumentation plane are displayed in Table 14.

Table 14 - CWIT Thermocouple Data Used for Comparison to Simulation Results³⁸

Plane	Pin Number							Pressure Tube	End Fitting (External)		
	1	10	24	30	31	34	37		Top	Mid	Bottom
B	Y	Y		Y	Y	Y	Y	Y			
D	Y	Y	Y	Y	Y	Y	Y	Y			
F1		Y	Y			Y	Y	Y			
G1	Y	Y		Y	Y			Y			
I	Y	Y	Y	Y	Y	Y	Y	Y			
K	Y	Y	Y	Y	Y	Y	Y	Y			
U1									Y	Y	Y
U2									Y	Y	Y
D1									Y	Y	Y
D2									Y	Y	Y

4.1 Simple Analytical Models of CWIT

Before these results are presented, some simple analytical calculations will be considered. The results of such simple models are useful for comparison to the results of more detailed models, both as a rationality check and to consider the effect of the inclusion of various phenomena.

4.1.1 Adiabatic Pin Heatup

The simplest case to consider is the adiabatic heatup of thermally isolated pins. Using the FES heat capacity of 5.6 J/C-cm of element length, at 800 C [25] (and treating this value as invariant with respect to temperature), and using linear pin power ratings for each ring and half bundle (see Table 15 and Table 16), adiabatic pin heatup rates can be calculated:

³⁸ Not all planes were instrumented at each thermocouple locations, and some thermocouples malfunctioned. The thermocouples were selected based on the relevance of the data as well as the reliability of the instrument.

Table 15 - Adiabatic Pin Heatup Rates – 20 kW / Channel³⁹

Volume Number ⁴⁰	Outer Ring (°C/s)	Middle Ring (°C/s)	Inner Ring (°C/s)	Centre Pin (°C/s)
1	0.0439	0.0356	0.0316	0.0299
2	0.0764	0.0619	0.0550	0.0520
3	0.1078	0.0873	0.0776	0.0733
4	0.1375	0.1114	0.0990	0.0935
5	0.1652	0.1338	0.1189	0.1123
6	0.1904	0.1542	0.1371	0.1295
7	0.2127	0.1723	0.1532	0.1447
8	0.2319	0.1878	0.1670	0.1577
9	0.2476	0.2005	0.1782	0.1683
10	0.2595	0.2102	0.1869	0.1765
11	0.2676	0.2168	0.1927	0.1820
12	0.2717	0.2201	0.1956	0.1847
13	0.2717	0.2201	0.1956	0.1847
14	0.2676	0.2168	0.1927	0.1820
15	0.2595	0.2102	0.1869	0.1765
16	0.2476	0.2005	0.1782	0.1683
17	0.2319	0.1878	0.1670	0.1577
18	0.2127	0.1723	0.1532	0.1447
19	0.1904	0.1542	0.1371	0.1295
20	0.1652	0.1338	0.1189	0.1123
21	0.1375	0.1114	0.0990	0.0935
22	0.1078	0.0873	0.0776	0.0733
23	0.0764	0.0619	0.0550	0.0520
24	0.0439	0.0356	0.0316	0.0299

Table 16 - Adiabatic Pin Heatup Rates – 131 kW / Channel⁴¹

Volume Number ⁴²	Outer Ring (°C/s)	Middle Ring (°C/s)	Inner Ring (°C/s)	Centre Pin (°C/s)
1	0.2877	0.2330	0.2071	0.1956
2	0.5005	0.4054	0.3604	0.3403
3	0.7059	0.5717	0.5082	0.4800

³⁹ Test #1617⁴⁰ See Figure 34⁴¹ Test #1613⁴² See Figure 34

4	0.9006	0.7295	0.6485	0.6124
5	1.0819	0.8763	0.7790	0.7357
6	1.2470	1.0100	0.8978	0.8479
7	1.3933	1.1286	1.0032	0.9475
8	1.5188	1.2302	1.0935	1.0328
9	1.6215	1.3134	1.1675	1.1026
10	1.7000	1.3770	1.2240	1.1560
11	1.7529	1.4199	1.2621	1.1920
12	1.7796	1.4415	1.2813	1.2101
13	1.7796	1.4415	1.2813	1.2101
14	1.7529	1.4199	1.2621	1.1920
15	1.7000	1.3770	1.2240	1.1560
16	1.6215	1.3134	1.1675	1.1026
17	1.5188	1.2302	1.0935	1.0328
18	1.3933	1.1286	1.0032	0.9475
19	1.2470	1.0100	0.8978	0.8479
20	1.0819	0.8763	0.7790	0.7357
21	0.9006	0.7295	0.6485	0.6124
22	0.7059	0.5717	0.5082	0.4800
23	0.5005	0.4054	0.3604	0.3403
24	0.2877	0.2330	0.2071	0.1956

This can be viewed as a bounding rate of pin heatup. It would be expected that shortly after a given pin is exposed to steam, its rate of temperature increase would be close to this, however as the temperature of the pin increases heat transfer to the steam and radiant heating (not included in the GOTHIC model), would tend to slow this.

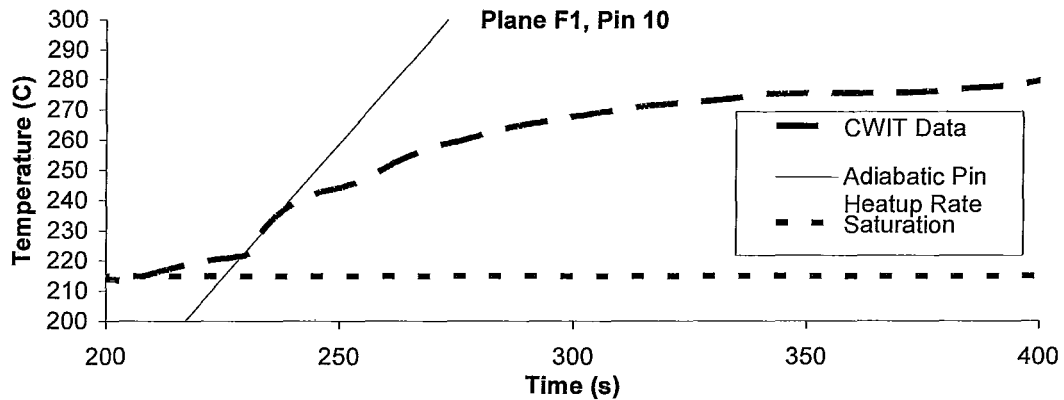


Figure 40 - Near-Adiabatic Pin Heatup During CWIT Test #1613

As Figure 40 demonstrates, fuel element simulator heatup rates approaching the adiabatic limit were reached briefly during CWIT Test #1613. Possible explanations for the slowing of heatup after vapour exposure include: splashing of liquid onto the FES from lower in the channel, increasingly efficient heat transfer to steam through increased steam Reynolds numbers, an increasing temperature difference between the steam and the FES, and radiative cooling.

4.1.2 Single-Phase Channel Heatup

The heatup rate of the channel in single phase is a valuable figure to be aware of when examining the results of the GOTHIC simulations. The heatup rate of each half-bundle sized volume in the GOTHIC model is calculated using the heat capacity of the fuel element simulators and water⁴³, and the fuel element simulators, water, and pressure tube. Heat transfer from the pressure tube to the moderator is not considered, and each half-bundle volume is considered to be thermally isolated from its neighbours. Finally, these calculations implicitly ignore temperature stratification of the coolant in the channel. The heatup rates

⁴³ For this calculation, the properties of all elements are taken to be constant, most importantly, the density and specific heat of water are taken to be 1000 kg/m³ and 4.2 kJ/kg-°C, respectively.

derived from these calculations are presented in Table 17, and the values arrived at are presented graphically in Figure 41.

Table 17 - Single-Phase Channel Heatup Rates

Volume Number ⁴⁴	Test #1617 (20 kW/channel)		Test #1613 (131 kW/channel)	
	Heatup Rate Considering FES, Water (°C/s)	Heatup Rate Considering FES, Water, and Pressure Tube (°C/s)	Heatup Rate Considering FES, Water (°C/s)	Heatup Rate Considering FES, Water, and Pressure Tube (°C/s)
1	0.0227	0.0210	0.1487	0.1375
2	0.0395	0.0365	0.2588	0.2393
3	0.0557	0.0515	0.3649	0.3375
4	0.0711	0.0657	0.4656	0.4306
5	0.0854	0.0790	0.5593	0.5173
6	0.0984	0.0910	0.6447	0.5962
7	0.1100	0.1017	0.7203	0.6662
8	0.1199	0.1109	0.7852	0.7262
9	0.1280	0.1184	0.8383	0.7754
10	0.1342	0.1241	0.8789	0.8129
11	0.1384	0.1280	0.9062	0.8382
12	0.1405	0.1299	0.9200	0.8509
13	0.1405	0.1299	0.9200	0.8509
14	0.1384	0.1280	0.9062	0.8382
15	0.1342	0.1241	0.8789	0.8129
16	0.1280	0.1184	0.8383	0.7754
17	0.1199	0.1109	0.7852	0.7262
18	0.1100	0.1017	0.7203	0.6662
19	0.0984	0.0910	0.6447	0.5962
20	0.0854	0.0790	0.5593	0.5173
21	0.0711	0.0657	0.4656	0.4306
22	0.0557	0.0515	0.3649	0.3375
23	0.0395	0.0365	0.2588	0.2393
24	0.0227	0.0210	0.1487	0.1375

⁴⁴ See Figure 34

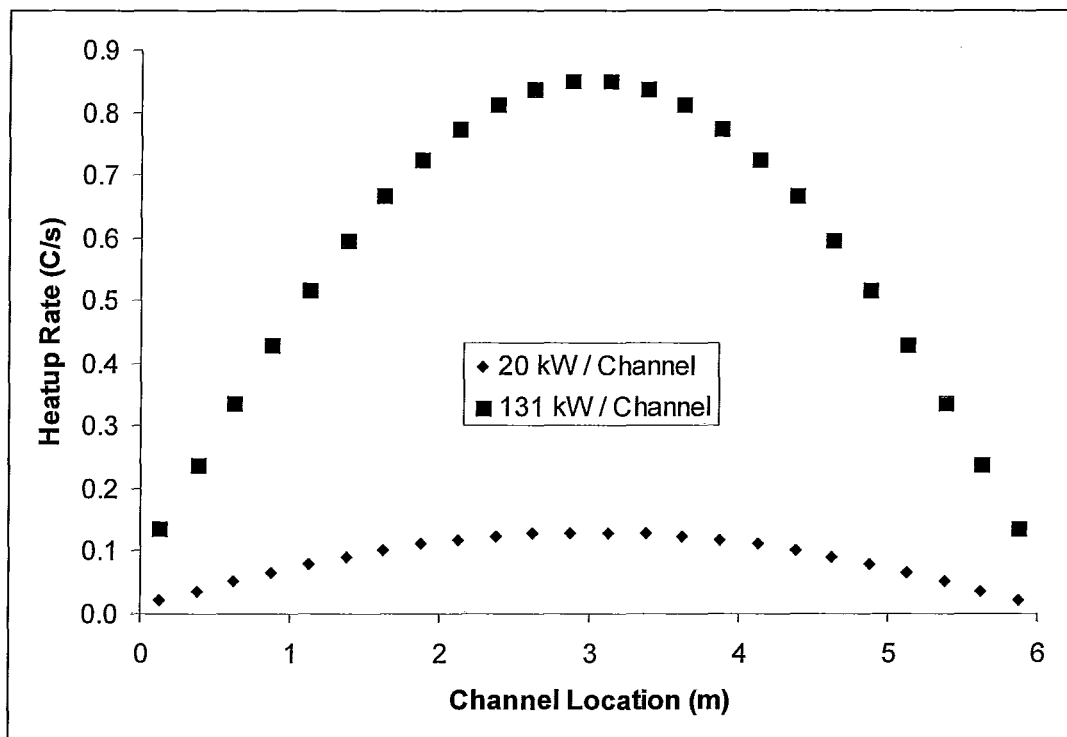


Figure 41 - Single Phase Channel Heatup Rates⁴⁵

The axial flux profile has an obvious impact on the heatup rates presented in Figure 41, however some axial heat exchange through conduction and convection can be expected along the channel (effects which have not been considered in this simple model). In the limit of infinite axial heat conductivity (where the heat capacity of the pressure tube is included), this leads to a total channel heatup rate of $0.0881 \text{ } ^\circ\text{C/s}$ for the 20 kW/channel case and $0.5774 \text{ } ^\circ\text{C/s}$ for the 131 kW/channel case.

⁴⁵ The data points in the figure reflect a calculation of heat capacity that includes the fuel element simulators, water, and pressure tube.

Comparisons between the average and local single-phase heatup rates along the channel and data from the CWIT tests are presented in Figure 42 – Figure 45.

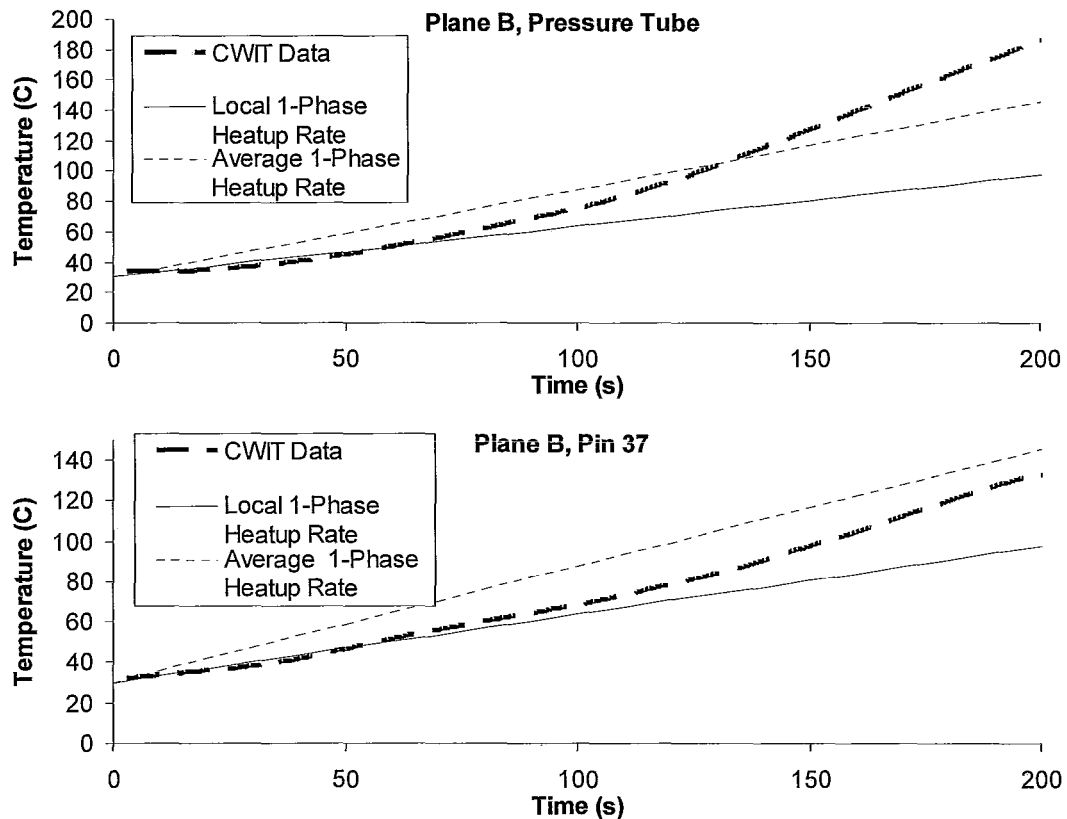


Figure 42 - Single Phase Channel Heatup Rate, Comparison of Simple Model Prediction to CWIT Test #1613 Data – Plane B⁴⁶

The effects of temperature stratification are clearly visible in the temperature difference between the pressure tube and the centre pin of the bundle. While the temperature at the surface of the pin would be expected to be somewhat above that of the surrounding liquid, the difference should not be large at these power levels while the pin is submerged. There is a reasonable correspondence between the predicted heatup rate and that observed during CWIT test #1613, and

⁴⁶ Boiling began shortly after 200s during test #1613.

the deviation is in the direction one would expect as a result of fluid moving from the centre of the channel toward the end fittings.

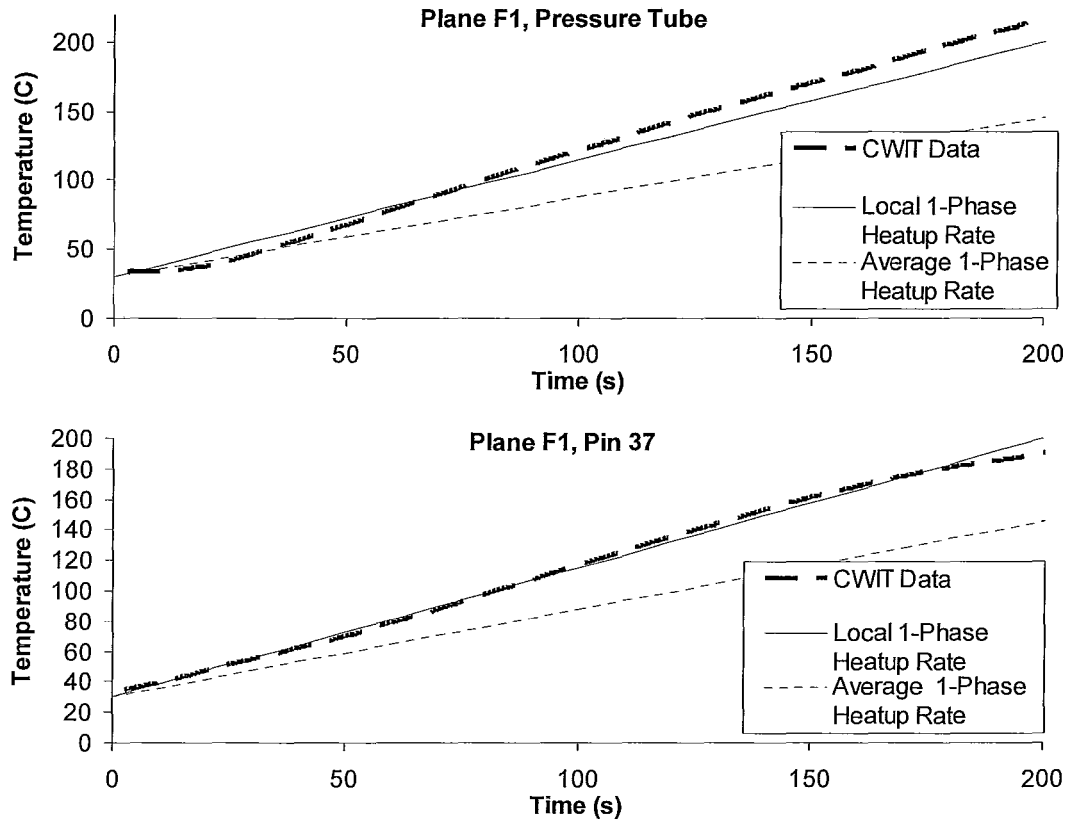


Figure 43 - Single Phase Channel Heatup Rate, Comparison of Simple Model Prediction to CWIT Test #1613 Data – Plane F1

Again the stratification of liquid can be seen in the temperature difference between the pressure tube and the centre pin. The local heatup rate prediction agrees very well with the test data, lending credence to the explanation that fluid movement caused the unexpectedly fast heatup rate at plane B.

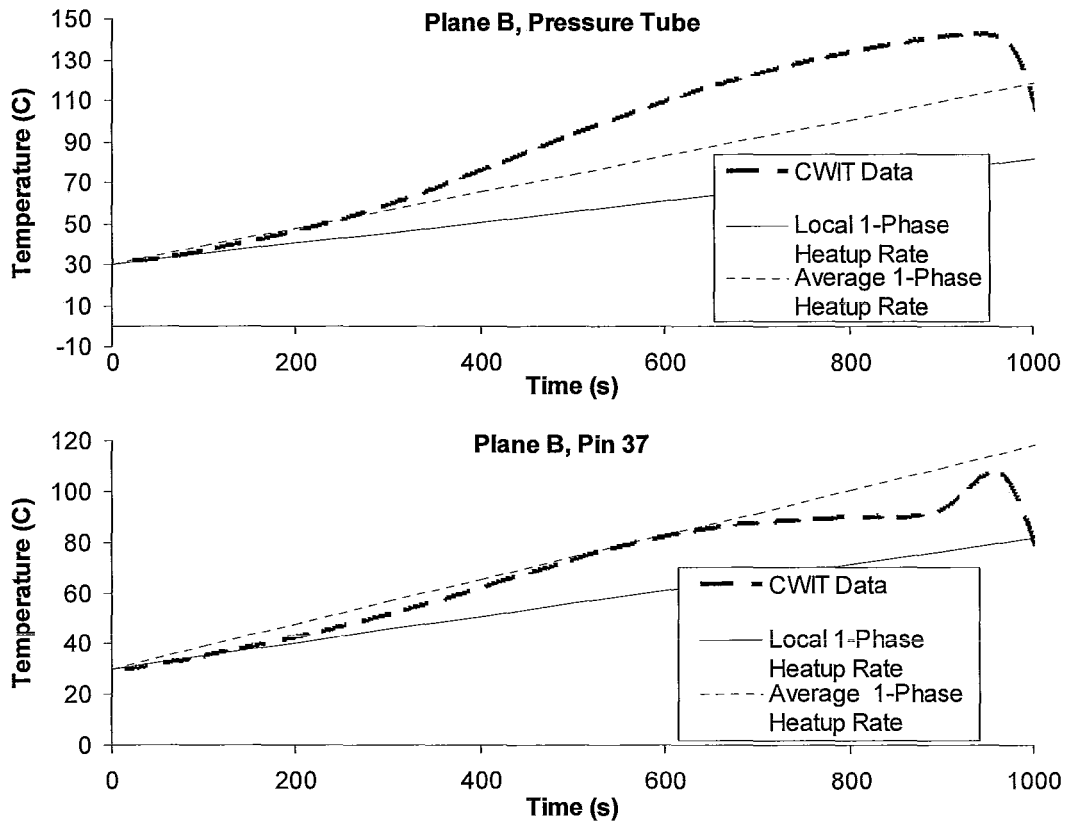


Figure 44 - Single Phase Channel Heatup Rate, Comparison of Simple Model Prediction to CWIT Test #1617 Data – Plane B

The same effects seen in the Figure 42 and Figure 43 are visible over a longer timescale in Figure 44 and Figure 45. The local heatup rate somewhat under-predicts the observed heatup of the centre pin in plane B, but predicts it quite effectively for the centre pin in plane F1. In both tests, the channel eventually vented in the direction of plane B. It is likely that some small flow in that direction (through recirculation or a deviation from stagnation), was manifest well in advance of the venting in both cases.

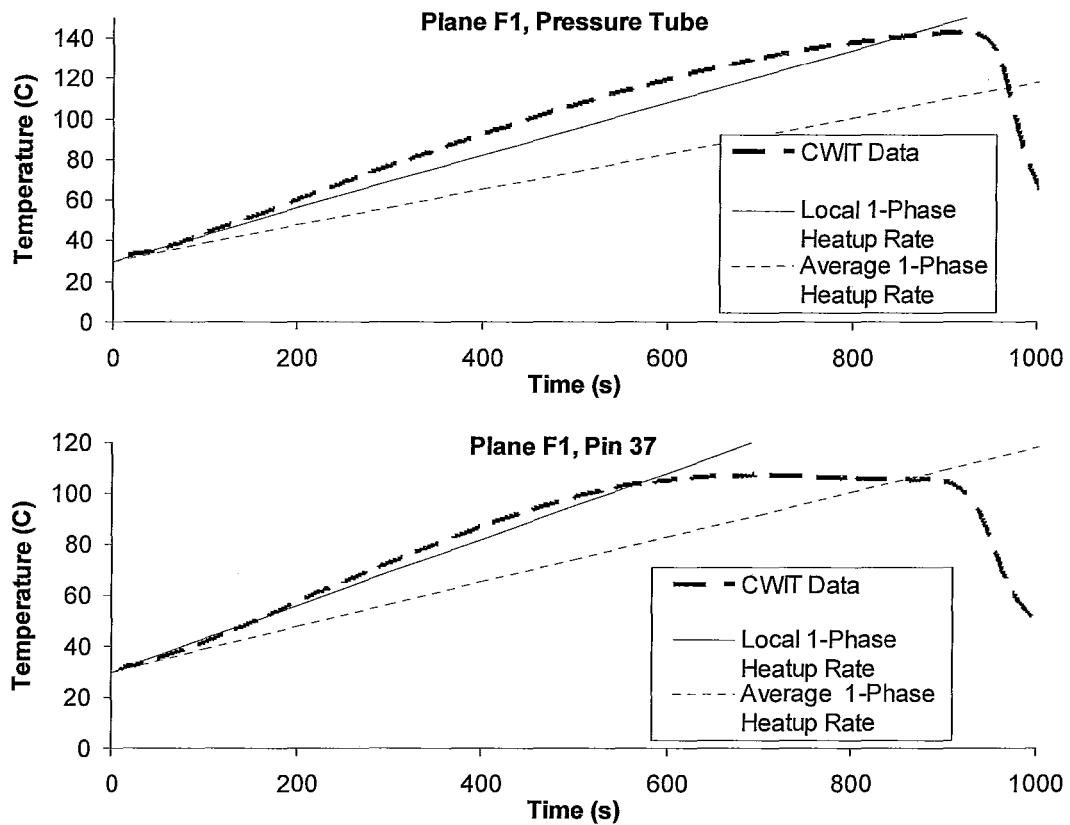


Figure 45 - Single Phase Channel Heatup Rate, Comparison of Simple Model Prediction to CWIT Test #1617 Data – Plane F1

4.1.3 Vapour Production Rate

The rate of vapour production is an important factor in two-phase IBIF, and is the main mode of heat transport from the fuel to the end fittings. The rate of vapour production is greatly affected by the coolant level in the channel, as uncovered pins have little effect on vapour production. The simplest calculation that can be done here is the vapour production rate of a saturated channel, with all pins covered (that is, near instantaneous transport of vapour from the channel to the end fittings). The vapour production rates for saturated conditions are presented in Table 18.

Table 18 - Vapour Production Rates At Saturated Conditions

	Test #1617 (20 kW/channel)	Test #1613 (131 kW/channel)
Pressure (kPa)	7100	2100
Latent Heat of Vapourisation (kJ/kg)	1498.7	1879.4
Vapour Density (kg/m ³)	37.1	10.5
Vapour Production Rate (g/s)	13.3	69.7
Vapour Production Rate (L/s)	0.36	6.6

In considering the volumetric production rate of vapour, it is worth noting that the free volume of the channel is 10.4 L, and the free volume of each end fitting is 11.7 L. Although it is clearly an unreasonable proposal⁴⁷, this rate of vapour production would completely fill the channel and end fittings in 94.1 s or 5.1 s for the 20 kW/channel and 131 kW/channel cases, respectively. Note that these timescales are much shorter than the time required to boil all liquid off – which is not a relevant value to consider for IBIF.

The uncovering of pins and its effect on vapour production rate are coupled processes. It is reasonable to state that the depth of vapour in the channel will vary axially (dependent on where it is produced, pressure tube sag, etc.). This axial variation in pin coverage, combined with the axial and radial power profiles, impacts the rate of vapour production in a way that demands more complex modelling.

⁴⁷ Two main points are that this would violate the assumption that all pins are covered in liquid, and this would also require the vapour to ‘push’ the water out of the channel and end fittings.

4.1.4 End Fitting Heatup

One of the main processes in two-phase IBIF is the heatup of the end fittings through condensation heat transfer. Condensation heat transfer is so efficient that effectively, vapour cannot vent through the feeder until top of the end fitting between the channel and the feeder reaches saturation. Some insight into the thermal behaviour of the end fittings during IBIF can be gained through some simple calculations. The thermal characteristics of the parts of the end fitting body between the pressure tube and the feeder, as well as the dead space are outlined in Table 19.

Table 19 - End Fitting Component Thermal Characteristics

	Mass (kg)	MC _p (kJ/C)
End Fitting Body	111.8	53.7
Dead Space Composite	102.7	79.5

Assuming that all heat produced in the fuel is transported to the end fittings, a heatup rate for the end fittings can be calculated. Approaching the problem this way ignores heat stored in the fuel (as is likely to take place if some fuel pins are exposed) and heat lost to the moderator, and additionally assumes that heat will be transported upstream and downstream equally, and that each end fitting will heat up uniformly. It is quite likely, however, that vapour will contact the end fittings only close to the top, making heatup rates for fractions of the end fittings instructive (specifically, the top half and top quarter of the end fitting body). These calculations treat radial heat conduction is infinite and azimuthal heat conduction as zero. Values for heatup rates and heatup times from 30C to saturation are presented in Table 20 and Table 21, respectively.

Table 20 - End Fitting Heatup Rate

Component	Heatup Rate (C/s)
End Fitting Body	1.22
Dead Space	0.82
End Fitting Body and Dead Space Together	0.49
50% of End Fitting Body and Dead Space	0.98
25% of End Fitting Body and Dead Space	1.97

Table 21 - End Fitting Heatup Time From 30C to Saturation⁴⁸

Component	Heatup Time (s)
End Fitting Body	151
Dead Space	225
End Fitting Body and Dead Space Together	376
50% of End Fitting Body and Dead Space	188
25% of End Fitting Body and Dead Space	94

Due to the efficiency of condensation heat transfer, a reasonable simplification is that no vapour will penetrate the end fittings beyond the farthest section that has been heated to saturation. It is thus appropriate to consider a rate of progression of heating to saturation in the end fitting if axial heat conduction is ignored, both for the full end fitting and fractional approximations of it. As CWIT test #1617 did not involve two-phase conditions, these calculations are performed only for 131 kW, the power of test #1613. Values of end fitting saturation temperature progression rate are presented in Table 22.

⁴⁸ For CWIT test #1613, the saturation temperature in the end fittings is 214.9 C.

Table 22 - End Fitting Heatup From 30C to Saturation Axial Progression Rate

Component	Progression Rate of Heated Limit (cm/s)⁴⁹
End Fitting Body - Region 1 ⁵⁰	0.76
End Fitting Body - Region 2	1.43
Dead Space	0.73
Region 2 End Fitting Body and Deadspace Together	0.48
50% of End Fitting Body - Region 1	1.52
50% of End Fitting Body - Region 2	2.85
50% of Dead Space	1.45
50% of Region 2 End Fitting Body and Deadspace Together	0.96
25% of End Fitting Body - Region 1	3.04
25% of End Fitting Body - Region 2	5.71
25% of Dead Space	2.91
25% of Region 2 End Fitting Body and Deadspace Together	1.93

Figure 46 and Figure 47 provide some comparisons between the heatup rates listed in Table 20 and data from CWIT test #1613 taken by thermocouples on the outside of the end fittings.

⁴⁹ For reference, the lengths of regions 1 and 2 are approximately 20 cm and 179 cm, respectively. The dead space begins shortly after region 2, and is 163 cm long.

⁵⁰ The end fitting has different thickness in Region 1 and Region 2, see Figure 27 and Figure 37.

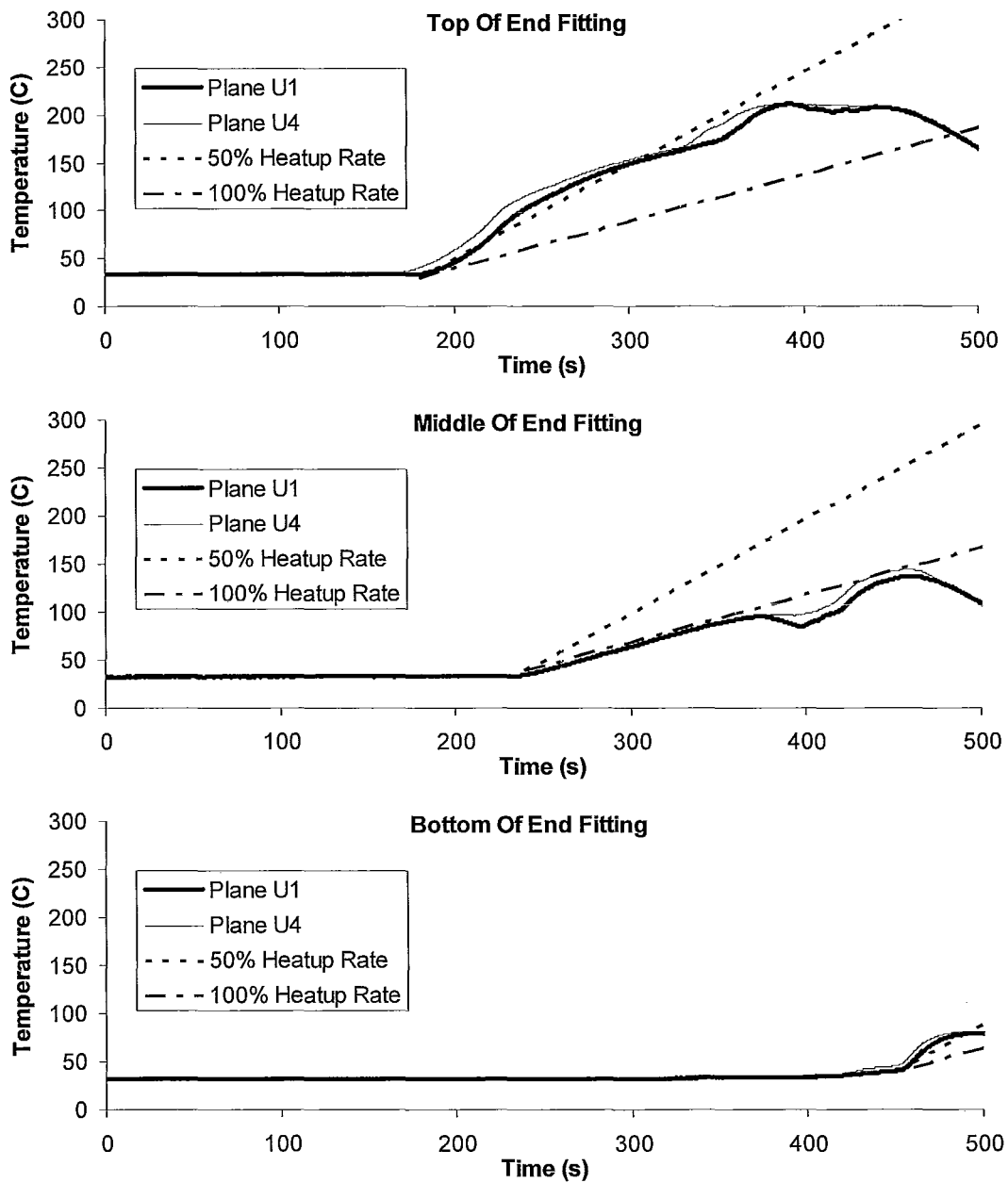


Figure 46 - Upstream End Fitting Temperature Transients – CWIT Test #1613⁵¹

⁵¹ The 50% and 100% heatup rates listed in the figure refer to the percentage of the end fitting and dead space mass considered in calculating the heatup rate (see Table 17)

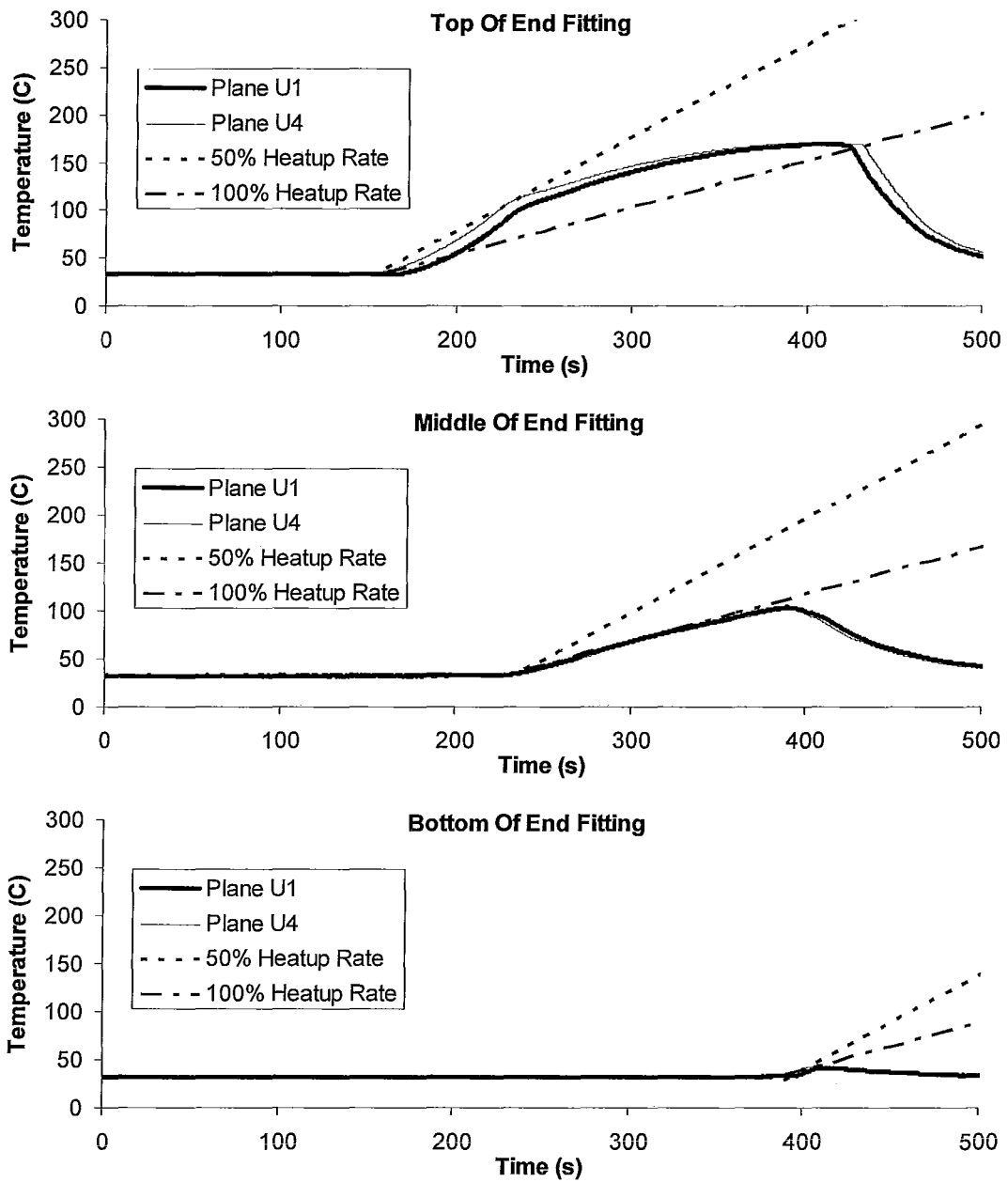


Figure 47 - Downstream End Fitting Temperature Transients – CWIT Test #1613⁵²

⁵² The 50% and 100% heatup rates listed in the figure refer to the percentage of the end fitting and dead space mass considered in calculating the heatup rate (see Table 17)

It is apparent from these figures that the vent occurred in the direction of the upstream end fitting, as the top thermocouples on this end fitting are the only ones that reached the saturation temperature. Although there is a small delay observed between the temperature rise in plane U1 relative to plane U4, this delay is far smaller than expected if one ignores axial heat conduction and treats the limit of saturation-temperature metal in the end fitting as a solid barrier to vapour advancement. With these issues in mind, the approach of considering a percentage of the end fitting mass predicts the heatup of the top and middle portions of the end fittings reasonably well. Based on the data, this approach, as utilised in some earlier IBIF models (see Section 2.2), could reproduce the test results with an impressive degree of accuracy given an appropriately selected end fitting mass.

4.2 Reference Case Results

4.2.1 Low Power

The most important results to consider in IBIF simulations are the venting time, and the maximum temperature reached by the hottest of the fuel pins. Due to the axial and radial power profiles, along with the coolant stratification that takes place in stagnant conditions, the highest temperatures are reached by the top fuel pins (pins 9 and 10, see Figure 30) in the centre of the channel. The temperature of pin 10 at planes F1 and G1 (see Figure 29), is shown as a function of time in Figure 48. It should be noted that the maximum temperatures of each fuel pin are over 100 °C below the saturation temperature.

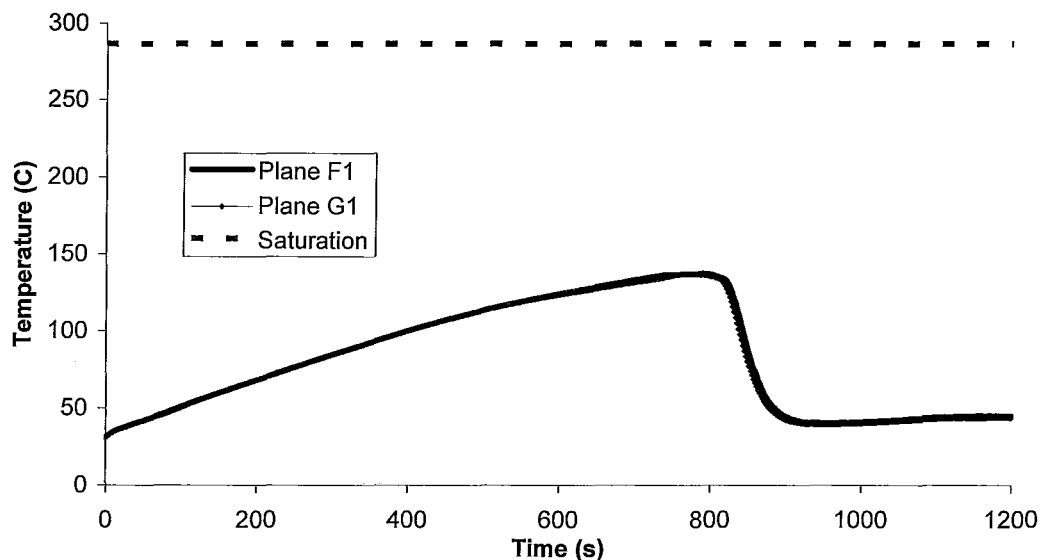


Figure 48 - Pin 10 Temperature vs. Time, Planes F1 and G1

The venting process that brings cold water into the channel and cools the pins can be seen most clearly in Figure 49. Note that the total free volume of the channel is approximately 10.4 L, so total replacement of the coolant is accomplished in less than 20 seconds at the depicted peak flow rates. Although the amplitude is very small, it is also worth noting that there is some positive flow into the feeders at each end of the channel as a result of liquid swell during heatup. This movement of warmer liquid to the end fittings plays a role in the timing of the venting process.

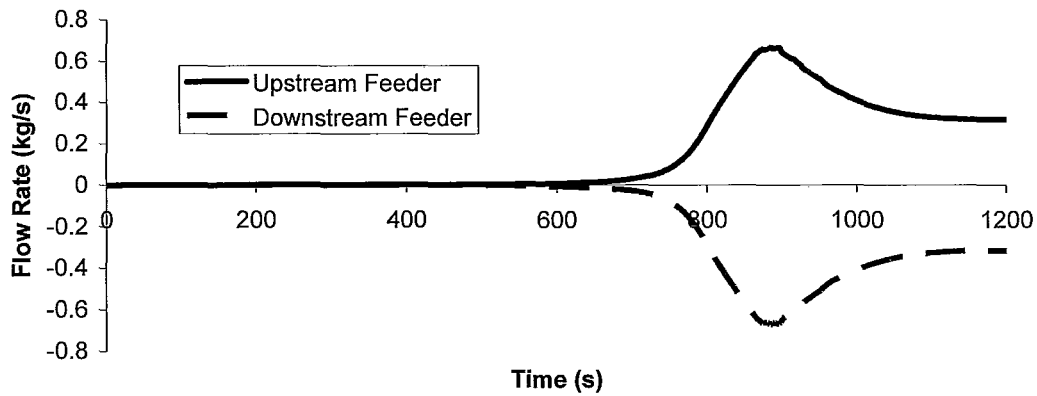


Figure 49 - Flow Into End Fittings From Feeders⁵³

In examining the mechanisms of the initiation and progression of venting, considering the radial flow velocity profile across the channel may provide some insight. In order to simplify the presentation of this data, the values for a string of cells from the top to the bottom of the channel and end fitting are presented at a given timestep (see Figure 51 and Figure 52).

⁵³ The flow paths from the upstream and downstream feeders to the end fittings are #19 and #20 (see Figure 34), respectively. A positive value indicates flow from the end fitting to the feeder.

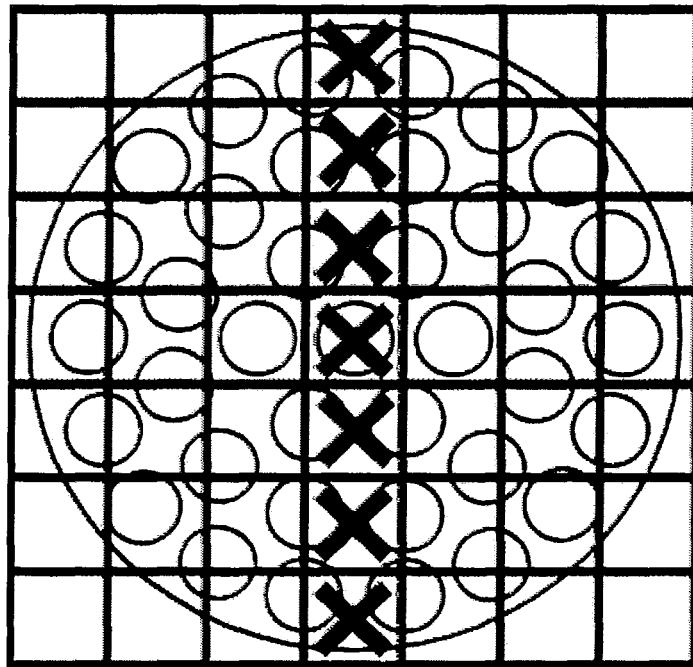


Figure 50 - Flow Velocity Profile Cells – Channel

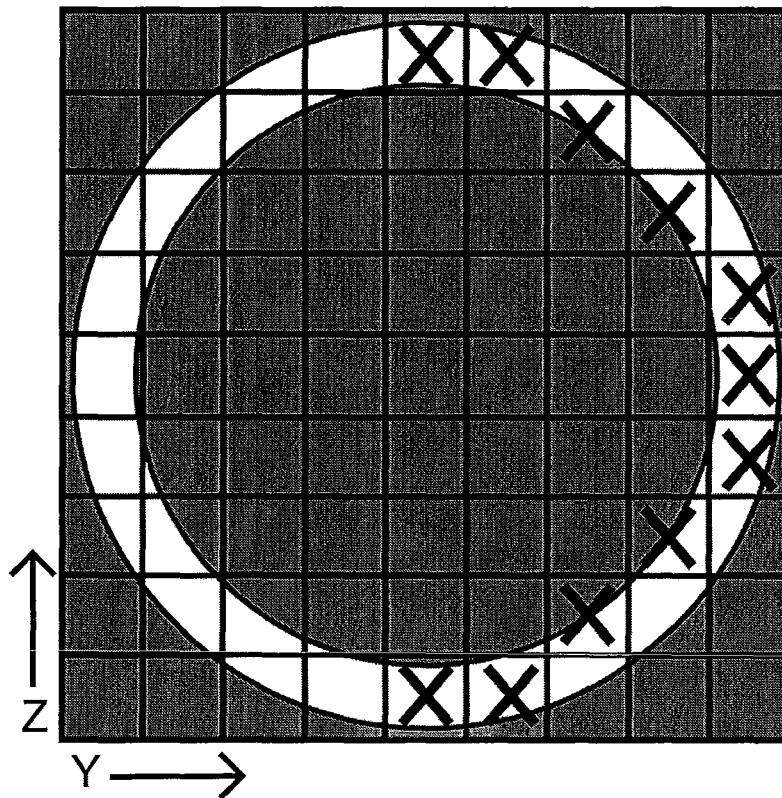


Figure 51 - Flow Velocity Profile Cells – End Fitting

Axial flow velocity profiles for timesteps leading up to and including the venting process are presented in Figure 52 - Figure 55.

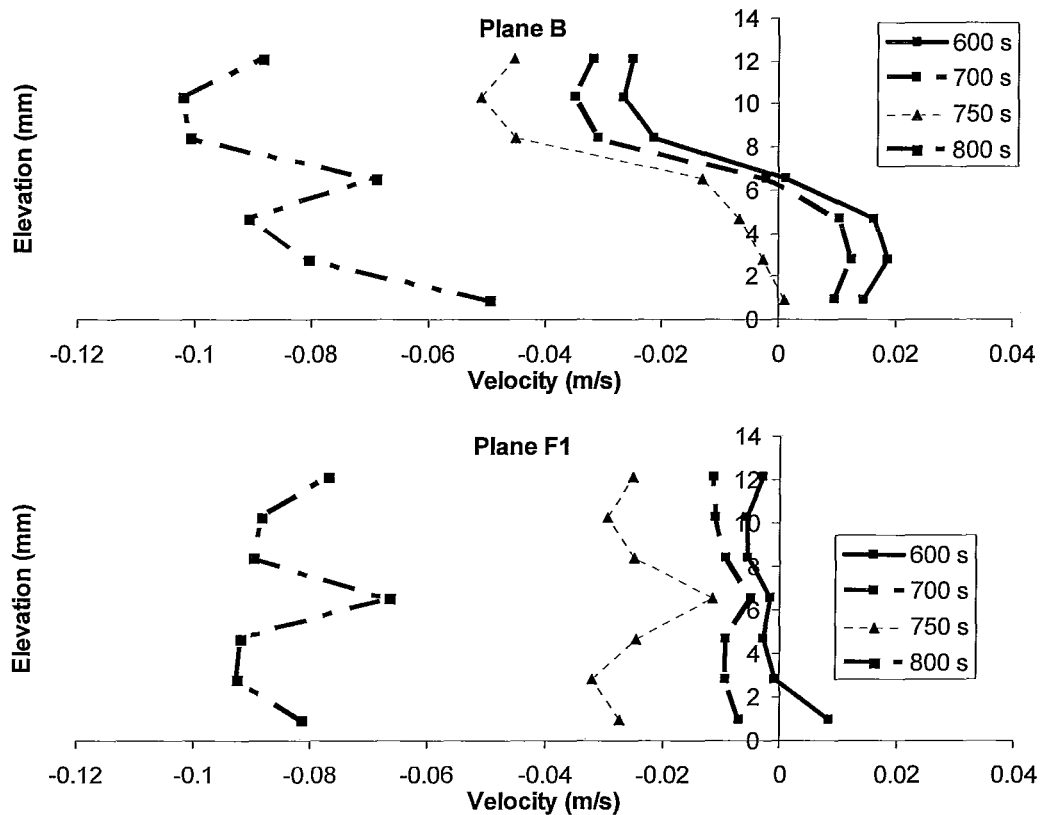


Figure 52 - 20 kW Reference Case Axial Flow Velocity Profile – Planes B and F1

Convective flow is apparent when considering plane B in Figure 52, the liquid in the bottom of the channel flows toward the centre bundles, while the liquid in the top of the channel flows toward the end fittings. This effect is less pronounced close to the middle of the channel in plane F1, which is consistent with a cycle of cold fluid transported from the end fittings along the bottom of the channel, warming and up-welling in the centre of the channel, and flowing back toward the end fittings. The slower flows at the centre cell once venting begins (most apparent at 800s), are most likely a result of a large surface area in that cell (it contains the entirety of pin 37), and the low porosity, leading to high flow resistance. A similar effect is seen at the top and bottom of the channel, where the surface of the pressure tube has an impact.

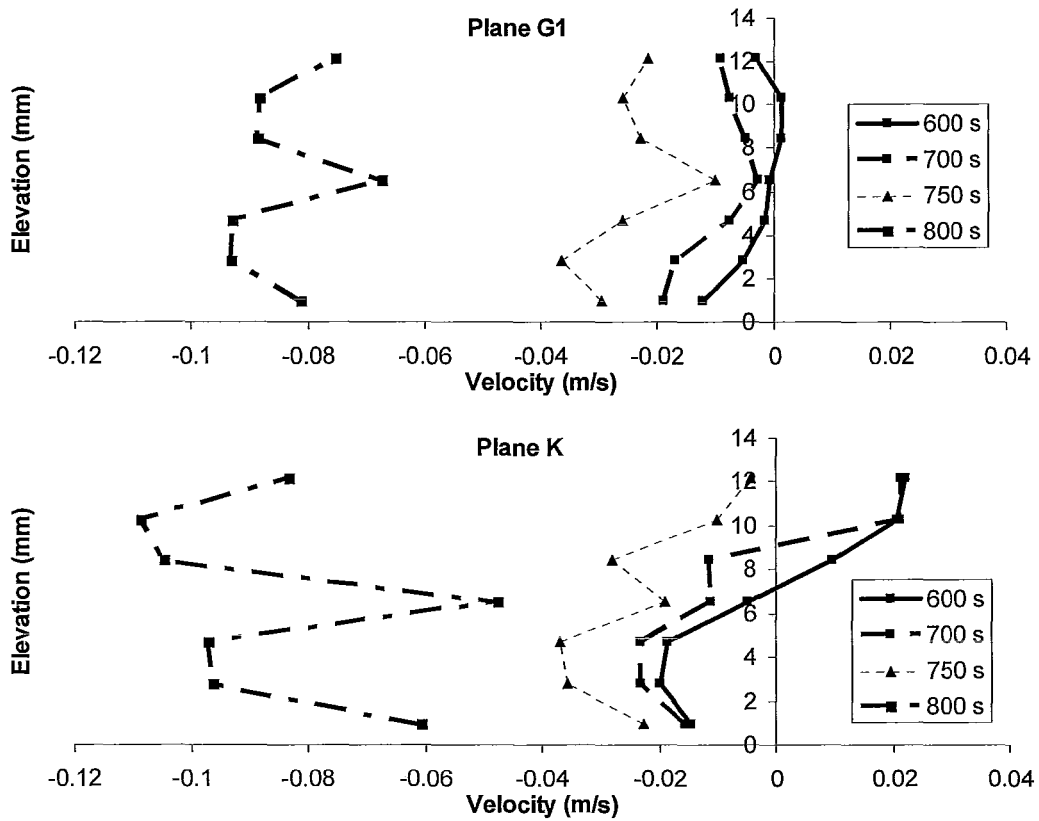


Figure 53 - 20 kW Reference Case Axial Flow Velocity Profile – Planes G1 and K

The same effects seen in Figure 52 are apparent in Figure 53. Most notably, the convective flow seen in plane K is the reverse of that seen in plane B.

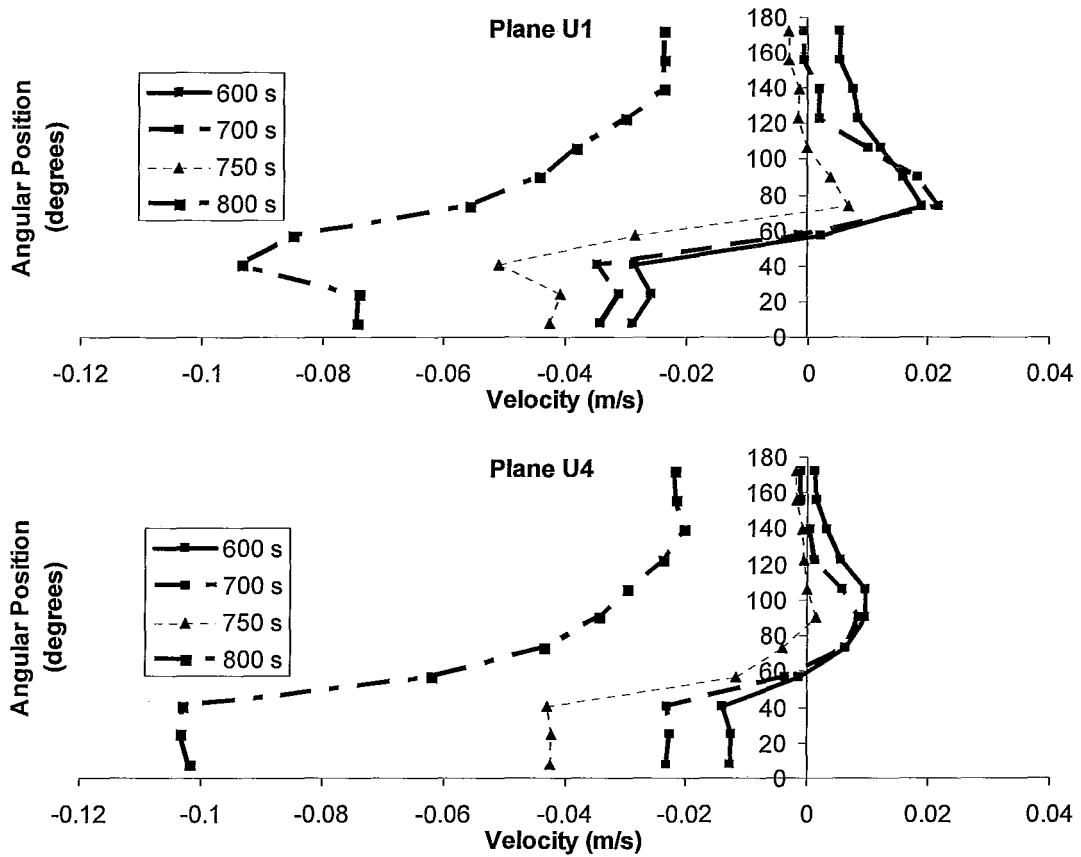


Figure 54 - 20 kW Reference Case Axial Flow Velocity Profile – Planes U1 and U4⁵⁴

The effects of liquid stratification and feeder opening location are obvious in both planes U1 and U4 (Figure 54) – the hot fluid flows along the top of the end fitting and into the feeder.

⁵⁴ The angular position is measured from the top of the end fitting – 0 is at the top, 180 is at the bottom.

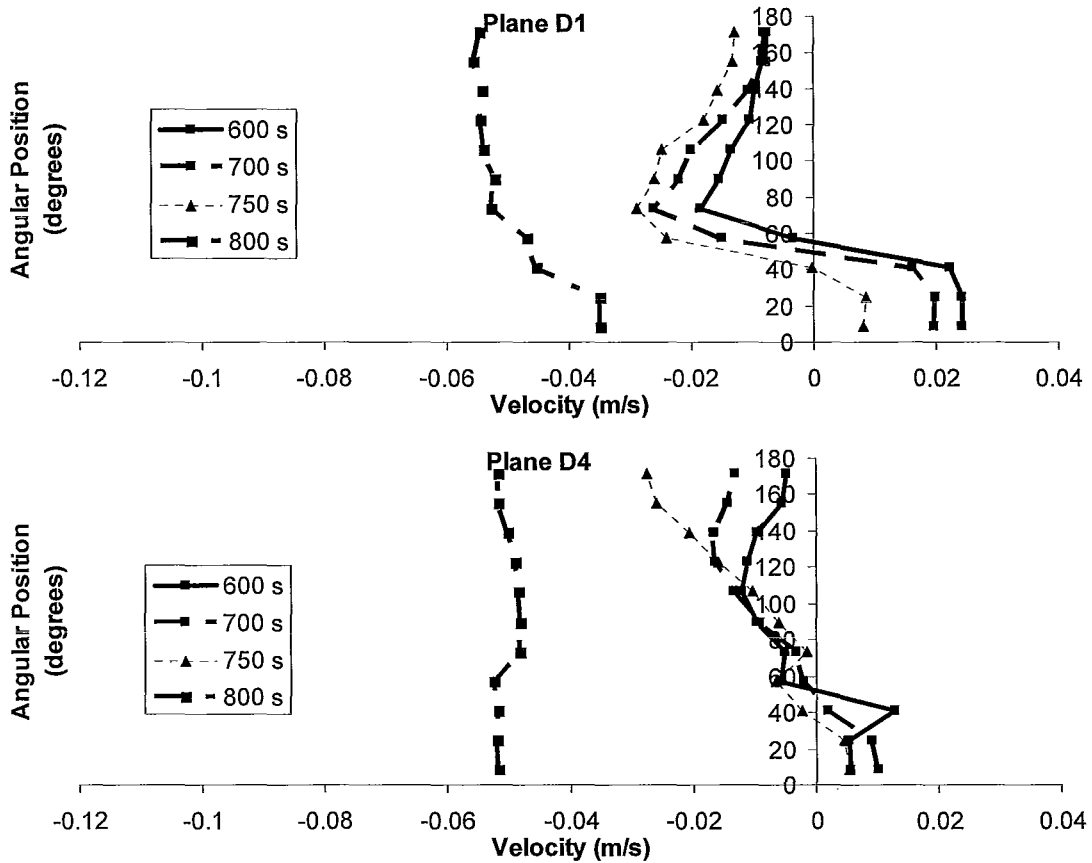


Figure 55 - 20 kW Reference Case Axial Flow Velocity Profile – Planes D1 and D4

The differences between Figure 54 and Figure 55 are instructive. During venting, the fluid flows into the downstream end fitting at a temperature of 30 C. The lack of temperature stratification leads to a fairly constant flow velocity profile across the end fitting once venting takes place. Before venting, some inflow of hot liquid along the top of the end fitting and outflow of cold liquid along the bottom are apparent.

Temperature transients of various components and channel locations during the IBIF cycle are presented in Figure 56 - Figure 59.

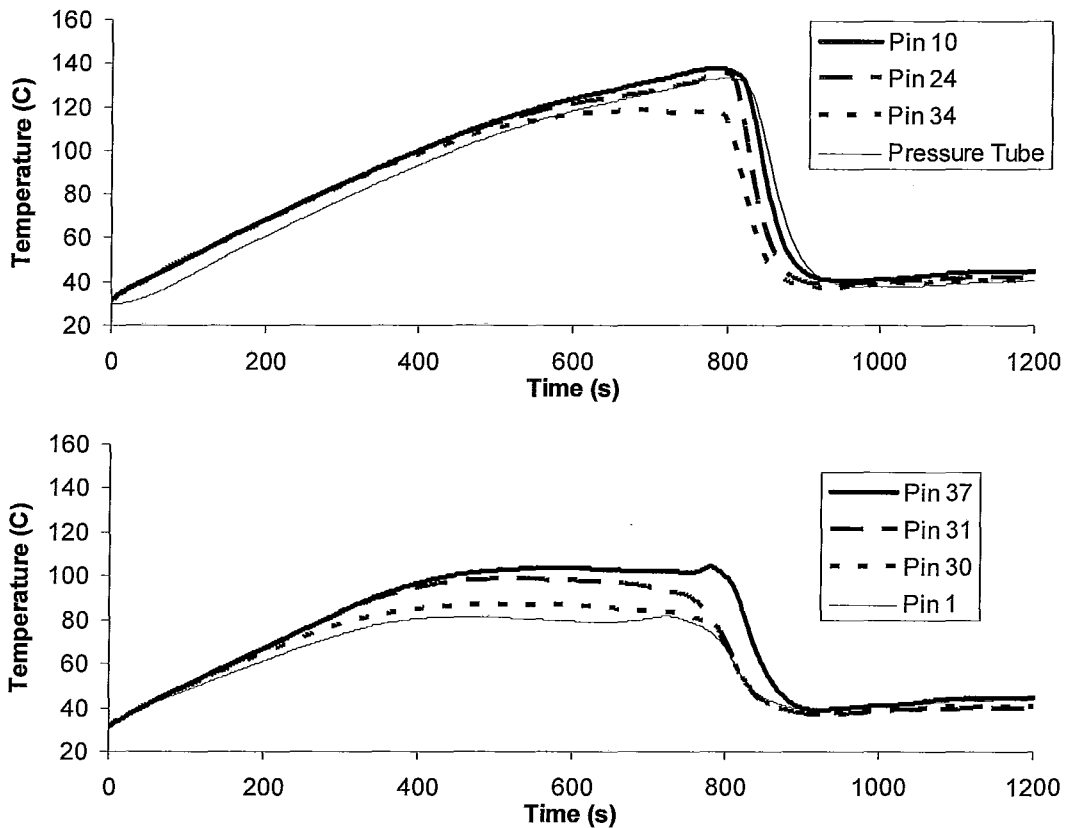


Figure 56 - Temperature Transients At Plane F1

The values of several fuel element simulators and the pressure tube are presented in Figure 56. The effect of temperature stratification is obvious when considering the difference between pins in the bundle. Even the significant radial power profile is overpowered by this effect, with pin 37 being significantly hotter than pin 1 despite having a power level of only 68% of the outer ring.

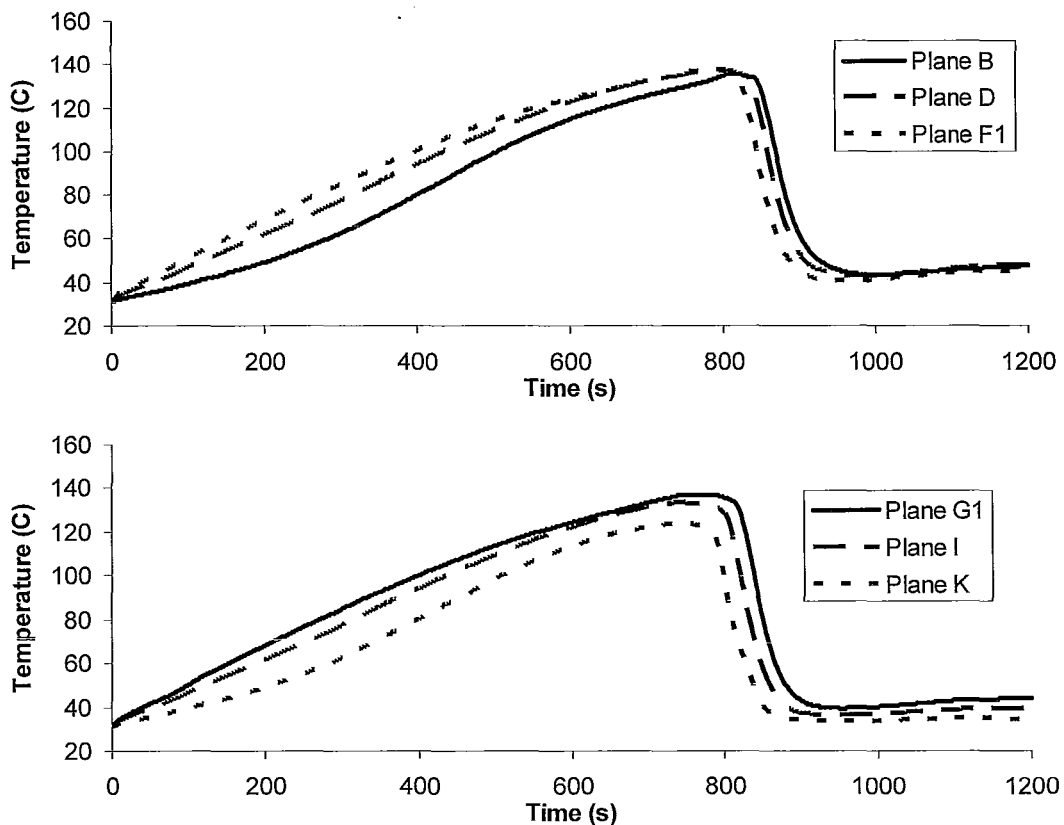


Figure 57 - Pin 10 Temperature Transients Along Channel

The temperature transient of pin 10 at several locations along the channel is presented in Figure 57. The direction of venting can be observed in this figure, as the cold liquid from the downstream feeder quickly reduced the temperature in planes I and K, while the hot liquid from planes F1 and G1 was flushed into planes B and D, allowing them to reach a much higher temperature than their counterparts in the opposite half of the channel.

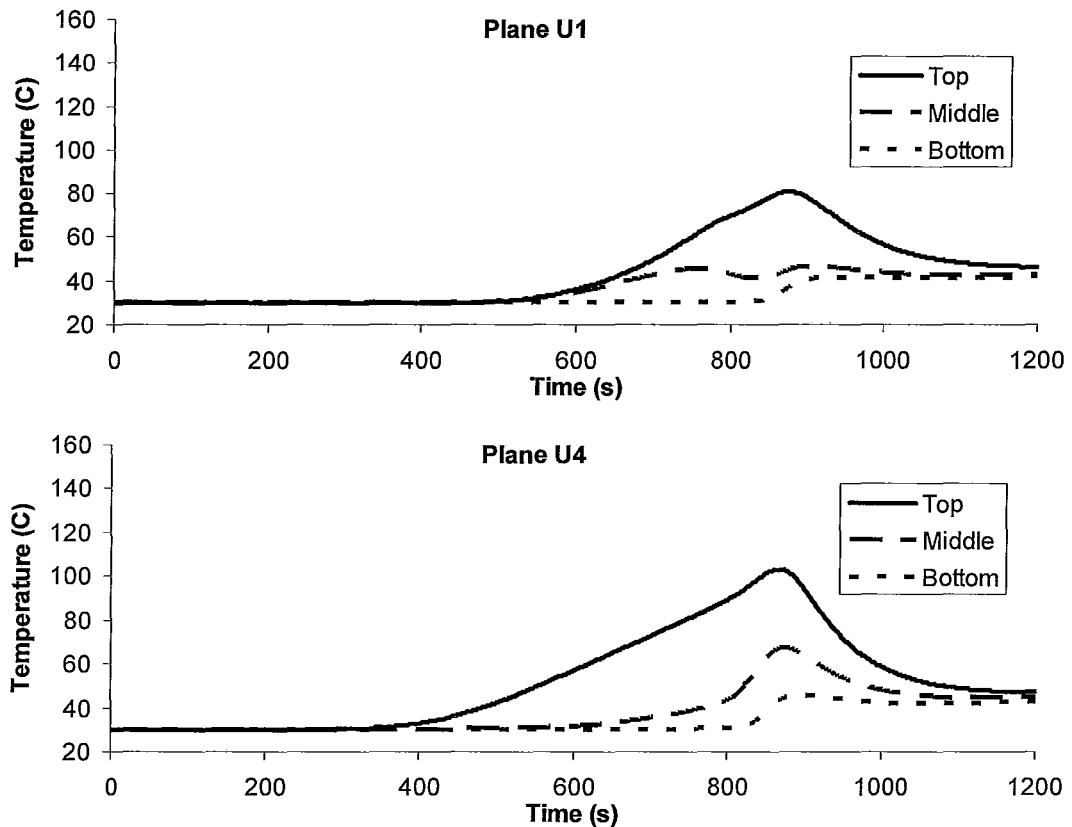


Figure 58 - Upstream End Fitting Temperature Transients

The temperature transient of several locations in the upstream end fitting is presented in Figure 58. The effect of liquid stratification is apparent in the temperature transients, with higher temperatures reached at the top of the end fitting. The cooling effect of the end fitting body and dead space is also apparent in the lower temperatures experienced at plane U1 as compared to U4.

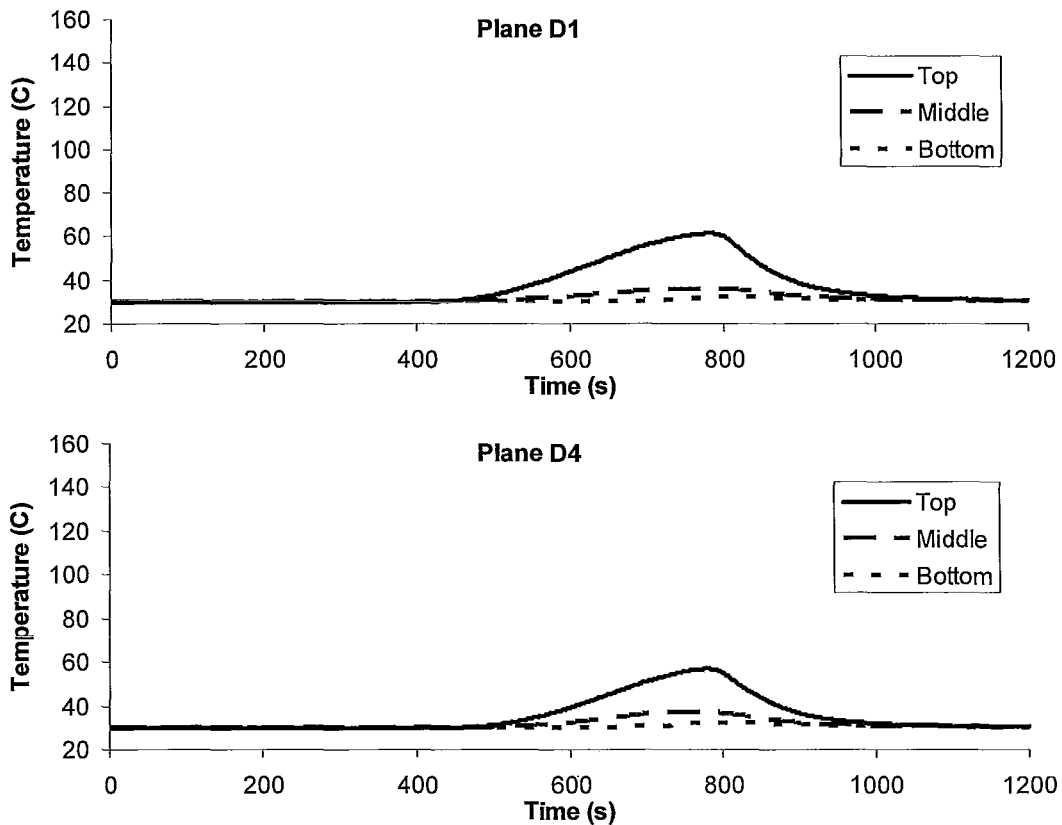


Figure 59 - Downstream End Fitting Temperature Transients

The temperature transients of several points in the downstream end fitting body are presented in Figure 59. As in Figure 58, the effect of liquid stratification is apparent in here, although the temperatures reached are not as high due to the venting bringing cold water into the end fitting.

4.2.2 High Power

4.2.2.1 Flow Oscillation

As mentioned at the beginning of Section 4, the high power simulations were unable to complete in a reasonable time period. The progress of the

solutions has been slowed tremendously by auto-reduction of timestep size. The factor directly limiting timestep size is the Courant limit⁵⁵ in the end fitting cells connecting to the feeder flow paths (see Figure 39). The flows causing this issue are shown in Figure 60.

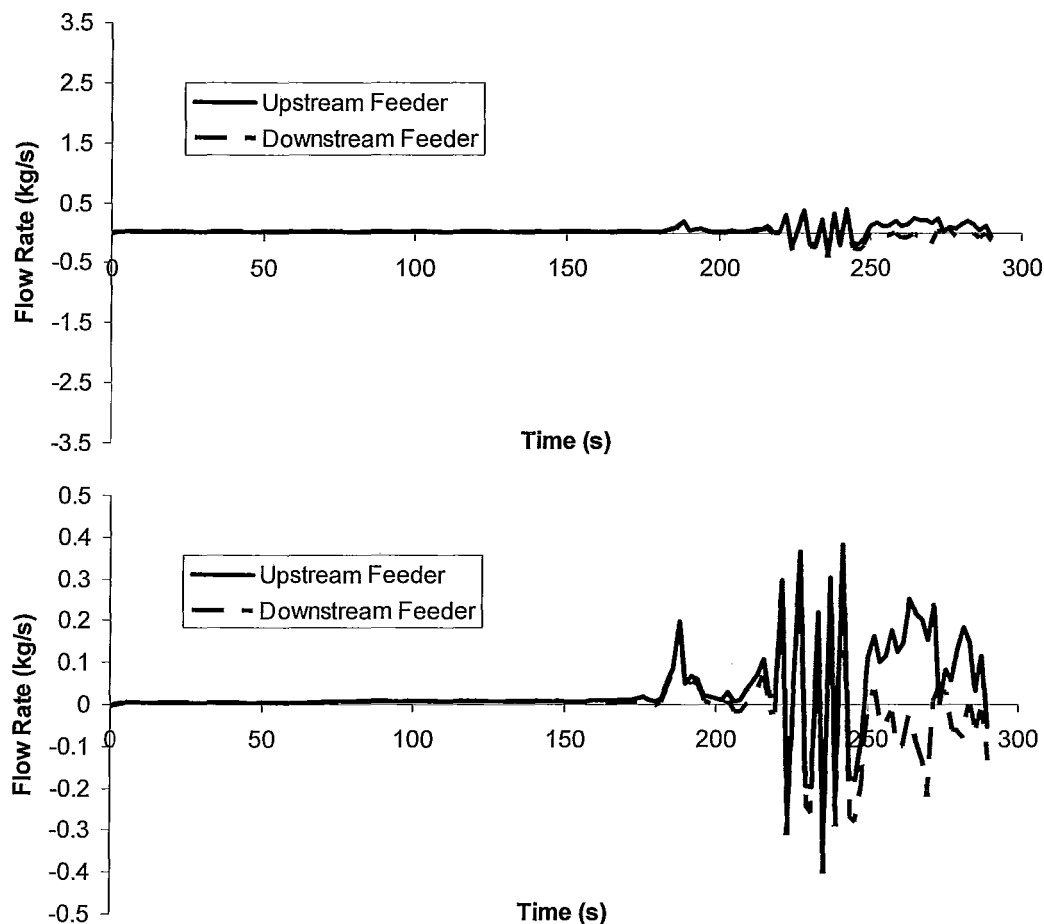


Figure 60 – High Power Reference Case Feeder Flow Rate Transients⁵⁶

⁵⁵ The ‘Courant limit’ refers to the condition that the volumetric flow through a cell in a given timestep must be less than the fluid volume in the cell at the beginning of the timestep for each phase. The Courant limit is outlined more quantitatively in Appendix A.

⁵⁶ The two figures present the same data, but on two different scales for greater clarity and resolution.

Flow oscillations can be clearly seen in Figure 60. The first figure displays the oscillations on the approximate scale one would expect of outward flow resulting from vapour production in a saturated channel (see Table 18). These oscillations explain the Courant limitations placed on timestep size in the simulations. It should be noted that the sampling rate for data in these simulations is 2 seconds⁵⁷. Given this and the rate of oscillation seen in Figure 60, it is plausible that the frequency of simulated oscillation is higher than that reflected in the figure, and also that amplitude of the oscillations is larger than what is shown.

The most likely explanation for these flow oscillations is vapour collapse in the end fittings – that is, the rapid condensation of vapour in a cell due to highly efficient heat transfer with the cool body and dead-space of the end fitting. The rapid condensation results in flow from neighbouring cells; this process is accompanied by pressure variation in the cell. This change in pressure is a potential timestep-limiting factor, however the factor limiting timesteps in the high power cases is the Courant limit. While rapid condensation in the end fittings is a real and important phenomenon, the sizable and rapid flow oscillations seen in Figure 60 are likely not reflective of any process occurring in the CWIT facility.

The end fitting model could be modified in two ways to address the issue of vapour-collapse-induced Courant limit timestep limitation. The impact of vapour collapse in a given cell could be limited by decreasing the cell volumes in the areas that condensation is likely to take place. Such a grid refinement could be either uniform over the end fitting control volume, or else variable, with smaller cells located around the outside (see Figure 38). The impact of a given vapour collapse could be limited by changing the modelling of the end fitting –

⁵⁷ Due to the size of the model and the amount of data that must be saved, the output files may become prohibitively large, if data is saved at a very high frequency.

feeder flow path junction (see Figure 38). As a result of modelling the junction as a real-sized opening in the end fitting body, the cell to which the feeder flow path is currently connected is largely occupied by the end fitting body, resulting in a low free volume of the cell. The free volume of the cell is directly proportional to the size of the Courant limit in a given timestep – consequently, abandoning the ‘opening’ model of the flow path junction in favour of a direct connection to a cell ‘inside’ the end fitting model would result in a significant increase in timestep size (while sacrificing some adherence to the experiment).

4.2.2.2 High Power Reference Case Results

As the high power simulations exhibit timesteps which may not provide final results within a practical period, the most important task to perform in examining the high power reference case results is to determine whether they are physically reasonable.

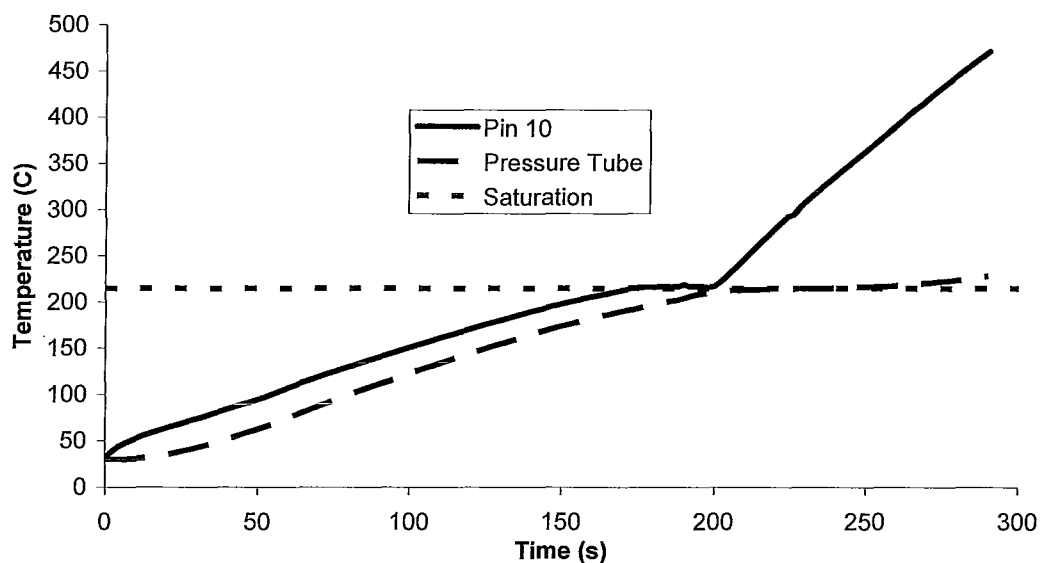


Figure 61 – Temperature Transients, Plane F1

The temperature transients seen in Figure 61, demonstrate that saturation is reached at approximately 175 s, where the temperature of pin 10 ceases to

increase. The relative efficiencies of heat transfer through nucleate boiling and single phase conduction and convection to liquid and steam is reflected in the slope of the pin 10 transient as it passes from an environment of subcooled liquid, to saturated liquid, to steam (at which point the slope is nearly identical to the adiabatic pin heatup rate calculated in Table 16). The temperature profile of the pressure tube is similarly in line with expectations. The temperature increase of the pressure tube lags that of pin 10, as heat is transported from the pin to the pressure tube via the intermediary of the coolant (in liquid or gaseous state). Additionally, the temperature increase of the pressure tube slows markedly after saturation is reached, reflecting the low heat transfer capabilities of steam (when not condensing).

The profiles of vapour fraction, vapour velocity, and liquid velocity are shown at several times during the simulation and at planes B, F1, G1, and K in Figure 62 - Figure 65. These figures demonstrate the large scale behaviour of the channel during the simulation.

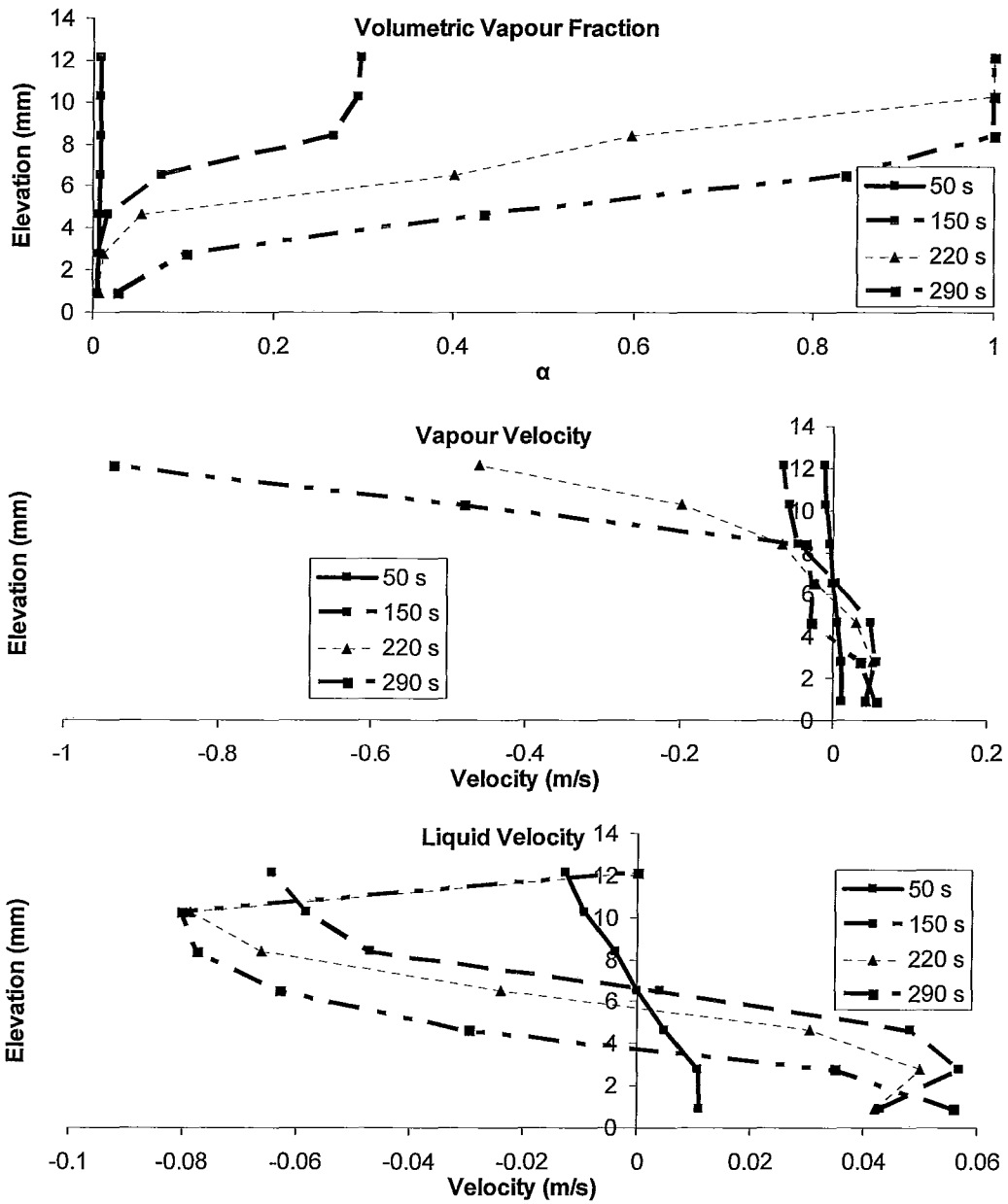


Figure 62 – Vapour Fraction and Liquid and Vapour Velocity Profiles, Plane B

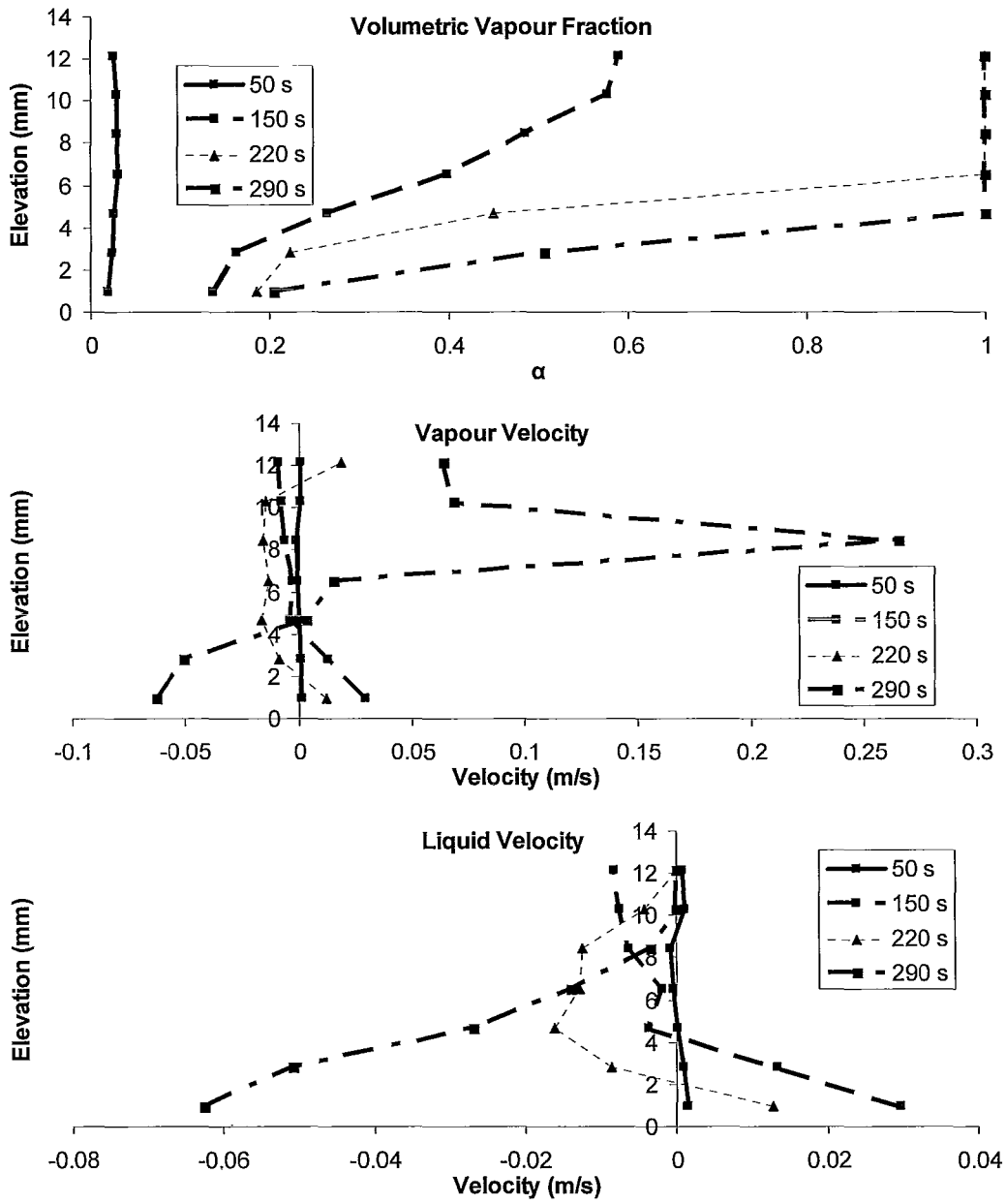


Figure 63 – Vapour Fraction and Liquid and Vapour Velocity Profiles, Plane F1

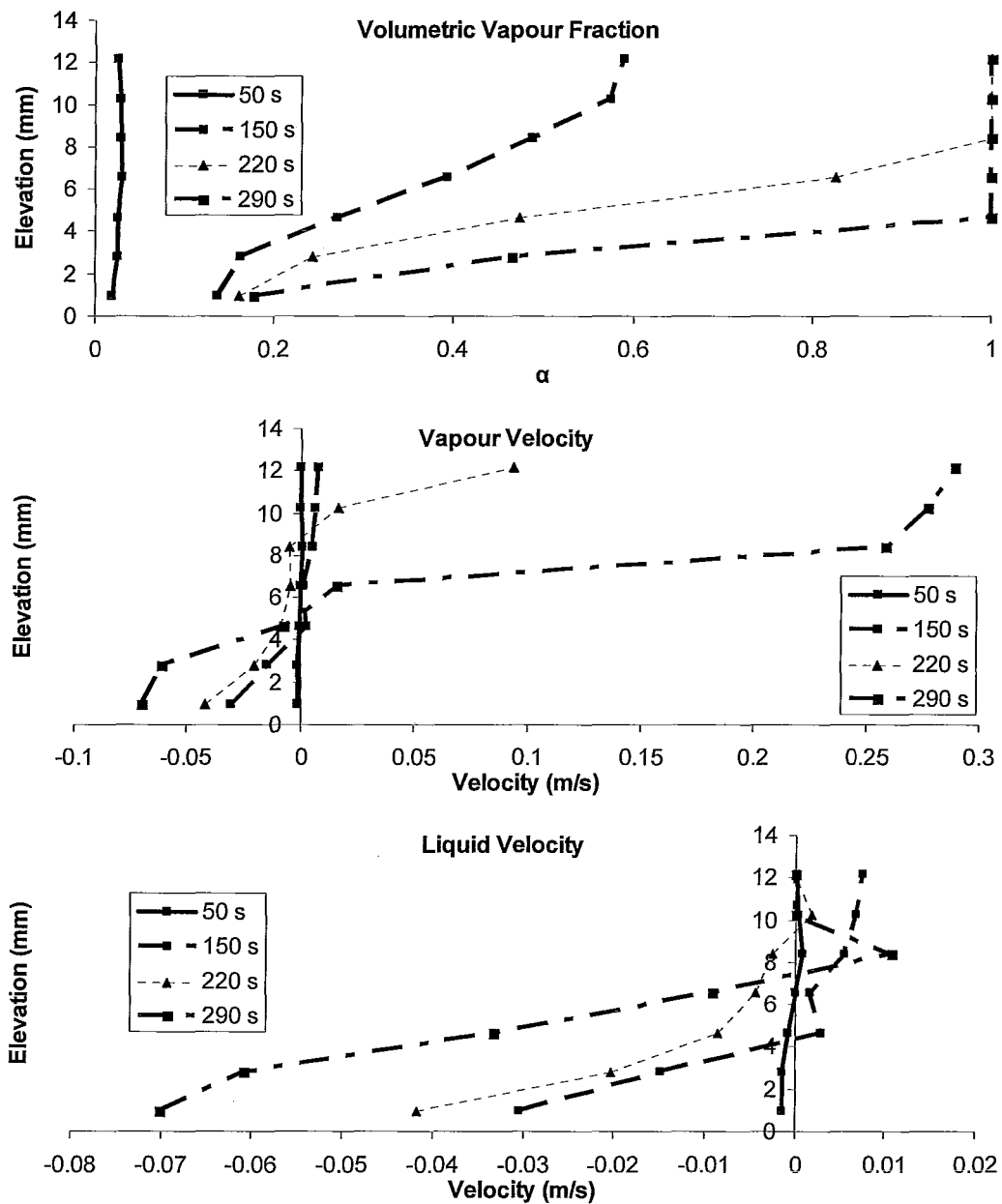


Figure 64 – Vapour Fraction and Liquid and Vapour Velocity Profiles, Plane G1

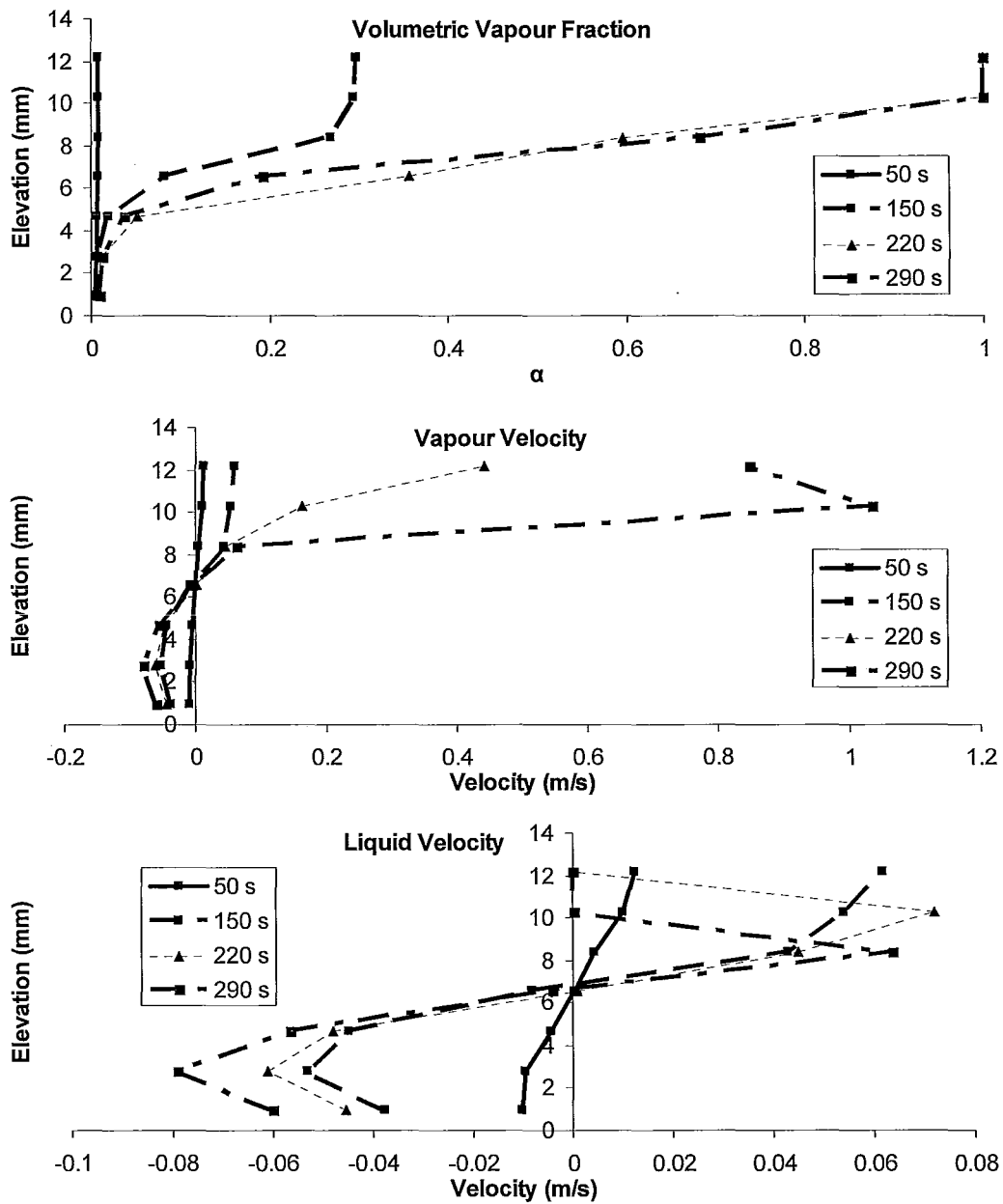


Figure 65 – Vapour Fraction and Liquid and Vapour Velocity Profiles, Plane K

Before discussing Figure 62 - Figure 65, it should be pointed out that the velocity profiles portrayed (for vapour in particular), are likely subject to a degree of oscillation as a result of vapour collapse in the end fittings. With that said, the general trend of the vapour fraction to increase and spread from the top of the

channel to the bottom with time is as expected. Furthermore, it appears that the increase in vapour ‘depth’ slows markedly between 220 and 290 seconds, an indication that a stable vapour profile has been reached or is near at 290 seconds. Comparing the vapour fraction profiles of each figure, it is apparent that there is more vapour at the centre of the channel, as expected.

Considering the velocity profiles in each figure, a strong circulation pattern, with vapour flowing from the centre of the channel toward the end fittings and liquid flowing from the end fittings toward the centre, is apparent. Additionally, the vapour velocities are much higher, reflecting conservation of mass and the lower density of steam. Superimposed on this circulation pattern is the establishment of flow from the downstream to the upstream end of the channel, as seen after approximately 250 s in Figure 60. This effect is small in comparison with the impact of the circulation pattern, but it is apparent. The liquid flow into the channel from the downstream end fitting is higher than from the upstream end fitting. Additionally, the vapour flow from the centre of the channel to the upstream end fitting is higher than the flow to the downstream end fitting.

The temperature transients of elements from the top to the bottom of the channel are shown in Figure 66.

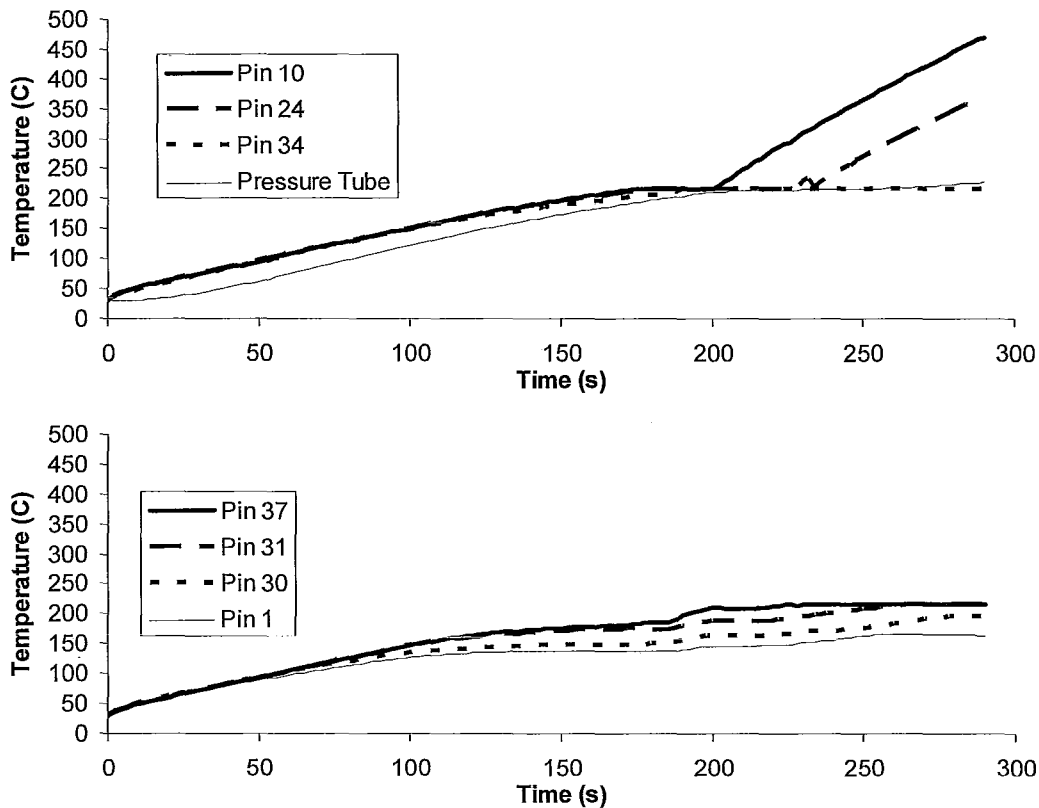


Figure 66 – Element Temperature Transients, Plane F1

The temperature transients seen in Figure 66 are consistent with the stratification seen in Figure 63. As the highest elevation pins are uncovered, they commence an approximately adiabatic heatup rate. Arrival at saturation is apparent in some of the lower pins, which cease their temperature increase and are presumed to supply a continuous flow of steam, allowing the circulation pattern seen in Figure 62 - Figure 65.

The variation of the pin 10 temperature transient along the channel is shown in Figure 67.

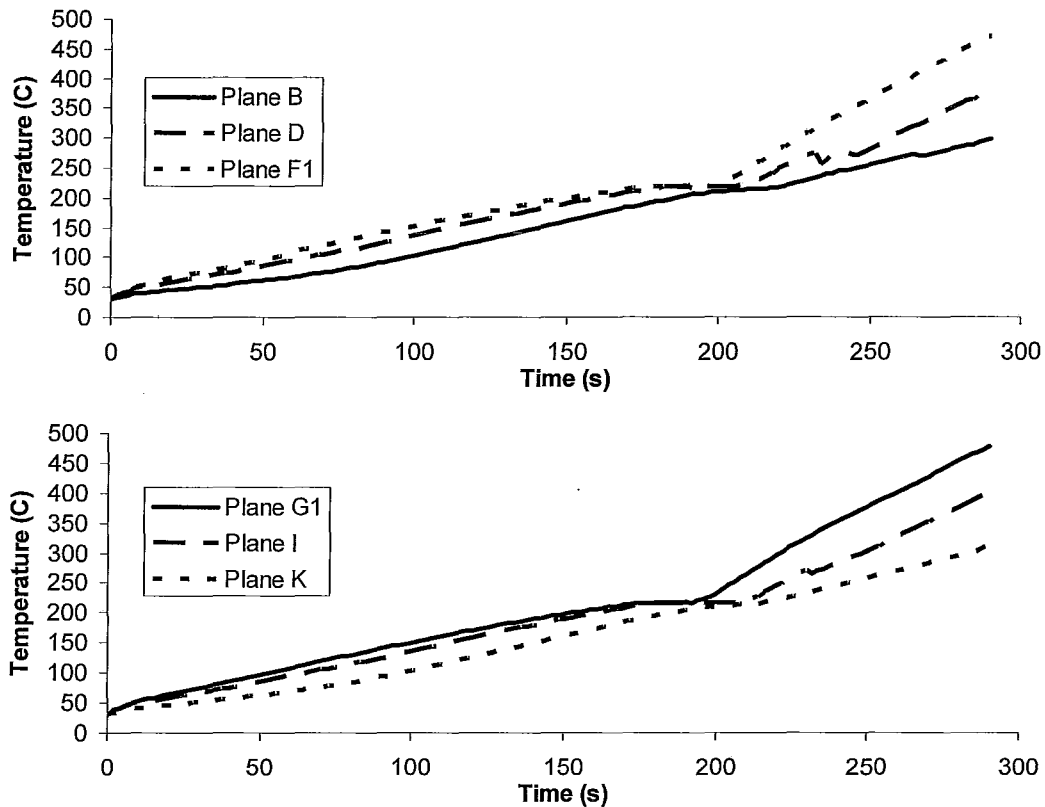


Figure 67 – Pin 10 Temperature Transient Along Channel

As expected, the temperature increase of the centre pins is fastest at the centre of the channel where the pin power is highest. Competing with this effect is the transport of heat, via liquid and then steam, from the centre of the channel toward the end fittings, presumably increasing in temperature while passing over the pins along the way. This effect may have an impact before saturation is reached, however, due to the low heat transfer coefficients associated with steam, this has little impact on the heatup rates of the pins after exposure to vapour – with the transients approximating adiabatic heatup rates reflective of the axial power profile.

The temperature transients of the end fittings are displayed in Figure 68 and Figure 69.

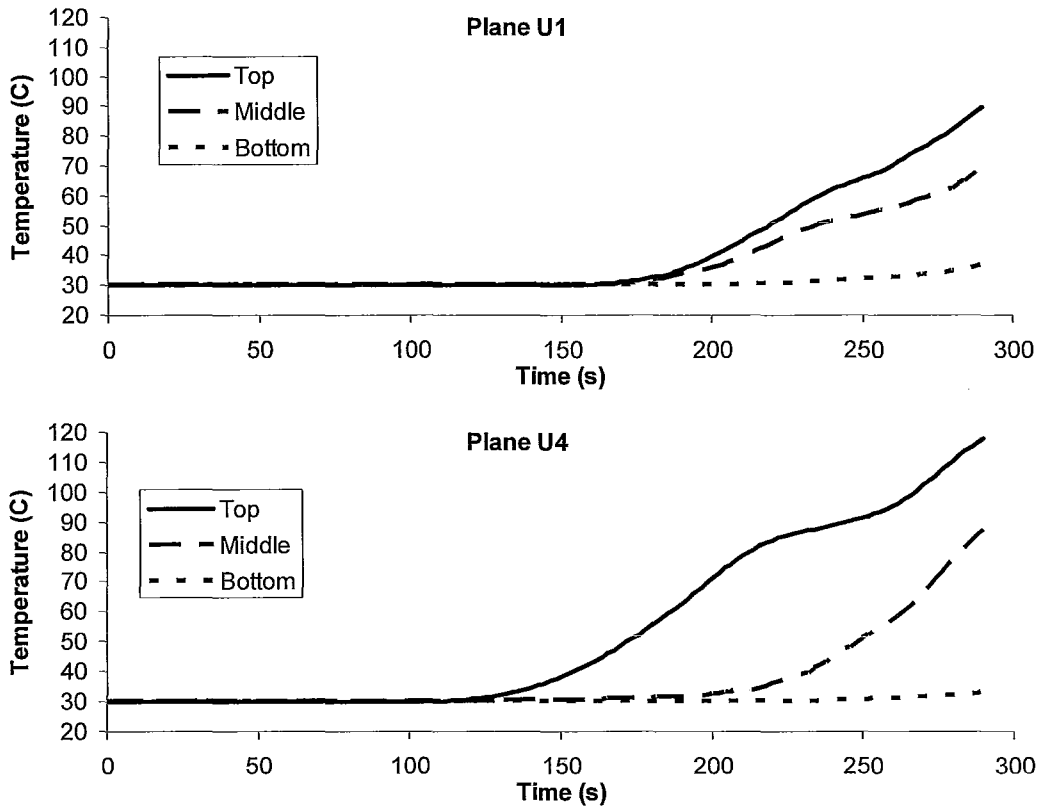


Figure 68 – Upstream End Fitting Temperature Transients

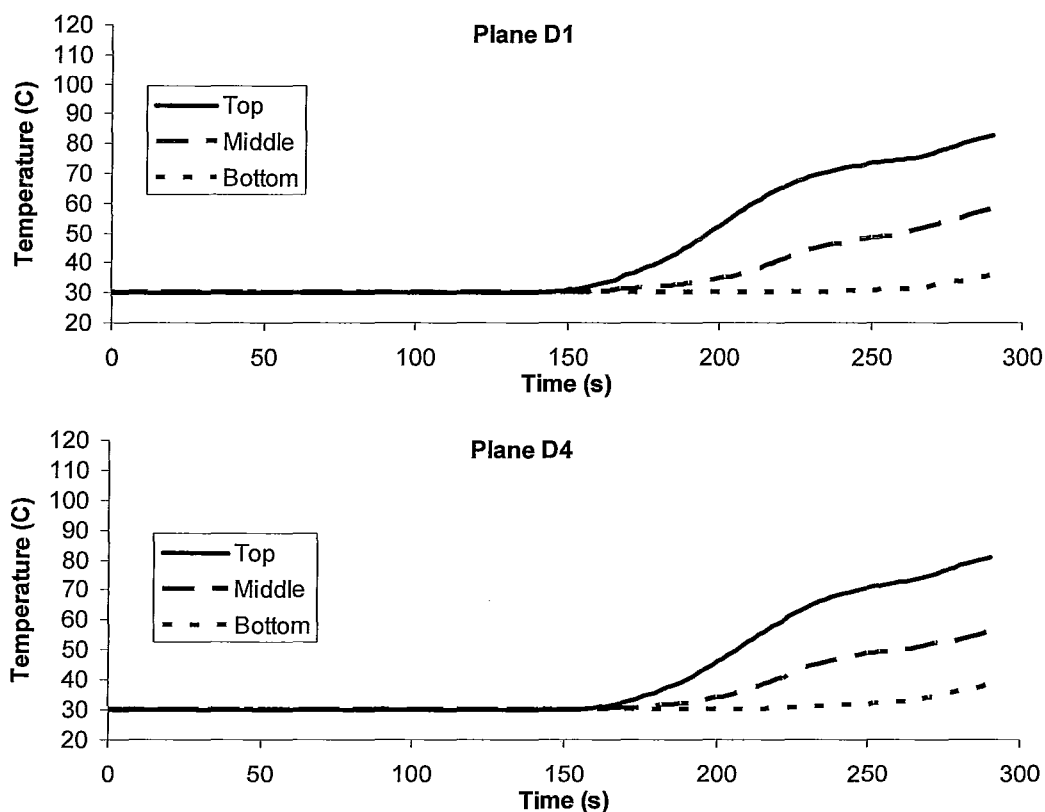


Figure 69 – Downstream End Fitting Temperature Transients

The effect of the flow asymmetry noted in Figure 60 is readily apparent in comparing Figure 68 and Figure 69, the flow from downstream to upstream results in more heating of the upstream end fitting. While the simulation has not completed, this asymmetry is a strong indication that venting will eventually take place in the direction of the upstream end fitting.

4.2.2.3 High Power Reference Case Venting Projection

While final results of the high power simulation are not available, it is possible to make approximate projections of the venting time based on the observation that the top of the end fitting must reach saturation before venting takes place. Some flow in the direction of the upstream end fitting has led to a swifter temperature increase at that end, consequently the temperature at the top

of the end fitting at plane U1⁵⁸ is considered. From the beginning of condensation on the end fitting to the end of the simulation, the temperature at plane U1 increases at an average rate of approximately 0.509 °C/s. An extrapolation based on this heatup rate is depicted in Figure 70, and results in a predicted venting time of approximately 536 s.

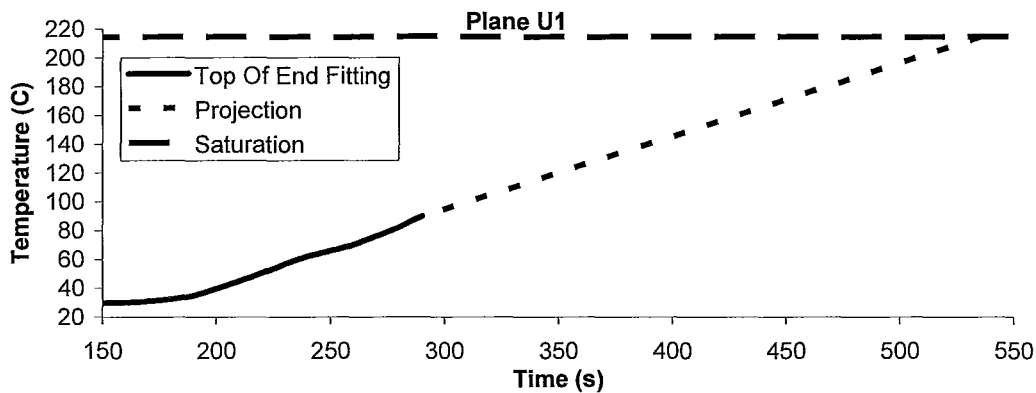


Figure 70 – Extrapolated End Fitting Heatup

This extrapolation may over-predict or under-predict the ultimate venting time that would be simulated by the high power model, based on the impact of a number of factors after the first 290 seconds of the simulation. The most important of these factors are outlined below:

- It is likely that increasing pre-venting flow from the downstream to upstream end of the channel would result in an increase in the fraction of heat transported to the upstream end fitting relative to the downstream end fitting, and a faster venting time than predicted.
- Variation in the fraction of heat transported to the top of the end fitting during the simulation (relative to the lower portions of the end fitting and

⁵⁸ Plane U1 is used rather than U4, as it is located next to the feeder junction, and will be the last part of the end fitting to reach saturation before venting.

the dead space), could have a positive or negative impact on the venting time.

- The amount of heat transported to the end fittings is impacted by the amount of heat stored elsewhere in the system. As more fuel pins are uncovered, they will tend to store more heat, and slow the heatup rate of the end fittings. The impact of this is dependent on the variation of the amount of vapour in the channel with time.

As mentioned above, the heatup rate used in arriving at the predicted venting time of 536 s is 0.509 °C/s. This value is very close to the heatup rate for the entire end fitting body and dead space taken together (see Table 20). Since the heatup rate of lower parts of the end fitting body is far below that of the top (see Figure 68 and Figure 69), and heatup of the two end fittings is asymmetrical (while the values presented in Table 20 are calculated for symmetrical cases), the impact of heat storage in the uncovered pins and pressure tube is apparent.

4.3 Sensitivity Simulation Results

The sensitivity of the model to various parameters is an important consideration in determining the merits of the model. Sensitivity to nodalisation and feeder flow path location is examined in this section.

4.3.1 End Fitting – Feeder Flow Path Location Sensitivity

Due to the localisation of the feeder flow path location to a single cell in the model (see Section 3.3.2.7.4), the sensitivity of the model to this location has been considered. Simulations were performed connecting the feeder flow path to each of the cells the corresponding to the feeder location in the CWIT test rig. The locations of sensitivity locations S1 – S4 are shown in Figure 71.

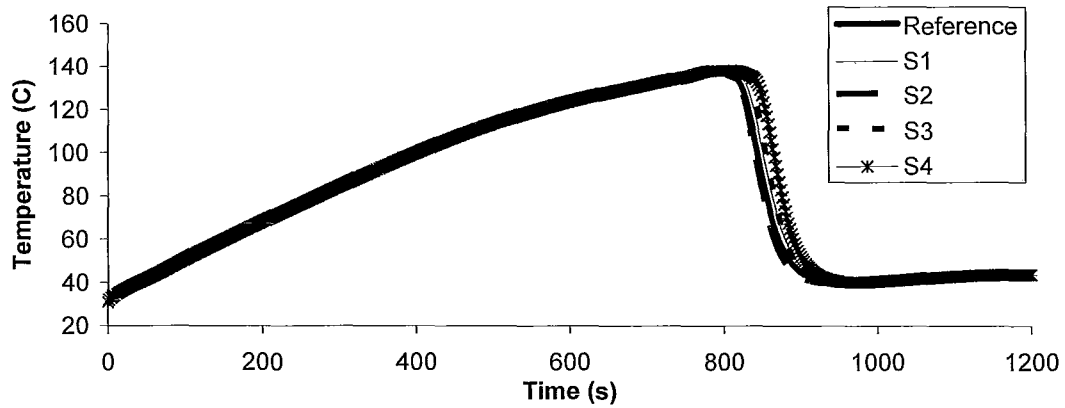


Figure 71 - Temperature Transient, Pin 10, Plane F1, Feeder Position Sensitivity

Figure 71 displays the temperature transients for each of the sensitivity models and the reference model of Pin 10 at plane F1. It can be observed that there is a small difference in venting time and a very small difference in maximum temperature.

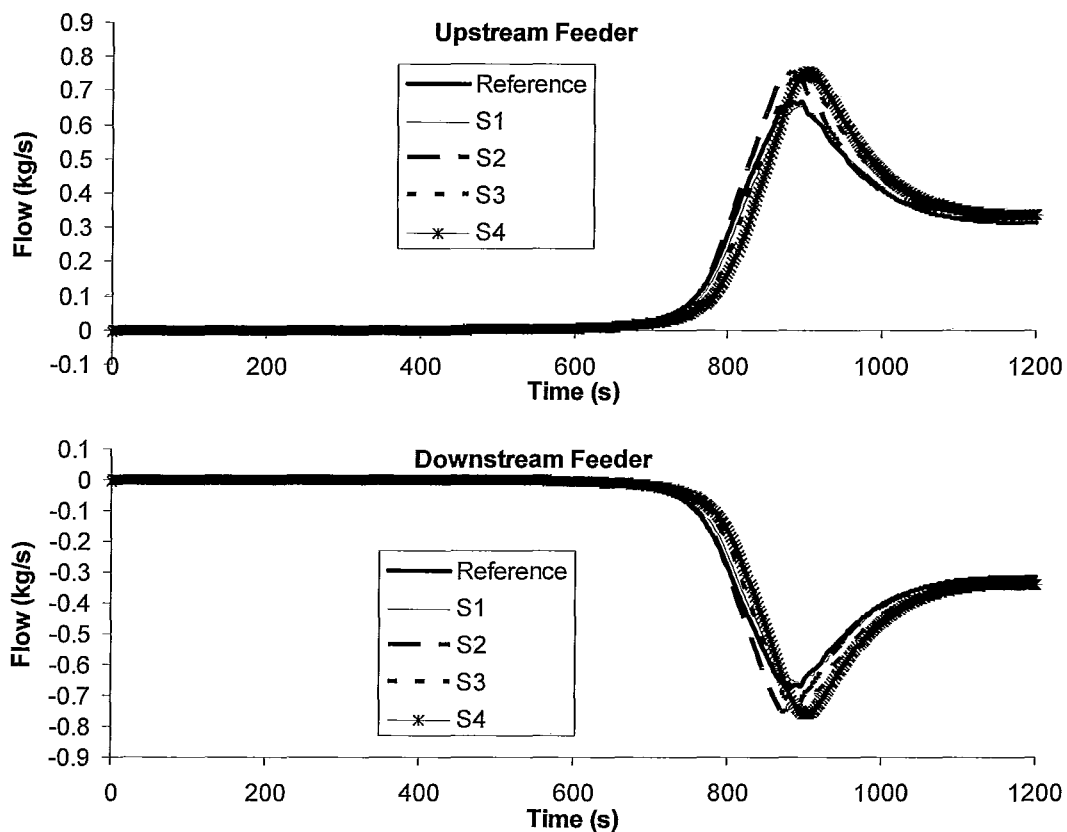


Figure 72 - Feeder Flow Rate, Feeder Position Sensitivity

The coolant flow through each of the feeders is displayed in Figure 72. Some variation in this parameter is inevitable, as each of the cells at the end fitting have different porosities and hydraulic diameters. Nonetheless, the variation in flow rate is not overwhelming, and most importantly, the timing of the vent is not affected significantly.

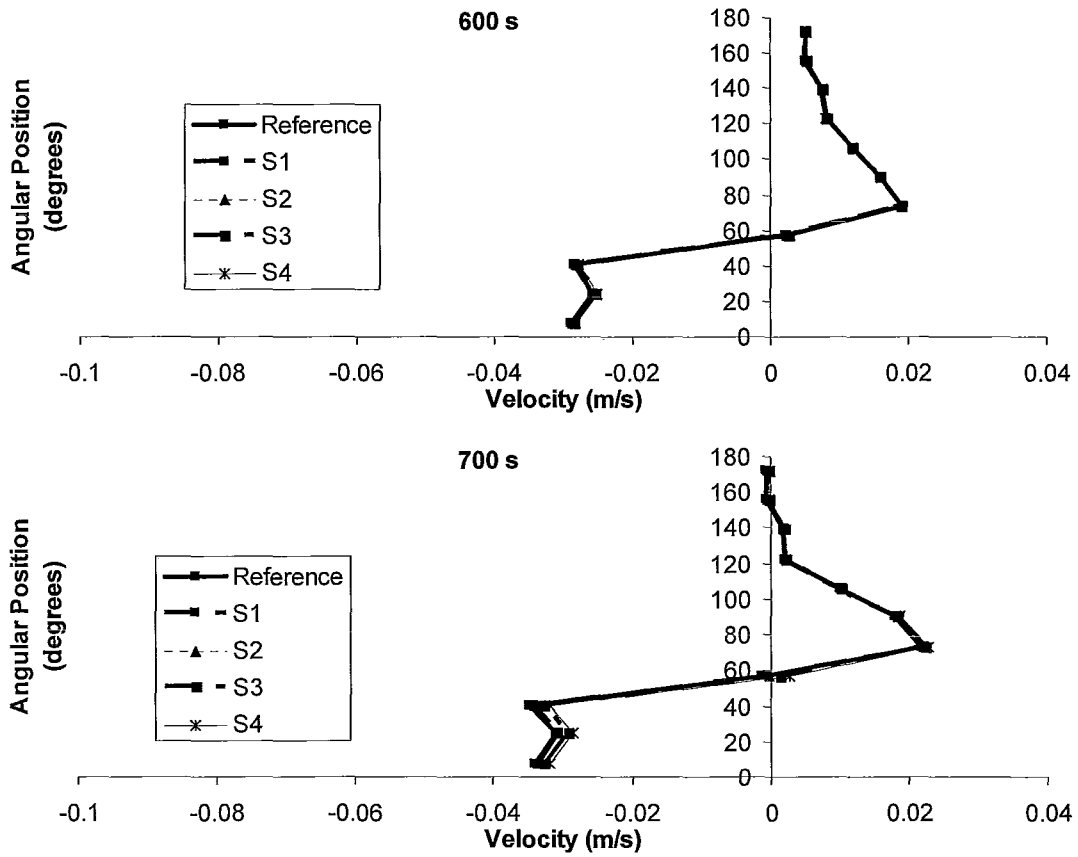


Figure 73 - Axial Flow Velocity Profile In Upstream End Fitting, Feeder Position Sensitivity – Plane U1

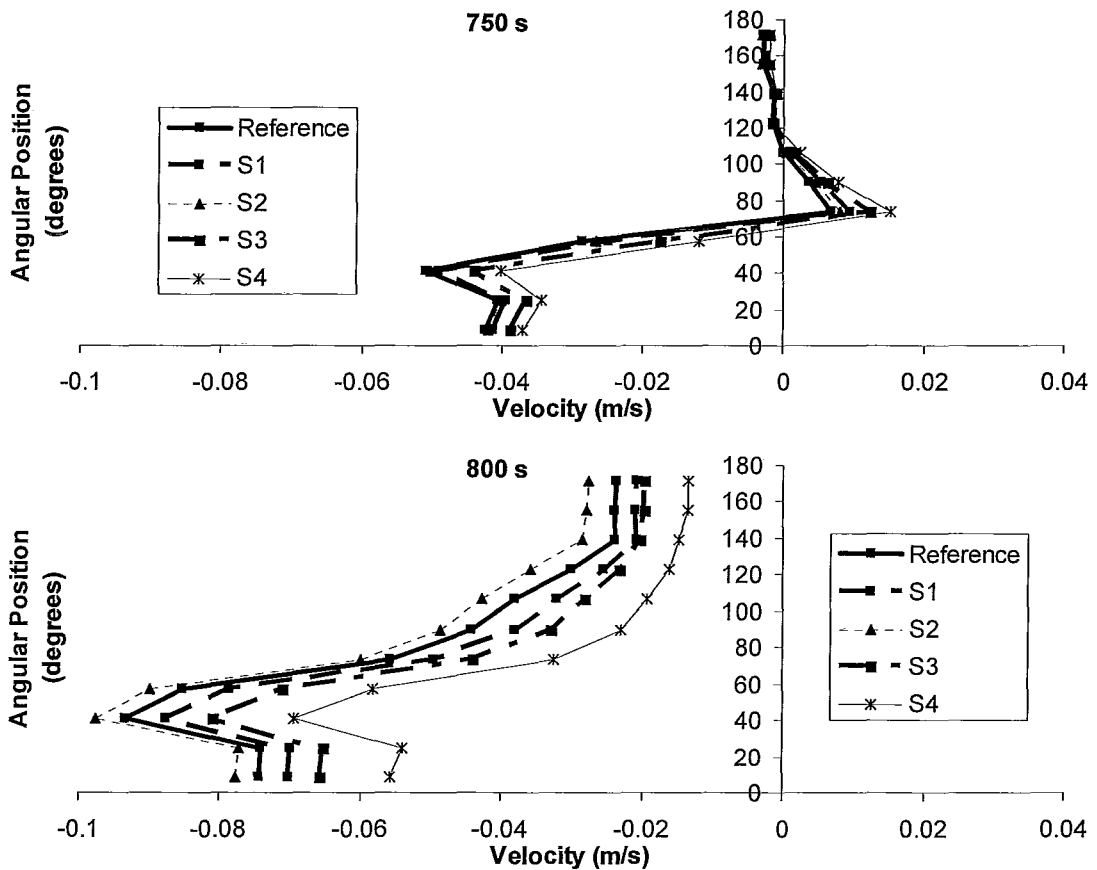


Figure 74 - Axial Flow Velocity Profile In Upstream End Fitting, Feeder Position Sensitivity – Plane U1

The greatest impacts of feeder location would be expected to be apparent at planes U1 and D1 of the end fittings. The flow velocity profiles at plane U1 is depicted in Figure 73 and Figure 74. While there is some difference in the magnitude of flows as venting develops (to be expected after considering Figure 72), the profiles of the flows in the end fittings appear to be nearly identical for each sensitivity simulation.

The sensitivity of the model to feeder flow path location is not significant or a cause for concern.

4.3.2 Nodalisation Sensitivity

The sensitivity of the model's simulations to nodalisation has been studied by increasing the degree of volume subdivision and performing a simulation of CWIT test #1617. The number of cells for each non-lumped volume was increased by approximately a factor of 3 (see Table 23).

Table 23 - Nodalisation Details Used For Reference and Sensitivity Models

Volume Number	X-Dimension Subdivision		Y-Dimension Subdivision		Z-Dimension Subdivision	
	Reference Model	Fine Mesh Model	Reference Model	Fine Mesh Model	Reference Model	Fine Mesh Model
1-24	2	3	7	10	7	10
25, 26	3	3	7	10	7	10
27, 28	5	7	9	14	9	14
29-46	1 (lumped)	1 (lumped)	1 (lumped)	1 (lumped)	1 (lumped)	1 (lumped)

The temperature transient of pin 10 in plane F1 is displayed in Figure 75. A small delay in the vent time is apparent, as well as a slightly increased temperature in the approximately 300 seconds leading up to the vent. This relative temperature increase is likely due to higher temperature fluid in the cells at the top of the channel as stratification is established. The higher temperature follows from the smaller cells, reducing the effects of temperature averaging that the GOTHIC solver performs. The maximum temperature is 6 °C higher in the fine mesh case – 5.3% of the total temperature rise, or 4.2% of the separation from saturation.

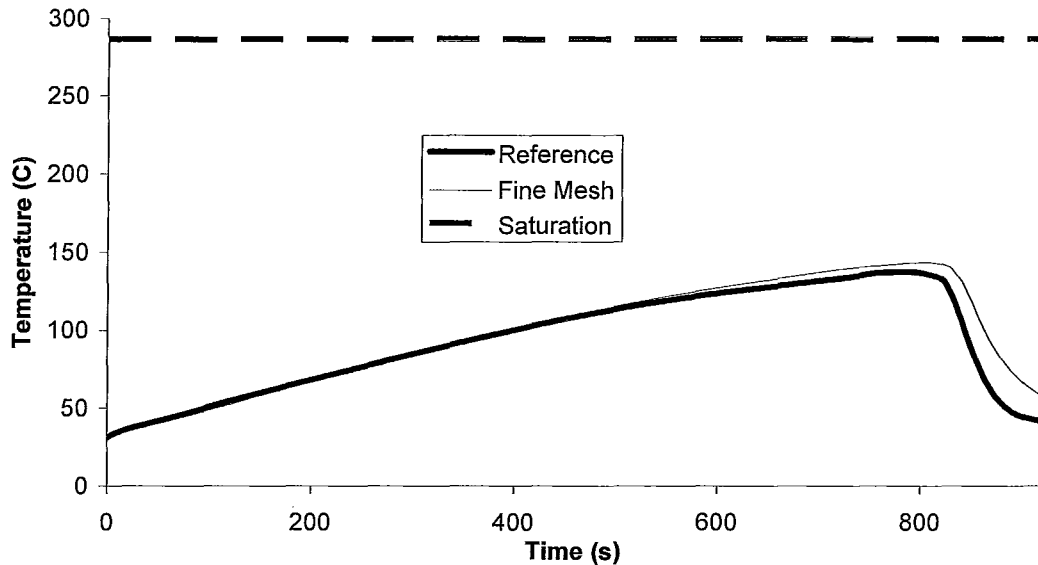


Figure 75 - Pin 10, Plane F1 Temperature Transient – Fine Mesh vs. Reference Model

The flow rate from the feeders into the end fittings is displayed in Figure 76. Although it appears that venting may begin slightly earlier in the case of the fine mesh model, the increase in flow rate is slower, leading to the later venting time observed in Figure 75. The reduced flow rate is likely due to an increase in flow resistance in the end fittings of the fine mesh model. This could in part be explained by the fact that the feeders connect to only one cell in each end fitting, resulting in potentially large flow rates through a small area. Due to its smaller cells, this area is smaller in the case of the fine mesh model, in all likelihood resulting in greater flow resistance.

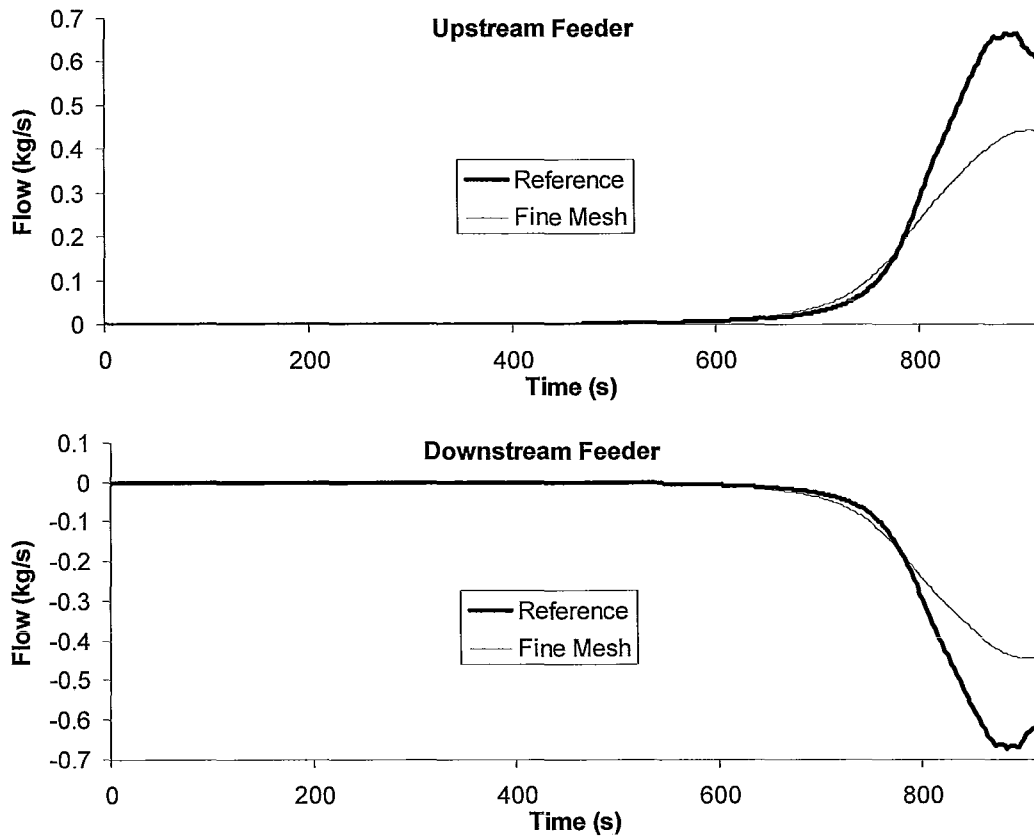


Figure 76 - Flow Rate Into End Fittings From Feeders – Fine Mesh vs. Reference Model

4.4 Benchmarking of Reference Simulations Against CWIT Facility Data

In this section, results from a simulation of CWIT test #1617 are compared against the data collected from that test to determine the accuracy of the model in predicting the behaviour of the CWIT facility.

4.4.1 Low Power

The GOTHIC model of CWIT test #1617 predicted the results of the reasonably well. For both the experimental data and the simulated results, the maximum temperature reached by the highest-temperature pin in each plane is

displayed in Figure 77, and further comparison between the two sets of data-points is made in Table 24.

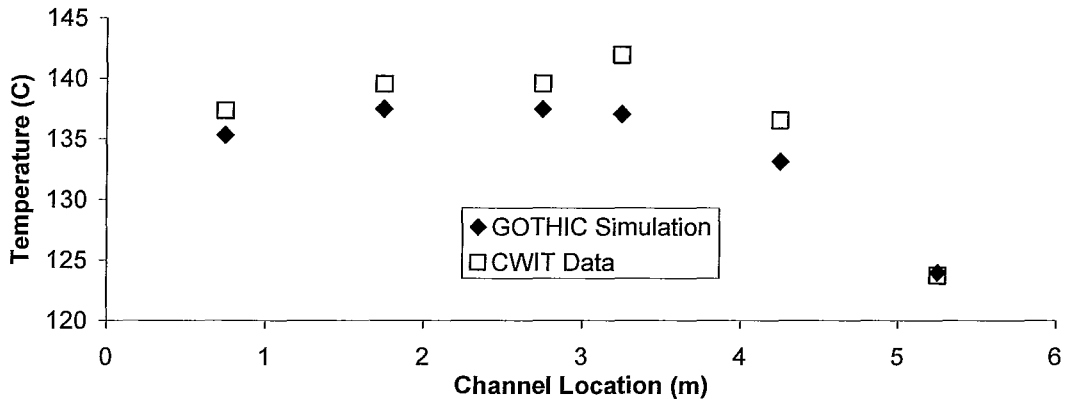


Figure 77 - Maximum Temperature Reached At Different Planes During IBIF – Pin 10

The maximum temperature variation profile along the channel is predicted well, in addition to a reasonable match at each data point. The temperature scale on this figure is compressed for a higher resolution comparison between data sets, it bears emphasising that the saturation temperature is well beyond the maximum temperature shown on the figure.

Table 24 - Deviation of GOTHIC Results from CWIT Data

Plane	CWIT Maximum Pin 10 Temperature (°C)	GOTHIC Maximum Pin 10 Temperature (°C)	Difference in Maximum Pin 10 Temperature (°C)	Difference as a Percentage of Rise from 30 °C (%)	Difference as a Percentage of Minimum Subcooling (%)
B	137.4	135.3	2.0	1.9	1.4
D	139.5	137.5	2.1	1.9	1.4
F1	139.6	137.5	2.1	1.9	1.4
G1	141.9	137.0	4.9	4.4	3.4
I	136.5	133.1	3.4	3.2	2.3
K	123.8	124.0	-0.3	-0.3	-0.2

Table 24 displays the numerical value of each of the data points shown in Figure 77, and additionally provides a sense of proportion through comparison of the deviation of predicted and observed maximum temperatures to the temperature rise from initial conditions and the degree of subcooling at the maximum temperature. A measure of the success of the simulation is the observation that the largest deviation of predicted from observed maximum temperatures is 4.4% of the total temperature rise from the 30 C initial state of the system, or 3.4% of the extent of subcooling.

Figure 78 - Figure 85 present transient data comparing simulation and experimental results at a number of different locations in the fuel channel and end fittings.

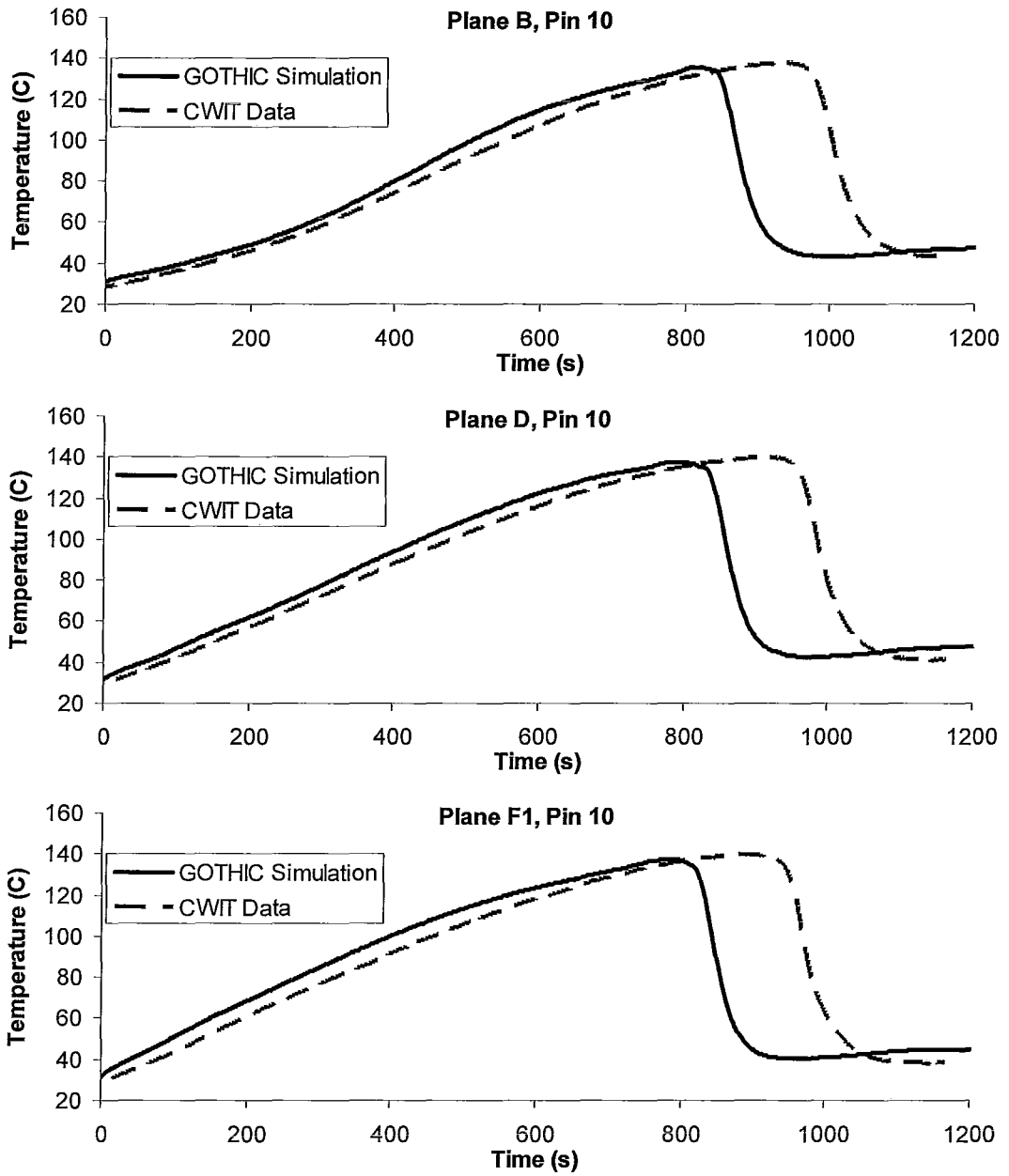


Figure 78 - Predicted and Observed Temperature Transients, Pin 10 – Test #1617

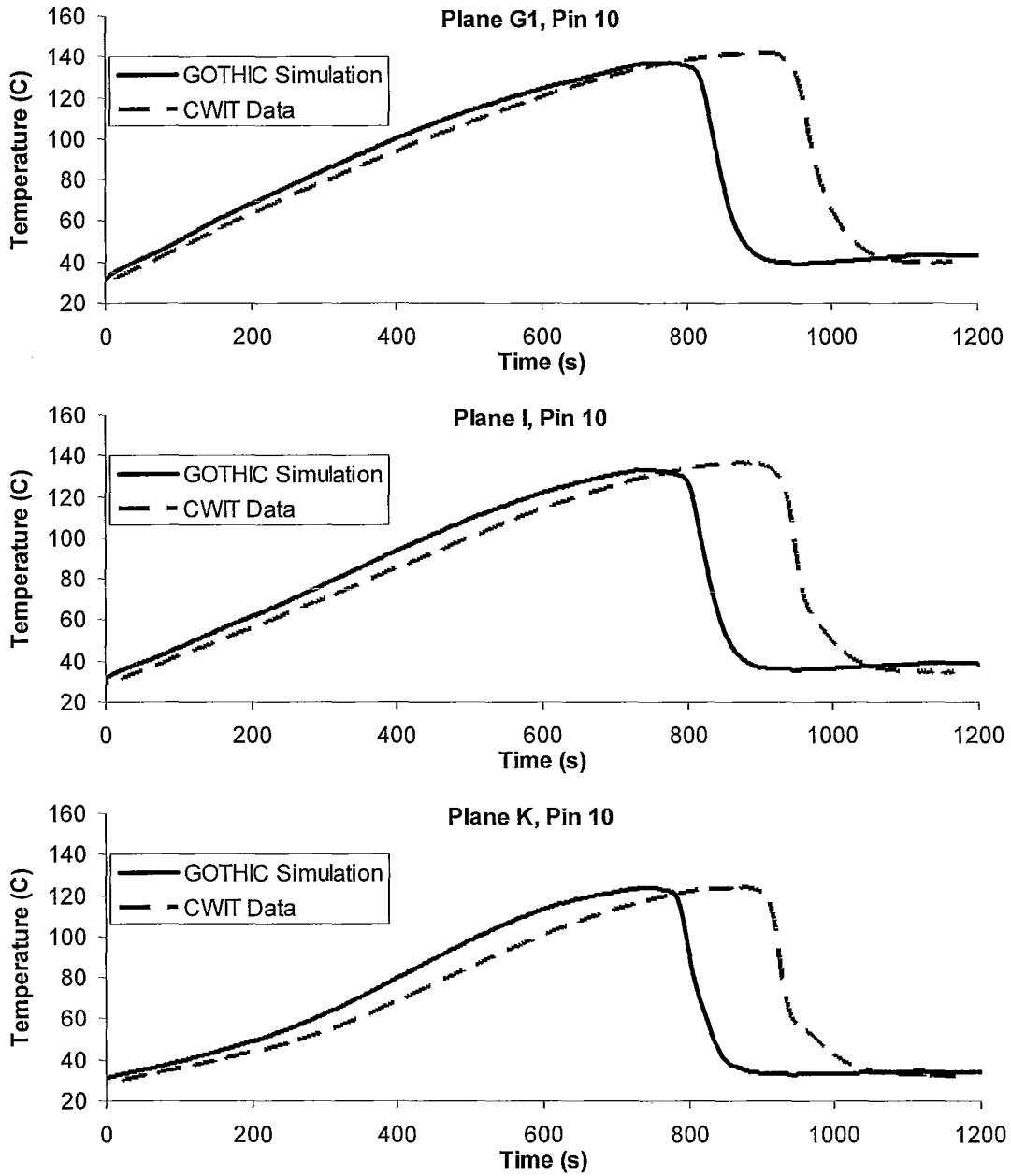


Figure 79 - Predicted and Observed Temperature Transients, Pin 10 – Test #1617

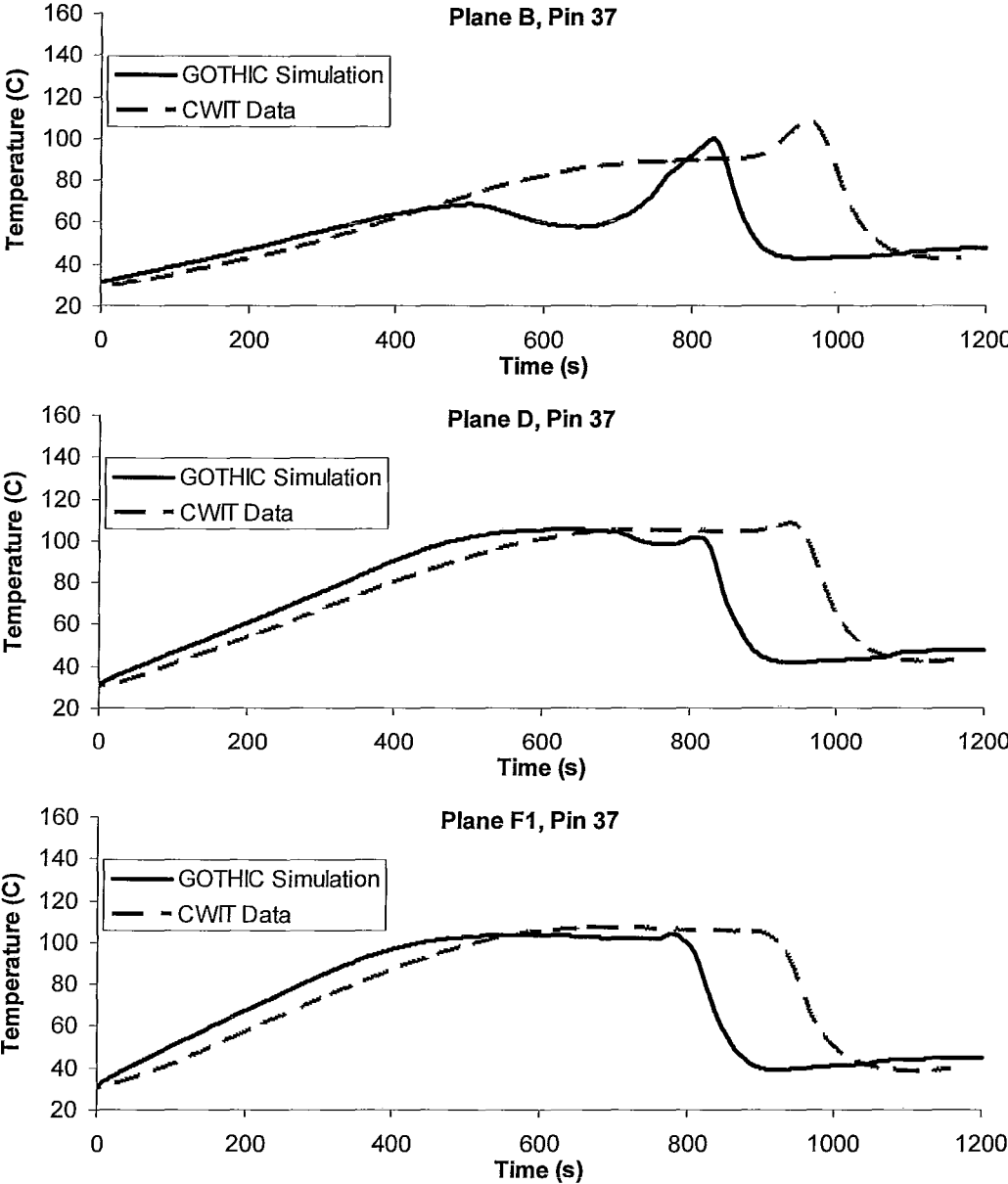


Figure 80 - Predicted and Observed Temperature Transients, Pin 37 – Test #1617

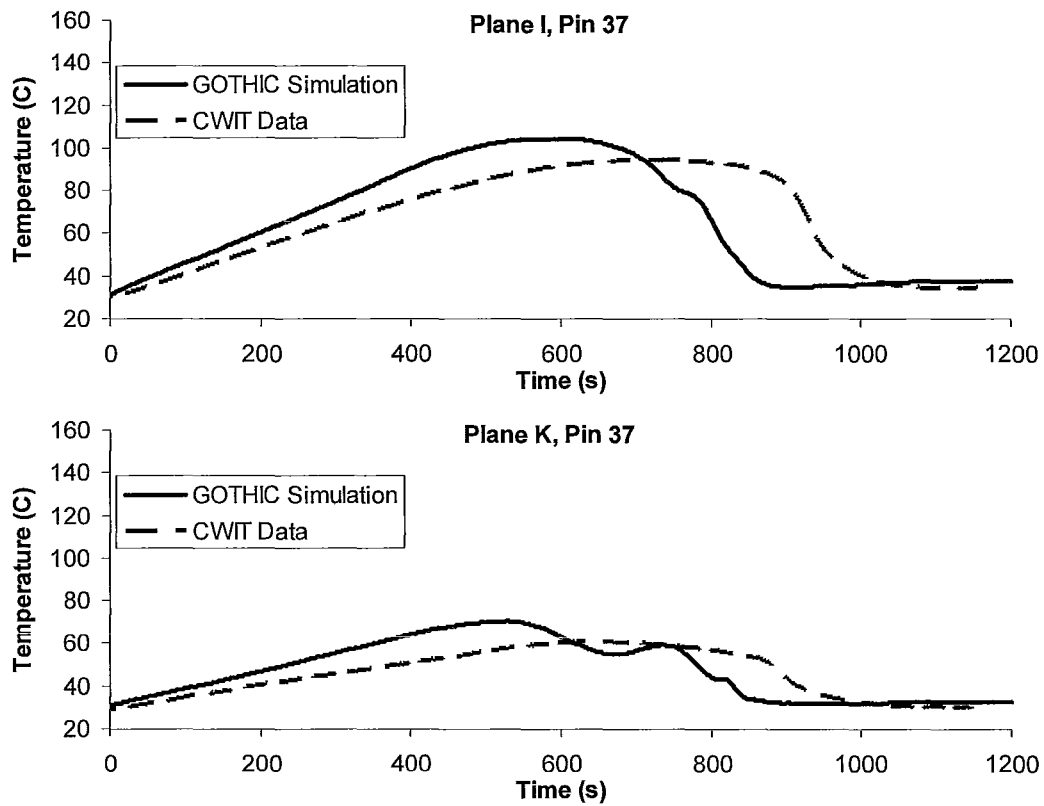


Figure 81 - Predicted and Observed Temperature Transients, Pin 37 – Test #1617

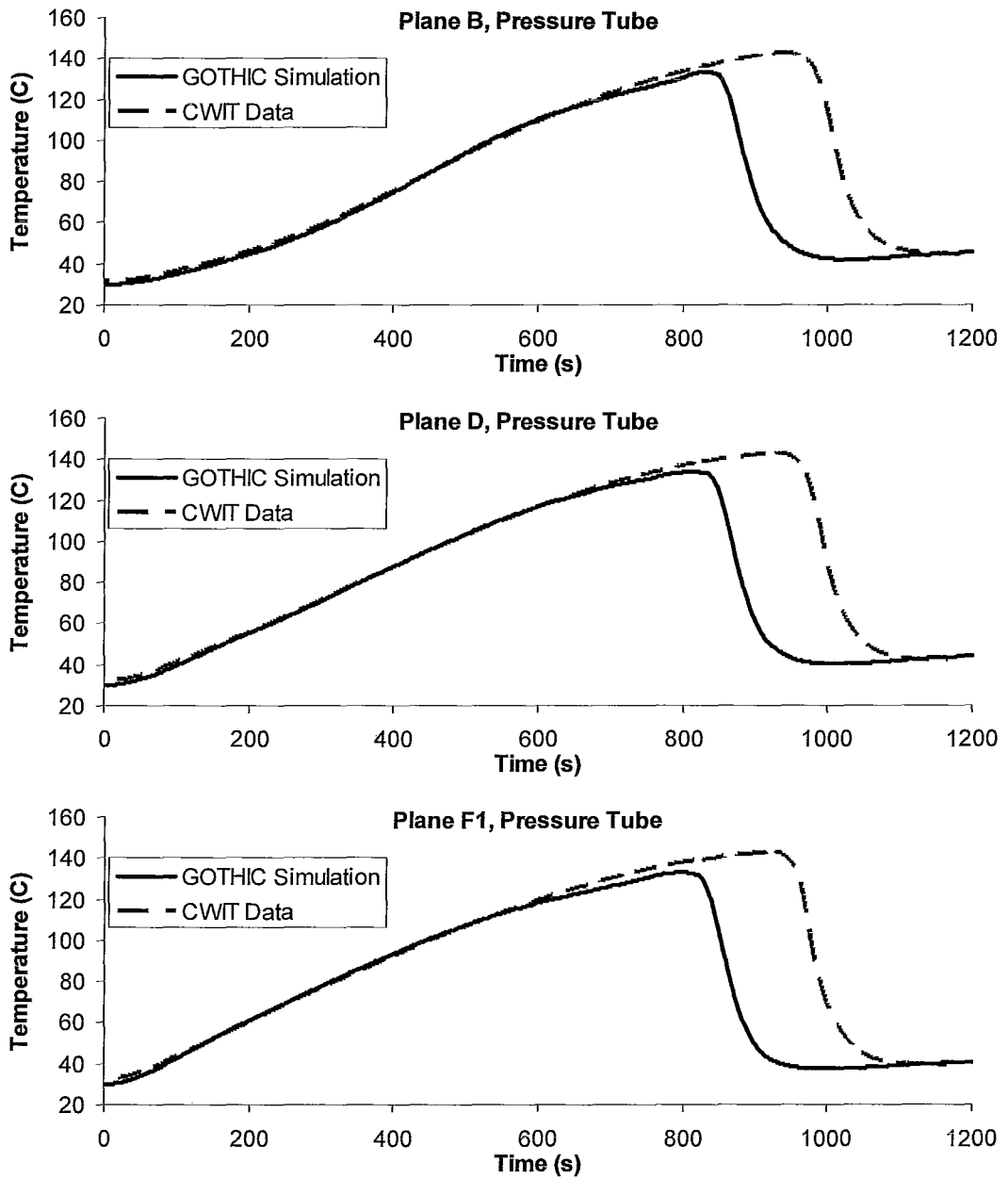


Figure 82 - Predicted and Observed Temperature Transients, Pressure Tube – Test #1617

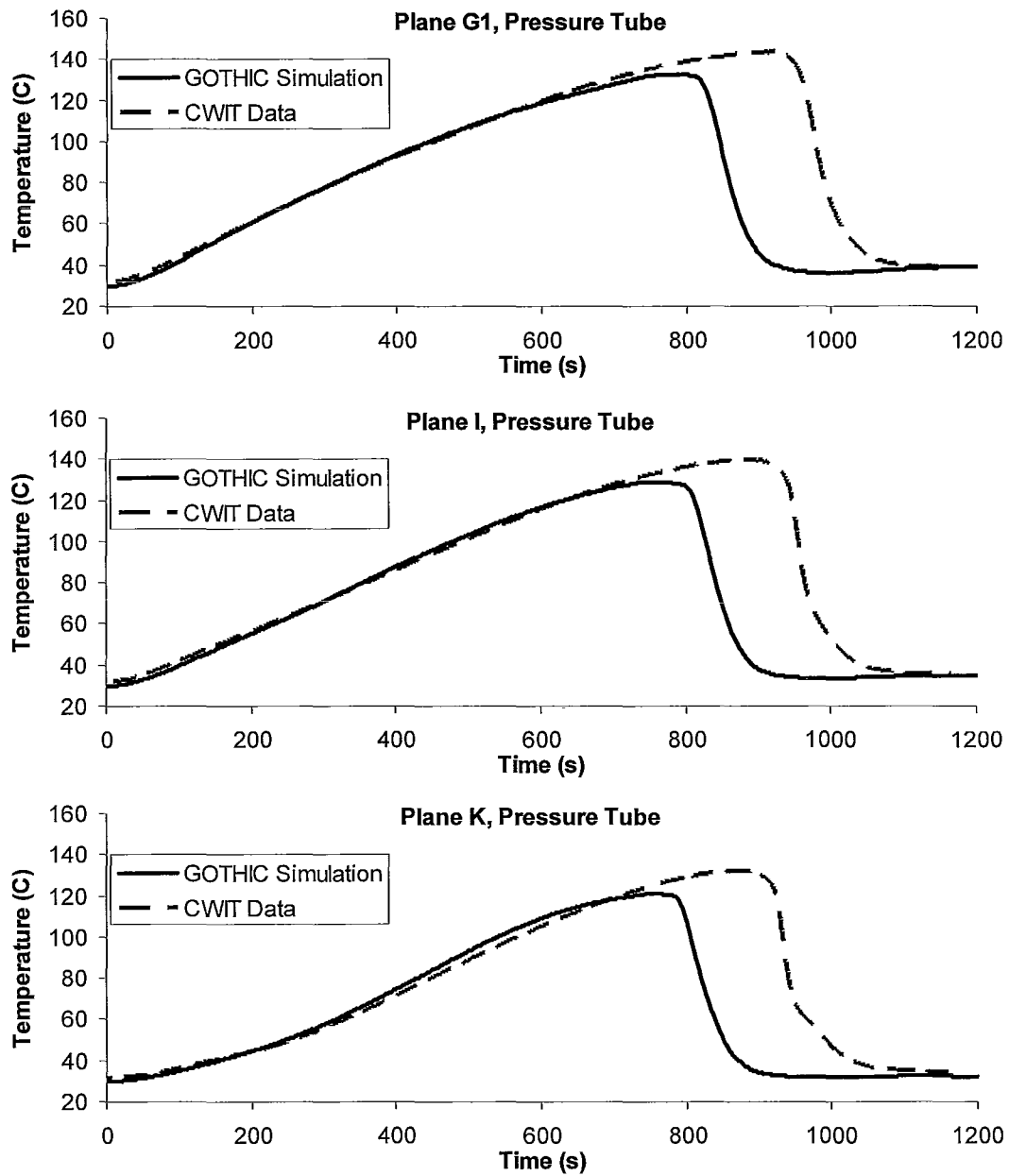


Figure 83 - Predicted and Observed Temperature Transients, Pressure Tube – Test #1617

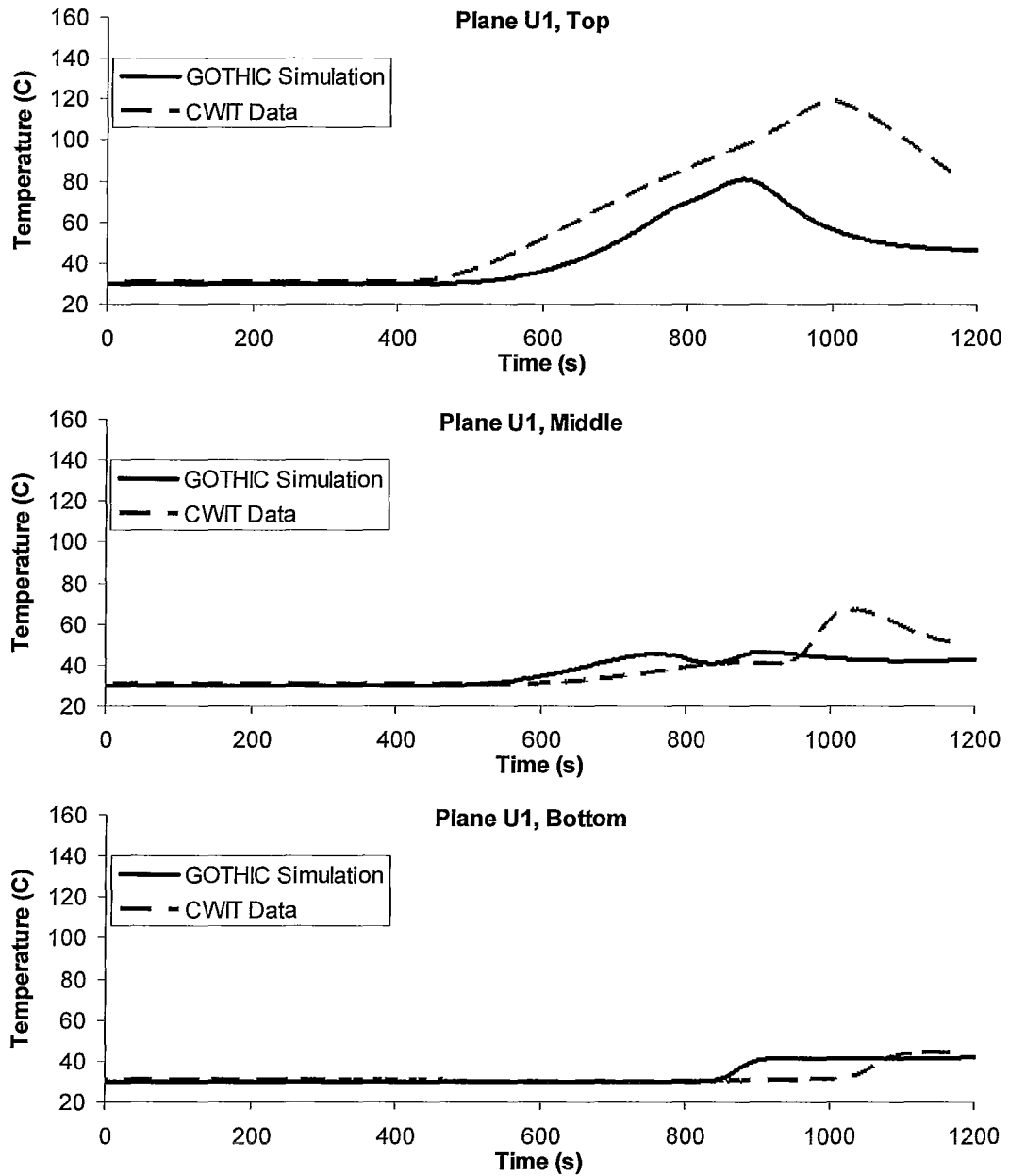


Figure 84 - Predicted and Observed Temperature Transients, Plane U1 – Test #1617

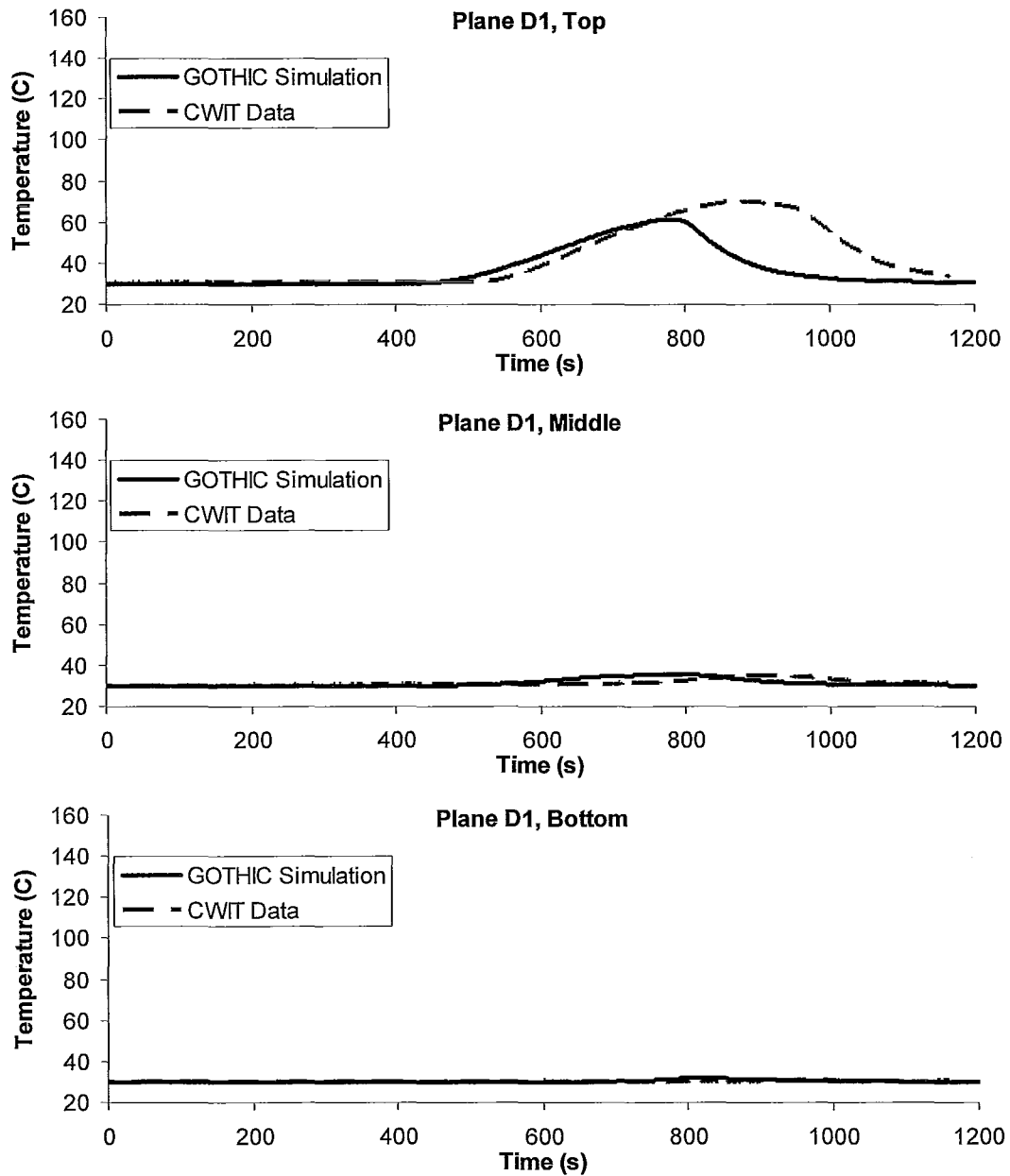


Figure 85 - Predicted and Observed Temperature Transients, Plane D1 – Test #1617

The main difference between predicted and observed behaviour apparent in the preceding figures is that the GOTHIC model predicts earlier venting than was observed during the CWIT experiment. While this moderate timing error is

systematic, the key parameter is the maximum temperature reached in the hottest pins during the IBIF cycle, which has been shown to be predicted accurately.

The prediction of an earlier venting time may be attributable to insufficient flow in the channel and end fitting. Lower flow losses could be a result of GOTHIC's internal flow loss calculations (which would likely have some sensitivity to nodalisation), or the absence in the model of some components in the CWIT test rig that provide losses, such as FES spacers.

4.4.2 High Power

Since the simulation of test #1613 was unable to reach completion in a reasonable timeframe, there is no good metric for comparison of the simulation to experimental results. While not ideal, comparing the predicted to the observed results in a somewhat qualitative manner may still provide some useful insight.

A comparison between the pin 10 thermocouple temperature data gathered during CWIT test #1613 and the simulation of that test is shown in Figure 86 and Figure 87.

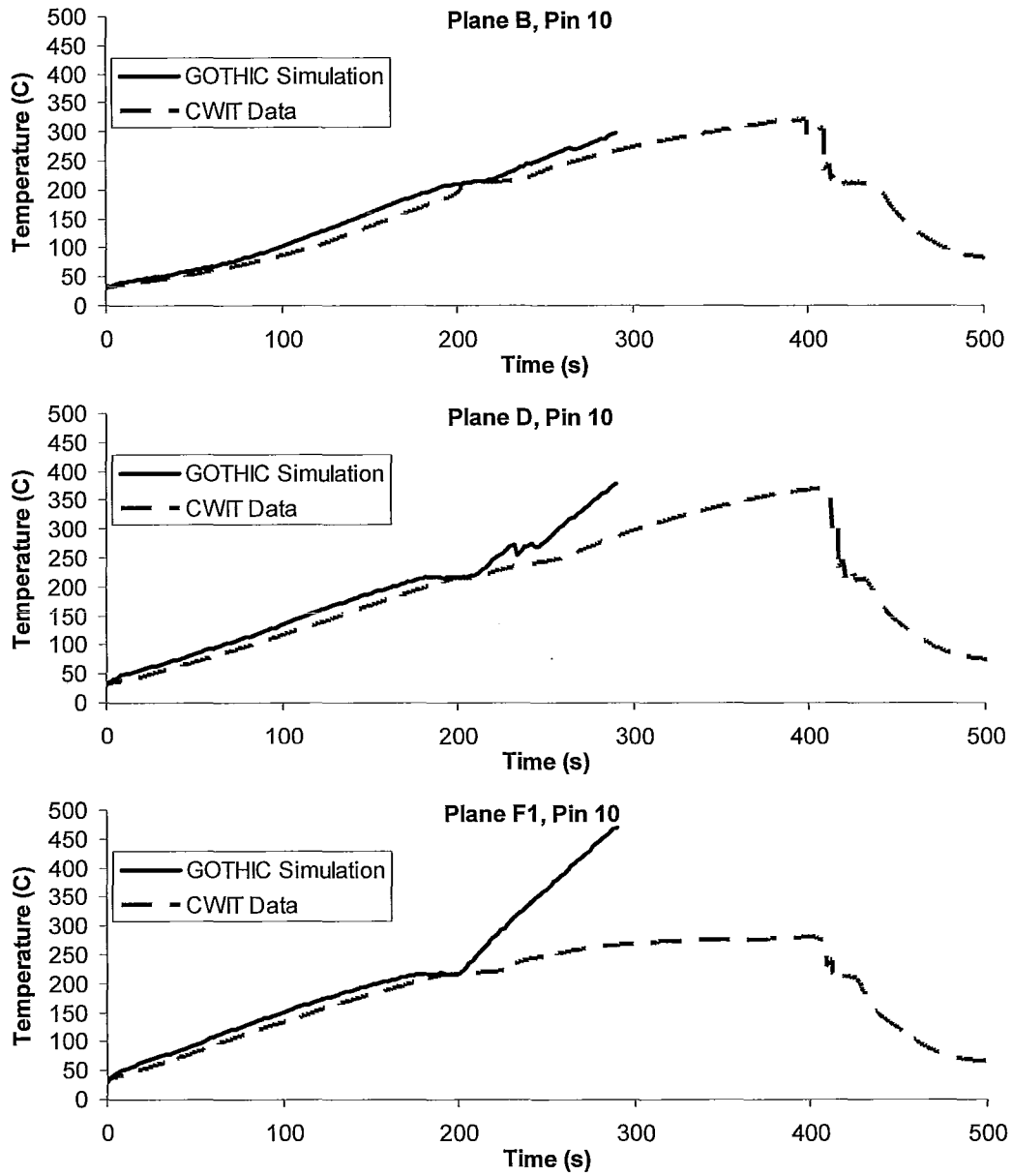


Figure 86 – Predicted and Observed Temperature Transients, Pin 10 – Test #1613

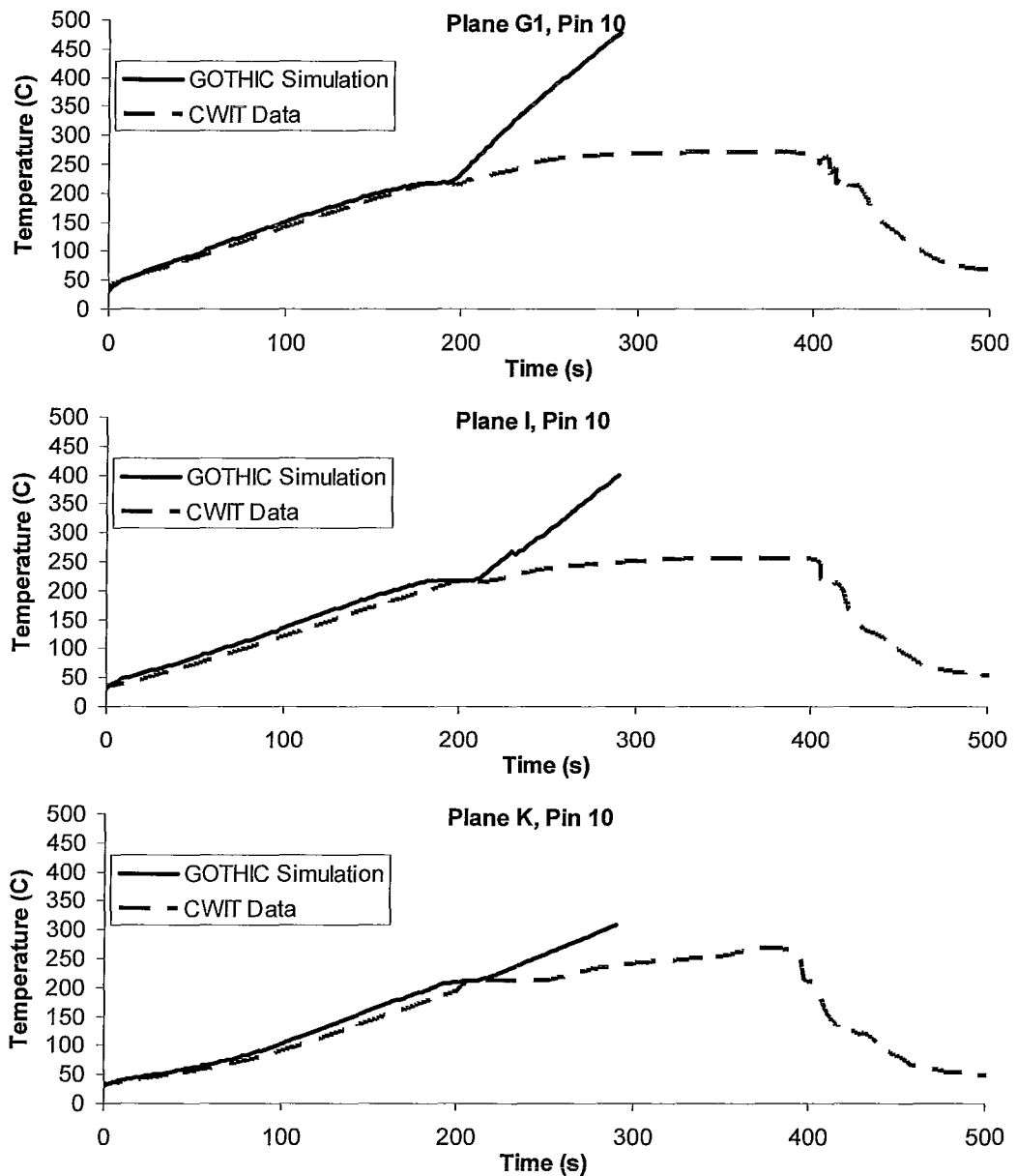


Figure 87 – Predicted and Observed Temperature Transients, Pin 10 – Test #1613

While the single-phase heatup period up to approximately 180 s is modelled reasonably well, the behaviour after saturation is very divergent. As observed in Section 4.2.2, the simulation predicts that after a period spent at saturation, pin 10 does not come into contact with liquid, and increases in

temperature as predicted by an adiabatic approximation (see Table 16). While the temperature of pin 10 does increase after saturation in the CWIT experiment is reached, the slow rate of the increase suggests some interaction with liquid. Although no data from the tests is available to support or refute the hypothesis, it is possible that dispersed water droplets or froth in the upper part of the channel were responsible for the slow temperature increase of pin 10 in the experiment.

A comparison between the pin 24 and pin 37 thermocouple temperature data gathered during CWIT test #1613 and the simulation of that test is shown in Figure 88 - Figure 91.

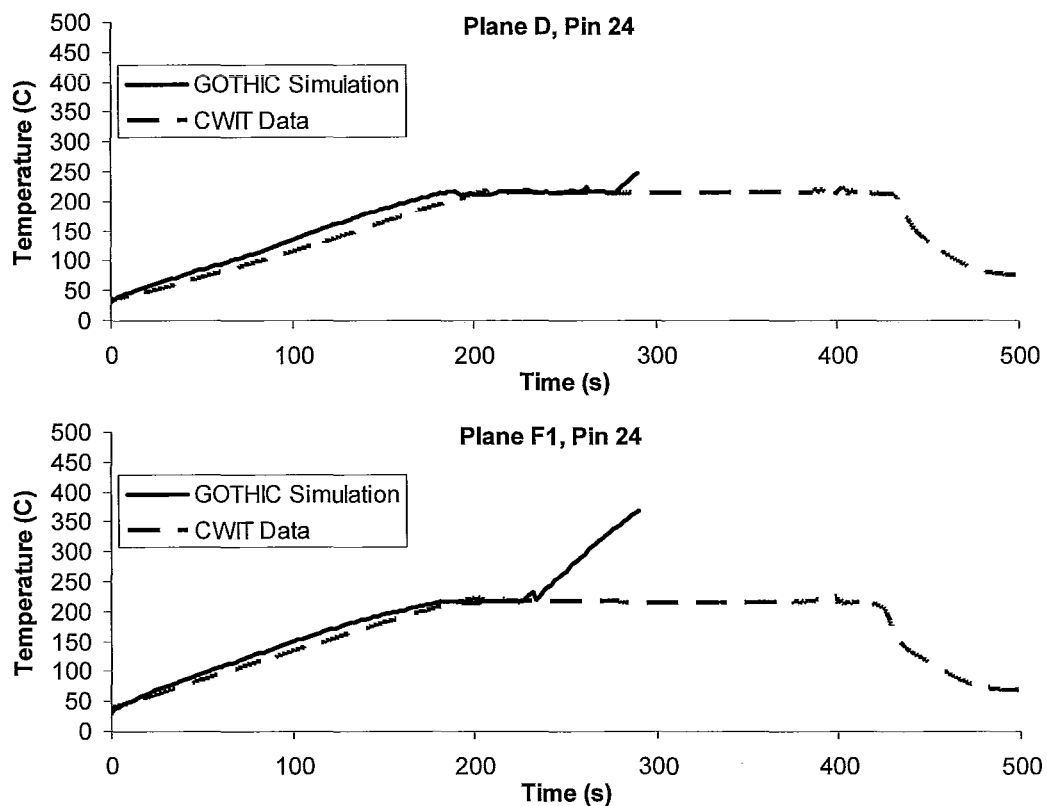


Figure 88 – Predicted and Observed Temperature Transients, Pin 24 – Test #1613

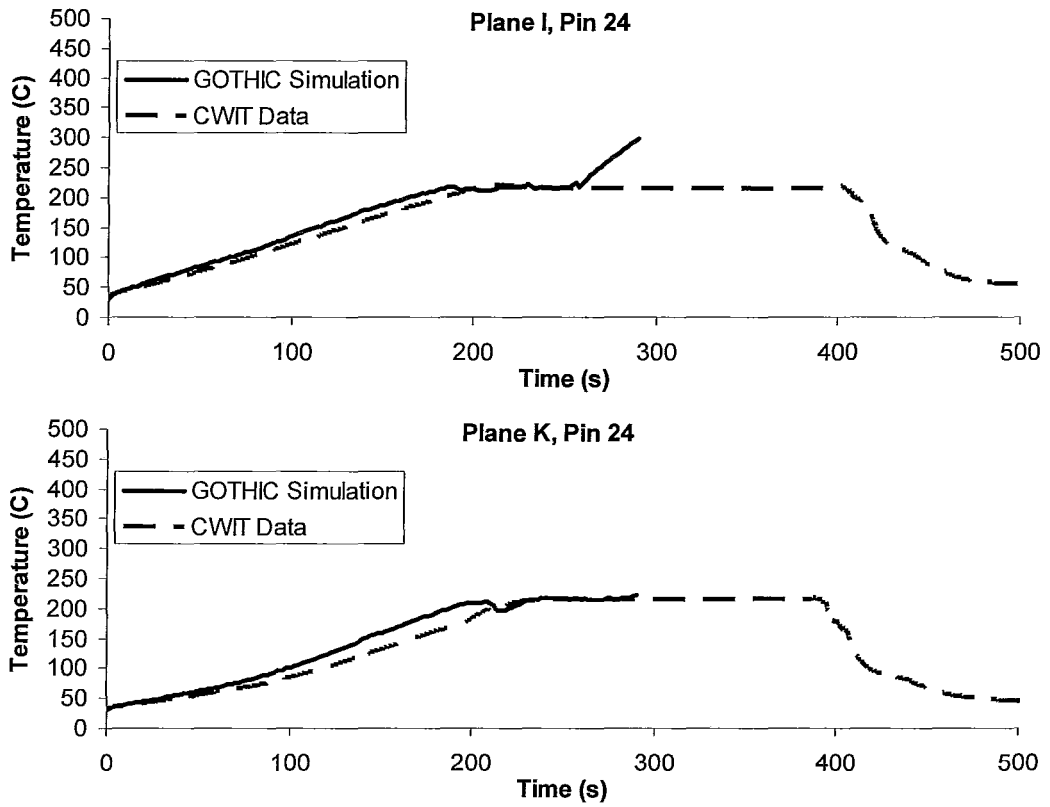


Figure 89 – Predicted and Observed Temperature Transients, Pin 24 – Test #1613

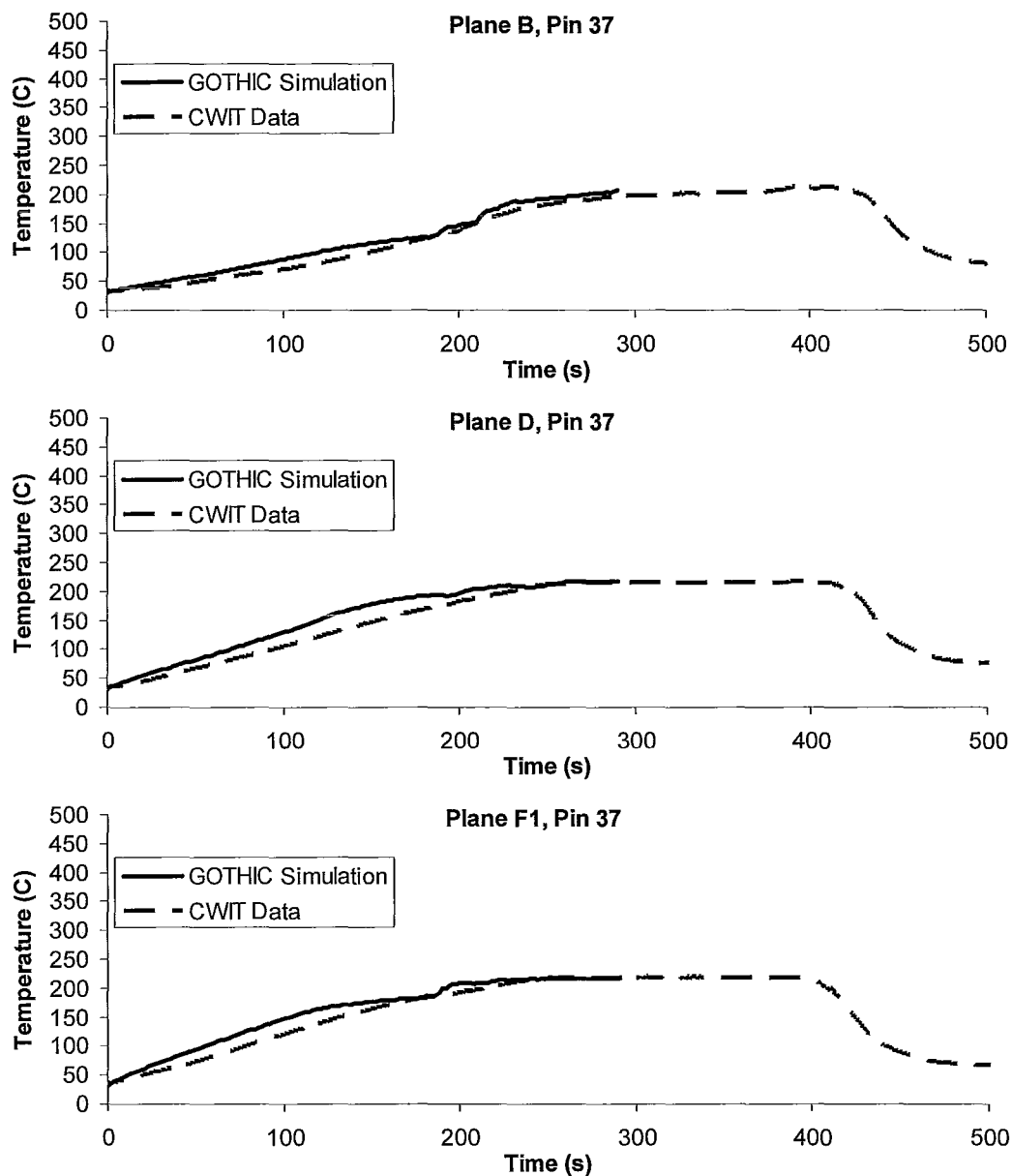


Figure 90 – Predicted and Observed Temperature Transients, Pin 37 – Test #1613

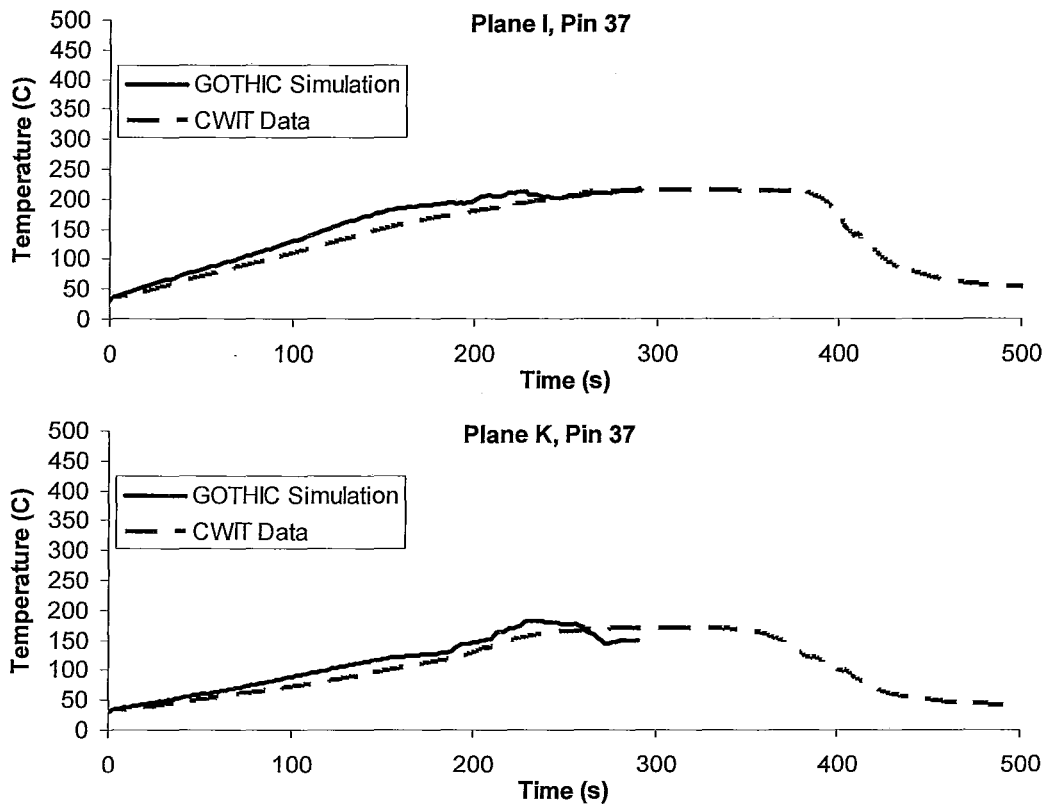


Figure 91 – Predicted and Observed Temperature Transients, Pin 37 – Test #1613

The effect of stratification can be seen in comparing the pin 24 and pin 37 temperature transients; pin 24 is located at a higher elevation and – in the simulation – is exposed to steam in some of the planes. Similarly to the simulated pin 10 temperature transients, the heatup rate of pin 24 approaches the adiabatic approximation (a significant over-prediction), when exposed to steam; however the temperature transients for pin 37 (and pin 24 below and at saturation), predict the experimental results reasonably well.

A comparison between the pressure tube thermocouple temperature data gathered during CWIT test #1613 and the simulation of that test is shown in Figure 92 and Figure 93.

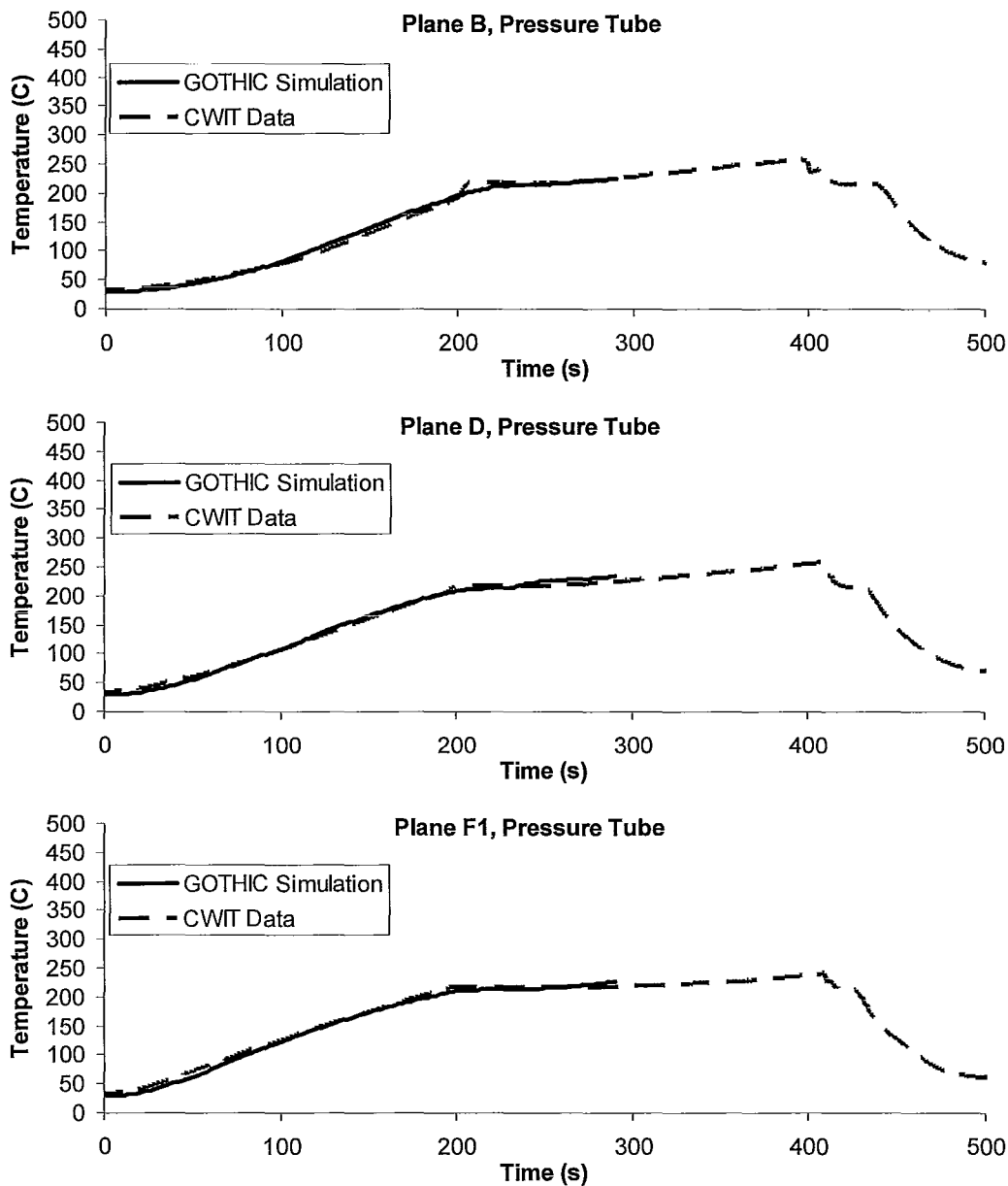


Figure 92 – Predicted and Observed Temperature Transients, Pressure Tube – Test #1613

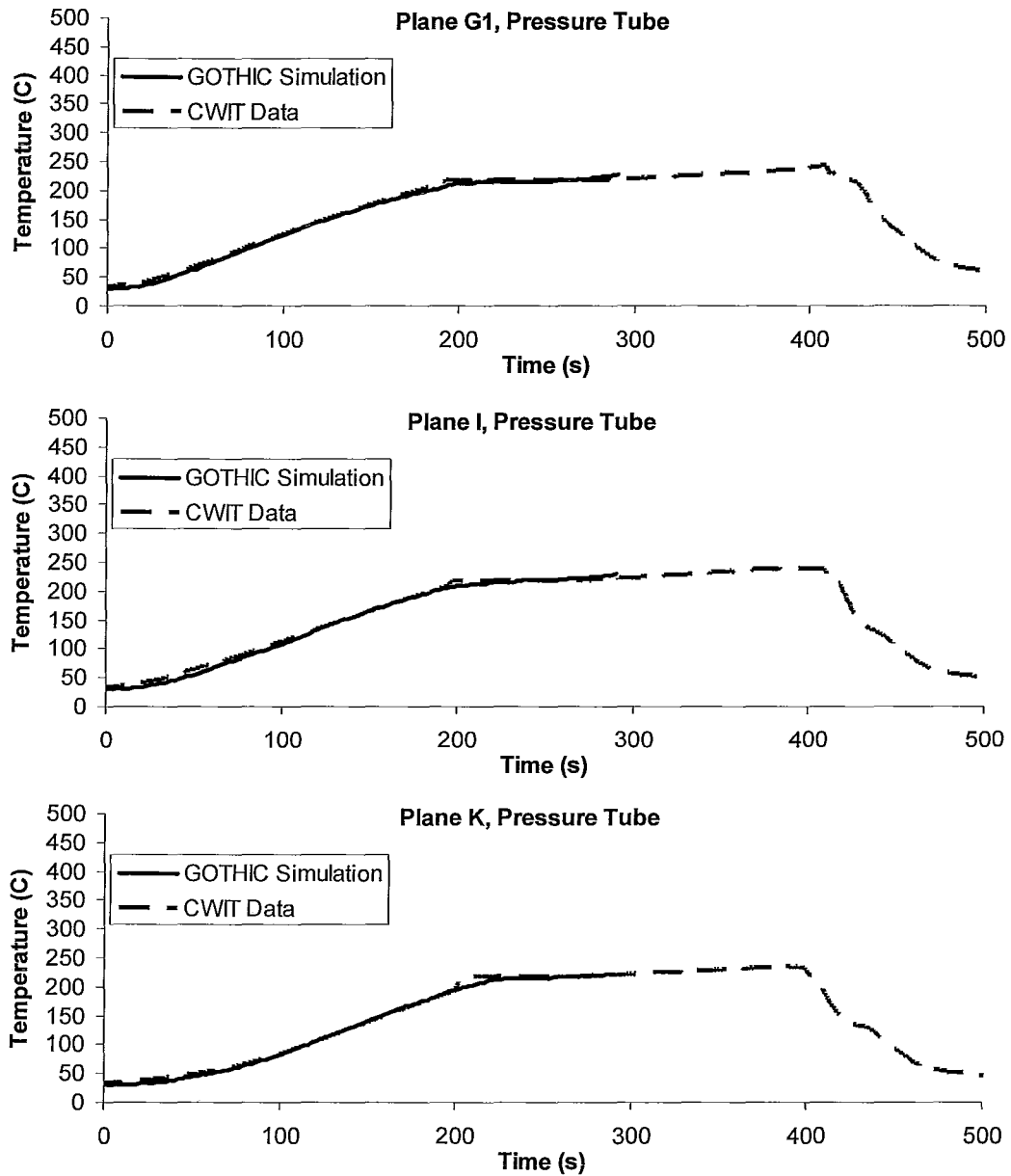


Figure 93 – Predicted and Observed Temperature Transients, Pressure Tube – Test #1613

The pressure tube transient temperature is much more accurately predicted by the simulation than the pin 10 temperature. An overprediction of vapour fraction in the top of the channel, or an absence of dispersed droplets or froth would not be expected to impact this transient to a great degree.

A comparison between the end fitting thermocouple temperature data gathered during CWIT test #1613 and the simulation of that test is shown in Figure 94 and Figure 95.

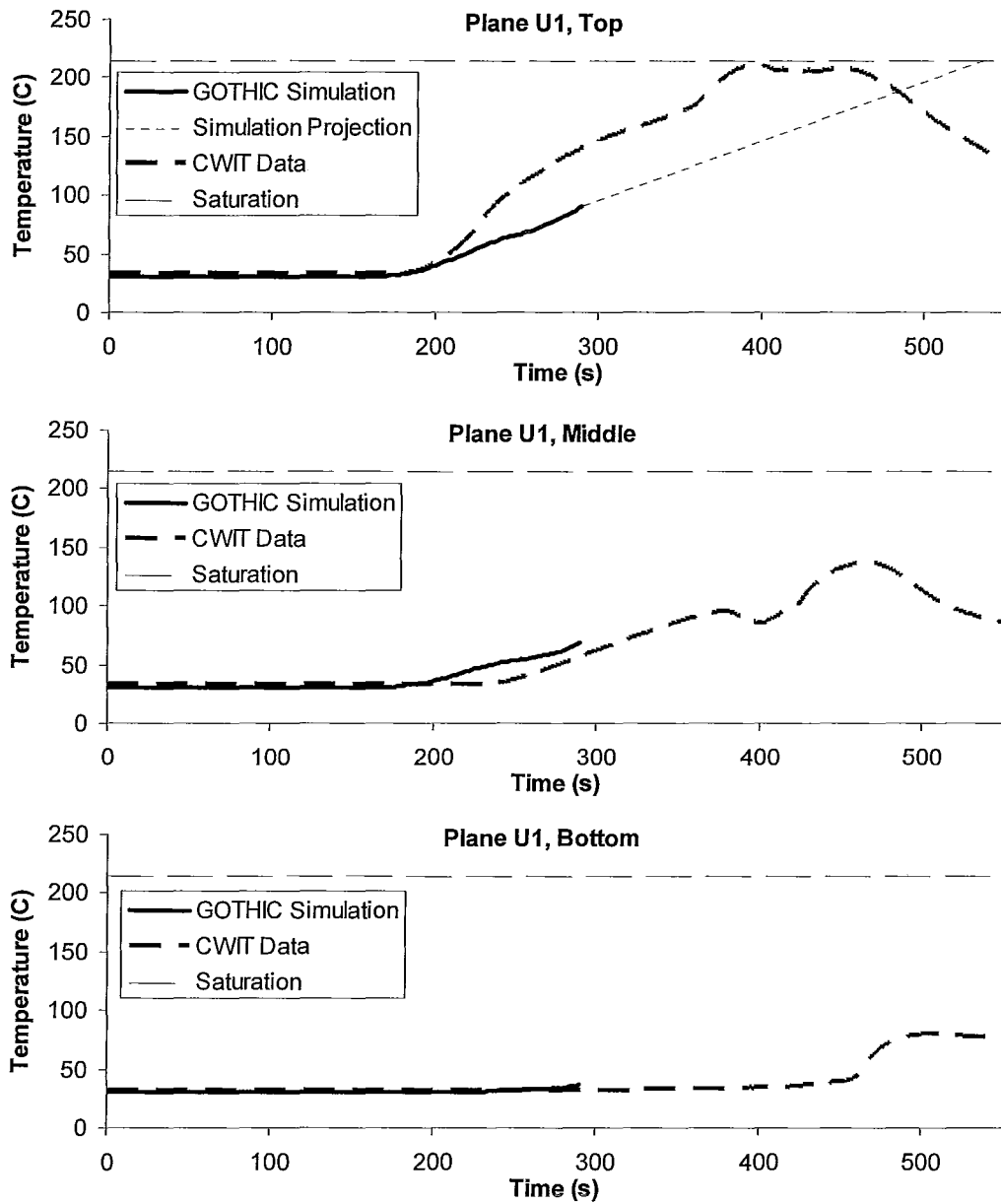


Figure 94 – Predicted and Observed Temperature Transients, Plane U1 – Test #1613⁵⁹

⁵⁹ The projected temperature shown for the top of the end fitting is detailed in Section 4.2.2.3.

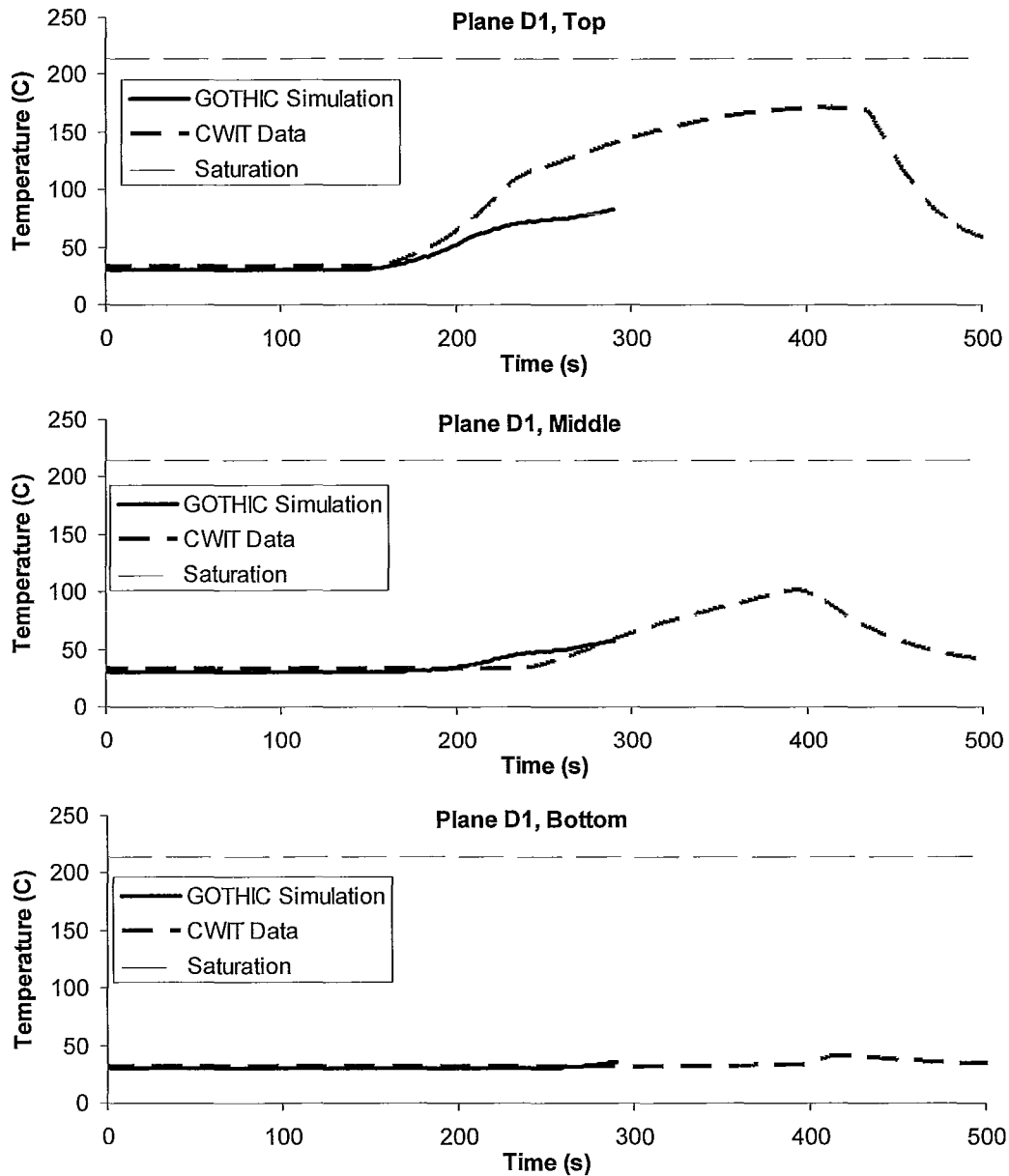


Figure 95 – Predicted and Observed Temperature Transients, Plane D1 – Test #1613

It should be considered a random result due to the symmetry of the channel, however the higher temperature in the upstream end fitting in both cases indicates that the venting of the CWIT test and the impending venting of the simulation are in the same direction. While the temperature at the middle and

bottom thermocouples are predicted reasonably well in both end fittings, there is a significant underprediction of temperature increase in both top thermocouples. This is consistent with the greater pin temperature increase observed in Figure 86 and Figure 87, which indicates that less of the heat produced in the channel is being transported to the end fittings (primarily through reduced steam production), in the simulation than in the experiment. It is also possible that the model is predicting more heat absorption by the dead space than occurred during the experiment; however this cannot be examined due to an absence of thermocouples on the liner tube surrounding the dead space.

The projected temperature transient shown in Figure 94 provides an indication that the simulation will predict a longer venting time than was observed in the CWIT experiments. Notably, this is opposite to the under-prediction of venting times seen in the low power case.

4.5 Asymmetrical Obstruction Model Results

The primary findings of this study are presented in this section, namely, the impact of the introduction of an asymmetrical partial obstruction on maximum pin temperature and venting time during an IBIF cycle.

4.5.1 Low Power

All obstructions are referred to in this study by the percentage area of an empty fuel channel that they block. There are several equivalent and edifying ways of referencing blockages presented in Section 3.4.1 (see Table 10).

The impact of partial asymmetrical obstructions on single-phase venting is presented in Figure 96, and Table 25. The general trend is that the maximum temperature and venting time increase with blockage extent, while remaining well below saturation for all but the most extensive blockages.

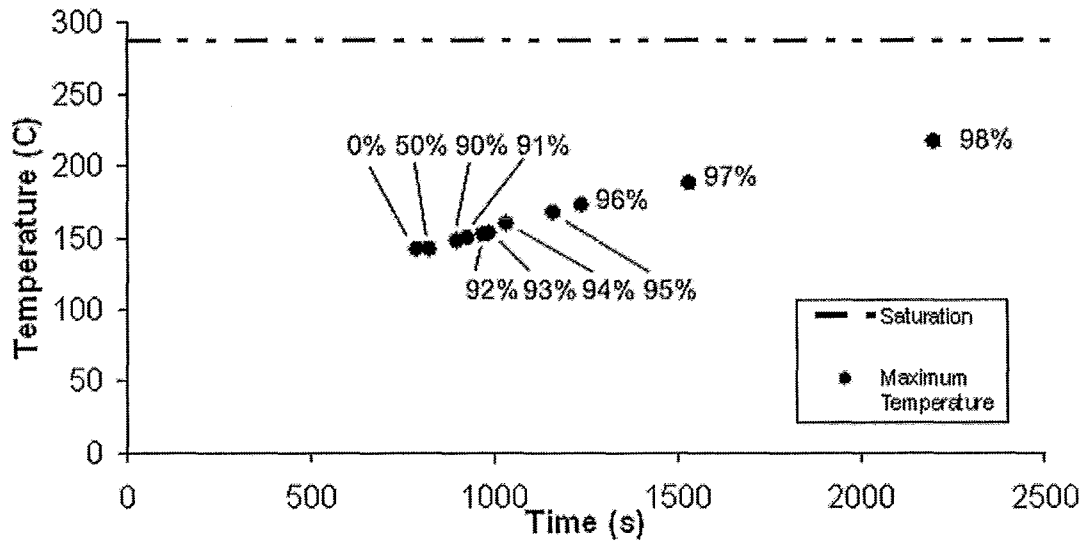


Figure 96 - Maximum Pin Temperatures Reached During IBIF Cycle^{60 61}

Table 25 - Maximum Pin Temperatures Reached During IBIF Cycle

Obstruction Extent (% of Channel Area)	Obstruction Radius (cm)	Percentage of Flow Area ⁶²	Intrinsically Calculated K-Factor of Vol. 25s ⁶³	Time At Which Maximum Temperature Was Reached (s)	Maximum Temperature Reached (C)
0%	0	0.43	2.7	787.00	137.45
50%	3.670	48.29	15.4	819.97	141.44
90%	4.924	76.94	445.4	897.18	147.80
91%	4.951	78.66	746.1	928.18	149.34
92%	4.978	80.71	1415.2	972.08	151.91
93%	5.005	83.10	1339.0	989.43	152.99
94%	5.032	85.52	3242.4	1033.53	158.86
95%	5.059	87.93	9179.7	1163.26	167.40
96%	5.085	90.34	17724.7	1239.03	172.51
97%	5.112	92.76	92696.6	1531.47	187.98

⁶⁰ Temperature taken at plane F1, pin 10.

⁶¹ At 99% and 100% blockages, no venting was simulated, hence no maximum temperature was reached.

⁶² The flow area here is defined as the free area inside the pressure tube which is not occupied by fuel element simulator extensions.

⁶³ Details of the calculation of the k-factors are presented in Appendix A.

98%	5.138	95.17	1007839.6	2201.47	215.73
99%	5.164	97.59	63241589.7	No venting simulated	No venting simulated
100%	5.190	100.00	$\sim\infty$	No venting simulated	No venting simulated

The impact of blockages from 0% - 91% on pin temperature transients and feeder flow rates are considered in greater detail in Figure 97 - Figure 99.

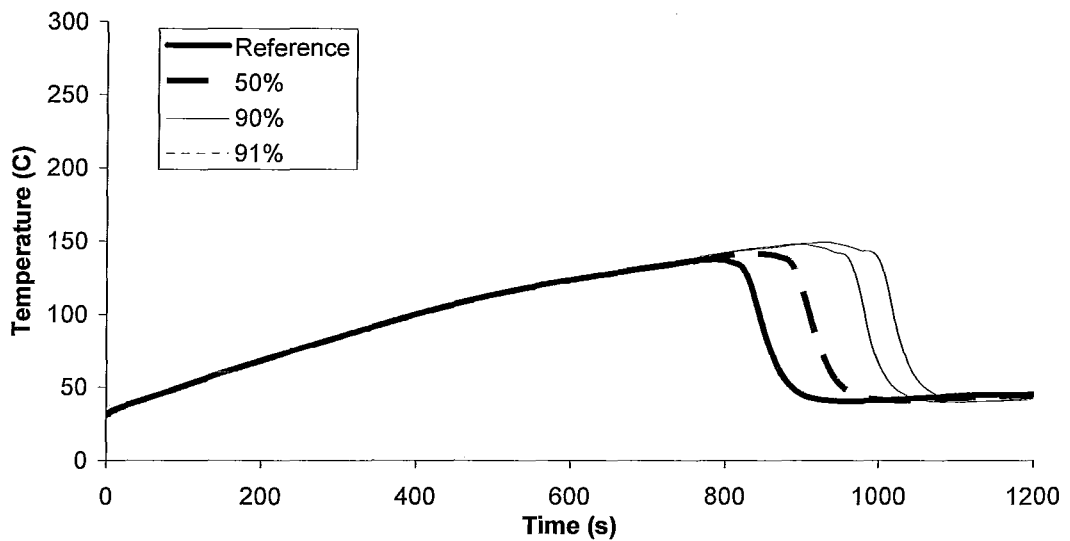


Figure 97 - Temperature Transients For 0% - 91% Obstruction Cases - Pin 10, Plane F1

The increasing maximum pin temperature and delayed vent time with increased obstruction can be seen in Figure 97. As expected, the impact of the obstruction is negligible prior to venting.

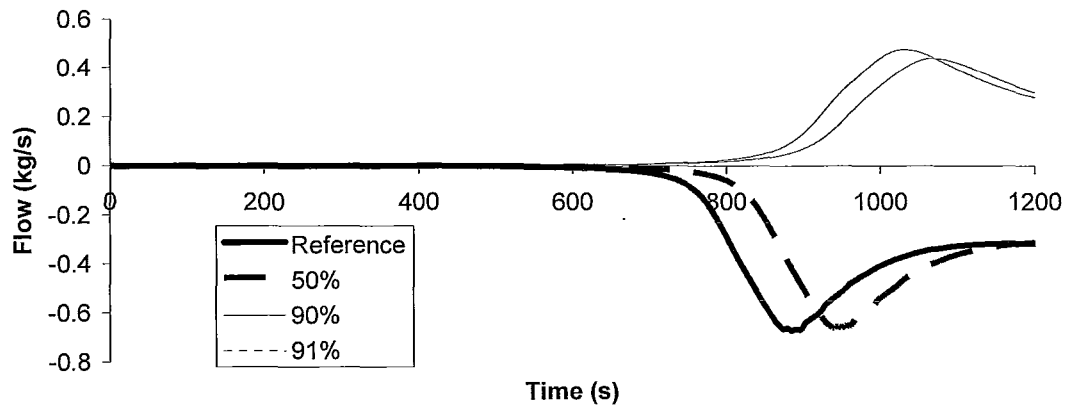


Figure 98 - Fluid Flow Through Downstream Feeder For 0% - 91% Obstruction Cases

The most striking effect of obstruction displayed in Figure 98 is that venting is reversed above 50%, with flow exiting through the downstream feeder. The impact of the higher flow resistances seen with increased obstruction can also be seen in the reduction in maximal flow rates.

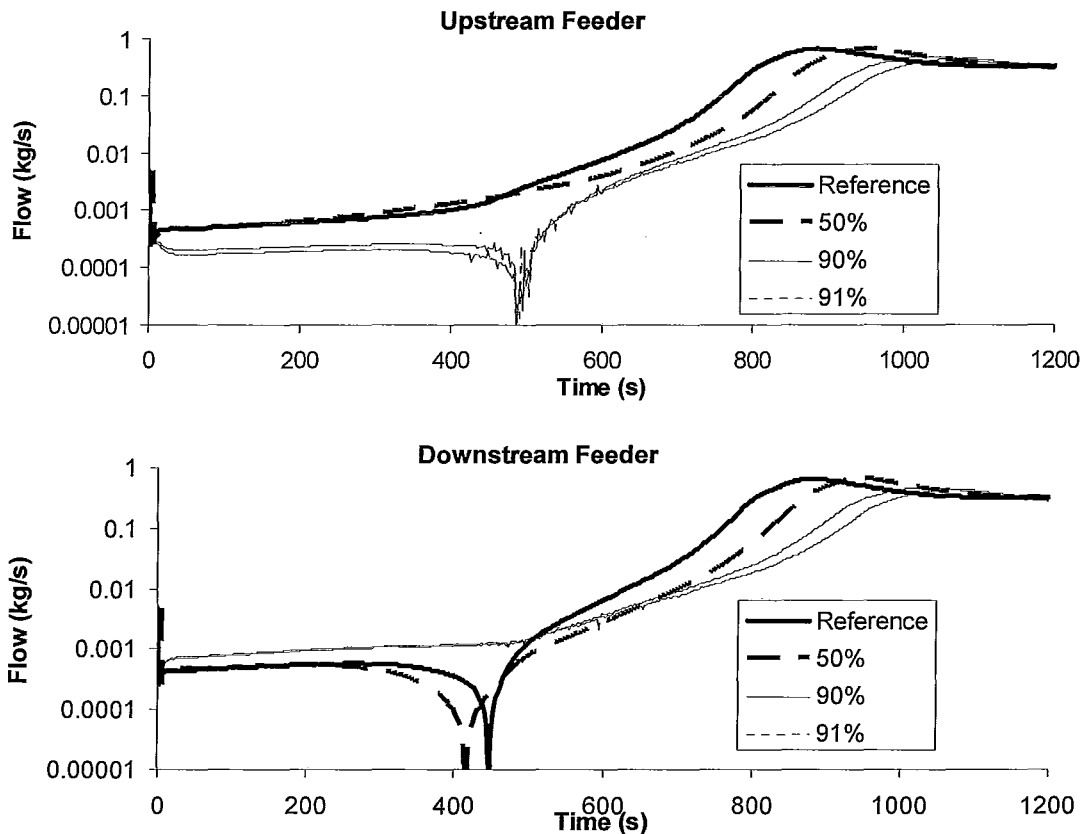


Figure 99 - Logarithmic Plots of Fluid Flow Through Feeders For 0% - 91% Obstruction Cases⁶⁴

The impact of obstructions on flow earlier in the simulations can be seen in Figure 99. Over the first 400 s of the simulation, thermal expansion of the coolant results in some flow out of each of the feeders. Between 400 s and 500 s, the presence of a slightly larger quantity of less dense liquid in the feeders results in a pressure differential across the channel, leading to a flow reversal at the opposite feeder and venting.

While it stands to reason that increased obstruction would reduce the rate of venting, an earlier initiation of venting due to a reduction in symmetry could

⁶⁴ The absolute values of flow rate through the feeders are displayed in this figure.

also be expected. This seems to be the case with the 50% blockage case, but the opposite seems to be true for the 90% and 91% cases.

The impact of blockages from 92% - 95% on pin temperature transients and feeder flow rates are considered in detail in Figure 100 - Figure 102.

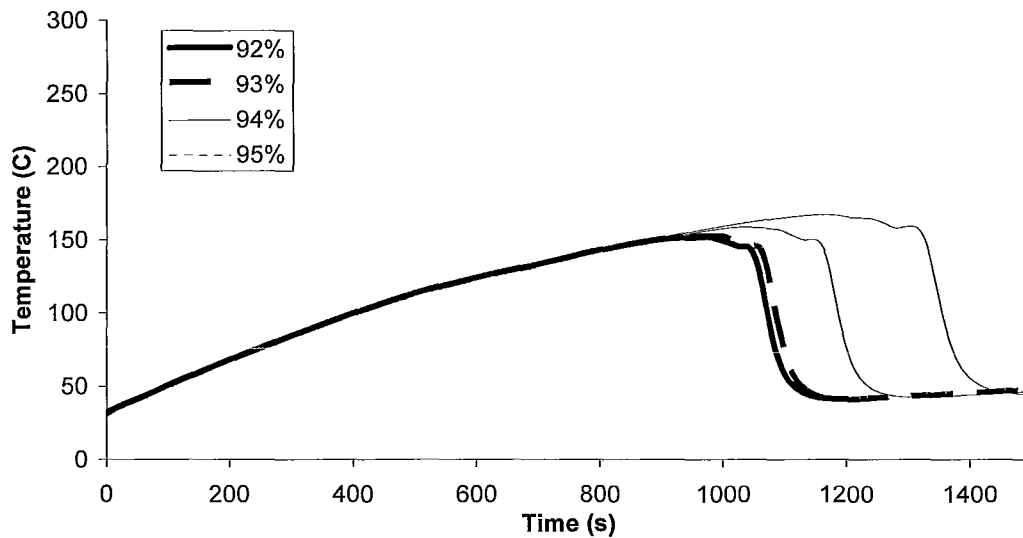


Figure 100 - Temperature Transients For 92% - 95% Obstruction Cases - Pin 10, Plane F1

A continued increase in maximum temperature and venting time with obstruction percentage can be seen in Figure 100.

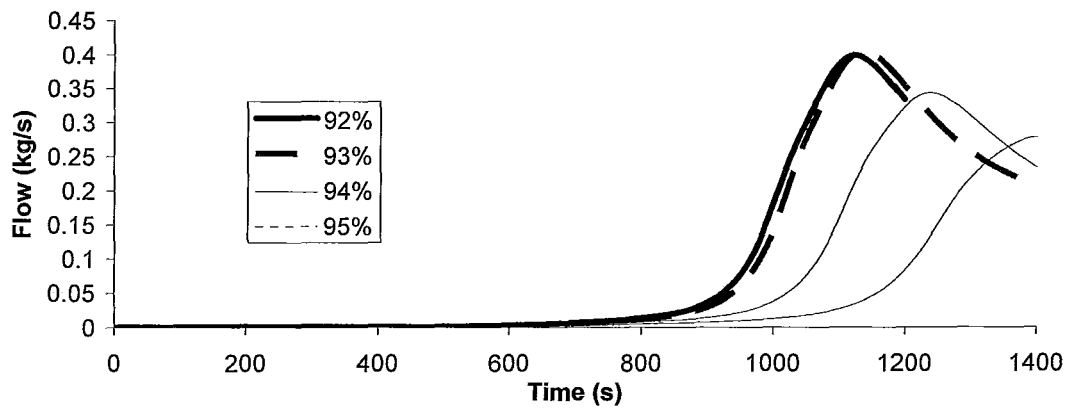


Figure 101 - Fluid Flow Through Downstream Feeder For 92% - 95% Obstruction Cases

The continuation of the trend in venting through the downstream feeder is seen in Figure 101, along with a reduction in flow rates as obstruction flow resistance increases.

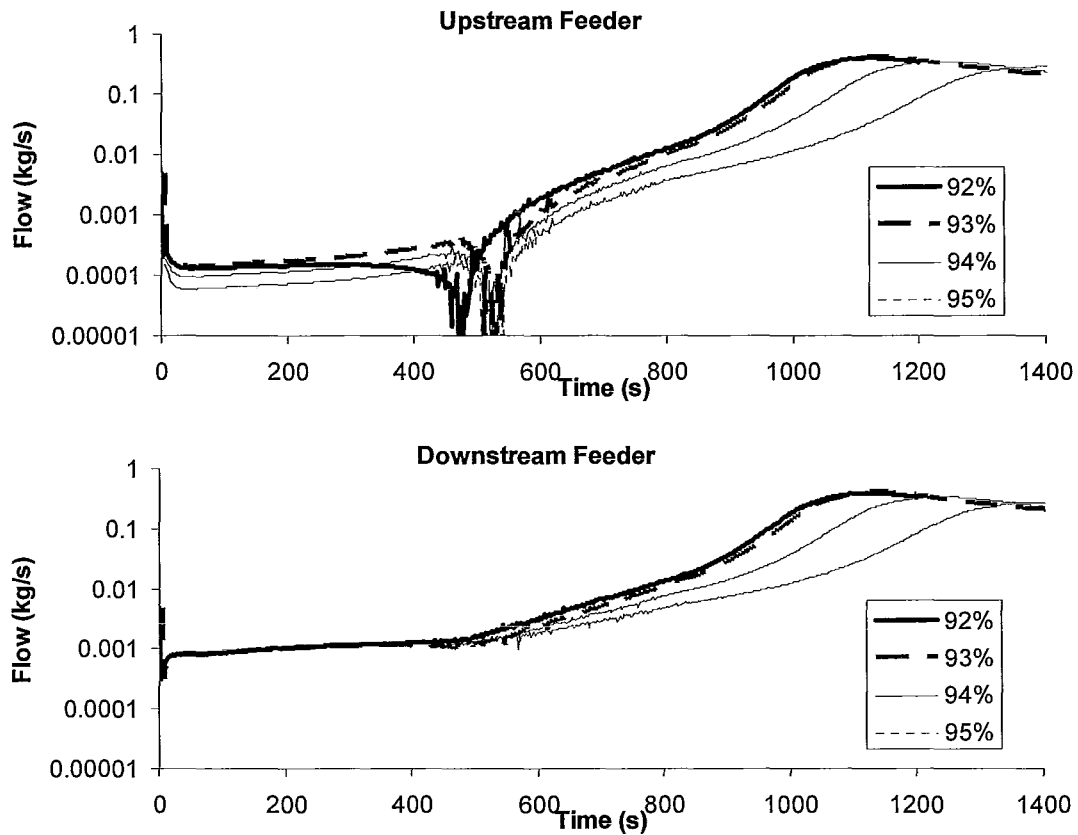


Figure 102 - Logarithmic Plots of Fluid Flow Through Feeders For 92% - 95% Obstruction Cases

While thermal expansion through the downstream feeder appears to be relatively uninfluenced by the blockage extent, a reduction flow through the upstream feeder is apparent in Figure 102. This is consistent with increasing flow resistance in that direction due to obstruction.

The impact of blockages from 96% - 100% on pin temperature transients and feeder flow rates are considered in detail in Figure 103 - Figure 105.

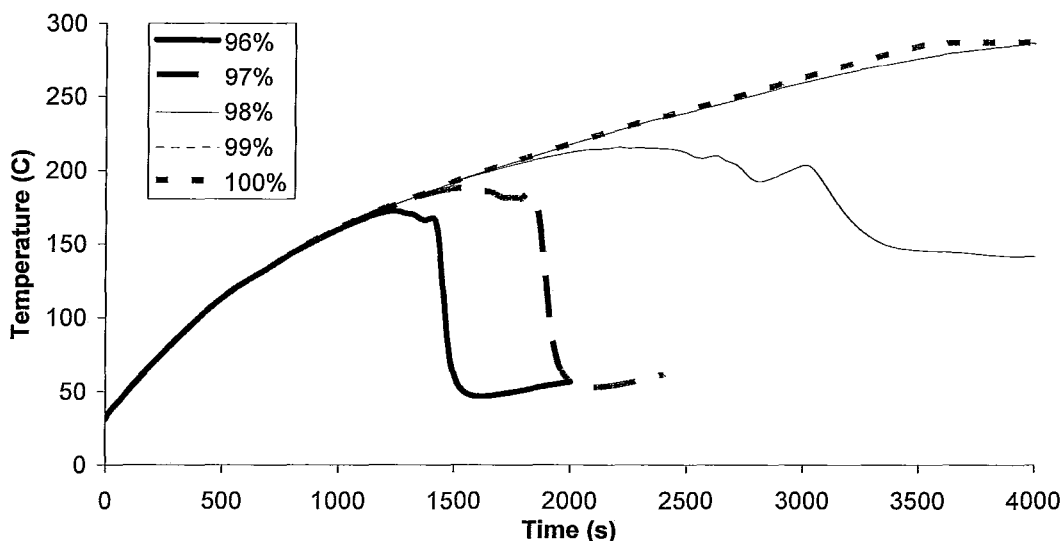


Figure 103 - Temperature Transients For 96% - 100% Obstruction Cases - Pin 10, Plane F1

The impact of blockages is more dramatic at higher percentages of channel area, as seen in Figure 103. The effectiveness of nucleate boiling as a heat transfer mechanism can be seen in the stalled temperature increase of the pin temperature in the 100% blockage case after 3600 s. The increasing impact of convection inside the channel can be seen as the blockage increases as well, with slower venting allowing processes inside the channel to have an impact even after some pressure differential across the channel is established.

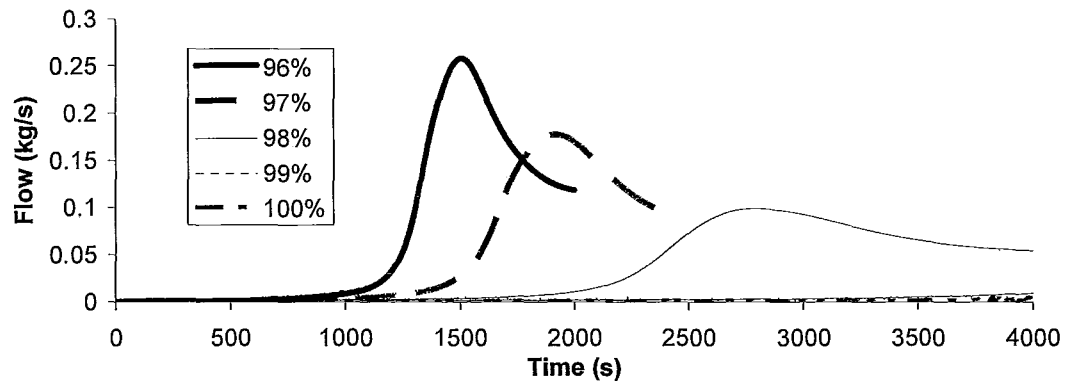


Figure 104 - Fluid Flow Through Downstream Feeder For 96% - 100% Obstruction Cases

The impact of increasing flow resistance is obvious in the reduction of maximum flow rate at higher blockage percentages.

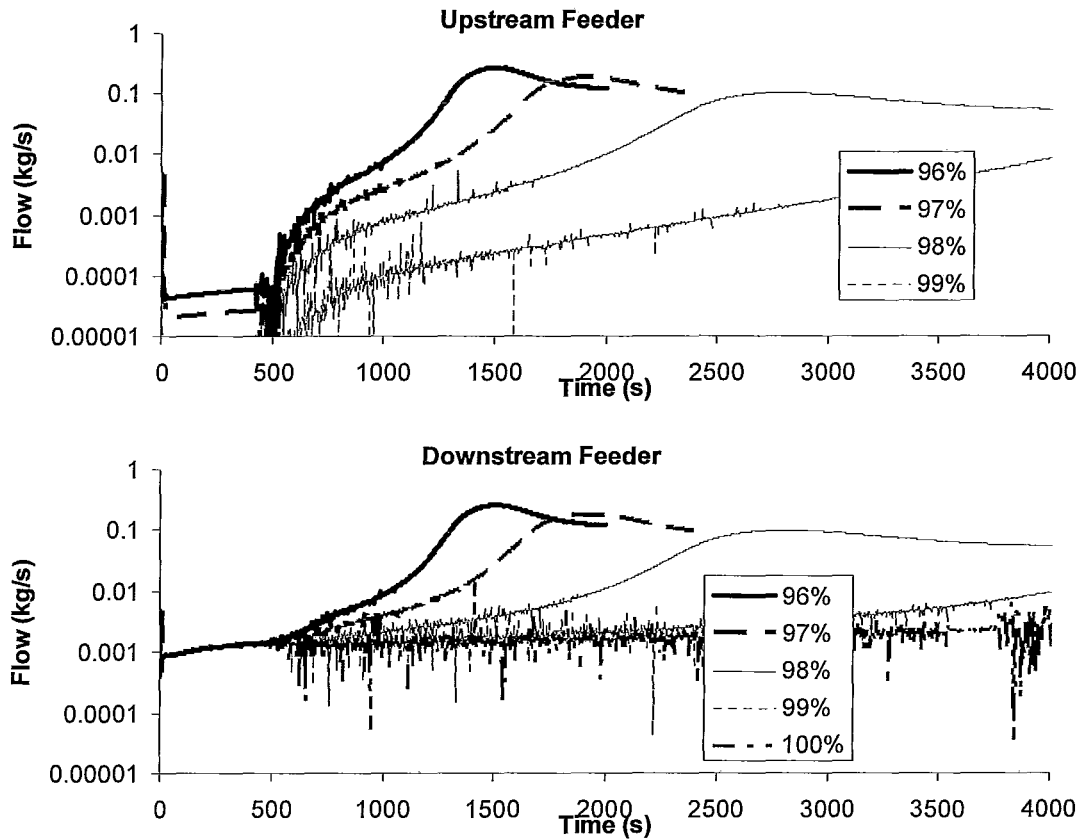


Figure 105 - Logarithmic Plots of Fluid Flow Through Feeders For 96% - 100% Obstruction Cases⁶⁵

As a result of very high flow resistances due to obstructions, extremely slow acceleration of flow through the downstream feeder can be seen in Figure 105. With heated coolant in the end fittings during this period, this effect may not be representative of how the CWIT facility would behave in a similar situation. While GOTHIC is capable of modelling counter-current flow between phases in a lumped volume, such behaviour in a single phase can only be captured with subdivided volumes. It is possible that in an experiment involving a similar blockage and low power, a circulation pattern could be established, with hot

⁶⁵ The flow in the upstream feeder is not included for the 100% obstruction case because it is effectively zero.

liquid rising through the downstream feeder with cold liquid flowing through the same feeder in the opposite direction. Despite this possible shortcoming of the model, it is likely that establishment of the effectiveness of IBIF at nearly complete blockages would not be a priority.

The most probable situations leading to asymmetrical channel obstructions involve the insertion of maintenance tools into the channel. Some tolerance must be allowed for these tools to fit into the channel dependably. Referring to Table 25, in order for a tool to cause a 96% blockage of the channel, a concentrically located tool with a circular cross section would need to have a gap of 1.05 mm between its outer limit and the pressure tube. While determining trends in IBIF behaviour across all obstruction scenarios is a valuable procedure, it is unlikely that a tool fitting more tightly than that leading to a 96% blockage would be utilised during a maintenance procedure.

4.5.2 High Power

As the high power simulations were unable to reach completion in a reasonable timeframe, a definitive comparison of the predicted impact of partial asymmetrical blockages on venting times and maximum pin temperatures cannot be made. Consequently, the insights gained from examination of the results are summarized here, and the results are presented in more complete form in Appendix B.

- The flow oscillations seen in the reference case continues to be evident after the addition of an obstruction.
- The pre-venting flow in the upstream direction that is observed in Section 4.2.2.2 is reversed when an obstruction is added.

- Increasing blockage sizes impacts the ‘depth’ of vapour across the channel, with an increase in vapour particularly evident at the end of the channel adjacent to the obstruction.
- Vapour in the lower portions of the channel exhibits temperatures below saturation. This result is non-physical, and calls for examination of the subcooled boiling model employed by GOTHIC.
- The temperature profiles in the end fitting when blockages are present in the channel appear to be non-physical. Despite stratification of fluid in the end fittings, the end fitting temperature increases more quickly in the lower part of the end fitting than in the upper part. This result is not explained.

5 CONCLUSIONS

5.1 *Single-Phase IBIF*

The benchmarking of the single-phase model was relatively successful, with peak pin temperatures within 4.9 °C of the CWIT experimental results, or 4.4% of the rise from the initial state of the system.

The introduction of an obstruction at one end of the channel resulted in an increase in venting time and peak pin temperature. For the case studied, the peak temperature remained well below saturation for all but the most complete blockages.

5.2 *Two-Phase IBIF*

Complete simulations of two-phase IBIF were not possible as a result of excessive computational demands. While benchmarking of a full IBIF cycle was not possible, a comparison between the simulation results and the data collected during the first stages of the CWIT experiment demonstrated a reasonable prediction of pin heatup prior to the exposure of pins to vapour. After pin exposure, the model predicted an approximately adiabatic heatup rate, while the temperature of the pins in the CWIT experiment increased more slowly – suggesting that some froth or spray was present throughout the steam in the experiment. A projection of the end fitting temperature suggested that the model would over-predict venting time if the simulation were to run to completion.

5.3 *Recommendations for Future Work*

A number of areas of future work are suggested by the information presented here. First, alteration of the end fitting models could be undertaken, to speed two-phase simulations, and resolve the unexplained temperature

distribution observed in the end fitting body. Success in this area would allow for stronger statements regarding the impact of obstructions on two-phase IBIF.

The faster venting time predicted in single-phase IBIF invites a study of flow losses in the channel and end fittings, determining whether losses are sensitive to nodalisation, and the impact of increasing the losses.

An exploration of the boundary between single-phase and two-phase IBIF could be useful. Such a study could establish the degree of blockage below which single phase venting takes place, for a range of channel power levels, pressures, and initial system subcooling.

REFERENCES

- [1] “American National Standard for Decay Heat Power in Light Water Reactors”, ANSI/ANS-5.1-1979, American Nuclear Society, 1979.
- [2] Luxat, J.C., “Thermal-Hydraulic Aspects of Progression to Severe Accidents in CANDU Reactors”, *Nuclear Technology*, v 167, n 1, p 187-210, 2009.
- [3] Lei Q.M.; Gulshani P., “Assessment of Fuel Fitness-for-Service After Standing-Start Process Under Gentilly 2 Shutdown Conditions”, *CNS 19th Annual Conference*, 1998.
- [4] Lei Q.M.; Gulshani P., “Assessment of Fuel Fitness-for-Service After Standing-Start Process Under Gentilly 2 Shutdown Conditions”, *CNS 19th Annual Conference*, 1998.
- [5] C.K. McCallum; J.M. Wedgwood, “Description of the Cold Water Injection Test Facility”, COG File COG-96-255, June 10, 1996.
- [6] Gulshani P., “THERMOSS-II: A Model for Thermohydraulics of CANDU Fuel Channel with Subcooled Stagnant Initial Conditions”, *CNS 9th Annual Conference*, 1988.
- [7] Z.W. Lian, L.N. Carlucci, “Evolution of the ELOCA Code: Mk6 to the Present”, AECL-11920, www.collectionscanada.gc.ca.
- [8] K.M. Lee, M.Y. Ohn, H.S. Lim, J.H. Choi, S.T. Hwang, “Evaluation of gap heat transfer model in ELESTRES for CANDU fuel element under normal operating conditions” *Journal of the Korean Nuclear Society*, v 27, n 3, p 344-357, June 1995.
- [9] Z. Karchev; M. Kawaji, A Study of Intermittent Buoyancy Induced Flow Phenomena in CANDU Fuel Channels, The 13th International Topical Meeting on Nuclear Reactor Thermal Hydraulics (NURETH-13), September 27-October 2, 2009.
- [10] Soedijono P.; Osamusali S.; Tahir A.; Wan P., “A Mechanistic Model to Predict ΔP_{HH} under Two-Phase Natural Circulation Flow and Comparison against Experimental Results in RD-14M”, *CNS 22nd Annual Conference*, 2001.
- [11] Francesco D’Auria, Monica Frogheri, “Use of a Natural Circulation Map for Assessing PWR Performance”, *Nuclear Engineering and Design* 215 (2002) 111 – 126.

- [12] Jalil Jafari, Francesco D’Auria, Hossein Kazeminejad, Hadi Davilu, “Reliability Evaluation of a Natural Circulation System”, *Nuclear Engineering and Design* 224 (2003) 79-104.
- [13] Puustinen, M, “Natural Circulation Flow Behavior at Reduced Inventory in a VVER Geometry”, *Nuclear Engineering and Design*, v 215, n 1-2, p 99-110, June 2002.
- [14] Mousavian, S.K.; D’Auria, F; Salehi, M.A., “Analysis of Natural Circulation Phenomena in VVER-1000”, *Nuclear Engineering and Design*, v 229, n 1, p 25-46, April 2004.
- [15] Chang, D., “Inactive Loop Flow Stagnation During Natural Circulation Cooldown”, *Transactions of the American Nuclear Society*, v 94, p 454-455, *Transactions of the American Nuclear Society 2006 Annual Meeting and Embedded Topical Meeting - Nuclear Fuels and Structural Materials for the Next Generation Nuclear Reactors*, 2006
- [16] Jiang, S.Y.; Zhang, Y.J.; Wu, X.X.; Bo, J.H.; Jia, H.J., “Flow Excursion Phenomenon and its Mechanism in Natural Circulation”, *Nuclear Engineering and Design*, v 202, n 1, p 17-26, November 1, 2000a.
- [17] Frank Rahn, GOTHIC Containment Analysis Package Technical Manual – Version 7.2b(QA), March 2009, EPRI, NAI-8907-06 Rev. 17.
- [18] Frank Rahn, GOTHIC Containment Analysis Package User Manual – Version 7.2b(QA), March 2009, EPRI, NAI-8907-02 Rev. 17.
- [19] R.P. Ofstun, S.W. Claybrook, T.L. George, “Modeling of the FLECHT SEASET Natural Circulation Tests with GOTHIC”, Tenth International RETRAN Meeting, Jackson, Wyoming, October 14-17, 2001.
- [20] Dittus, FW. And L.M.K. Boelter, University of California, *Pub. Eng.*, vol. 2, p. 443, 1930.
- [21] McAdams, W.H., “Heat Transmission”, Third Edition, McGraw-Hill Book Company, New York, NY, p. 172, 1954.
- [22] Chen, JC, “A Correlation for Boiling Heat Transfer to Saturated Fluids in Convective Flow”, ASME 63-HT-34, American Society of Mechanical Engineers, 1963.

- [23] Uchida, H., et al., “Evaluation of Post-Incident Cooling Systems of Light Water Power Reactors”, U. of Tokyo, International Conference on Peaceful Uses of Atomic Energy, New York, 1965.
- [24] Gido, R.G., and A. Koestel, “Containment Condensing Heat Transfer”, Second International Topical Meeting on Nuclear Reactor Thermal-Hydraulics, Santa Barbara, CA, January, 1983.
- [25] J.R. Buell, “Analysis of CANDU End-Shield/Moderator Heat-Transfer Experiments”, COG-98-145, 1998.
- [26] Tom George, “GOTHIC Web Seminar #8 – Intrinsic Losses In Subdivided Modelling”, Numerical Applications, Inc., June 3, 2008.
- [27] R.I. Lindsay, “Pickering Generating Station Design Manual: Coolant Shield Plugs”, 44-31130, AECL, August 1971, Page A6-2.
- [28] P.C. Watson, “Memorandum: Partially Filled Pressure Tube Operating Temperature Limits”, Ontario Hydro, N-31110.032, December 13, 1982.
- [28] “Source book on industrial alloy and engineering data.”, American Society for Metals, 1978.

APPENDIX A GOTHIC MODEL DEVELOPMENT

Appendix A.1 Materials Modelling

The values used in defining Inconel-600, Zircalloy 2.5% Niobium, Type-403 Stainless Steel, and the water substitute used in the end fitting deadspace can be found in Table 26 - Material Data – Inconel-600 [28] Table 26, Table 27, Table 28, and Table 29.

Table 26 - Material Data – Inconel-600 [28]

Temperature (C)	Density (kg/m ³)	Conductivity (J/s-m-C)	Specific Heat (kJ/kg-C)
21	8430	14.8	0.444
93	8430	15.7	0.444
204	8430	17.4	0.444
316	8430	19.2	0.444
427	8430	20.9	0.444
927 ⁶⁶	8430	20.9	0.444

Table 27 - Material Data – Zircalloy-2.5% Niobium

Temperature (C)	Density (kg/m ³)	Conductivity (J/s-m-C)	Specific Heat (kJ/kg-C)
0	6570	12.7	0.281
27	6570	12.7	0.281
127	6570	14	0.302
367	6570	17	0.337
967 ⁶⁷	6570	17	0.337

⁶⁶In order to prevent numerical instability during the solution process, the temperature range was extended to very high temperatures, with properties taken to be constant.

⁶⁷(see above)

Table 28 - Material Data – Type-403 Stainless Steel [29]

Temperature (C)	Density (kg/m ³)	Conductivity (J/s-m-C)	Specific Heat (kJ/kg-C)
0	7750	24.9	0.4605
900 ⁶⁸	24.9	12.7	0.4605

Table 29 - Material Data – Water Substitute

Temperature (C)	Density (kg/m ³)	Conductivity (J/s-m-C)	Specific Heat (kJ/kg-C)
0	2000	0.58	4.224
25	2000	0.58	4.194
50	2000	0.58	4.182
75	2000	0.58	4.190
100	2000	0.58	4.216
125	2000	0.58	4.261
925 ⁶⁹	2000	0.58	4.261

Appendix A.2 Fuel Element Simulators**Table 30 – Pin Location in Channel Control Volumes**

	Y coordinate (m)	Z coordinate (m)
pin 1	0.05200	0.05200
pin 2	0.05945	0.06485
pin 3	0.06690	0.05195
pin 4	0.05945	0.03904
pin 5	0.04455	0.03904
pin 6	0.03710	0.05195
pin 7	0.04455	0.06485
pin 8	0.05945	0.07976
pin 9	0.07236	0.07231
pin 10	0.07982	0.05940
pin 11	0.07982	0.04449
pin 12	0.07236	0.03158
pin 13	0.05945	0.02413

⁶⁸ (see above)⁶⁹ (see above)

pin 14	0.04455	0.02413
pin 15	0.03164	0.03158
pin 16	0.02418	0.04449
pin 17	0.02418	0.05940
pin 18	0.03164	0.07231
pin 19	0.04455	0.07976
pin 20	0.05951	0.09454
pin 21	0.07363	0.08940
pin 22	0.08513	0.07975
pin 23	0.09264	0.06674
pin 24	0.09525	0.05195
pin 25	0.09264	0.03715
pin 26	0.08513	0.02414
pin 27	0.07363	0.01449
pin 28	0.05951	0.00935
pin 29	0.04449	0.00935
pin 30	0.03038	0.01449
pin 31	0.01887	0.02414
pin 32	0.01136	0.03715
pin 33	0.00875	0.05195
pin 34	0.01136	0.06674
pin 35	0.01887	0.07975
pin 36	0.03038	0.08940
pin 37	0.04449	0.09454

Table 31 – High Power Case FES Volumetric Power (kW/m³)

	O-ring	M-ring	I-ring	centre
vol 1	1321.755	1070.622	951.6639	898.7937
vol 2	2299.804	1862.841	1655.859	1563.867
vol 3	3243.384	2627.141	2335.236	2205.501
vol 4	4138.354	3352.066	2979.615	2814.081
vol 5	4971.3	4026.753	3579.336	3380.484
vol 6	5729.739	4641.089	4125.412	3896.223
vol 7	6402.304	5185.866	4609.659	4353.566
vol 8	6978.914	5652.92	5024.818	4745.661
vol 9	7450.927	6035.251	5364.668	5066.631
vol 10	7811.27	6327.129	5624.115	5311.664
vol 11	8054.542	6524.179	5799.27	5477.088
vol 12	8177.096	6623.448	5887.509	5560.425
vol 13	8177.096	6623.448	5887.509	5560.425
vol 14	8054.542	6524.179	5799.27	5477.088
vol 15	7811.27	6327.129	5624.115	5311.664
vol 16	7450.927	6035.251	5364.668	5066.631
vol 17	6978.914	5652.92	5024.818	4745.661
vol 18	6402.304	5185.866	4609.659	4353.566
vol 19	5729.739	4641.089	4125.412	3896.223

vol 20	4971.3	4026.753	3579.336	3380.484
vol 21	4138.354	3352.066	2979.615	2814.081
vol 22	3243.384	2627.141	2335.236	2205.501
vol 23	2299.804	1862.841	1655.859	1563.867
vol 24	1321.755	1070.622	951.6639	898.7937

Table 32 – Low Power Case FES Volumetric Power (kW/m³)

	O-ring	M-ring	I-ring	centre
vol 1	201.7947	163.4537	145.2922	137.2204
vol 2	351.1151	284.4032	252.8029	238.7583
vol 3	495.1731	401.0902	356.5246	336.7177
vol 4	631.8097	511.7659	454.903	429.6306
vol 5	758.9771	614.7715	546.4635	516.1044
vol 6	874.7693	708.5631	629.8339	594.8431
vol 7	977.4509	791.7353	703.7647	664.6666
vol 8	1065.483	863.0412	767.1478	724.5284
vol 9	1137.546	921.4124	819.0332	773.5314
vol 10	1192.56	965.9739	858.6435	810.941
vol 11	1229.701	996.0578	885.3848	836.1967
vol 12	1248.412	1011.213	898.8564	848.9199
vol 13	1248.412	1011.213	898.8564	848.9199
vol 14	1229.701	996.0578	885.3848	836.1967
vol 15	1192.56	965.9739	858.6435	810.941
vol 16	1137.546	921.4124	819.0332	773.5314
vol 17	1065.483	863.0412	767.1478	724.5284
vol 18	977.4509	791.7353	703.7647	664.6666
vol 19	874.7693	708.5631	629.8339	594.8431
vol 20	758.9771	614.7715	546.4635	516.1044
vol 21	631.8097	511.7659	454.903	429.6306
vol 22	495.1731	401.0902	356.5246	336.7177
vol 23	351.1151	284.4032	252.8029	238.7583
vol 24	201.7947	163.4537	145.2922	137.2204

Appendix A.3 Initial Conditions

As the CWIT tests were performed from a cold start, 30 C is the initial temperature of all components of the model with the exception of the heated sections of the fuel element simulators. The heaters are started at 31 C as the effect on the model is negligible and this avoids some possible numerical issues at the first timestep. Reasonable values for the initial pressure in each volume are

also selected based on elevation relative to the header. These values are detailed in Table 33 and Table 34.

Table 33 – Initial Pressure in Each Volume – Low Power Case (feeder volumes in order from closest to end fitting to path to boundary condition)

Volume(s)	Initial Pressure (kPa)
Pressure Tube, Blockage Volumes, End Fittings	7100
Feeder Volume 1	7099
Feeder Volume 2	7098
Feeder Volume 3	7098
Feeder Volume 4	7041
Feeder Volume 5	7040
Feeder Volume 6	7011
Feeder Volume 7	7010
Feeder Volume 8	7003
Feeder Volume 9	7002

Table 34 – Initial Pressure in Each Volume – High Power Case (feeder volumes in order from closest to end fitting to path to boundary condition)

Volume(s)	Initial Pressure (kPa)
Pressure Tube, Blockage Volumes, End Fittings	2100
Feeder Volume 1	2099
Feeder Volume 2	2098
Feeder Volume 3	2098
Feeder Volume 4	2041
Feeder Volume 5	2040
Feeder Volume 6	2011
Feeder Volume 7	2010
Feeder Volume 8	2003
Feeder Volume 9	2002

Appendix A.3 Dead Space Conductor Component Details

Liner Tube

Inner radius: .05118 m

Outer radius: .05667 m

Liner tube mass:

$$\pi * (.05667[m]^2 - .05118[m]^2) * 1.63195[m] * 7750[kg / m] = 23.5[kg] \quad (23)$$

Water

Water volume ~ 8.5L [l] = 8.5 kg

Heater Extensions

The total volume of the heater extensions is scaled to the length of the end fitting.

$$.00497 \text{ m}^3 * 1.9304 \text{ m} / 2.3622 \text{ m} = .00497 \text{ m}^3 \quad (24)$$

End Fitting Assembly in Dead Space

The values used to calculate the total end fitting mass in Section 3.3.2.7 are used here to calculate the end fitting mass in the deadspace.

$$(.08457[m]^2 - .0562[m]^2) * \pi * .37465[m] = .0047[m^3] \quad (25)$$

Dead Space Conductor Composition

Liner Tube

The modelling of the liner tube is based directly on its real geometry in the CWIT rig.

Inner radius: .05118 m

Outer radius: .05667 m

Water Substitute

The dead space in the CWIT rig has a larger volume than the conductor in the model. To allow for this, the density of the water substitute is taken to be 2000 kg/m³.

Water substitute volume:

$$\frac{8.5[\text{kg}]}{2000[\text{kg} / \text{m}^3]} = .00425[\text{m}^3] \quad (26)$$

Outer radius: .05118 m

Inner radius:

$$\left(.05118[\text{m}]^2 - \frac{.00425[\text{m}^3]}{1.63195[\text{m}] * \pi} \right)^{1/2} = .0423[\text{m}] \quad (27)$$

Aside from density, the properties of the water substitute used are those of the GOTHIC technical manual [17]. As stated above, the density of the water substitute is taken to be 2000 kg/m³ at all temperatures.

Heater Extensions

Outer radius: .0423 m

Inner radius:

$$\left(.0423[m]^2 - \frac{.004058[m^3]}{1.63195[m]*\pi} \right)^{1/2} = .0316[m] \quad (28)$$

End Fitting Assembly in Dead Space

Outer radius: .0316 m

Inner radius:

$$\left(.0316[m]^2 - \frac{.0047[m^3]}{1.63195[m]*\pi} \right)^{1/2} = .00907[m] \quad (29)$$

Appendix A.4 Feeder Data

Table 35 – Minor Loss Coefficients for Feeder Components

Component	Examples / Feeder	Forward Coefficient	Backward Coefficient
90 deg, 2.5", SR	2	0.3	0.3
90 deg, 3", SR	1	0.3	0.3
90 deg, 2", LR	2	0.2	0.2
90 deg, 3", LR	4	0.2	0.2
45 deg, 3", LR	1	0.2	0.2
reducer 2.5x2	1	0.0625	0.04
reducer 3x2	1	0.25	0.111

Table 36 – Feeder Flow Path Geometry (in order from closest to end fitting to path to boundary condition)

	End A Elevation (m)	End A Height (m)	End B Elevation (m)	End B Height (m)
1	0.187093148	0.059	0.187093148	0.059
2	0.245993148	0.0001	0.246093148	0.0001
3	5.911893148	0.0492	5.911893148	0.0492
4	5.973243148	0.0001	5.973343148	0.0001
5	8.946643148	0.0737	8.946643148	0.0737
6	9.020243148	0.0001	9.020343148	0.0001
7	9.708643148	0.0737	9.708643148	0.0737

8	9.782243148	0.0001	9.782343148	0.0001
9	10.00328835	0.0001	10.00338835	0.0001

Table 37 – Feeder Flow Path Information A (in order from closest to end fitting to path to boundary condition)

	Flow Area (m²)	Hydraulic Diameter (m)	Inertia Length (m)	Friction Length (m)
1	0.00273397	0.059	1.010091217	1.010091217
2	0.00190117	0.0492	3.801	3.801
3	0.00190117	0.0492	4.3405	4.3405
4	0.00426604	0.0737	3.0065	3.0065
5	0.00426604	0.0737	2.178	2.178
6	0.00426604	0.0737	1.0355	1.0355
7	0.00426604	0.0737	2.1705	2.1705
8	0.00426604	0.0737	1.9195	1.9195
9	0.00426604	0.0737	0.26	0.13

Table 38 – Feeder Flow Path Information B (in order from closest to end fitting to path to boundary condition)

	Relative Roughness	Forward Loss Coefficient	Reverse Loss Coefficient
1	0.000129153	0.8625	0.84
2	0.000154878	0.2	0.2
3	0.000154878	0.311	0.45
4	0.000103392	0.2	0.2
5	0.000103392	0.4	0.4
6	0.000103392	0.2	0.2
7	0.000103392	0.4	0.4
8	0.000103392	0.3	0.3
9	0.000103392	0.2	0.2

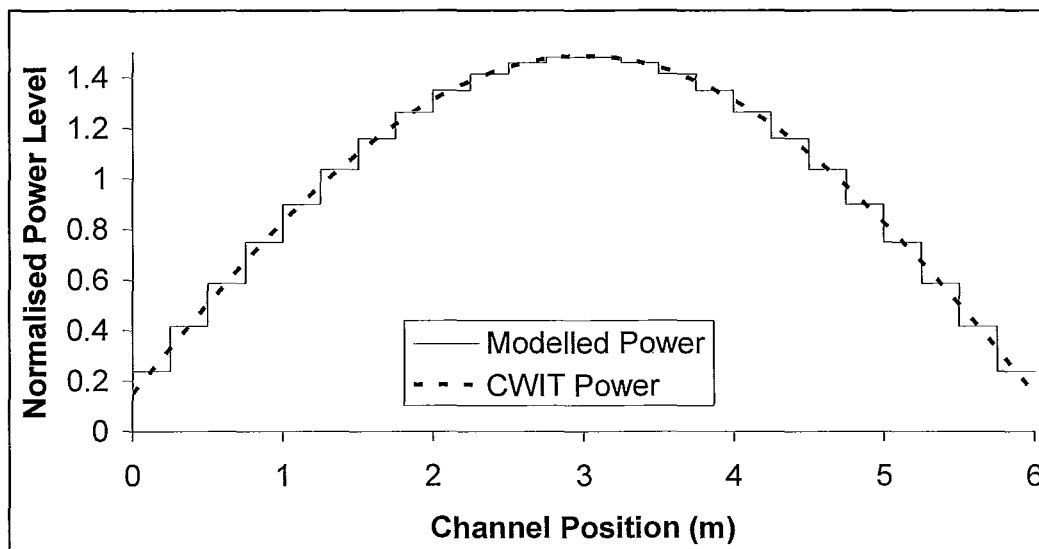
Appendix A.5 Axial Power Variation In Fuel Element Simulators

Figure 106 – CWIT and Modelled Power Level As a Function of Axial Channel Position

Appendix A.6 Courant Limit

The expression for the Courant limit in one dimension is given in equation 30. u refers to the velocity of the fluid, Δt is the timestep, and Δx is the length of the cell.

$$C > \frac{u\Delta t}{\Delta x} \quad (30)$$

APPENDIX B HIGH POWER OBSTRUCTION MODEL RESULTS

As the high power simulations were unable to reach completion in a reasonable timeframe, a definitive comparison of the predicted impact of partial asymmetrical blockages on venting times and maximum pin temperatures cannot be made; however a comparison of the development of the simulations may offer some insight into the processes that are affected, and the potential outcome.

The impact of blockage on the temperature profile of pin 10 at plane F1 is shown in Figure 107.

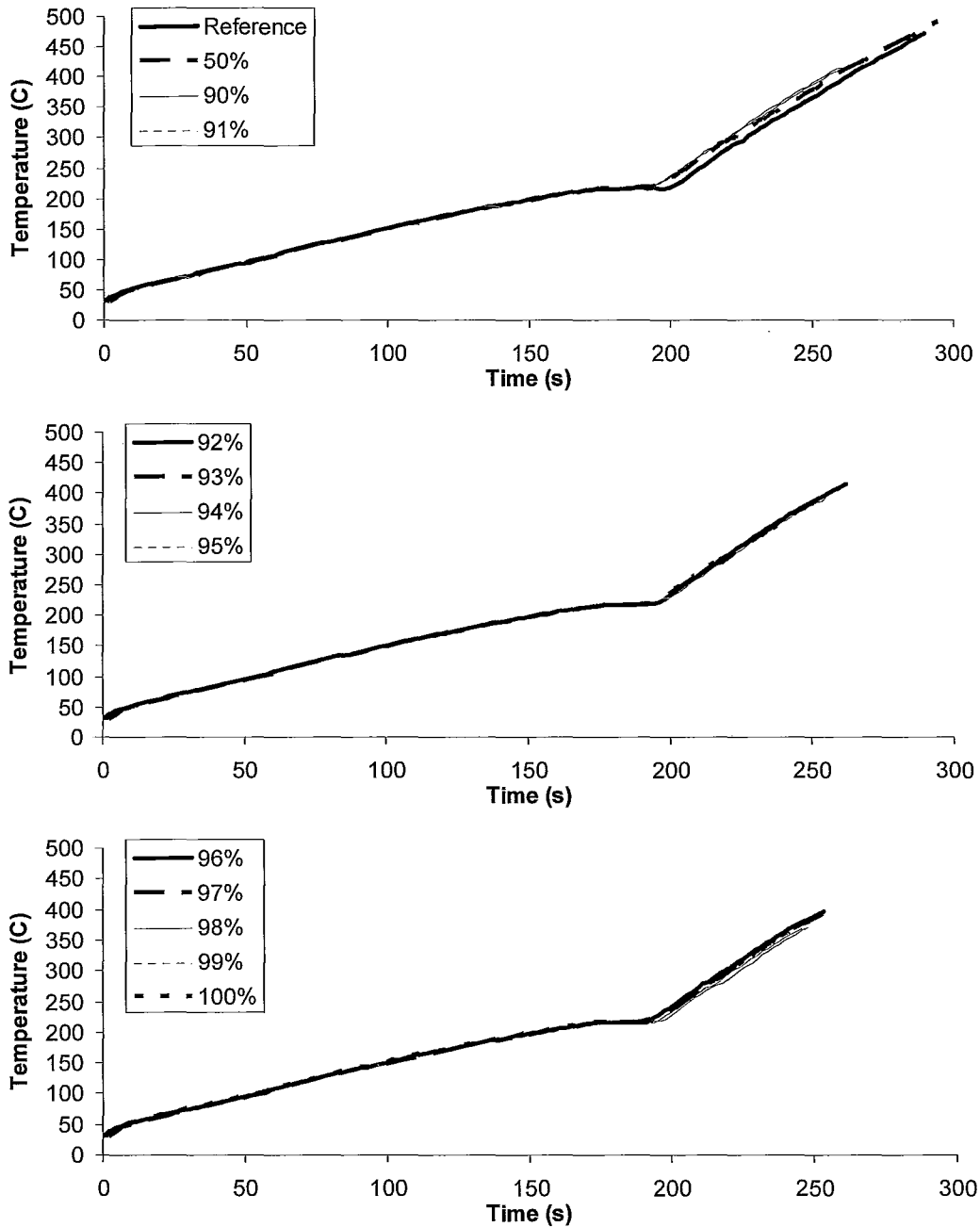


Figure 107 – Pin 10 Temperature Transient Variation With Blockage, Plane F1

The impact of blockage on the temperature transient of pin 10 at plane F1 is minimal as far as the simulations have progressed.

The flow through the feeders in each of the blockage cases demonstrates similar oscillations to those seen in the reference case (see Section 4.2.2.1). In order to clarify the overall flow in the channel, the difference between flow in the upstream and downstream feeders is shown in Figure 108.

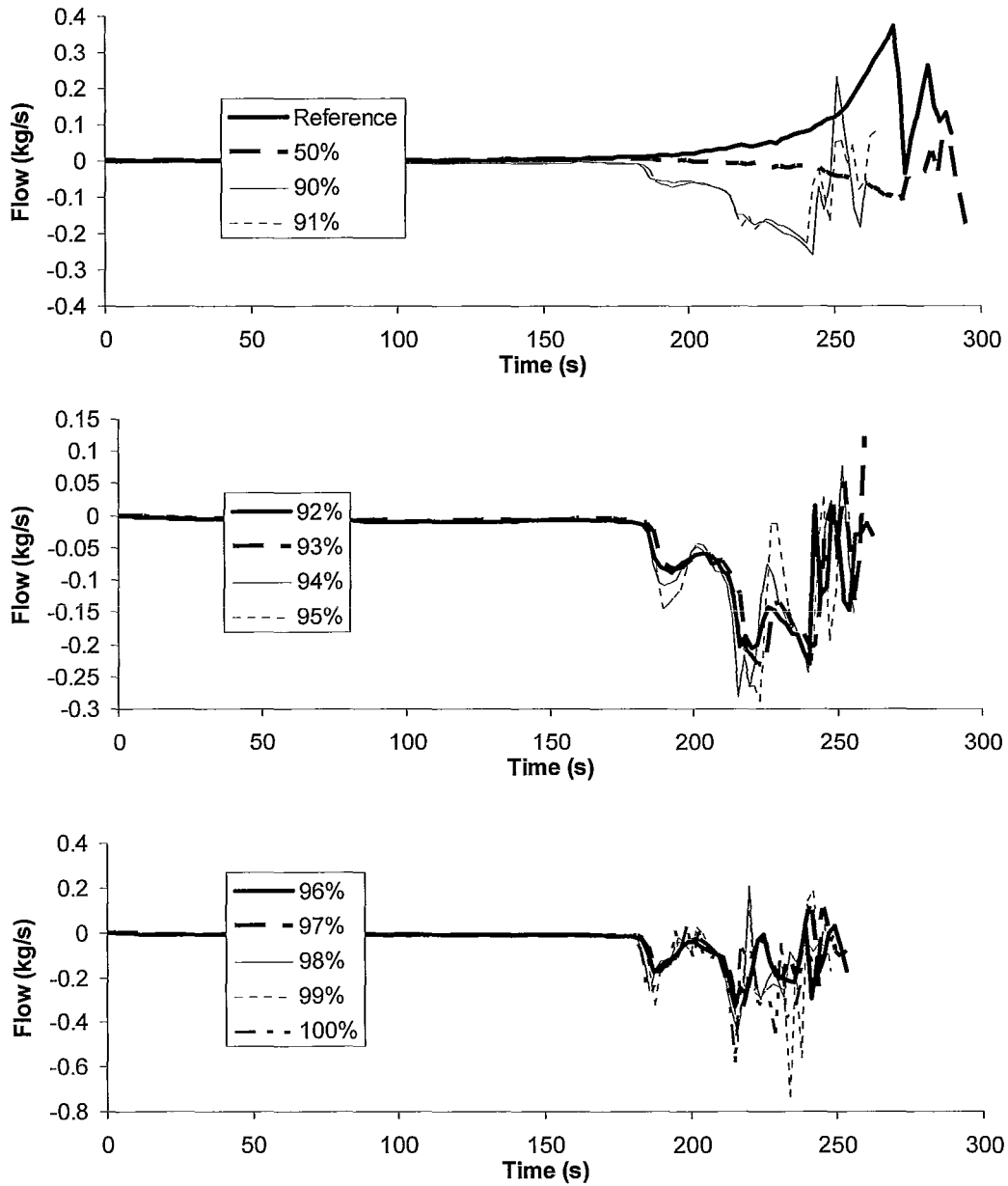
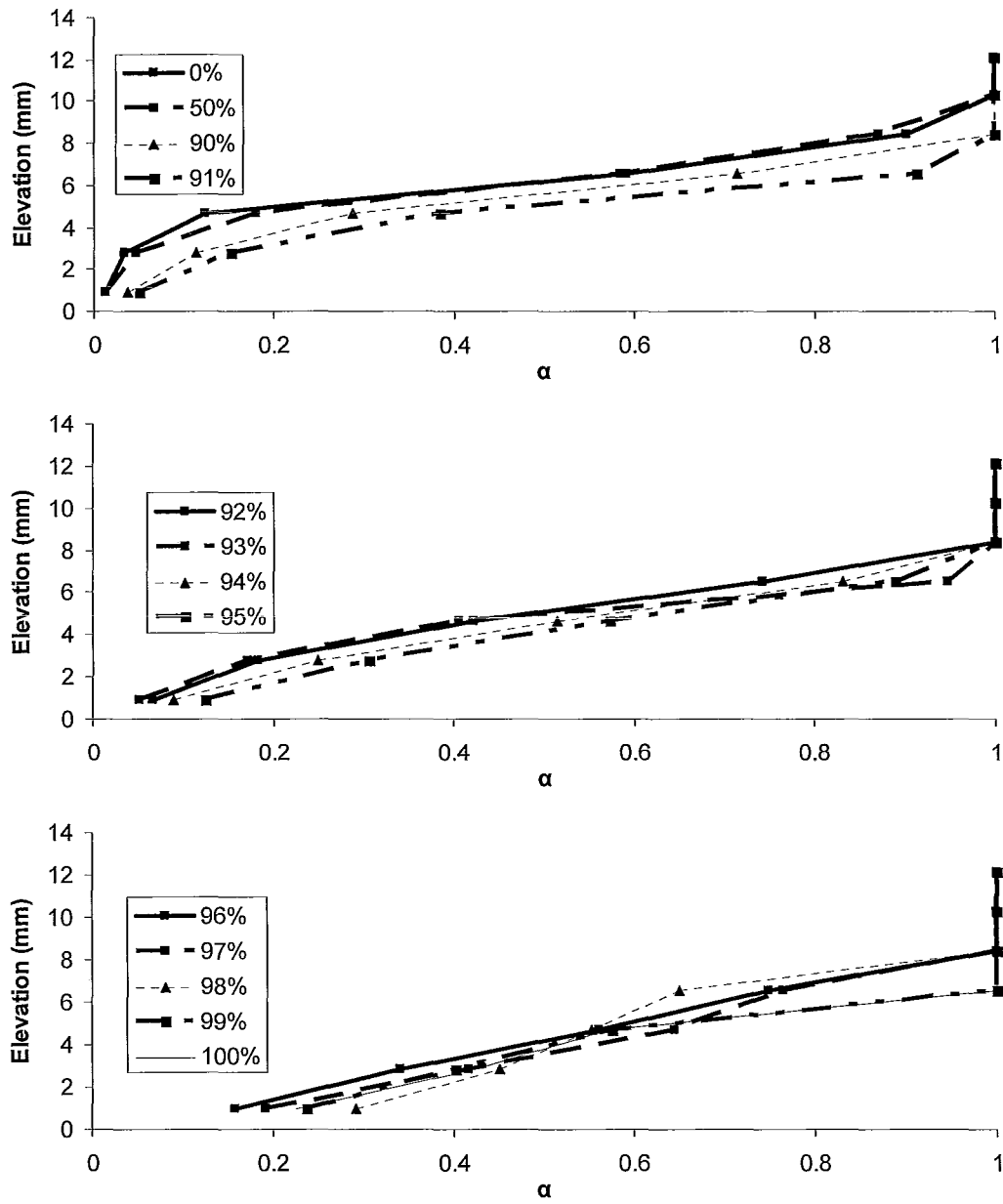


Figure 108 – Feeder Flow Difference (Upstream Flow – Downstream Flow)¹

While it was observed in Section 4.2.2.2 that a flow across the whole channel from downstream to upstream was established in the reference case, the flow is in the opposite direction for all blockage cases. This is consistent with the expected effect of fluid expansion in the asymmetrical channel resulting in flow in

the direction of least resistance (in the blockage cases, downstream). The presence of warmer liquid in the end fittings ultimately sets up a pressure differential across the channel when it reaches the feeder, accelerating the flow.

For each of the blockage cases, the vapour fraction profiles at planes B, F1, G1, and K, 245 s into the simulation are displayed in Figure 109 - Figure 112.



**Figure 109 – Vapour Fraction Profile as a Function of Blockage:
Plane B, 245 s**

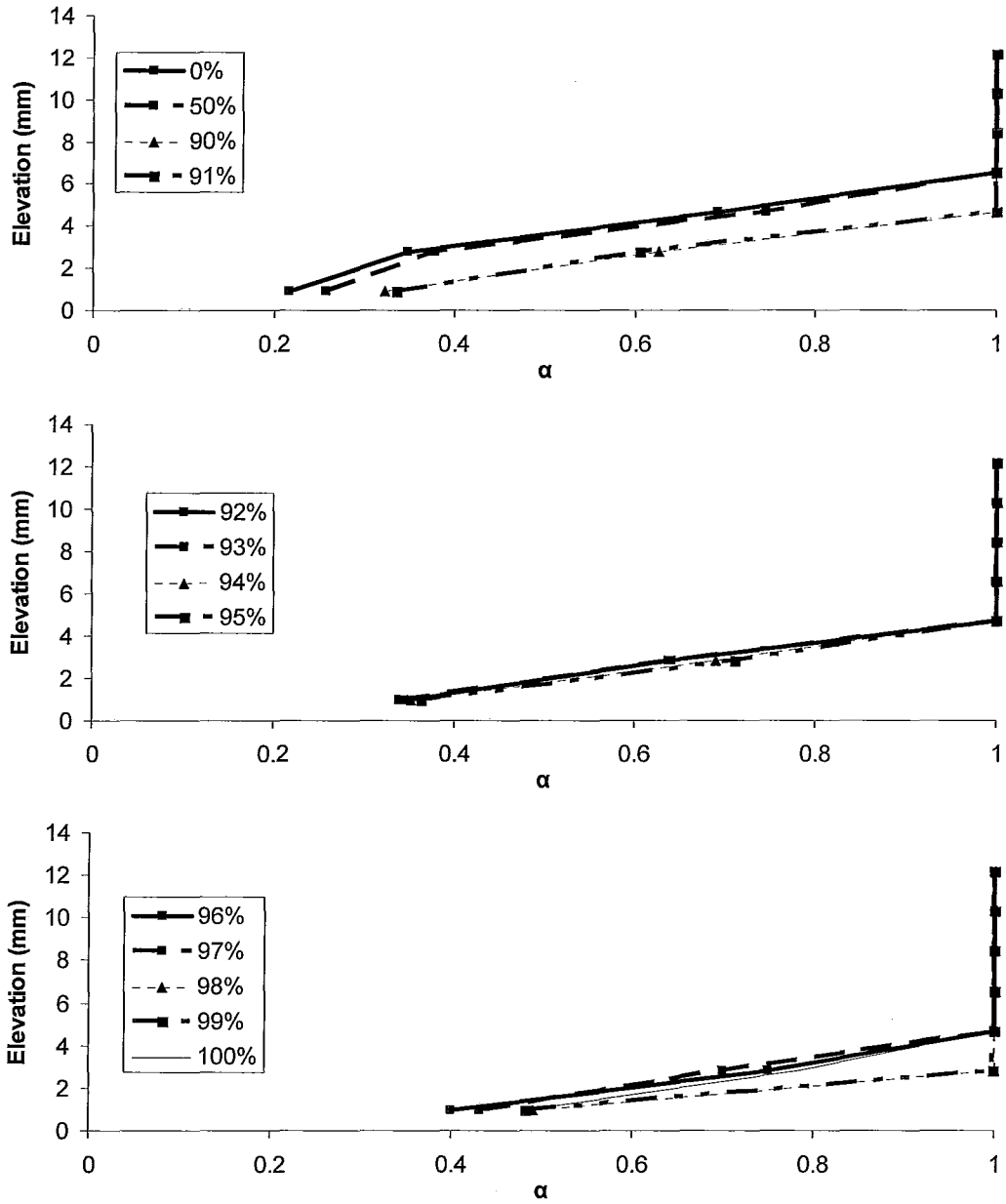


**Figure 110 – Vapour Fraction Profile as a Function of Blockage:
Plane F1, 245 s**

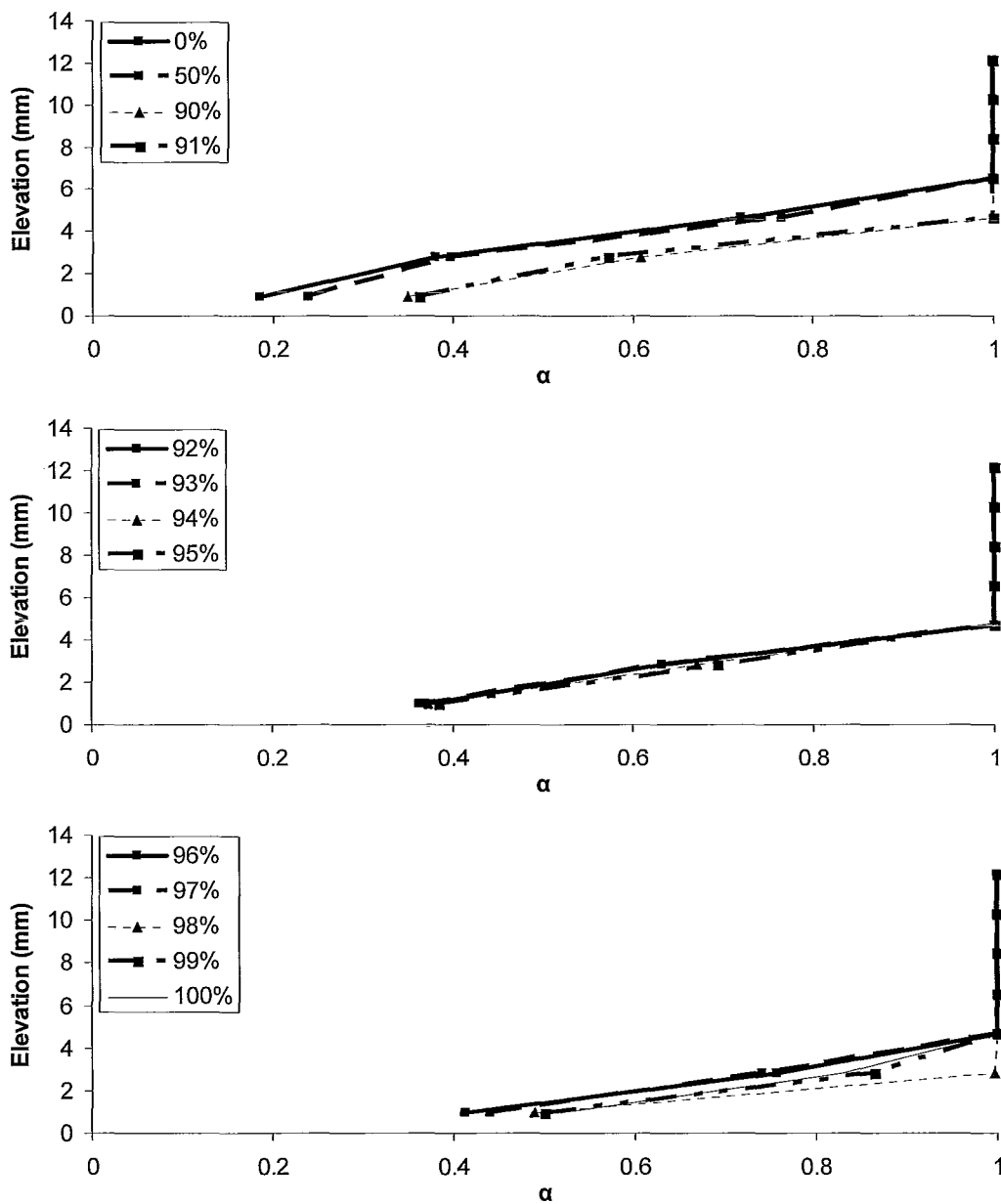


**Figure 111 – Vapour Fraction Profile as a Function of Blockage:
Plane G1, 245 s**

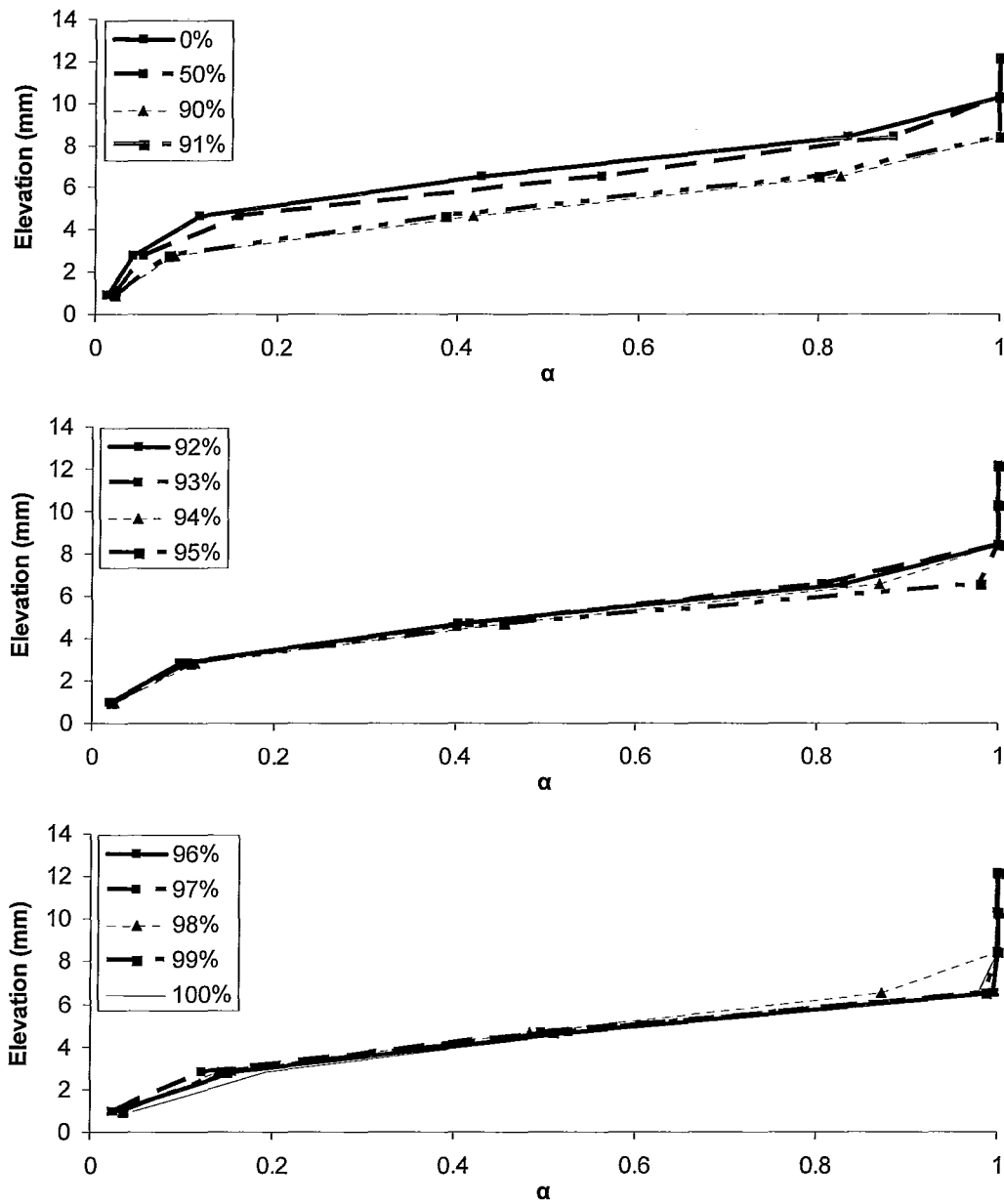


**Figure 112 – Vapour Fraction Profile as a Function of Blockage:
Plane K, 245 s**

The impact of the different blockage sizes can be seen in the variation of vapour ‘depth’ across the channel. The depth of the vapour bubble at the upstream end of the channel increases with blockage extent, consistent with

increased flow resistance slowing the migration of vapour toward the upstream end fitting. This effect is most pronounced at plane B, but persists to some extent through the other planes. The increased vapour fraction in the channel should decrease the amount of heat transported to the end fittings⁷⁰ by reducing the vapour generation rate.

The impact of blockages on the vapour temperature across the channel is examined in Figure 113 - Figure 116.

⁷⁰ With higher vapour fractions, a greater proportion of heat is expected to be stored in the pins and pressure tube relative to the end fittings.

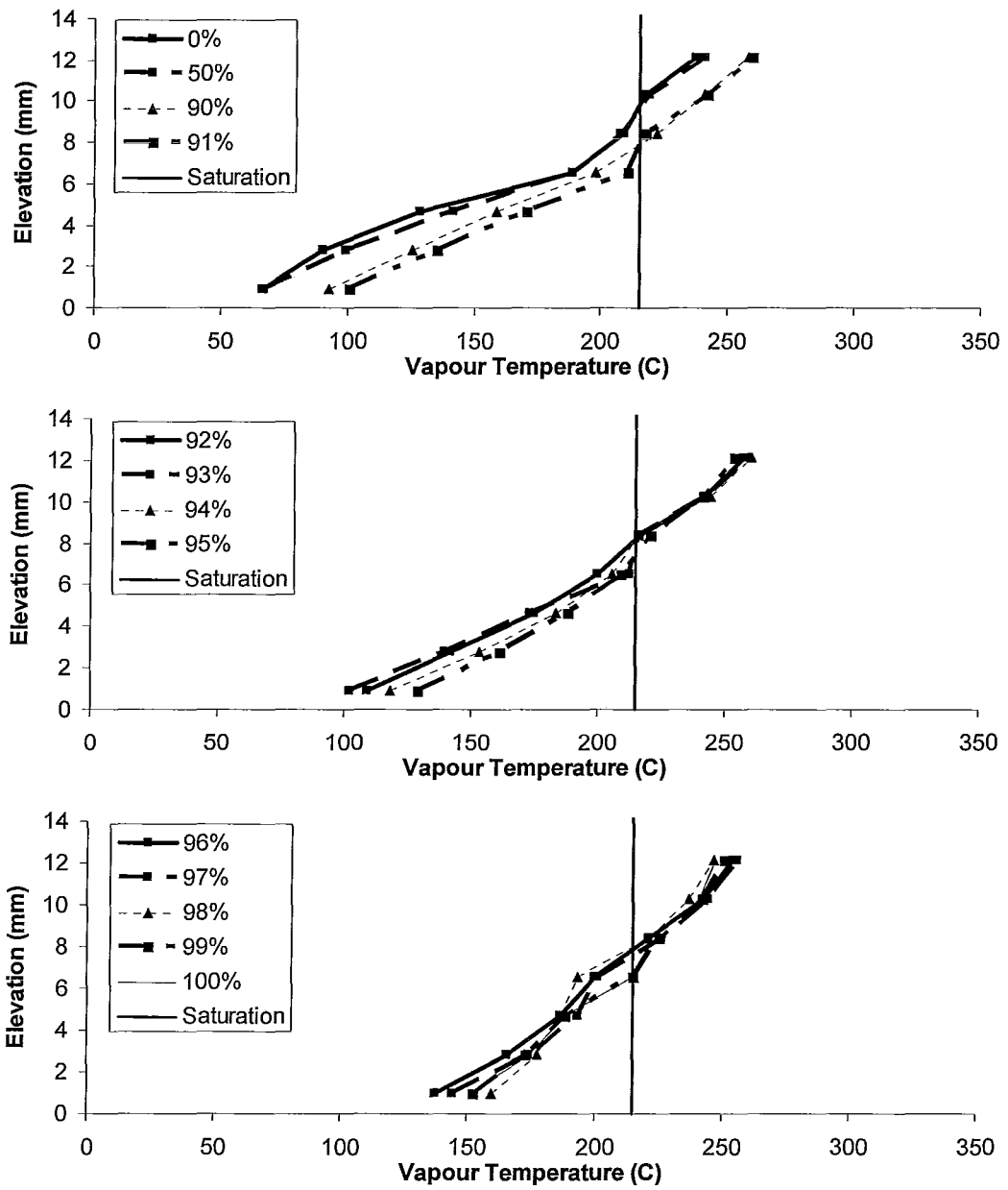


**Figure 113 – Vapour Temperature Profile as a Function of Blockage:
Plane B, 245 s**

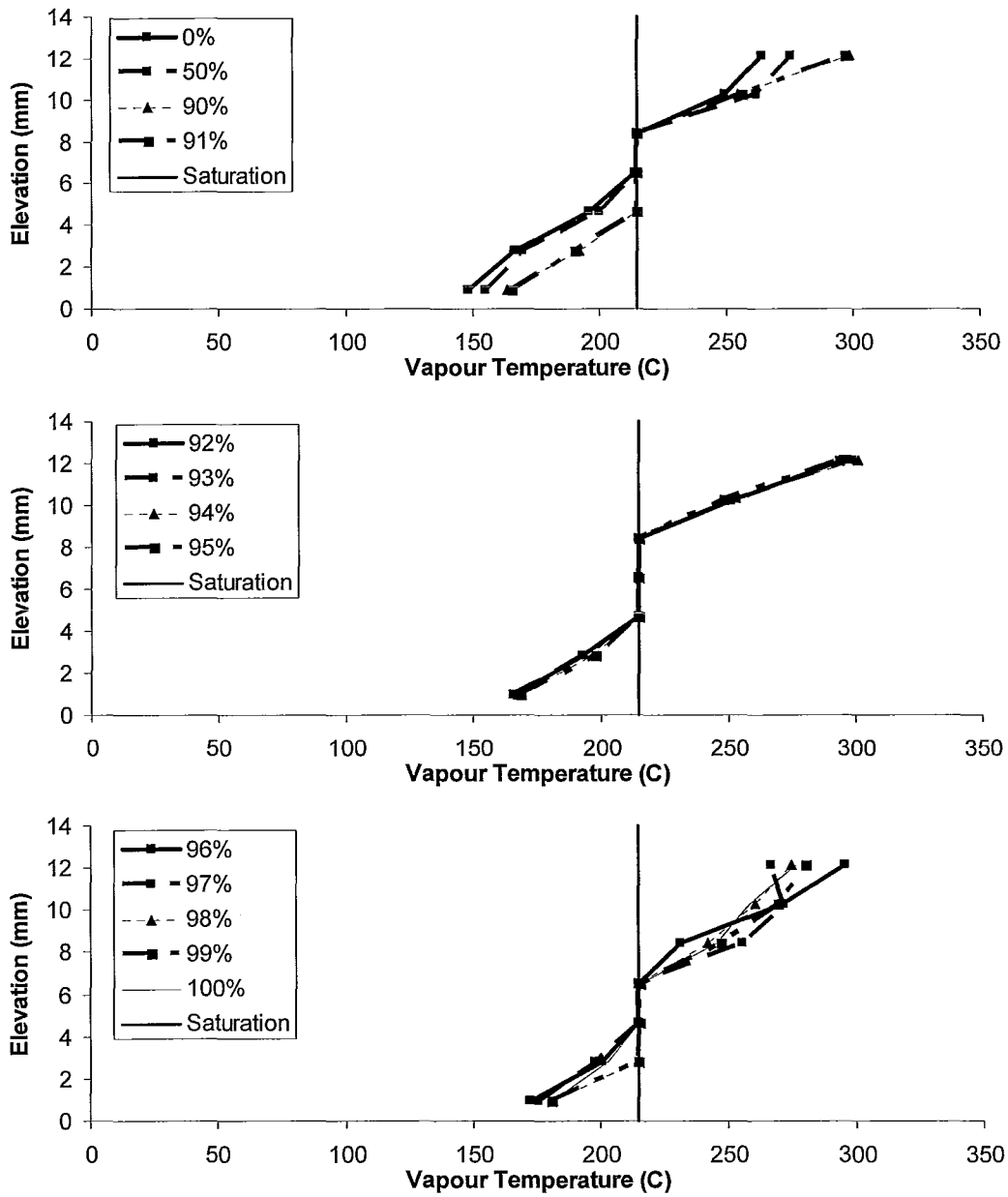


**Figure 114 – Vapour Temperature Profile as a Function of Blockage:
Plane F1, 245 s**

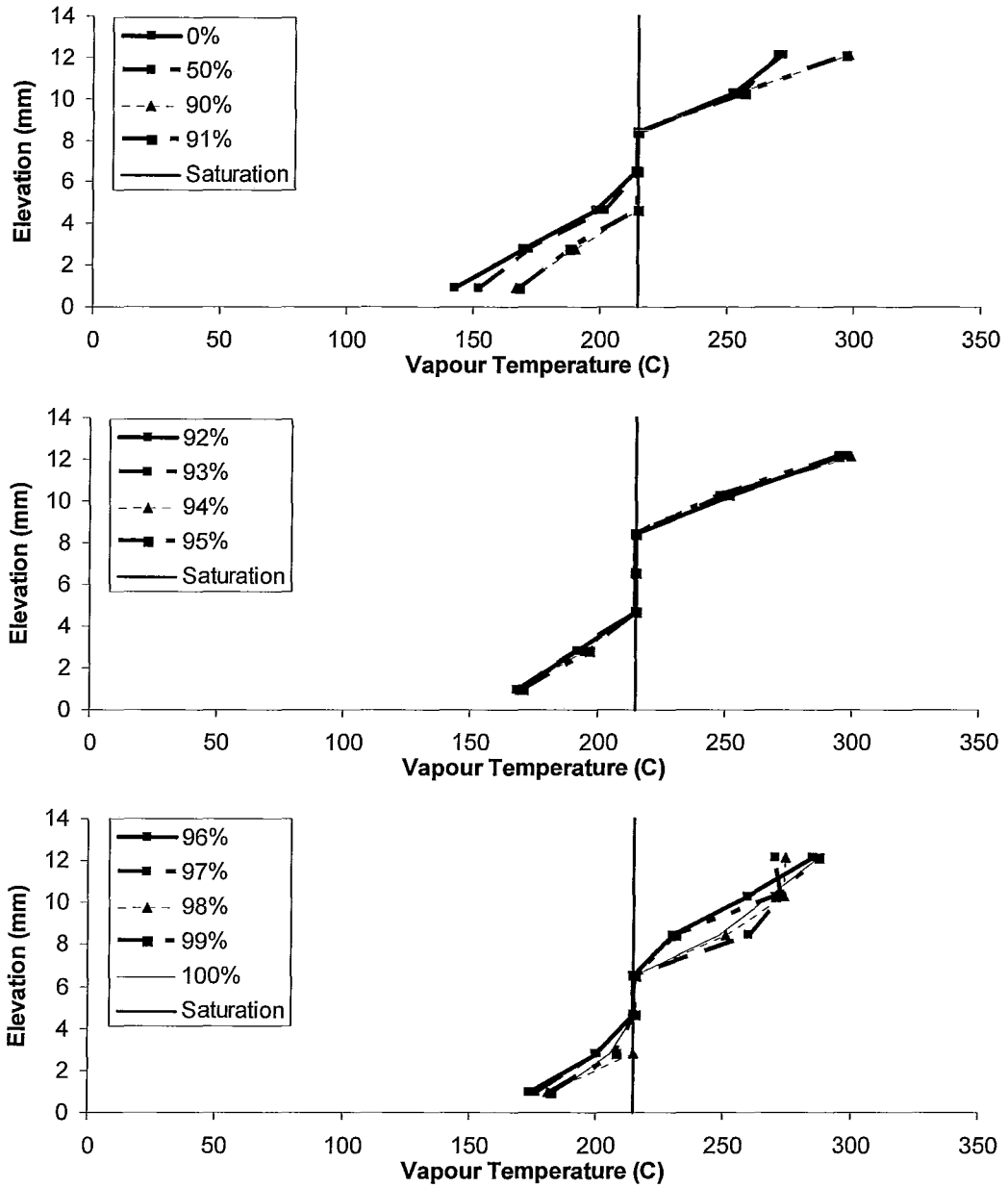


**Figure 115 – Vapour Temperature Profile as a Function of Blockage:
Plane G1, 245 s**

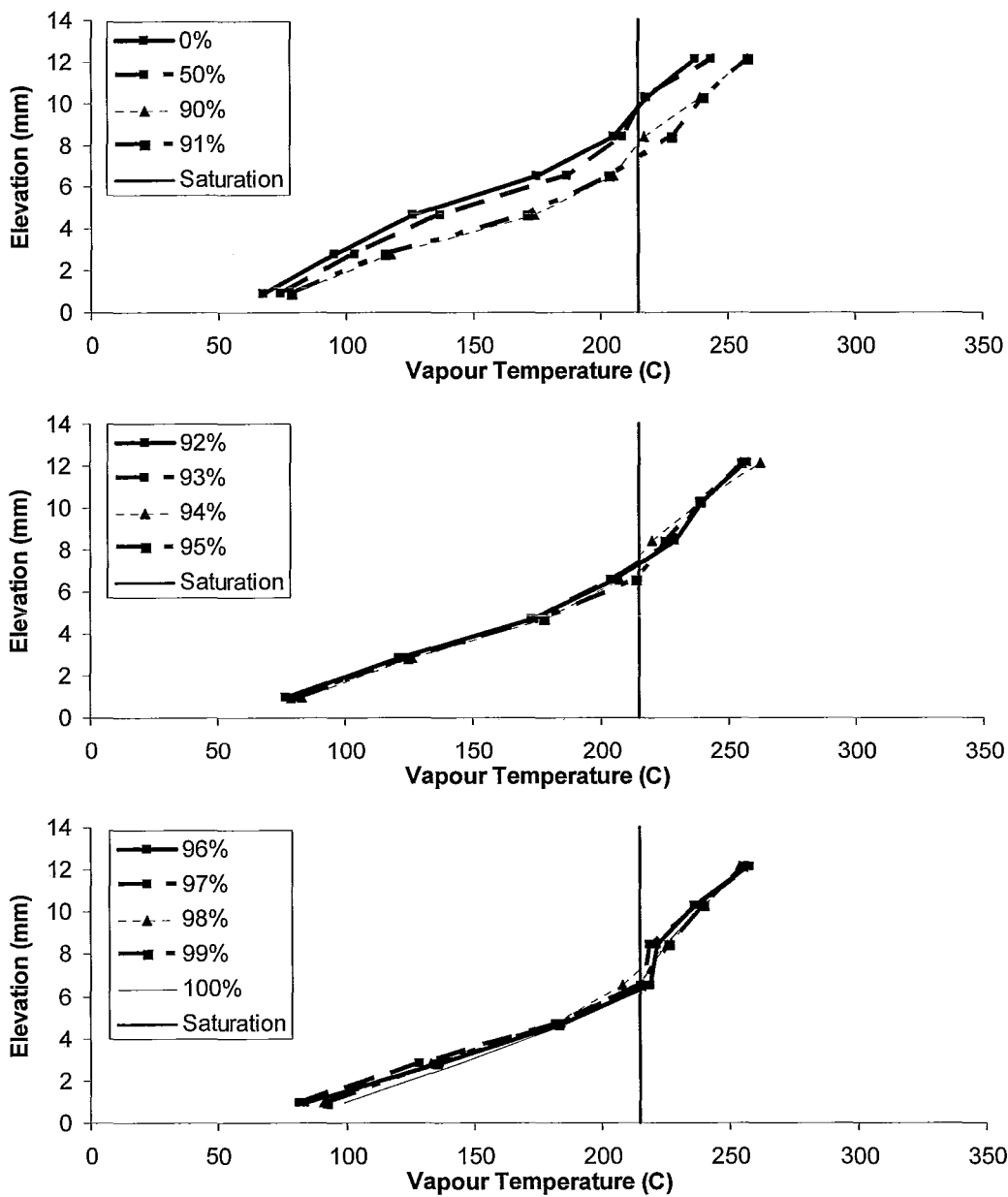


**Figure 116 – Vapour Temperature Profile as a Function of Blockage:
Plane K, 245 s**

A disturbing aspect of Figure 113 - Figure 116 is the presence of vapour at temperatures well below saturation – a non-physical result. A comparison with Figure 109 - Figure 112 indicates that these temperatures represent cells with

significant vapour fractions in some cases. Examination of the data reveals that the vapour temperatures in these cells are very close to the liquid temperatures¹. Further investigation of the subcooled boiling model¹ is warranted by these results.

Despite the questionable nature of the vapour temperature in the subcooled region of the channel, the vapour temperature profile higher in the channel is consistent with expectations. In the cells where saturated boiling takes place, the vapour temperature stays very close to saturation, while at higher elevations where the volumetric vapour fraction reaches unity, the vapour is superheated and stratified. Some increase in vapour temperature as a result of blockages can also be observed, which is consistent with the increased vapour fraction in the channel and delayed transport of vapour to the end fittings.

While the overall progress of the simulations is reasonable, an example of unexplained, non-physical behaviour is apparent in the temperature profiles of the end fittings for non-zero blockage scenarios. A comparison of the end fitting temperature profiles of the reference and 99% blockage cases is presented in Figure 117 and Figure 118. As the channel flow is in different directions for each, the temperature profile of the upstream end fitting is displayed for the reference case, and the downstream end fitting is shown for the 99% blockage case.

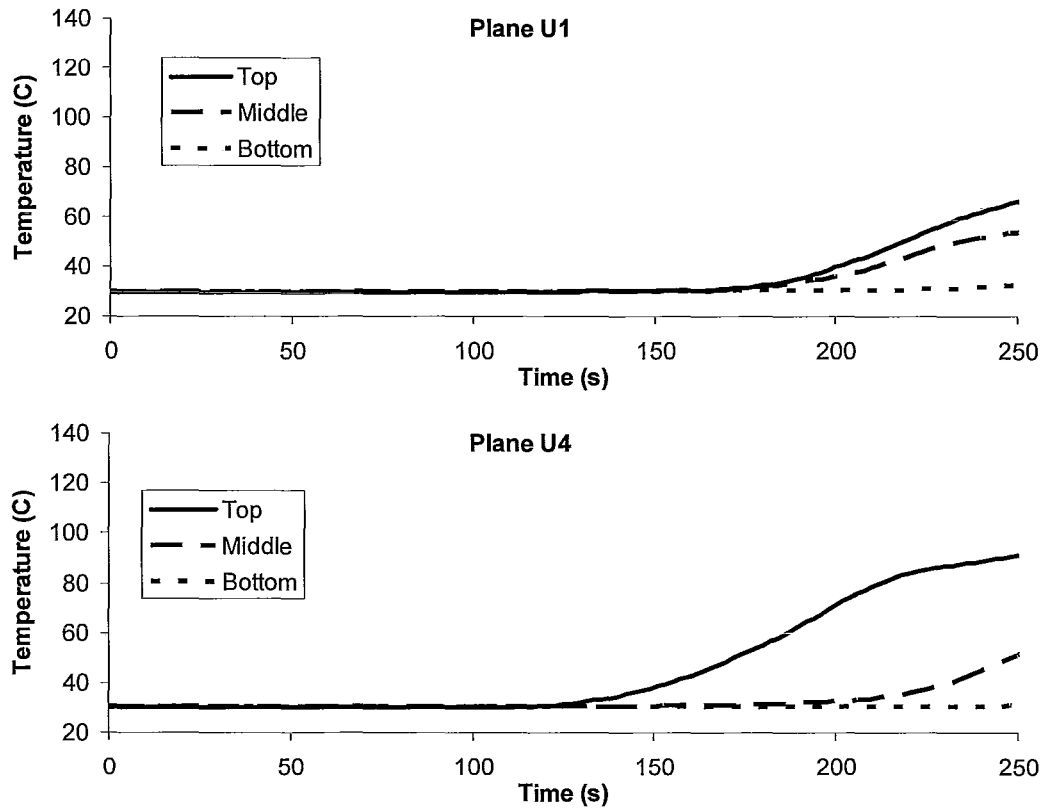


Figure 117 – End Fitting Temperature Profile, Reference Case

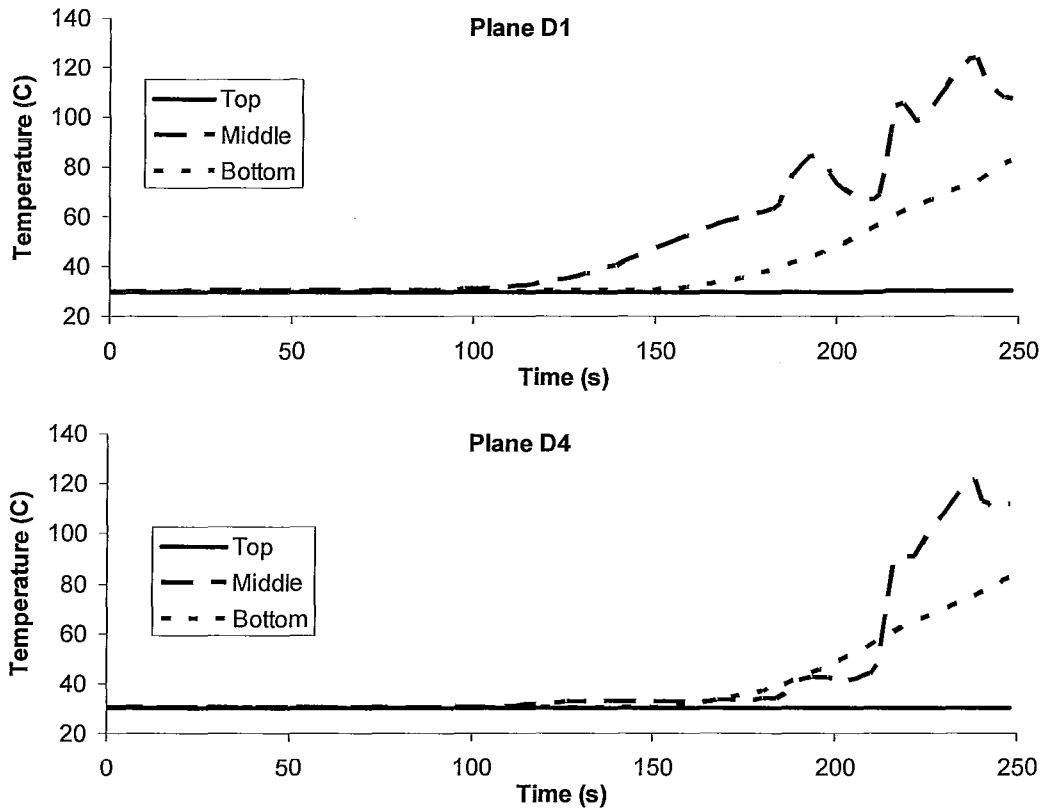


Figure 118 – End Fitting Temperature Profile, 99% Blockage Case

The temperature profile from top to bottom in the reference case is as expected, the stratification of coolant in the end fitting results in a greater temperature increase at the top of the end fitting body than at the bottom. Inexplicably, this situation is reversed for cases involving blockages, with the effect becoming more pronounced as the blockages increase. This effect appears to be associated in some way with the calculation of heat transfer from fluid to the end fitting body rather than fluid behaviour, as the presence of hot liquid in contact with the top of the end fitting has been verified. Even more baffling is the dependence of this effect on the degree of blockage at the opposite end of the channel, at 50% blockage the temperature increase at the top of the end fitting is appreciable, while at 100% it is exactly zero.

A comparison between temperature transients at the middle of the end fitting for each blockage case is shown in Figure 119.

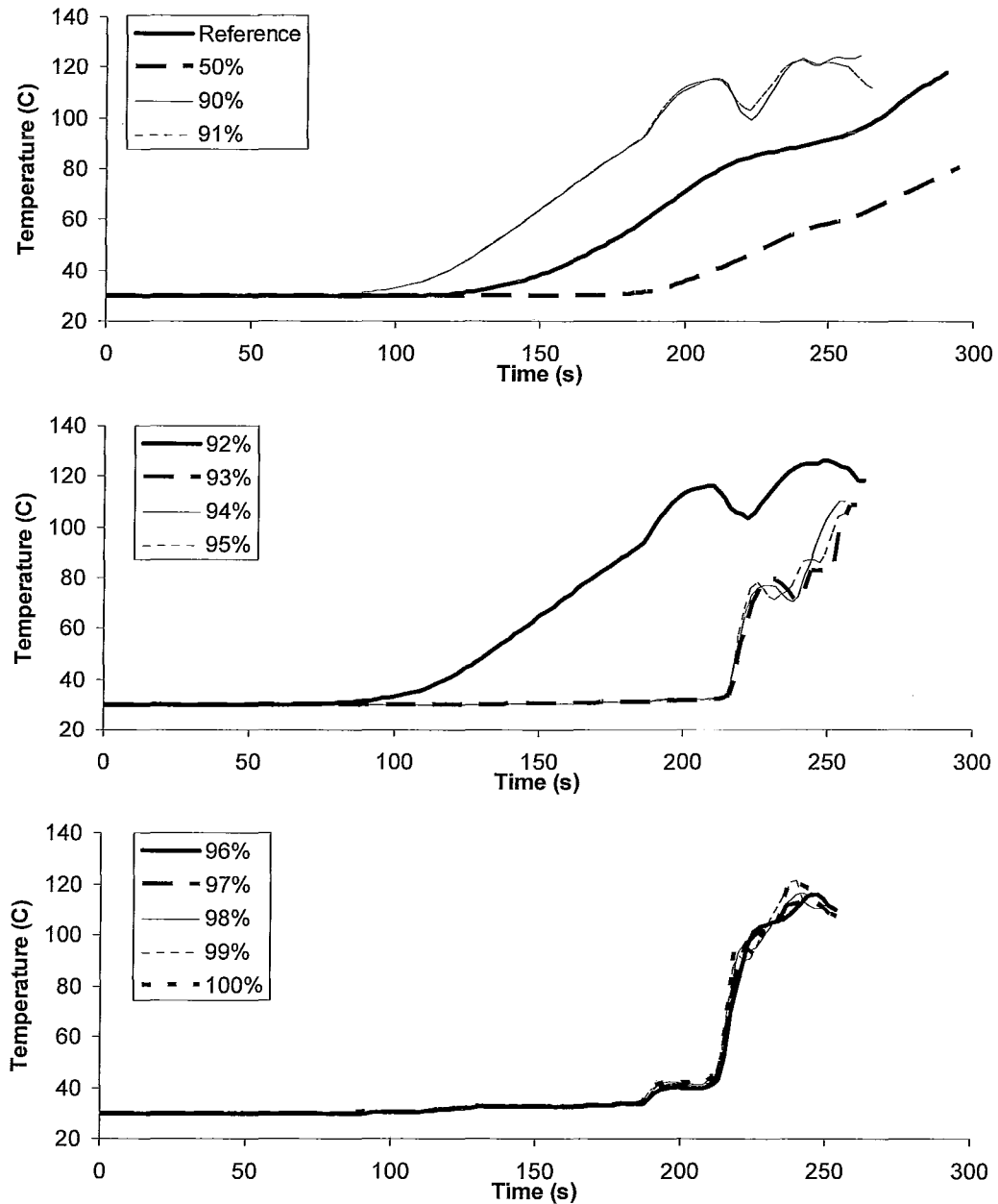


Figure 119 – Downstream End Fitting Temperature Profiles, Middle Elevation¹

While the end fitting temperature data must be viewed with some suspicion, the trend of maintained or increased end fitting heatup seen in Figure 119 can be explained by the increasing fraction of vapour transported to the

downstream end fitting as a result of flow resistance at the upstream end of the channel. This effect would be expected to be offset to some extent by decreased vapour generation rate resulting from an increased void fraction in the channel noted in Figure 109 - Figure 112.

While this result may offer some qualitative affirmation of physical intuition regarding the effect of asymmetrical blockages, the unexplained thermal behaviour of the end fitting demands that further work be done to rectify the issue before the results can be viewed with confidence.

APPENDIX C END FITTING HEAT TRANSFER COEFFICIENTS

As a rationality check, the heat transfer coefficients used by GOTHIC are considered. For the low power simulations, only the heat transfer coefficient between end fitting and liquid is considered, as no vapour is generated in these simulations.

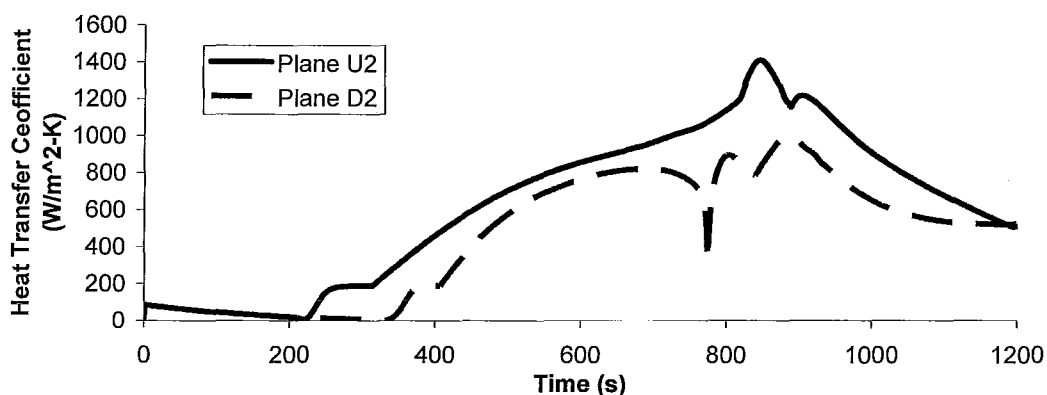


Figure 120 – Heat Transfer Coefficient Between Liquid and Top of End Fitting, Low Power Reference Case

The effect of liquid velocity on the heat transfer coefficient can be seen through a comparison with Figure 49.

At high power, both liquid and vapour phases are present, however, the data extracted from GOTHIC indicate that the heat transfer coefficient between the vapour and the end fitting is zero despite its presence. This situation calls for further investigation.

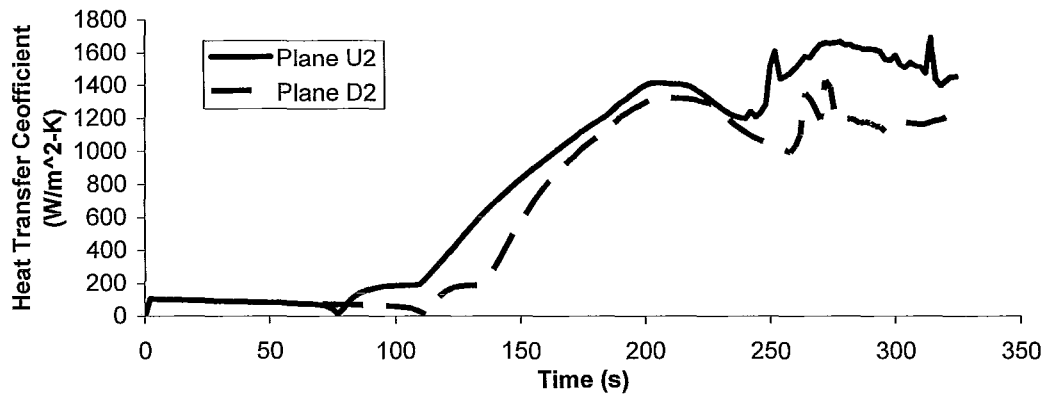


Figure 121 – Heat Transfer Coefficient Between Liquid and Top of End Fitting, High Power Reference Case

As discussed in Section 4.5.2, the heat transfer coefficient behaves non-physically for high power blockage cases. When blockages are present, the heat transfer coefficient at the top of the end fitting is zero. This is an issue that demands further study.

APPENDIX D REYNOLDS NUMBERS DURING TRANSIENTS

Figures representing the Reynolds number of liquid and vapour during the transients are presented below.

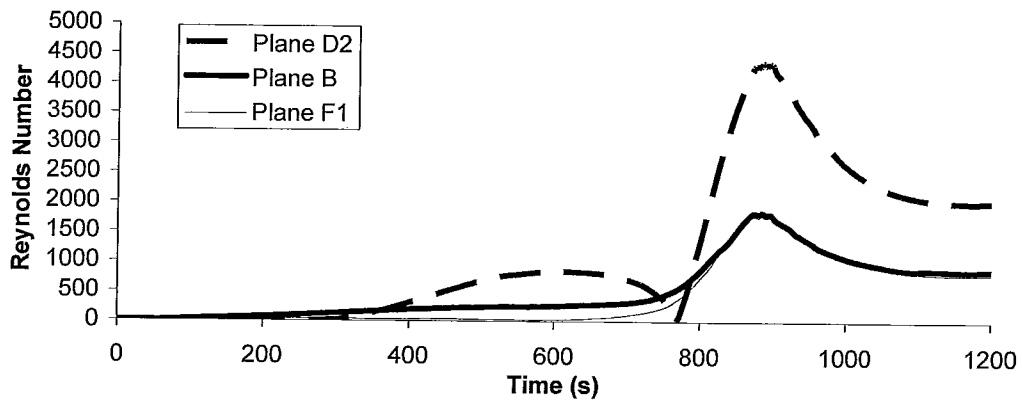


Figure 122 – Liquid Reynolds Number Transient, Low Power Reference Case

The Reynolds number transients in the low power case clearly reflect the channel flow transient (see Figure 49).

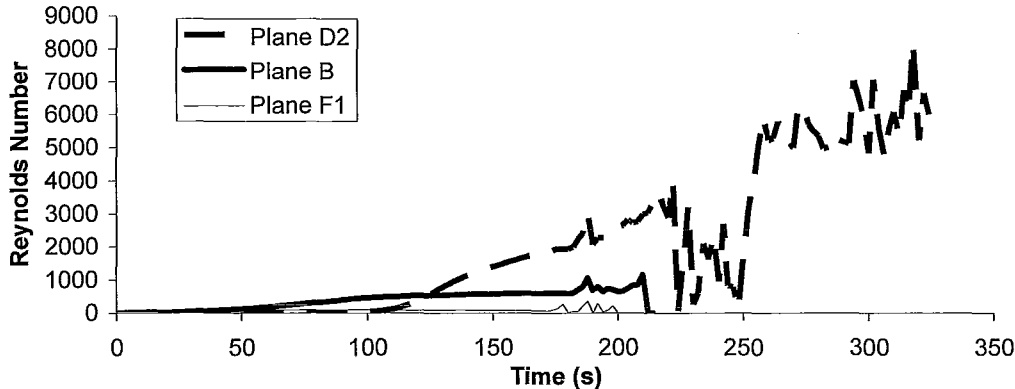


Figure 123 – Liquid Reynolds Number Transient, High Power Reference Case

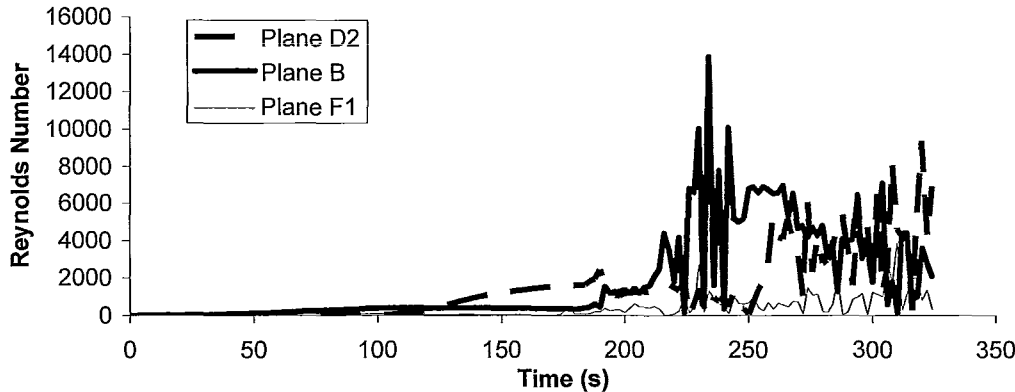


Figure 124 – Vapour Reynolds Number Transient, High Power Reference Case

APPENDIX E VERTICAL VAPOUR VELOCITY IN CENTRE OF CHANNEL

The vertical velocity of vapour in the channel during boiling may give some indication of the prevalence of splashing and froth during the transient. The vertical velocity of vapour at plane F1 is presented below.

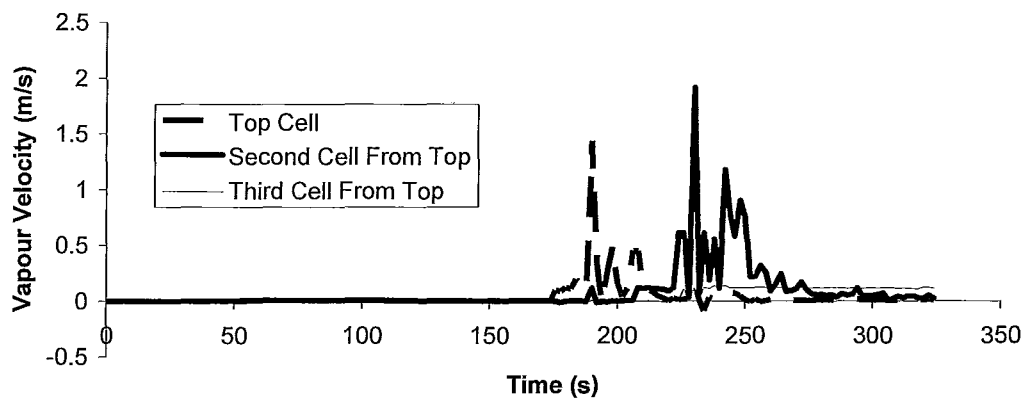


Figure 125 – Vertical Component of Vapour Velocity, Plane F1, High Power Reference Case, Linear Scale

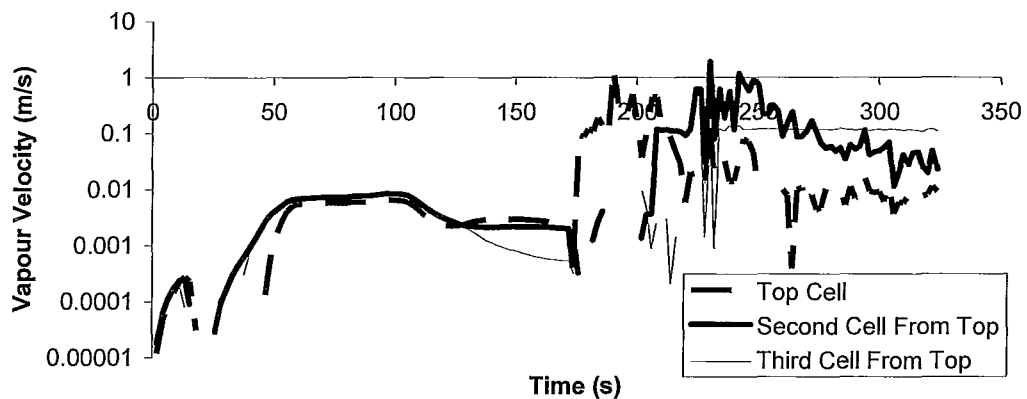


Figure 126 – Vertical Component of Vapour Velocity, Plane F1, High Power Reference Case, Log Scale